Comparative Equilibrium Denaturation Studies of the Neurotrophins: Nerve Growth Factor, Brain-Derived Neurotrophic Factor, Neurotrophin 3, and Neurotrophin 4/5†

David E. Timm,‡,§ Pieter L. de Haseth,‡ and Kenneth E. Neet*,‖

Department of Biochemistry, Case Western Reserve University, Cleveland, Ohio 44106, and Department of Biological Chemistry, UHS/Chicago Medical School, 3333 Green Bay Road, North Chicago, Illinois

Received November 16, 1993; Revised Manuscript Received February 8, 1994⊛

ABSTRACT: The neurotrophins are a family of small dimeric proteins required for the development and survival of vertebrate neurons. Solvent denaturation studies were used to compare recombinant human nerve growth factor (hNGF), brain-derived neurotrophic factor (BDNF), neurotrophin 3 (NT-3), and neurotrophin 4/5 (NT-4/5) to nerve growth factor isolated from mouse submaxillary glands (mNGF). Although greater than 50% sequence identity is conserved among this family, significant structural differences were revealed by the folding and unfolding of these proteins. Denaturation in guanidine hydrochloride and renaturation at pH 7 and 3.5 were monitored by fluorescence intensity, fluorescence polarization, and circular dichroism. The midpoint of equilibrium unfolding curves for all four neurotrophins was independent of the technique but was dependent on protein concentration, indicating that a two-state model involving native neurotrophin dimers and denatured neurotrophin monomers (N_2 = 2D) describes the equilibrium between folded and unfolded neurotrophins. The conformational stabilities of the dimeric neurotrophins revealed that mNGF had the lowest conformational stability (19.3 kcal/mol); hNGF, NT-3, and NT-4/5 had intermediate stabilities, and BDNF had the highest stability (26.4 kcal/mol). Recovery of native spectroscopic characteristics upon removal of denaturant indicated that the unfolding process is reversible. Accordingly, unfolding and refolding curves were coincident for mNGF or NT-4/5 at pH 7 and 3.5 and for BDNF at pH 3.5. However, BDNF and NT-3 unfolding and refolding curves were not coincident at pH 7. The stability of the neurotrophins decreased as pH decreased, with compact monomeric intermediates (N_2 = [2I] = 2D) becoming populated below pH 4. The differences in stability, pH dependence, and coincidence of refolding curves distinguish the homologous structures of the neurotrophins.

Neurotrophins are target-derived factors required for the development and survival of specific verebrate neuronal populations. The neurotrophin family is comprised of nerve growth factor (NGF), brain-derived neurotrophic factor (BDNF),[1] neurotrophin 3 (NT-3), and neurotrophin 4/5 (NT-4/5). These factors exhibit different cell type specificities and receptor binding characteristics that are presumably defined by sequence and structural differences (Bradshaw et al., 1993).

The structure of NGF, the first neurotrophin identified, is well characterized. The NGF monomer contains 118 residues and three intramolecular disulfide bonds (Angeletti et al., 1973a,b). The NGF subunits associate as dimers through strong noncovalent interactions having a subpicomolar dissociation constant (Bothwell & Shooter, 1977). The three-dimensional crystal structure of mNGF (McDonald et al., 1991) reveals that the NGF monomers are comprised of four central antiparallel β-strands with exposed loop regions at either end of the molecule. The monomers dimerize in a roughly parallel arrangement through hydrophobic interactions between the central β-sheet structures.

Approximately 55% sequence identity is conserved among the neurotrophins. All six cysteine residues are universally conserved among the family, and the highest sequence homologies occur in residues comprising the four central β-strands of the mNGF structure (McDonald et al., 1991; Ebendal, 1992; Bradshaw et al., 1993). On the basis of these homologies, the neurotrophin structures are all expected to be similar to the mNGF structure. The neurotrophins have also been grouped in a "cystine-knot" structural superfamily, which includes platelet-derived growth factor BB and transforming growth factor β1 (McDonald & Hendrickson, 1993).

Several recent studies have characterized the stability, conformation, and biophysical properties of the neurotrophins. Equilibrium denaturation of mNGF in Gdn-HCl at pH 7 has been described by a two-state model involving native dimeric and denatured monomeric mNGF (N_2 = 2D), and mNGF was found to have a high thermodynamic stability of 19.3 kcal/mol (Timm & Neet, 1992). Recombinant human NGF, BDNF, and NT-3 have been shown to associate as dimers (Radziejewski et al., 1992; Narhi et al., 1993a,b) and to undergo cooperative unfolding in Gdn-HCl (Radziejewski et al., 1992); however, thermodynamic analysis of the denaturation curves was not reported. Spectroscopic analysis of mNGF, hNGF, BDNF, and NT-3 by CD and FTIR (Timm & Neet, 1992; Radziejewski et al., 1992; Narhi et al., 1993a) has shown that the neurotrophins all have high β-sheet content

† This work was supported by the National Institutes of Health, Grant NS24380, and a National Science Foundation equipment grant (DIR88-20739). D.E.T. was supported by a NIH training grant (GM08056).

* Author to whom correspondence should be addressed [telephone (708) 578-3220; fax (708) 578-3240].

‡ Case Western Reserve University.

§ Present address: Structural Molecular Biology, Unit, Birkbeck College, London WC1E 7HX, U.K.

‖ Chicago Medical School.

⊛ Abstract published in *Advance ACS Abstracts,* March 15, 1994.

[1] Abbreviations: hNGF, human nerve growth factor; mNGF, mouse nerve growth factor; BDNF, brain-derived neurotrophic factor; NT-3, neurotrophin 3; NT-4/5, neurotrophin 4/5; Gdn-HCl, guanidine hydrochloride; CD, circular dichroism; Gdn50, Gdn-HCl denaturation curve midpoint; $\Delta G_D^{H_2O}$, conformational stability.

0006-2960/94/0433-4667$04.50/0

but small structural differences exist among family members. Moreover, estimates of secondary structure elements vary by several fold in different studies (Radziejewski et al., 1992; Narhi et al., 1993a). The studies presented here were undertaken to quantitate the stabilities of recombinant human NGF, BDNF, NT-3, and NT-4/5 and to address the noncoincidence of recombinant BDNF and NT-3 unfolding and refolding curves (Radziejewski et al., 1992) by studying equilibrium denaturation at low pH. Significant differences between the neurotrophin structures are revealed by the spectroscopic properties, conformational stabilities, and behavior of these proteins in denaturant solutions.

EXPERIMENTAL PROCEDURES

Proteins and Reagents. The mNGF was purified from mouse submaxillary glands as the 7S complex; the subunits were separated as previously described (Stach et al., 1977; Smith et al., 1968; Woodruff & Neet, 1986) and stored at pH 4, −20 °C. The mNGF was further purified by reversed-phase high-performance chromatography as described (Petrides & Shooter, 1986) and lyophilized to dryness. The mNGF ran as a single band on Coomassie blue-stained sodium dodecyl sulfate polyacrylamide gels after electrophoresis, and concentrations were determined using $A_{280}^{0.1\%} = 1.6$. Recombinant human BDNF and NT-3 were provided by Amgen, Inc. (Thousand Oaks, CA); NT-4/5 was provided by Regeneron, Inc. (Tarrytown, NY); and hNGF was provided by Cephalon, Inc. (Westchester, PA). Each of these proteins was characterized by the manufacturer as greater than 90% homogeneous; experimental concentrations were based on dilutions of stock solutions from concentrations determined by the manufacturers. All solutions were prepared using distilled, deionized water and ultrapure grade reagents. The Gdn-HCl was purchased from Boehringer Mannheim, ICN, and U.S. Biochemicals. Citric acid was purchased from J. T. Baker, Inc. Sodium acetate and sodium phosphate were purchased from Sigma Chemical Co.

Equilibrium Denaturation of the Neurotrophins. Equilibrium denaturation was performed by incubating individual samples of neurotrophins at the indicated Gdn-HCl concentrations. To measure unfolding, samples were equilibrated in Gdn-HCl for 48–72 h prior to fluorescence measurements. To measure refolding, the samples were initially incubated for 2–24 h at Gdn-HCl concentrations sufficient for complete unfolding (>4 M Gdn-HCl). The samples were then diluted to the final Gdn-HCl concentration and equilibrated for 72 h. These equilibration times were previously determined to be adequate for mNGF unfolding and refolding (Timm & Neet, 1992). Solutions contained 50 mM Na_2HPO_4 and 50 mM NaH_2PO_4 as a buffer at neutral pH, 100 mM sodium acetate as a buffer at pH 4, and 100 mM citrate/phosphate buffer in the pH 3–7 range. All incubations and measurements were performed at room temperature (23 ± 2 °C).

Fluorescence Measurements. Fluorescence measurements were made using a Perkin-Elmer LS-5B spectrofluorometer, and emission spectra were recorded on a Perkin-Elmer GP-100 printer. Samples were excited at 295 nm for measuring tryptophan fluorescence. Measurements were made using Helma quartz microcuvettes containing sample volumes of 250–300 μL. The fraction of denatured protein, f_d, was calculated as the ratio of the difference between the observed fluorescence intensity (Y) and the native intensity (Y_n) to the difference between the native and denatured (Y_d) intensities (Pace, 1986):

$$f_d = (Y - Y_n)/(Y_d - Y_n) \quad (1)$$

Steady-state fluorescence polarization was measured using a manual polarizer accessory installed in the emission and excitation paths. Polarization measurements were made with excitation and emission wavelengths of 295 and 340 nm, respectively. Polarization was calculated as

$$P = [(I_{II})_V - G(I_I)_V]/[(I_{II})_V + G(I_I)_V] \quad (2)$$

where

$$G = (I_{II})_H/(I_I)_H \quad (3)$$

The emission intensity is measured parallel $(I_{II})_V$ and perpendicular $(I_I)_V$ to the vertically polarized plane of excitation light, and the correction factor (G) is calculated by measuring the parallel and perpendicular emission intensities following excitation with horizontally polarized light. This correction factor had a value of 1.4 and accounts for the different efficiencies that the excitation and emission monochromators have for horizontally and vertically polarized light (Lakowicz, 1983). The fraction of denatured protein (f_d) was calculated from polarization data using the following equation to account for the change in relative fluorescence intensity that occurs upon denaturation (Lakowicz, 1983):

$$f_d = [(P - P_n)/(P_d - P)R + (P - P_n)] \quad (4)$$

R is the ratio of the denatured to native fluorescence intensities at each denaturant concentration, P is the observed polarization, and P_n and P_d are the native and denatured polarization values, respectively. The correction, R, results in a slight decrease in the denaturation curve midpoint.

Conformational Stability Calculations. Denaturation curves were evaluated according to the linear extrapolation method (Pace, 1986) for dimeric proteins (Bowie & Sauer, 1989). Briefly, an equilibrium constant, K_D, is calculated at each point in the denaturation curve transition according to the fraction of unfolded protein, f_d. According to the two-state model for denaturation of dimeric proteins, K_D is defined as

$$K_D = 2Pt[f_d^2/(1 - f_d)] \quad (5)$$

where Pt is the concentration of protein monomer (Bowie & Sauer, 1990). The linear dependence of the Gibbs free energy of unfolding ($\Delta G_D = -RT \ln[K_D]$) on the denaturant concentration observed in the transition region is assumed to continue to zero denaturant concentration (Schellman, 1978), described as

$$\Delta G_D = \Delta G_D^{H_2O} - m[\text{denaturant}] \quad (6)$$

where $\Delta G_D^{H_2O}$ represents the difference in Gibbs free energy between the unfolded and folded protein in the absence of denaturant. The neurotrophin conformational stabilities were determined by iterative fitting of denaturation curves to the above parameters using the program BASICFIT, which employs a Marquadt gradient-analytical search (Bevington, 1969).

Circular Dichroism Measurements. Circular dichroism spectra were recorded using a Jasco J600 spectropolarimeter. CD data were processed using software provided by Jasco and a Wyse (IBM compatible) computer. Measurements were made using neutrophin concentrations of 50 μg/mL in 1-mm Helma quartz cuvettes. Spectra were recorded as an average of six scans from 260 to 184 nm at 10 nm/min.

RESULTS

Neurotrophin Intrinsic Fluorescence Properties. Denaturation of the recombinant neurotrophins at pH 7 was followed

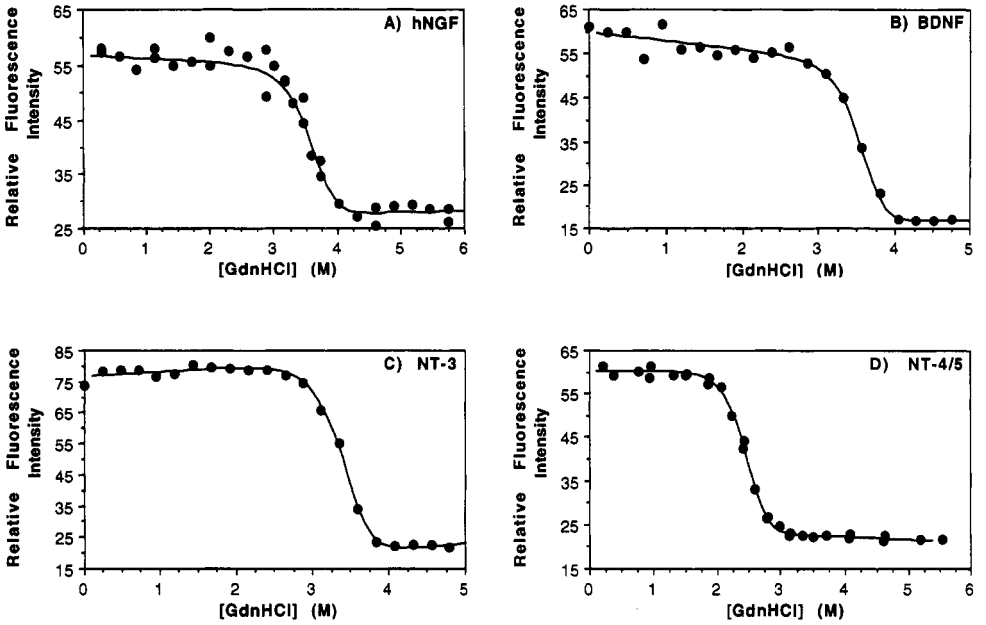

FIGURE 1: Neurotrophin equilibrium unfolding curves based on relative fluorescence intensity. The relative fluorescence intensity of (A) 30 μg/mL hNGF, (B) 50 μg/mL BDNF, (C) 50 μg/mL NT-3, and (D) 10 μg/mL NT-4/5 is plotted vs Gdn-HCl concentration. The solutions were buffered at pH 7 with 100 mM sodium phosphate. The solid lines were generated by nonlinear least-squares analysis of the data according to the two-state model for denaturation of neurotrophin dimers (Experimental Procedures). The neurotrophin conformational stabilities and the dependence of their stabilities on denaturant concentration derived from these fits are listed in Table 1.

by measuring intrinsic tryptophan fluorescence intensity and fluorescence polarization as a function of Gdn-HCl concentration. Fluorescence emission following excitation at 295 nm is due primarily to Trp residues (Brand & Witholt, 1967; Lakowicz, 1983). Conserved Trp residues are found in the neurotrophins at positions 21, 76, and 99, relative to the mNGF sequence. An additional Trp 101 occurs in NT-3 and NT-4/5. Fluorescence emission spectra for the mNGF, hNGF, BDNF, and NT-3 have been presented previously (Timm & Neet, 1992; Radziejewski et al., 1992; Narhi et al., 1993a,b). The mNGF and hNGF had the lowest relative fluorescence intensities, which were approximately 80% of the BDNF and NT-4/5 intensities and 60% of the NT-3 intensity.[2] The mNGF, hNGF, and BDNF fluorescence emission maxima occurred near 340 nm, and NT-4/5 and NT-3 had maxima at 338 and 336 nm, respectively. Denaturation of the neurotrophins results in decreased relative fluorescence intensity (Figure 1) and an increase in the emission maximum to about 352 nm (Timm & Neet, 1992; Radziejewski et al., 1992).

Fluorescence polarization is sensitive to fluorophore rotational mobility, decreasing with increasing mobility (Lakowicz, 1983). The native and denatured steady-state polarization values for the neurotrophins fell in two groups (Figure 2; Table 1). The fluorescence polarization of NGF, hNGF, and BDNF decreased from approximately 0.15 to 0.10 upon denaturation. In contrast, NT-3 and NT-4/5 polarization values increased slightly upon denaturation from about 0.08 to about 0.10.

Two-State Model (N_2 = 2D) for Neurotrophin Unfolding in Gdn-HCl. Monophasic, sigmoidal curves characteristic of cooperative protein unfolding transitions resulted when the neurotrophin fluorescence properties were plotted vs Gdn-HCl concentration (Figures 1 and 2). Consistent with a two-state model (N_2 = 2D), the curves based on relative fluorescence intensity, fluorescence emission maximum, and fluorescence polarization are coincident for the individual

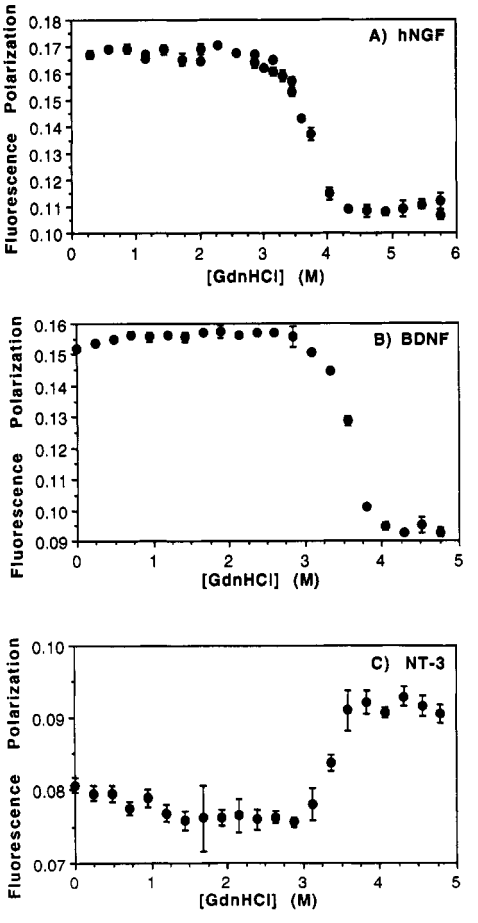

FIGURE 2: Neurotrophin equilibrium unfolding curves based on fluorescence polarization. The fluorescence polarization of (A) hNGF, (B) BDNF, and (C) NT-3 is plotted vs Gdn-HCl concentration. The same solutions described in Figure 1 were used in making these determinations. Data points represent the average of triplicate readings (±SD) made using a single sample.

[2] We have not observed the 7-fold lower fluorescence intensity of recombinant NGF relative to BDNF and NT-3 that was reported by Narhi et al. (1993a). In our laboratory authenic mouse NGF, recombinant mNGF, or recombinant hNGF had fluorescence intensities within 20–40% that of the other neurotrophins. The differences may be due to the methods of expression and purification of the recombinant hNGF preparations.

Table 1: Neurotropin Denaturation Characteristics

	$\Delta G_D^{H_2O}$ [a] (kcal/mol)	m [b] (kcal mol^{-1} M^{-1})	Gdn50 [c] (M)	polarization [d] P_n	polarization [d] P_d	emission max (nm)	coincidence [e]
			pH 7				
mNGF	19.3 ± 1.1	4.8 ± 0.4	2.3/2.5	0.145	0.095	341	+
hNGF	23.0 ± 3.0	4.3 ± 0.8	3.5/3.6	0.167	0.107	340	ND [g]
BDNF	26.4 ± 2.4	5.3 ± 0.6	3.5/3.6	0.156	0.094	339	-
NT-3	22.7 ± 1.3	4.5 ± 0.4	3.3/3.4	0.077	0.092	336	-
NT-4/5	20.8 ± 1.2	5.1 ± 0.5	2.5/2.6	0.08	0.10	338	+
			pH 3.5				
mNGF [f]	12.7 ± 0.7	3.4 ± 0.4	1.4/ND	0.137	0.094	341	+
BDNF [f]	17.0 ± 1.4	4.0 ± 0.6	2.2/ND	ND	ND	339	+
NT-4/5 [f]	19.0 ± 1.1	5.1 ± 0.3	2.1/ND	ND	ND	338	+

[a] Conformational stability. [b] Dependence of stability on denaturant concentration. The mNGF value at pH 7 represents the average value reported in Timm and Neet (1992). The hNGF, BDNF, NT-3, and NT-4/5 values and standard deviations were derived from nonlinear regression to the data in Figure 1 for pH 7 and in Figure 4 for pH 3.5. [c] Midpoints of theoretical Gdn-HCl unfolding curves are based on the listed $\Delta G_D^{H_2O}$ and m values at 10 and 50 μg/mL protein concentrations. [d] Polarization values observed for the native, P_n, and denatured, P_d, proteins. [e] The coincidence of relative fluorescence intensity unfolding and refolding curves is indicated by +. NT-3 at pH 3.5 was noncoincident (see text). [f] These values are calculated by assuming the two-state dimer model. For NGF some divergence of fluorescence intensity and polarization curves has begun at this pH (Figure 8B). For BDNF and NT-4/5 the m and Gdn50 values indicate that they are still two-state conditions. [g] ND, not determined.

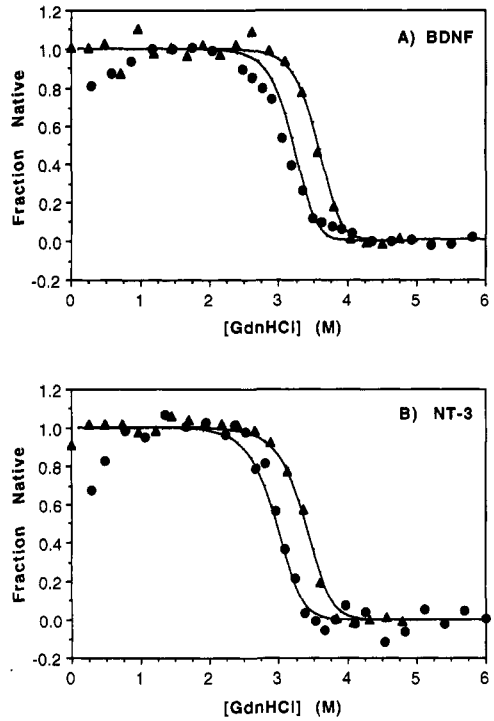

FIGURE 3: Dependence of BDNF and NT-3 concentrations on the midpoint of equilibrium unfolding curves. The fraction of native protein calculated from relative fluorescence intensity data collected at (A) 2 and 50 μg/mL BDNF and (B) 2 and 50 μg/mL NT-3 is plotted against Gdn-HCl concentration (Experimental Procedures). The solutions were buffered at pH 7 with 100 mM sodium phosphate. Higher concentrations produced fewer noisy data because the subtraction of the baseline was less significant. The solid line represent simulated curves based on the thermodynamic values obtained for the 50 μg/mL data presented in Figure 1 and Table 1.

neurotrophins at neutral pH. Fluorescence polarization and emission properties can be sensitive to identical structural events but in the case of mNGF are sensitive to different structural states (see below). Finally, the midpoint of the BDNF and NT-3 unfolding curves is dependent on protein concentration (Figure 3), as expected from a two-state transition between native dimeric and denatured monomeric protein (Bowie & Sauer, 1989). Similar results have been reported for mNGF (Timm & Neet, 1992); however, sufficient quantities of hNGF and NT-4/5 were not available for such study.

Conformational Stabilities of the Neurotrophins. The conformational stability ($\Delta G_D^{H_2O}$) of a protein in the absence of denaturant can be calculated from solvent denaturation curves by extrapolation of log K_D data to zero Gdn-HCl concentration (Pace, 1986). The $\Delta G_D^{H_2O}$ values for hNGF, BDNF, NT-3, and NT-4/5 at pH 7 were derived by nonlinear regression of the data in Figure 1 to the two-state model (see Experimental Procedures) and are summarized in Table 1. This analysis revealed significant quantitative differences in the neurotrophin stabilities, consistent with the qualitative results presented previously for BDNF and NT-3 (Radziejewski et al., 1992). The mNGF has the lowest conformational stability of 19.3 kcal/mol (Timm & Neet, 1992), while NT-4/5, hNGF, NT-3, and BDNF have apparent conformational stabilities approximately 1, 3, 3, and 7 kcal/mol greater than that of mNGF, respectively. This trend is also consistent with the midpoints of the neurotrophin unfolding curves (Figure 1; Table 1).

Reversibility of Neurotrophin Unfolding. The above thermodynamic analysis of the neurotrophin denaturation curves according to the two-state model ($N_2 = 2D$) requires that the unfolding process is reversible. However, the unfolding and refolding curve of BDNF and NT-3 at pH 7 were noncoincident (Radziejewski et al., 1992). Although native-like spectroscopic characteristics were recovered when unfolded BDNF and NT-3 solutions were diluted to 1 M Gdn-HCl, the midpoint of the BDNF and NT-3 refolding curves is about 1 M lower than that of the unfolding curves. In contrast, mNGF (Timm & Neet, 1992) and NT-4/5 unfolding and refolding curves were coincident at pH 7 (Figure 4A,C).

The noncoincidence between the BDNF and NT-3 unfolding and refolding curves at intermediate denaturant concentrations (between 1 and 4 M Gdn-HCl) may be due to a kinetically slow refolding step, which would not affect $\Delta G_D^{H_2O}$ calculations. However, hysteresis might also indicate deviation from the two-state model. Disulfide bond interchange could be a source of deviation from the two-state model at neutral pH but should be inhibited at acidic pH. Therefore, the coincidence of BDNF and NT-3 unfolding and refolding curves was also tested at low pH to determine if slow kinetic refolding processes or potential intermediates could be eliminated. The mNGF and NT-4/5 unfolding and refolding curves remained coincident at pH 3.5 (Figure 4B,D). The difference between the midpoints of BDNF unfolding and refolding curves was reduced by about 80% at pH 4 (data not shown) and is essentially eliminated at pH 3.5 (Figure 4E). However, NT-3 unfolding and refolding curves remained noncoincident at pH 3.5, and full recovery of native fluorescence properties did not occur at the lowest Gdn-HCl dilution made (Figure 4F).

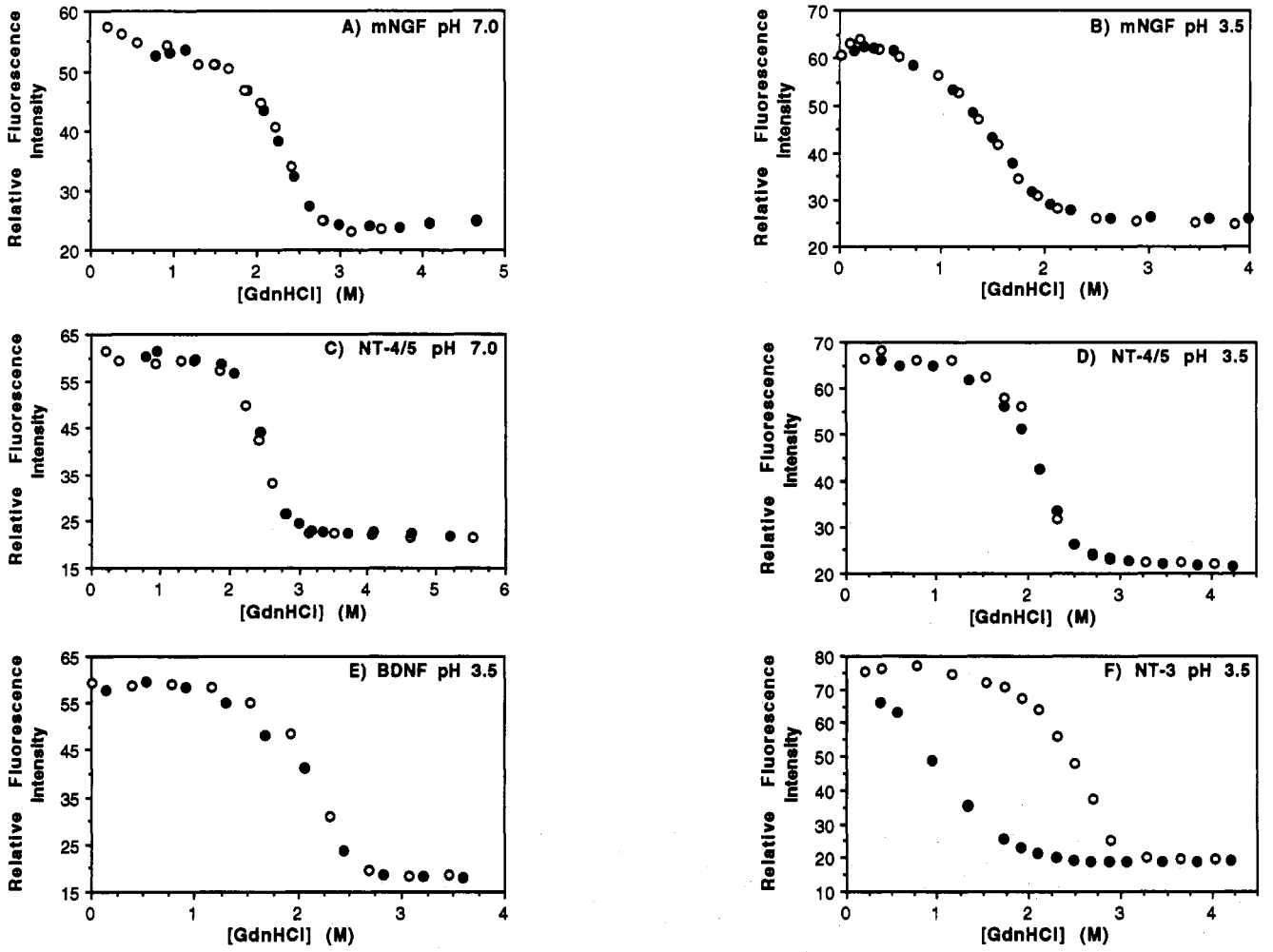

FIGURE 4: Neurotrophin folding and unfolding curves. The relative fluorescence intensity at 320 nm is plotted vs final Gdn-HCl concentration for (A) mNGF at pH 7.0, (B) mNGF at pH 3.5, (C) NT-4/5 at pH 7.0, (D) NT-4/5 at pH 3.5, (E) BDNF at pH 3.5, and (F) NT-3 at pH 3.5. The solutions contained 10 μg/mL of the neurotrophins and were buffered using 100 mM citrate/phosphate buffer. Samples to be refolded (●) were first unfolded in greater than 7 M Gdn-HCl for 8 h prior to dilution to the final Gdn-HCl concentration and allowed to equilibrate for 72 h. Samples for unfolding (○) were first incubated in 0.2 M Gdn-HCl for 8 h prior to dilution into the final Gdn-HCl concentration for 72 h. Conformational stabilities of 18.3 and 20.8 kcal/mol were calculated from the pH 7 data for NGF and NT-4/5, respectively. Several symbols, including the point at 2.1 M in panel D, are obscured by overlap. Note the different scales used in each panel.

Noncoincident curves were also obtained for BDNF and NT-3 when urea was used in place of Gdn-HCl at pH 4 (data not shown). All of the neurotrophins, except for NT-3, appeared to undergo two state transitions at low pH: NGF at pH 4, BDNF at pH 3.5, and NT4/5 at pH 3.5.

The midpoints of the neurotrophin denaturation curves (Gdn50) decreased at pH 3.5 relative to those at pH 7, as expected from previous mNGF studies (Timm & Neet, 1992). However, the differences between the pH 3.5 and 7 Gdn50 values for the individual neurotrophins were not equivalent (Figures 1 and 4). The mNGF Gdn50 value decreased by 0.9 M (40%) at pH 3.5 relative to that at pH 7; whereas the NT-4/5 Gdn50 value decreased by only 0.4 M (16%). BDNF, on the other hand, with the highest $\Delta G_D^{H_2O}$ at pH 7, experienced a 1.4 M (40%) decrease in Gdn50 at pH 3.5 to a value equivalent to that of NT-4/5.

Neurotrophin Circular Dichroism Spectra. The circular dichroism (CD) spectra of the neurotrophins were measured (Figure 5) to evaluate the reversibility of denaturation. Significant differences exist among the neurotrophin CD spectra as reported (Radziejewski et al., 1992; Narhi et al., 1993a,b; Dr. N. Panayotatos, Regeneron Pharmaceuticals, personal communication). The most striking features are the maximum around 230–232 nm and the additional minimum around 197 nm present in the BDNF, NT-3, and NT-4/5 spectra, which are absent in the hNGF (data not shown) and mNGF CD spectra. These distinctive features are retained at low pH (Figure 5, solid line) since the CD spectra are identical to those recorded at neutral pH [data not shown, see Timm and Neet (1992), Radziejewski et al. (1992), and Narhi et al. (1993a,b)]. Native-like CD spectra of mNGF, BDNF, NT-3, and NT-4/5 were recovered following the refolding of unfolded samples when Gdn-HCl was completely removed by dialysis (Figure 5, dashed line), suggesting that reformation of secondary structure occurred readily.

Denaturation of mNGF at Low pH. The denaturation of dimeric mNGF at pH 7 and at pH 4 was previously found to occur according to a two-state dimer model, based on the coincidence of fluorescence intensity and fluorescence polarization measurements and the dependence of protein concentration on the mNGF denaturation curve midpoint (Timm & Neet, 1992). The effect of pH on the mNGF structure was studied further to determine if neurotrophin $\Delta G_D^{H_2O}$ values could be better compared at pH 3.5, where BDNF unfolding and refolding curves were coincident. Denaturation curves were measured over the range pH 3–7 (Figure 6). The mNGF denaturation curves measured between pH 3.25 (not shown) and pH 7 are characterized by linear plateau regions which precede and follow a transition region. Initial plateau and final plateau regions are populated predominantly by native

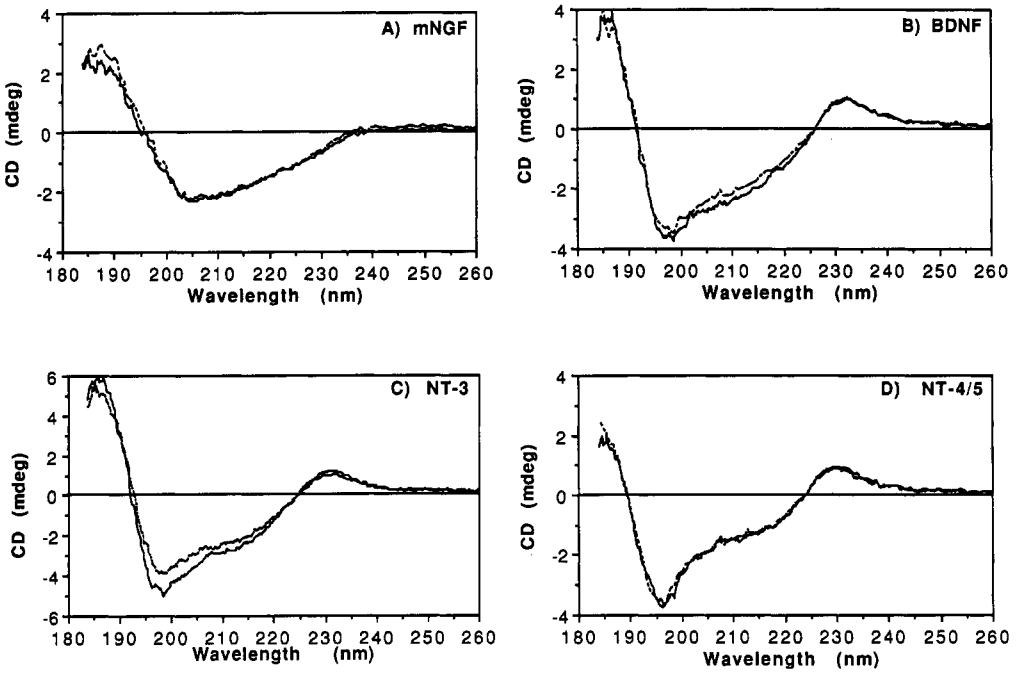

FIGURE 5: Restoration of the neurotrophin circular dichroism spectra following removal of Gdn-HCl at pH 3.8: (A) NGF; (B) BDNF; (C) NT-3; (D) NT-4/5. The refolded neurotrophin samples (dashed lines) were denatured in greater than 5.5 M Gdn-HCl, pH 3.5, for 6 h and then dialyzed against 10 mM NaH_2PO_4, pH 3.8, for 48 h. Control samples (solid lines) were treated identically but were initially treated with 0.3 M Gdn-HCl prior to dialysis. The spectra presented here do not differ significantly from native spectra recorded at pH 7 (data not shown).

and denatured protein, respectively (Pace, 1986). However, mNGF denaturation curves constructed at pH 3.0 lacked the initial native plateau region (Figure 6). The effect of pH on the midpoint of mNGF denaturation curves and on the conformational stability of mNGF (where applicable) is presented in Figure 7. The curve reveals a relatively small decrease in stability from pH 7 to 4 with a shallow slope, followed by a sharper decrease below pH 4 with a curve of greater slope.

The denaturation curves for mNGF based on relative fluorescence intensity measurements at pH 3.0 are noncoincident with those based on fluorescence polarization measurements (Figure 8A). In contrast to the broad decrease in fluorescence intensity occurring at low Gdn-HCl concentration, fluorescence polarization measurements at pH 3.0 revealed a linear native-like plateau region and a sharp transition with an apparent midpoint around 2.2 M Gdn-HCl. This midpoint is at least 1 M higher than that of the fluorescence intensity curve.

Noncoincidence of normalized fluorescence intensity and polarization data was reduced but still apparent at pH 3.5 (Figure 8B) and 3.25 (data not shown). As noted previously (Timm & Neet, 1992), normalization of polarization data according to eq 4 is necessary to account for the higher fluorescence intensity of native mNGF. Data at pH 3.0 could not be normalized because the native plateau region was absent. The normalized fluorescence intensity and polarization data were coincident at pH 4 (Figure 8C). A protein concentration dependent shift in the midpoint of the denaturation curves was apparent at pH 3.5 (Figure 8D).

DISCUSSION

Neurotrophin sequence alignments indicate that the members of this family will likely have three-dimensional structures similar to the prototypic mNGF structure (McDonald et al., 1991; Ebendal, 1992; Bradshaw et al., 1993). The data presented here support the concept that NGF, BDNF, NT-3, and NT-4/5 are indeed similar as nonhelical, dimeric proteins with high thermodynamic stabilities. However, differences in the biophysical characteristics of these proteins indicate significant structural differences will exist compared to the mNGF structure. Our studies provide a comparison of the known human neurotrophin structures, provide biophysical characterization of NT-4/5, and extend previous stability studies on these factors (Timm & Neet, 1992; Radziejewski et al., 1992; Narhi et al., 1993a,b).

Significance of the Free Energy of Stabilization. Denaturation of the neurotrophins by Gdn-HCl at equilibrium indicates that these proteins assume structures having different conformational stabilities ($\Delta G_D^{H_2O}$) and folding/unfolding characteristics. Denaturation of mNGF was previously described by a two-state model ($N_2 = 2D$) in which the folded dimer and unfolded monomer are the only species significantly populated at equilibrium (Timm & Neet, 1992). Consistent with this model, the recombinant human neurotrophins yielded monophasic sigmoidal unfolding curves in Gdn-HCl that were coincident when based on fluorescence intensity and polarization measurements (Figures 1 and 2). Although these measurements could be sensitive to the same structural transition, the denaturation of mNGF below pH 4 indicates that fluorescence intensity and polarization measurements are sensitive to different structural states (see below). Additionally, the midpoints of mNGF (Timm & Neet, 1992), BDNF, and NT-3 unfolding curves were dependent on protein concentration (Figure 3), as expected from the two-state model of dimeric protein denaturation and the law of mass action (Bowie & Sauer, 1989). The agreement between theoretical curves derived from eqs 5 and 6 and unfolding data at multiple protein concentrations (Figure 3) supports both the interpretation of a reversible equilibrium with a two-state, cooperative transition for dimeric neurotrophins and the reliability of the calculated $\Delta G_D^{H_2O}$. Protein concentration dependence is also expected for the hNGF and NT-4/5 curves, although sufficient quantities were not available for similar studies.

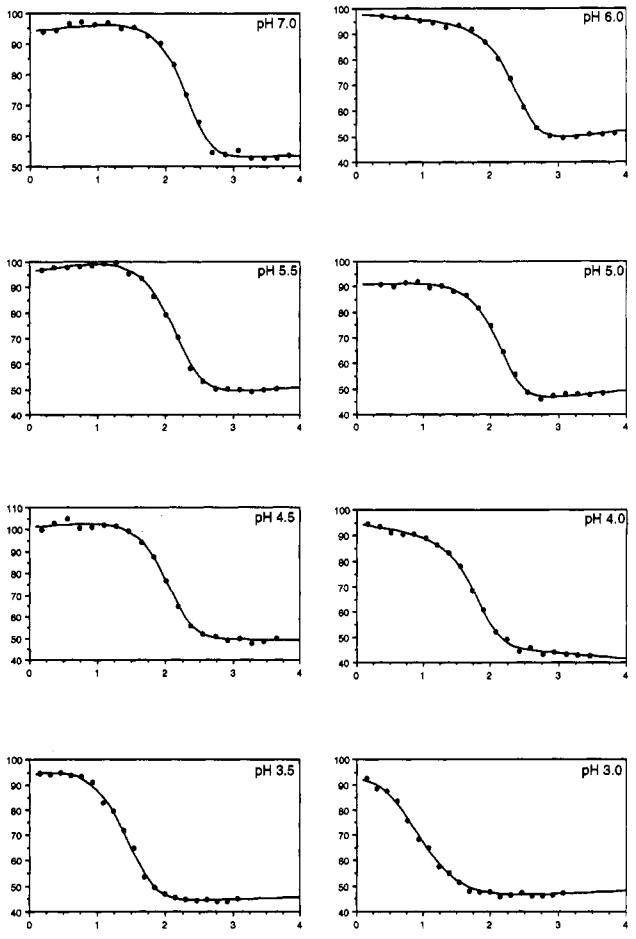

FIGURE 6: Denaturation of mNGF over the range pH 7–3. Equilibrium unfolding curves for mNGF from fluorescence intensity data are presented as a function of Gdn-HCl (M) at the indicated pH of each panel. The solutions contained 15 μg/mL mNGF and 100 mM citrate/phosphate buffer. The solid lines were derived from fitting the data to the two-state model of dimeric protein denaturation and represent $\Delta G_D^{H_2O}$ values of 17.5, 18.2, 15.6, 17.2, 16.1, and 15.7 kcal/mol for the data collected at pH 7.0–4.0. The solid lines in the pH 3 and 3.5 data are included here only for presentation and are not a theoretical fit.

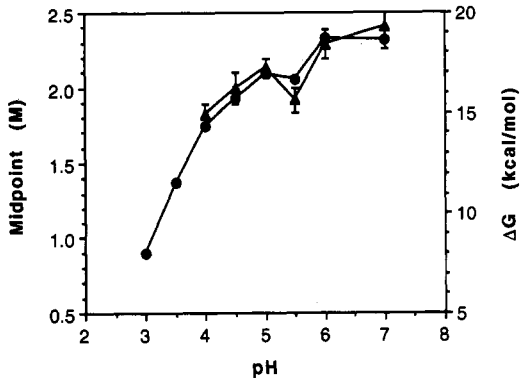

FIGURE 7: pH dependence of NGF denaturation curves. The Gdn50 (●) and $\Delta G_D^{H_2O}$ (▲) of 15 μg/mL mNGF denaturation curves are plotted vs pH. The midpoints of the pH 3 and 3.5 data were estimated from the curves in Figure 6. The points above pH 3.5 were derived from $\Delta G_D^{H_2O}$ and m values calculated from the curves shown in Figure 6 and from previously published data (Timm & Neet, 1992). Average $\Delta G_D^{H_2O}$ and m values were used at pH 4 and 7, where multiple determinations have been made.

The $\Delta G_D^{H_2O}$ values, calculated from the different neurotrophin unfolding curves at neutral pH according to the two-state model (Table 1), indicate that the individual neurotrophin structures are stabilized by different amounts of Gibbs free energy relative to their respective unfolded conformations. BDNF has the highest $\Delta G_D^{H_2O}$, while hNGF, NT-3, and NT-4/5 have intermediate $\Delta G_D^{H_2O}$ values and mNGF has the lowest $\Delta G_D^{H_2O}$. The different $\Delta G_D^{H_2O}$ values may be due to stabilization of the folded state or destabilization of the unfolded state. Due to the different midpoints of the unfolding and refolding curves for BDNF and NT-3, some uncertainty is associated with their reported $\Delta G_D^{H_2O}$ values. Recombinant mNGF unfolding and refolding curves are coincident and yield $\Delta G_D^{H_2O}$ values consistent with those reported for mNGF isolated from submaxillary glands (data not shown). Therefore, the recombinant origin of these proteins is not likely to account for the different $\Delta G_D^{H_2O}$ values or the aberrant BDNF and NT-3 refolding characteristics.

The $\Delta G_D^{H_2O}$ values reported for small dimeric proteins are generally higher than those reported for monomeric proteins (Pace, 1990). The neurotrophin stabilities of 19–26 kcal/mol (Table 1) are at the upper range of values reported for dimers (Bowie & Sauer, 1989; Gittelman & Matthews, 1990). The $\Delta G_D^{H_2O}$ for BDNF is higher than any previously reported. Data simulations based on eqs 5 and 6 (Experimental Procedures) indicate that a $\Delta G_D^{H_2O}$ of greater than 15 kcal/mol is required to maintain a significant population of folded dimeric protein in the concentration range of the neurotrophin receptor dissociation constants. For example, a dimeric protein having a $\Delta G_D^{H_2O}$ of 20 kcal/mol will be 98% folded at a concentration of 10 pM; however, the fraction of native protein drops to 40% if the $\Delta G_D^{H_2O}$ is reduced to 15 kcal/mol. Therefore, high stabilities may be a requirement of low physiological neurotrophin concentrations and the coupling of their unfolding/dissociation equilibria.

Neurotrophin Sequences and Stabilities. The high sequence identity between mNGF and hNGF may enable residues responsible for the 4 kcal/mol difference in the $\Delta G_D^{H_2O}$ values to be identified. In turn, residues identified by comparing the NGF sequences may be related to the $\Delta G_D^{H_2O}$ values of BDNF, NT-3, and NT-4/5. Of the 12 residues differing between mNGF and hNGF (Table 2), the following are unlikely to have stabilizing effects: the terminal residues 3, 6, 9, and 117 are apparently mobile in the mNGF structure (McDonald et al., 1991); the side chains of residues 65 and 94 have high solvent accessibilities; conservative changes occur at residue 50 and most of the aforementioned residues.

The substitution of Thr in mNGF by Met in hNGF at positions 37 and 92 could potentially account for some differences in $\Delta G_D^{H_2O}$ values, but these positions do not correlate with sequences and stabilities of BDNF, NT-3, and NT-4/5. Less conservative changes occur at positions 40, 60, and 61, and a correlation may exist between the order of $\Delta G_D^{H_2O}$ values at pH 7 and the residues present at positions 40 and 60: the mNGF ($\Delta G_D^{H_2O}$ = 19 kcal/mol) contains Ala at both of these positions; hNGF and NT-3 (23 kcal/mol) contain Gly 40 and an acidic residue at 60; NT-4/5 (21 kcal/mol) contains Gly 40 and Ala 60; BDNF (26 kcal/mol) contains Glu 40 and Pro 60. Acidic substitutions at positions 40 in BDNF and 60 in hNGF and NT-3 could also be sufficient to promote stability. The Glu 40 in BDNF could potentially stabilize the folded structure through an electrostatic interaction with Lys 26. This combination is lacking in the other neurotrophins, and titration of Glu 40 could also result in the larger change in Gdn50 between pH 7 and 3.5 observed for BDNF. Potential interactions for Asp 60 or Glu 60 are not readily apparent from the mNGF structure. These residues, 40 and 60, precede turns in mNGF. Therefore, the presence of Gly 40 in hNGF, NT-3, and NT-4/5, Pro 60 in BDNF, and Pro 61 in hNGF could have entropic effects on backbone

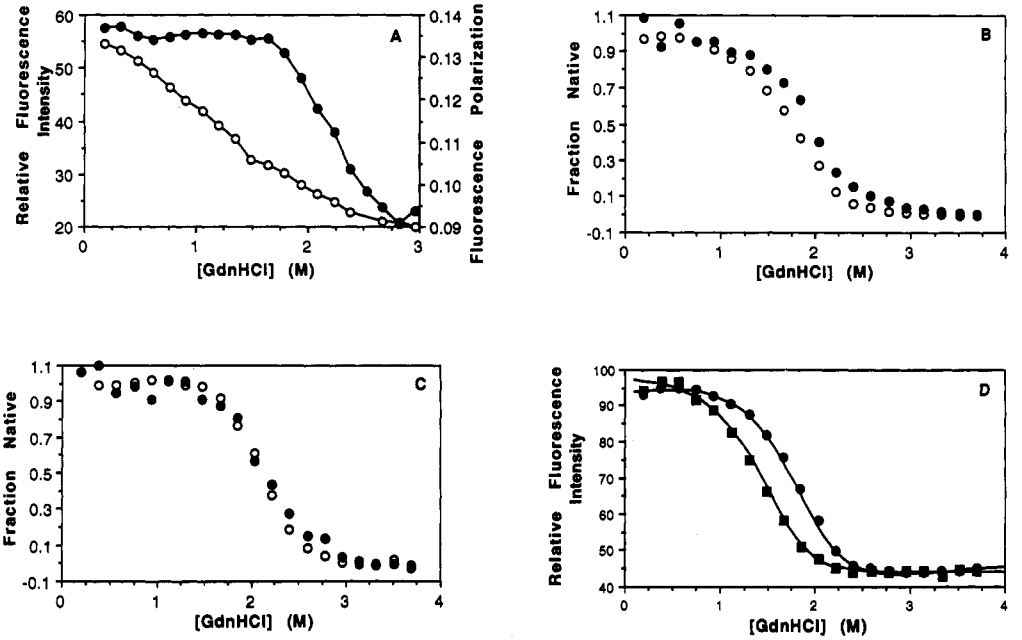

FIGURE 8: Equilibrium unfolding curves from fluorescence intensity and polarization data for mNGF at low pH: (A) fluorescence intensity (○) and polarization (●) curves for 100 μg/mL samples of NGF at pH 3.0; (B) fluorescence intensity (○) and polarization (●) curves for 100 μg/mL mNGF at pH 3.5 normalized to represent the apparent fraction of native protein at each Gdn-HCl concentration (Experimental Procedures); (C) fluorescence intensity (○) and polarization (●) curves for 50 μg/mL NGF at pH 4.0 normalized to represent the fraction of native protein at each Gdn-HCl concentration; (D) protein concentration dependent shift in the midpoint of fluorescence intensity unfolding curves for mNGF at 10 (■) and 100 (●) μg/mL at pH 3.5. Instrumental settings resulted in a 10-fold multiplication of the 10 μg/mL data.

Table 2: Residues Potentially Involved in Differential Stability of the Neurotropins

	stability[a]						
pH	mNGF	hNGF	BDNF	NT-3	NT-4/5		
7	low	high	highest	high	interm		
3.5	lowest	ND	interm	interm	interm		
	residue						
position[b]	mNGF	hNGF	BDNF	NT-3	NT-4/5	PSA[c]	proposed intramolecular role in stability
3	T	S	D	E	T		mobile terminus
6	V	I	A	S	A		mobile terminus
9	M	R	R	R	R		mobile terminus
30	D	D	D	D	D	0.4	destabilize dimer relative to monomer at low pH
37	T	M	T	T	E	61.9	none, minor difference between mNGF and hNGF
40	A	G	E	G	G	61.4	entropic or electrostatic (BDNF) effects
50	R	K	K	K	R	39.0	none, conservative substitution
60	A	D	P	E	A	39.5	entropic (BDNF) or electrostatic (hNGF, NT-3) effects
61	S	P	M	A	P	67.4	entropic effects (hNGF, NT-4/5)
65	E	D	K	K	G	111.1	none, high side-chain accessibility
92	T	M	M	S	A	38.1	none, minor difference between mNGF and hNGF
94	E	G	K	N	Q	114.1	none, high side-chain accessibility
117	T	V	G	G	G		mobile terminus

[a] Relative stability (highest, high, intermediate = interm, or low) based on $\Delta G_D^{H_2O}$ at pH 7 or Gdn50 at pH 3.5 (see Table 1). ND, not determined. [b] Positions (numbered relative to the mNGF sequence) considered in the list were based on differences between hNGF and mNGF sequences and potential titratable groups in the pH 3–7 range. [c] Percent solvent accessibility (Richmond & Richards, 1978) for all side-chain atoms from the mNGF structure (McDonald, et al., 1991).

conformation stability. NT-4/5 shows an intermediate $\Delta G_D^{H_2O}$ at pH 7 with relatively little change going to pH 3.5, suggesting the absence of a titratable group contributing to stability. No residues with pK_a values in the range pH 3–7 are distributed among the neurotrophins in such a way as to readily explain these variations. These proposed contributions to stability are testable by site-specific mutagenesis.

Dependence of NGF Denaturation on pH. The mNGF transition regions broadened between pH 4 and 3 (Figure 6), concomitant with a marked decrease in the *m* value below pH 3.5 (Table 1) to a value of 2.0 at pH 3 (data not shown). These effects indicate decreased cooperativity and a probable loss of two-state behavior below pH 4 (Pace et al., 1990). An increasing degree of noncoincidence between fluorescence intensity and polarization measurements for mNGF at pH 3.5 (Figure 8B), 3.25 (data not shown), and 3.0 (Figure 8A) confirms this possibility. The denaturation curves suggest a marginal stability of dimeric NGF below pH 3 even in the absence of denaturant.

These observations at low pH have been interpreted in terms of a three-state model ($N_2 = [2I] = 2D$) involving a monomeric mNGF intermediate. The initial transition from folded dimer to compact monomer would result in the decreased fluorescence intensity measurements, and the final unfolding transition would produce the fluorescence polarization changes (Figure 8). Tryptophan residues 21, 76, and 99 are located in the hydrophobic dimeric interface of the mNGF structure (McDonald et al., 1991). Exposure of these residues to solvent upon dissociation of the native mNGF dimer (N_2) to a partially structured monomer could account for the observed decrease

in fluorescence intensity that occurs at Gdn-HCl concentrations preceding complete unfolding. The data do not distinguish between single or multiple monomeric intermediates ([2I]) having residual structure that restricts the Trp mobilities and results in native-like fluorescence polarization. Complete unfolding at higher Gdn-HCl concentrations then results in increased Trp mobility and fluorescence depolarization with loss of secondary structure. The mNGF concentration dependence of the fluorescence intensity unfolding curves below pH 4 indicates that a dimeric species is involved in this equilibrium (Figure 8D). CD measurements indicate that the native mNGF structure is unaltered between pH 7 and 3 in the absence of denaturant and undergoes only slight changes at pH as low as 1.5 (data not shown). Thus, mNGF secondary structure does not appear to be greatly altered at low pH without denaturant. This observation is in contrast to the marked change in CD spectra of NGF generated by guanidine denaturation at neutral pH (Timm & Neet, 1992).

Surprisingly, this interpretation suggests that the formation of compact monomer is relatively more favorable at low pH, as indicated by the 2I intermediate. At pH 7 folded monomers are calculated to be stabilized by about 3 kcal/mol relative to unfolded monomer (Timm & Neet, 1992). The electrostatic nature of the intrasubunit interactions in the crystal and the hydrophobic interactions across the dimer interface (McDonald et al., 1991) would indicate that native monomer would be destabilized to a greater extent than folded dimer at low pH. Since the opposite situation apparently occurs, the destabilization of quaternary interactions at low pH is probably due to the presence of ionizable group(s) having increased pK_a values in the monomeric state and a shift to an altered conformation, I. Titration of Asp 30 might indirectly affect the stability of dimerization, since this conserved residue is buried within the monomer, is involved in main-chain hydrogen bonds in the β-turn of residues 30–33, and probably has an electrostatic interaction with Lys 34.

After this paper was submitted, kinetic evidence was presented for a molten globule intermediate monomer state of BDNF in renaturation from Gdn-HCl (Philo et al., 1993) and in acid denaturation in trifluoroacetic acid (Narhi et al., 1993b). This monomer is collapsed with significant amounts of secondary structure, but not the correct tertiary structure for dimerization (Philo et al., 1993; Narhi et al., 1993b). The intermediate we propose for NGF denaturation at low pH could represent the same state, although it is not characterized sufficiently to confirm this interpretation. The decrease in stability at low pH of all the neurotrophins (Figures 4 and 6; Table 1) could reflect the formation, lowered stability, and lack of tertiary or quaternary interactions of the molten globule monomer.

Noncoincidence of Unfolding and Refolding Curves. Noncoincidence of the unfolding and refolding curves for BDNF and NT-3 occurs at pH 7 (Figure 4; Radziejewski et al., 1992). However, in spite of the noncoincidence, the denaturation process is reversible, since native-like spectroscopic characteristics are recovered upon removal of denaturant by dialysis at pH 4 or 7 (Figure 5; Radziejewski et al., 1992). Since NT-3 achieved nearly full recovery of the far-UV CD spectra in 48 h (Figure 5C) but not fluorescence in the refolding period of 72 h (Figure 4F), the attainment of secondary structure does not appear to be limiting. Interestingly, NT-4/5, like mNGF, refolds relatively rapidly without hysteresis, even though it is the only neurotrophin that contains an insert of seven amino acids in the loop region at position 61. Several days are required for equilibrating mNGF samples in the denaturant transition region (Timm & Neet, 1992; Experimental Procedures); indeed, although mNGF is the fastest equilibrating of the neurotrophins, it is much slower than most other proteins that have been studied. Refolding mNGF samples require longer periods of time to equilibrate than do unfolding samples, as judged by recovery of the fluorescence signal. Moreover, protein folding kinetics generally appear to be more complex than unfolding kinetics (Kim & Baldwin, 1982). Therefore, a slow refolding step, exaggerated at intermediate Gdn-HCl concentrations, is likely to account for the hysteresis between these unfolding and refolding curves of BDNF and NT-3 at pH 7.

As the equilibration problems occur only at intermediate denaturant concentrations in the transition region, a denaturant-independent and relatively faster process such as proline isomerization (Kim & Baldwin, 1982) is unlikely to account for hysteresis between these curves. Disulfide bond interchange was also considered in terms of the noncoincident refolding and unfolding curves. However, denaturation studies under acidic conditions where interchange would be inhibited did not entirely alleviate these problems (Figure 4). The existence of the cystine-knot motif in NGF (McDonald & Hendrickson, 1993) suggests the possibility that interaction of the polypeptide chain through the restricted loop might hinder the rate of movement and attainment of equilibrium. We surmise, therefore, that the kinetic barrier may involve quaternary associations or a final rearrangement of the tertiary conformation of side chains near the tryptophans.

Comparison of Neurotrophin Spectra. Differences between the neurotrophins were also revealed by differences in their intrinsic fluorescence and circular dichroism spectra. Protein tryptophan fluorescence intensity and emission maxima are sensitive to the degree of fluorophore solvent accessibility (Lakowicz, 1983). The relative fluorescence intensities and emission maxima of the neurotrophins indicate that the degree of solvent exposure of Trp increases slightly from NT-3 to NGF (Table 1). Exposure of mNGF Trp residues to solvent has been indicated (Frazier et al., 1973; Cohen et al., 1980), in spite of their location in the dimeric interface (McDonald et al., 1991). The additional Trp 101 present in NT-3 and NT-4/5 does not account for all differences, as NT-3 has a higher relative fluorescence intensity and a lower emission maximum than NT-4/5. The unexpected increase in the NT-3 and NT-4/5 polarization values that accompanies unfolding is an indication that mobility of the dominant fluorophore decreases upon unfolding of NT-3 and NT-4/5. Some local residual interactions in Gdn-HCl may restrict the Trp rotation. In contrast, the unfolding of mNGF, hNGF, and BDNF results in fluorescence depolarization, indicating fluorophore mobility increases upon unfolding. The low native fluorescence polarization and the increase upon denaturation of NT-3 and NT-4/5 correlate with the presence of the additional Trp 101; however, if this Trp 101 fluorophore contributes strongly to the depolarization, it should not be quenched as suggested by Narhi et al. (1993a).

The circular dichroism spectra presented here were included to demonstrate the reversibility of the unfolding process. However, qualitative differences in the secondary structures of these proteins are also implied by these spectra. The hNGF spectrum is similar to that of mNGF, with a single minimum at 205 nm and a maximum at 190 nm (data not shown). The BDNF, NT-3, and NT-4/5 spectra have signals at 230–232 and 197 nm that are absent from the NGF spectrum (Figure 5). Furthermore, the 197- and 205-nm signals in the NT-3 and NT-4/5 spectra are more distinct than in the BDNF spectrum. Therefore, the NT-3 and NT-4/5 structures are expected to be most similar, while the NGF structure is

expected to be the least similar to the other neurotrophins. The 197- and 230–232-nm signals present in the BDNF, NT-3, and NT-4/5 spectra are at positions characteristic of either β-turns (Compton & Johnson, 1986) or random and aromatic/disulfide contributions (Perczel et al., 1992), as determined from deconvoluted protein CD spectra. Therefore, the structures located in the loop regions of BDNF, NT-3, and NT-4/5 may differ from those found in the mNGF structure. The seven-residue insert in the loop region of NT-4/5 at position 61 does not produce markedly different CD spectra, although NT-4/5 does have a slight shift of the trough from 197 to 195 nm. The conformations of the N or C termini may also contribute to differences in the CD spectra. Secondary structural estimates based on the CD spectra of mNGF, hNGF, BDNF, and NT-3 have been presented previously (Timm & Neet, 1992; Timm et al., 1994; Radziejewski et al., 1992; Nahri et al., 1993a,b) and are consistent with primarily β-sheet proteins.

Conclusions. Neurotrophin sequence variations are concentrated in loop regions of the mNGF structure and in the amino and carboxy termini, which are not defined in the mNGF crystal structure (McDonald et al., 1991). Variable structures in these loop regions may confer receptor binding specificities associated with the various neurotrophins (McDonald et al., 1991; Ebendal, 1992; Bradshaw et al., 1993) and account for differences in conformational changes observed upon binding to the low-affinity neurotrophin receptor (Timm et al., 1994). Indeed, mutations in one loop region of NGF decrease binding to the low-affinity neurotrophin receptor (Ibáñez et al., 1992), while deletion or mutation of the amino terminus of NGF decreases the binding of NGF to Trk A (Kahle et al., 1992; Ibáñez et al., 1993). The studies presented here suggest that structural variations in the loop regions and termini may contribute both to neurotrophin receptor binding specificity and to stability of the neurotrophins in solution. Engineered neurotrophins were recently proposed (Ibáñez et al., 1993) to have advantages in the potential therapeutic use of these proteins in treating nerve injury or degeneration. The differences in neurotrophin stabilities reported here may also be of therapeutic significance, as the half-life of an introduced foreign protein may be related to its thermodynamic stability.

ACKNOWLEDGMENT

We thank Dr. Sang B. Woo for providing recombinant mouse NGF; Dr. Sheryl Meyer, Cephalon, Inc., West Chester, PA, for recombinant human NGF; Dr. James Miller, Amgen, Thousand Oaks, CA, for recombinant human BDNF and NT-3; and Drs. Peter DiStefano and Nikos Panayotatos, Regeneron Pharmaceuticals, Tarrytown, NY, for recombinant NT-4/5. We also thank Dr. Alex Wlodawer for kindly providing the coordinates for NGF. We acknowledge Drs. Ben Bax and Judith Murray-Rust for help with modeling and structure discussions.

REFERENCES

Angeletti, R. H., Hermodson, M. A., & Bradshaw, R. A. (1973b) *Biochemistry 12*, 100–115.

Angeletti, R. H., Mercanti, D., & Bradshaw, R. A. (1973a) *Biochemistry 12*, 90–100.

Bevington, P. R. (1969) *Data reduction and error analysis for the physical sciences*, pp 235–237, McGraw-Hill, New York.

Bothwell, M. A., & Shooter, E. M. (1977) *J. Biol. Chem. 252*, 8532–8536.

Bowie, J. U., & Sauer, R. T. (1989) *Biochemistry 28*, 7139–7143.

Bradshaw, R. A., Blundell, T. L., Lapatto, R., McDonald, N. Q., & Murray-Rust, J. (1993) *Trends Biochem. Sci. 18*, 48–52.

Brand, L., & Witholt, B. (1967) *Methods Enzymol. 11*, 776–856.

Cohen, P., Sutter, A., Landreth, G., Zimmerman, A., & Shooter, E. M. (1980) *J. Biol. Chem. 255*, 2949–2954.

Compton, L. A., & Johnson, W. C., Jr. (1986) *Anal. Biochem. 155*, 155–167.

Ebendal, T. (1992) *J. Neurosci. Res. 32*, 461–470.

Frazier, W. A., Hogue-Angeletti, R. A., Sherman, R., & Bradshaw, R. A. (1973) *Biochemistry 12*, 3281–3293.

Gittelman, M. S., & Matthews, C. R. (1990) *Biochemistry 29*, 7011–7020.

Ibáñez, C. F., Ebendal, T., Barany, G., Murray-Rust, J., Blundell, T. L., & Persson, H. (1992) *Cell 69*, 329–341.

Ibáñez, C. F., Ilag, L. L., Murray-Rust, J., & Persson, H. (1993) *EMBO J. 12*, 2281–2293.

Kahle, P., Burton, L. E., Schmelzer, C. H., & Hertel, C. (1992) *J. Biol. Chem. 267*, 22707–22710.

Kim, P. S., & Baldwin, R. L. (1982) *Annu. Rev. Biochem. 51*, 459–489.

Lakowicz, J. R. (1983) *Principles of fluorescence spectroscopy*, Plenum Press, New York.

McDonald, N. Q., & Hendrickson, W. A. (1993) *Cell 73*, 421–424.

McDonald, N. Q., Lapatto, R., Murray-Rust, J., Gunning, J., Wlodawer, A., & Blundell, T. L. (1991) *Nature 354*, 411–414.

Narhi, L. O., Rosenfeld, R., Talvenheimo, J., Prestrelski, S. J., Arakawa, T., Lary, J. W., Kolvenbach, C. G., Hecht, R., Boone, T., Miller, J. A., & Yphantis, D. A. (1993a) *J. Biol. Chem. 268*, 13309–13317.

Narhi, L. O., Rosenfeld, R., Wen, J., Arakawa, T., Prestrelski, S. J., & Philo, J. S. (1993b) *Biochemistry 32*, 10819–10825.

Pace, C. N. (1986) *Methods Enzymol. 131*, 266–282.

Pace, C. N., Laurents, D. V., & Thomson, J. A. (1990) *Biochemistry 29*, 2564–2572.

Perczel, A., Park, K., & Fasman, G. D. (1992) *Proteins: Struct., Funct. Genet. 13*, 57–69.

Petrides, P. E., & Shooter, E. M. (1986) *J. Neurochem. 46*, 721–725.

Philo, J. S., Rosenfeld, R., Arakawa, T., Wen, J., & Nahri, L. O. (1993) *Biochemistry 32*, 10812–10818.

Radziejewski, C., Robinson, R. C., DiStefano, P. S., & Taylor, J. W. (1992) *Biochemistry 31*, 4431–4436.

Richmond, T. J., & Richards, F. M. (1978) *J. Mol. Biol. 119*, 537–555.

Schellman, J. A. (1978) *Biopolymers 17*, 1305–1322.

Smith, A. P., Greene, L. A., Fisk, H. R., Varon, S., & Shooter, E. M. (1968) *Biochemistry 7*, 3259–3268.

Stach, R. W., Wagner, B. J., & Stach, B. M. (1977) *Anal. Biochem. 83*, 26–32.

Timm, D. E., & Neet, K. E. (1992) *Protein Sci. 1*, 236–244.

Timm, D. E., Ross, A. H., & Neet, K. E. (1994) *Protein Sci.* (in press).

Woodruff, N. R., & Neet, K. E. (1986) *Biochemistry 25*, 7956–7966.

Structural Elements That Contribute to an Unusual Tertiary Interaction in a Transfer RNA†

Ya-Ming Hou

Department of Biochemistry and Molecular Biology, Thomas Jefferson University, 233 South 10th Street, Philadelphia, Pennsylvania 19107

Received December 7, 1993; Revised Manuscript Received February 8, 1994®

ABSTRACT: Transfer RNAs (tRNAs) contain a set of defined tertiary hydrogen-bonding interactions that are established between conserved and semiconserved nucleotides. Although the crystal structures of tRNAs describe each of the tertiary interactions in detailed molecular terms, little is known about the underlying structural parameters that stabilize the tertiary interactions. *Escherichia coli* (*E. coli*) $tRNA^{Cys}$ has an unusual tertiary interaction between G15 in the dihydrouridine (D) loop and G48 in the variable loop that is critical for cysteine aminoacylation. All other tRNAs have a purine 15 and a complementary pyrimidine 48 that establish a tertiary interaction known as the Levitt base pair [Levitt, M. (1969) *Nature 224*, 759–763; Klug et al. (1974) *J. Mol. Biol. 89*, 511–516]. In this study, the G15·G48 tertiary interaction in *E. coli* $tRNA^{Cys}$ was used to investigate the structural elements that contribute to its variation from the Levitt base pair. Analysis with chemical probes showed that substitution of U21 with A21 in the D loop and formation of a Watson–Crick base pair between nucleotides 13 and 22 in the D stem switch the hydrogen-pairing of G15·G48 to a Levitt-like G15·G48 base pair. This switch was accompanied by a decrease of the catalytic efficiency of aminoacylation by 2 orders of magnitude. In contrast, insertion of additional nucleotides in the D or variable loops had little effect. The results shed new light on the significance of A21 in tRNA structure, and suggest that the ability to establish tertiary interactions at U8·A14·A21 and at positions 13·22·46 that enhances the stacking interactions in the D-anticodon helix is a major determinant for the tertiary interaction between positions 15 and 48.

All tRNAs fold into an "L"-shaped structure through tertiary hydrogen interactions (Rich & RafBhandary, 1976). In the "L"-shaped three-dimensional structure of yeast $tRNA^{Phe}$, a G15·C48 Levitt base pair stacks with a U8·A14 reverse-Hoogsteen base pair to stabilize the joining of two long helical stems of L, the acceptor–TΨC stem and the D-anticodon stem (Kim *et al.*, 1974a; Robertus *et al.*, 1974; Ladner *et al.*, 1975; Quigley & Rich, 1976). The stacking interaction is such that G15 is protected from chemical probes. Studies with yeast $tRNA^{Phe}$, and with several others, have shown that the N7 of purine 15 is not reactive with the chemical probe dimethyl sulfate (DMS)[1] (Theobald *et al.*, 1988; Puglisi *et al.*, 1993). However, G15 in *Escherichia coli* $tRNA^{Cys}$ is reactive with DMS (Hou *et al.*, 1993). The reactivity with DMS suggests an alteration of the backbone structure at G15 such that it disrupts the stacking interaction of G15 with A14. Analysis of this tRNA with the chemical probe kethoxal suggests that G15 can form two hydrogen bonds with G48 to establish a tertiary interaction that involves protons donated from the exocyclic N2 and accepted by the guanine ring N3 (Hou *et al.*, 1993). This hydrogen donor–acceptor scheme has not been found in any other existing RNA structures, and is quite distinct from the predicted Levitt G15·G48 tertiary interaction, which would involve a hydrogen donor from N1 and a hydrogen acceptor of O6 (Figure 1). Thus, the unusual G15·G48 tertiary interaction in *E. coli* $tRNA^{Cys}$ is a variation of the Levitt base pair, and provides an opportunity in investigate the structural basis that contributes to this base pair.

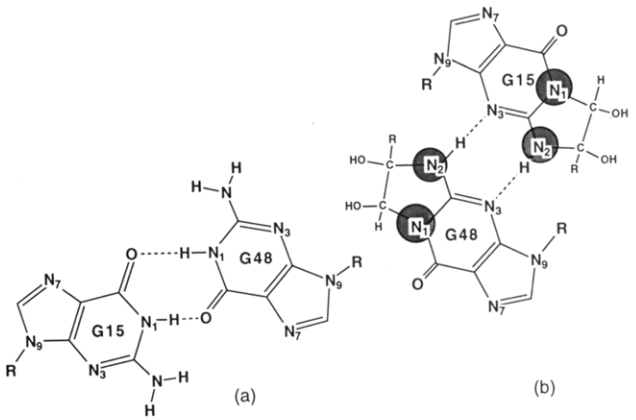

FIGURE 1: Proposed tertiary hydrogen-bonding interactions between G15 and G48 that mimic the Levitt base pair (a) or hydrogen interactions that involve a novel pairing scheme that was proposed for G15·G48 in *E. coli* $tRNA^{Cys}$ (b) (Hou *et al.*, 1993). Only the (b) configuration is capable of reacting the N1 and N1 hydrogens of guanines with kethoxal, $RC_2(H)_3(OH)_2$, to form a five-membered ring adduct (shaded in circles).

The unusual G15·G48 base pair in *E. coli* $tRNA^{Cys}$ has a critical role in the specific aminoacylation by *E. coli* cysteine–tRNA synthetase (Hou *et al.*, 1993; Hou, 1993). Alteration of this base pair to G15·C48 or C15·G48 essentially eliminates aminoacylation *in vitro*, while substitution of this base pair with G15·U48 or U15·G48 retains partial activity. The dependence of aminoacylation on G15·G48 is probably related to the unique backbone structure of G15. Structural modeling shows that the sugar–phosphate backbone at position 15 in the partially active mutants is aligned with that in the wild type, but substantially altered in the defective mutants (Hou *et al.*, 1993). It should be noted that in the Levitt configuration, alteration of nucleotides within the confines of base comple-

† This work was supported by Grant GM47935 from the National Institutes of Health.

® Abstract published in *Advance ACS Abstracts,* March 15, 1994.

[1] Abbreviations: DMS, dimethyl sulfate; DTT, dithiothreitol; SDS, sodium dodecyl sulfate.

0006-2960/94/0433-4677$04.50/0

mentarity does not have a significant effect on aminoacylation (Sampson *et al.*, 1990).

To elucidate the structural basis in *E. coli* $tRNA^{Cys}$ that contributes to the unusual G15·G48 base pair, the rationale was to introduce site-directed nucleotide substitutions to the tRNA and look for substitutions that switch the unusual G15·G48 base-pairing to the Levitt configuration. The nucleotide substitutions that confer the switch of base-pairing were interpreted as the structural elements that were required for the unusual base pair. The two types of base-pairings can be distinguished by chemical probes and by *in vitro* aminoacylation with cysteine–tRNA synthetase. The present studies show that substitution of U21 with A21 in the D loop and creation of a complementary U13·A22 base pair that replaces the mismatched A13·A22 collectively switch the unusual G15·G48 to a Levitt-like base pair. The switch is manifested by changes of hydrogen bonds and by an enhanced stacking interaction between G15 and A14 such that the N7 of G15 is protected from DMS. The switch results in decreased aminoacylation of *E. coli* $tRNA^{Cys}$, and confirms the dependence of the cysteine enzyme on the unusual G15·G48 for aminoacylation. The results were interpreted in the framework of stacking interactions in the crystal structure of tRNAs, and provided some insight into the predictions of RNA structure.

MATERIALS AND METHODS

Construction of tRNA Mutants. Plasmid derivatives of pTFMa that encode the genes for mutants of *E. coli* $tRNA^{Cys}$, flanked by the T7 RNA polymerase promoter and a *Bst*NI restriction site, were prepared by procedures described previously (Hou *et al.*, 1993; Putz *et al.*, 1991; Sampson *et al.*, 1988). Transcription of tRNA mutants was carried out at 37 °C for 3 h in 250-μL reaction mixtures that contained 25 μg of *Bst*NI-cleaved plasmid DNA, 4 mM each NTP, 16 mM GMP, 40 mM Tris-HCl, pH 8.1, 30 mM $MgCl_2$, 1 mM spermidine, 5 mM DTT (dithiothreitol), 0.01% Triton X-100, 0.4 unit/μL RNasin (Promega), and 80 units/μL T7 RNA polymerase. The transcription products were phenol-extracted, ethanol-precipitated, and separated by a 12% PAGE/7 M urea gel. Full-length transcripts were eluted from gel slices by a Schleicher & Schuell electroelution apparatus, and ethanol-precipitated. The yield is typically 50–100 μg for a full-length transcript.

Aminoacylation with Cysteine. Aminoacylation was assayed at 37 °C in 24 μL of a buffer containing 20 mM KCl, 10 mM $MgCl_2$, 25 mM DTT, 2 mM ATP, 20 mM Tris-HCl (pH 7.5), 50 μM cysteine, 0.385 μM [^{35}S]cysteine (New England Nuclear, greater than 600 Ci/mmol), and 1–10 μM purified tRNA transcript [in 10 mM Tris-HCl (pH 8.0)/1 mM EDTA] that was previously heated (70 °C, 2 min) and reannealed at room temperature (Hou *et al.*, 1993). Aminoacylation was initiated by adding 4 μL of an appropriately diluted purified *E. coli* cysteine–tRNA synthetase (e.g., 4 nM for the wild-type transcript) (Hou *et al.*, 1991). At various time points, aliquots of 4 μL of the aminoacylation reaction were removed to a 20-μL stop solution of 0.24 M iodoacetic acid/0.1 M sodium acetate (pH 5.0) in formamide, and the alkylation reaction was incubated at 37 °C for 30 min. A portion of the alkylation reaction (12 μL) was spotted onto a Whatman 3MM filter pad, precipitated with trichloroacetic acid, and washed as previously described (Schreier & Schimmel, 1972).

Chemical Modification with Dimethyl Sulfate (DMS). The tRNAs were labeled at the 3′ end with [5′-^{32}P]pCp (New England Nuclear) by T4 RNA ligase (New England Biolabs) at 4 °C overnight (Pan & Uhlenbech, 1992). The labeled tRNAs were purified by denaturing gel electrophoresis (12% PAGE/8 M urea), eluted by extraction of the gel slices with 0.125 M NH_4OAc, 0.125 mM EDTA, and 0.025% SDS, ethanol-precipitated, and counted. Modification with DMS was carried out with 4 μM tRNAs, 30 000 Cerenkov counts of the 3′-labeled tRNA in 10 mM $MgCl_2$/50 mM sodium cacodylate, pH 7.2, and 0.5% DMS (diluted in ethanol) for 5 min for the native condition. For the semi denaturing condition, tRNA was heated at 90 °C in water for 2 min, cooled on ice for 2 min, equilibrated in 1 mM EDTA and 50 mM sodium cacodylate, pH 7.2, and then treated with 0.5% DMS for 2 min. DMS resulted in chain scissions which, after aniline treatment (Peattie & Gilbert, 1980), generated labeled tRNA fragments that could be separated by gel electrophoresis and detected by autoradiography.

Chemical Modification with Kethoxal. Modification with kethoxal was carried out with 2.4 μM tRNAs in 50 mM sodium cacodylate, pH 7.2, and 0.02% kethoxal for 10 min at room temperature with 10 mM $MgCl_2$ for the native condition, and with 1 mM EDTA for the semidenaturing condition (previously heat–cool-treated as described for the DMS reaction) (Theobald *et al.*, 1988). Modifications were stopped by adding KOH–borate (pH 7.0) to a final concentration of 15 mM, followed by ethanol-precipitation. After modifications, tRNAs were denatured and annealed with a 5′-end-labeled oligonucleotide primer that was complementary to the 3′-end sequence of the tRNA from p61 to p76. The primer was extended by AMV reverse transcriptase (2 units, Life Sciences) in 6.3 mM Tris-HCl (pH 8.0), 6 mM $MgCl_2$, 40 mM KCl, 20 mM KOH–borate, and 0.25 mM each dNTP at 42 °C for 30 min. Primer extension stopped at the site of modification. The extended fragments were separated by denaturing gel electrophoresis and were detected by autoradiography (Theobald *et al.*, 1988; Wakao *et al.*, 1989; Ehresmann *et al.*, 1987).

RESULTS

E. coli $tRNA^{Cys}$ has a D3V4 configuration (three base pairs in the D stem and four nucleotides in the variable loop) rather than the D4V5 configuration that is observed in the cloverleaf structure for the majority of other tRNAs, including yeast $tRNA^{Phe}$. At position 13·22, where the D4V5 tRNAs have a complementary base pair, *E. coli* $tRNA^{Cys}$ has an A13·A22 mismatch. Adjacent to this mismatch is a U21 in the D loop, whereas more than 99% of all tRNAs have A21 or G21 (Sprinzl *et al.*, 1991). Inspection of available sequences of tRNAs shows that the coexistence of U21 and the D3V4 configuration is unique to *E. coli* $tRNA^{Cys}$, and is absent from all other tRNAs (Sprinzl *et al.*, 1991). Site-directed mutagenesis was performed in *E. coli* $tRNA^{Cys}$ to introduce substitution of A13 with U13 and of U21 with A21, and the addition of G47 to create a D4V5 configuration that carries an A21 (Figure 2). Individual nucleotide substitutions were also generated for comparison. Moreover, a U17 was added to the D4V5 configuration so that the size and shape of the D–V loops in *E. coli* $tRNA^{Cys}$ would resemble those in yeast $tRNA^{Phe}$. These nucleotide substitutions were tested for their ability to switch the base-pairing at G15·G48 to the Levitt configuration.

The switch was monitored by kethoxal reactivity at G48. Kethoxal can react with N1G and N2G to form a five-membered ring adduct (Figure 1) that can be detected during primer extension of the modified tRNA. The adduct was detected as the reverse transcriptase stopped the primer

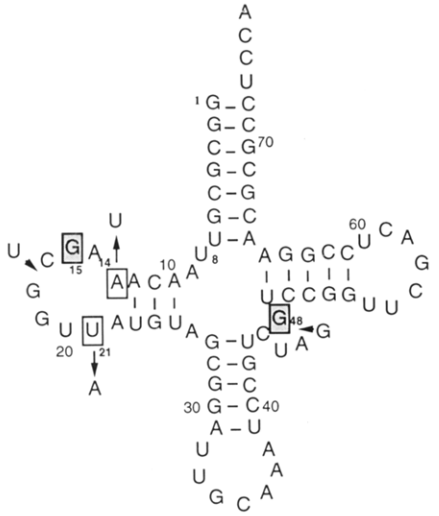

FIGURE 2: Nucleotide sequence and cloverleaf structure of *E. coli* $tRNA^{Cys}$. The G15 and G48 that establish an unusual tertiary interaction are indicated by shading. Nucleotide substitutions at A13 and U21 are indicated by open boxes, and insertion of G47 and U17 is shown by arrows.

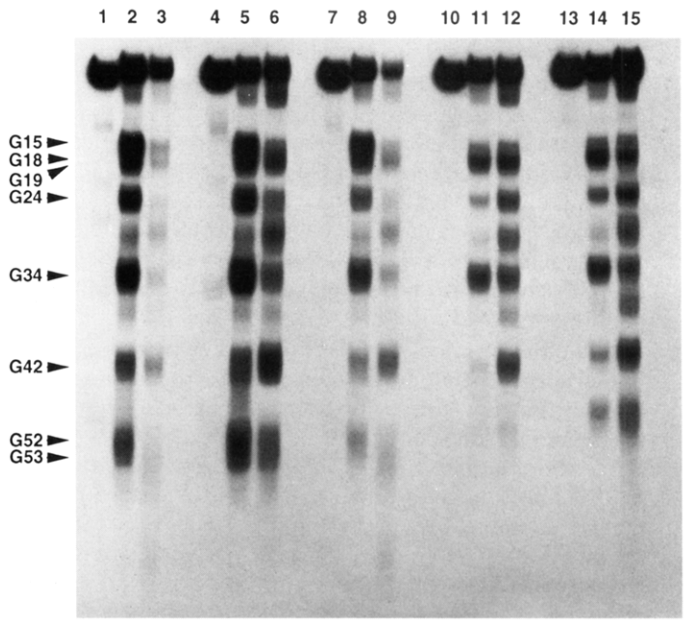

FIGURE 3: Phosphorimager analysis of the DMS reactivity at G15 in the wild type (lanes 1–3), U13 mutant (lanes 4–6), A21 mutant (lanes 7–9), U13A21 mutant (lanes 10–12), and U13A21/+G47 mutant (lanes 13–15) of *E. coli* $tRNA^{Cys}$. Lanes 1, 4, 7, 10, and 13 show controls, where individual tRNAs were not subjected to DMS treatment; lanes 2, 5, 8, 11, and 14 show the reactivity of individual tRNAs with DMS under native conditions; lanes 3, 6, 9, 12, and 15 show the reactivity of individual tRNAs with DMS under semidenaturing conditions. Arrows indicate the DMS cleavage products that end at G15, G18/G19, and G45, respectively.

extension on the tRNA template at the site of the kethoxal adduct. At G48 of the wild-type *E. coli* $tRNA^{Cys}$, kethoxal was reactive, indicating the presence of free N1G and N2G in the hydrogen-pairing scheme between G48 and G15 (Hou *et al.*, 1993). If the base-pairing had been converted to G15·G48 in a Levitt configuration, neither G48 nor G15 would have a free N1G, and thus neither would be reactive with kethoxal. Introduction of U13 or A21 alone had no effect on the kethoxal reactivity at G48 (Table 1). However, the combination of U13 and A21 substitutions reduced the kethoxal reactivity at G48 to a marginal level, indistinguishable from a control which did not react with kethoxal. It should be noted that the primer extension reaction had nonspecific stops at G48 due to random pauses by the reverse transcriptase (gels not shown), and therefore the reactivity of kethoxal at G48 was measured relative to the control. Further addition of G47 and U17 eliminated residual kethoxal reactivity at G48.

The elimination of kethoxal reactivity at G48 suggests that the N1 of G48 was involved in hydrogen-pairing with G15. If this base-pairing is maintained by sugar–phosphate backbones that mimic those in the Levitt base pair at positions 15 and 48, then the purine ring of G15 would stack with the purine ring of A14 such that the N7 of G15 would be protected from the chemical probe DMS. The reactivity with DMS at G15 was therefore determined for the mutants. The DMS reaction resulted in scission in the polynucleotide chain at G15, which could be detected as a truncated fragment on a denaturing polyacrylamide gel. The tRNA was end-labeled for the DMS reaction, and the intensity of the radioactivity for the DMS cleavage product at G15 was subjected to analysis by phosphorimager (Figure 3). The intensity was normalized to an internal control at G34 that also reacted with DMS. Introduction of U13, or A21, or the addition of G47 had no substantial effect on the reactivity with DMS at G15 (Table 1). The double substitution U13A21 markedly decreased the ability of G15 to react with DMS to only 5% of that of the wild type. The 20-fold decrease in the DMS reactivity at G15 would be consistent with an increased stacking interaction between G15 and A14. While other possibilities for a decrease in DMS reactivity at G15 exist, an increase in the stacking interaction would provide evidence for the switch of base-pairing at G15·G48 to a Levitt configuration. Subsequent addition of G47 and U17 did not enhance the stacking interaction further, and the mutant retained the 5% DMS reactivity at G15 as exhibited by the U13A21 mutant. Under

Table 1: Nucleotide Substitutions That Lead to Conversion of the Tertiary Base-Pairing at G15·G48 in *E. coli* $tRNA^{Cys}$

nucleotide substitutions	aminoacylation relative k_{cat}/K_m[a]	kethoxal reactivity at G48[b]	DMS reactivity at G15[c]
wild type	1.0	>1.0	1.0
A13 → U13	0.33	>1.0	0.73
U21 → A21	0.22	>1.0	0.67
addition of G47	0.81	nd[d]	1.0
A13 → U13 and U21 → A21	0.0067	1.0	0.05
A13 → U13, U21 → A21 and addition of G47	0.0069	0.41	0.05
A13 → U13, U21 → A21, and addition of G47 and U17	0.0064	<0.10	<0.05

[a] The initial rate of aminoacylation was measured with 4 nM cysteine–tRNA synthetase [specific activity, 1.8 nmol min^{-1} (μg of protein)$^{-1}$ and tRNA concentrations that ranged from 1 to 16 μM. The K_m of the wild-type tRNA transcript for the enzyme is 5 μM. The k_{cat}/K_m was obtained from the slope of the initial rates vs tRNA concentrations and had an accuracy of 10%. [b] The kethoxal reactivity at G48 was indicated as a relative ratio to the reactivity of G48 in the control that did not react with kethoxal. The ">1.0" denotes a greater reactivity than the control whereas a ratio that is equal to or smaller than 1.0 means no reactivity. [c] The DMS reactivity at G15 was measured by the phosphorimager to estimate the intensity of the reaction, which was then normalized to an internal control at G34. The reactivity is then given as a ratio to the wild type. [d] Not determined

the same reaction conditions, yeast tRNA^{Phe} showed no reactivity with DMS at G15 (not shown).

The residual 5% DMS reactivity at G15 in the U13A21 double mutant suggests some variation from the normal Levitt base pair. It is not known whether this variation reflects the intrinsic difference between a G·G base pair and a G·C base pair in the Levitt configuration. It should be noted that, by using Pb^{2+} cleavage of tRNA as an indicator for the overall structural integrity, a G15·G48 variant of yeast tRNA^{Phe} had a 5-fold reduced rate of cleavage compared to that of the wild type (Behlen *et al.*, 1990).

While the switch of G15·G48 to the Levitt configuration in the U13A21 mutant was supported by the kethoxal and DMS reactivities, it was also accompanied by a decrease in the aminoacylation activity with cysteine. The catalytic efficiency of aminoacylation for the cysteine enzyme (k_{cat}/K_m) was investigated with a series of tRNA concentrations that were below the K_m of the mutant. Under this condition, the initial rate was proportional to k_{cat}/K_m and was used to compare the catalytic efficiency of the mutant relative to the wild type. The U13A21 mutant and the mutants with these two substitutions and the addition of G47 and U17 all showed a more than 100-fold reduction in k_{cat}/K_m (Table 1). This decrease in k_{cat}/K_m is in the same range as the decrease of k_{cat}/K_m due to alteration of G15·G48 in the wild-type tRNA^{Cys} to either G15·G48 or C15·G48. The extents of reduction in aminoacylation among these three mutants were essentially the same. On the other hand, single substitution of U13 or A21 had a less than 2-fold effect on k_{cat}/K_m. The results highlighted the importance of the U13A21 double substitution in catalysis. Because catalysis is concomitant with tRNA conformational change, the lack of aminoacylation catalysis in the double mutant suggested a structural defect. Thus, the results of aminoacylation were consistent with the results of kethoxal and DMS chemical probes that showed a structural switch at G15·G48 upon introduction of U13 and A21.

DISCUSSION

The tRNAs investigated in this study are run-off transcripts that contain no modified bases. The native *E. coli* tRNA^{Cys} has modifications at positions 8, 20, 21, 32, 37, 39, 54, and 55. Previous study has shown that the native tRNA reacted to DMS and kethoxal in the same manner as the wild-type transcript, and has only a 5-fold higher catalytic efficiency of aminoacylation (Hou *et al.*, 1993). All the mutants that affect the G15·G48 base pair have a more than 100-fold decrease in catlaytic aminoacylation. Thus, it appears that although the modified bases are believed to contribute to the stability of overall tRNA tertiary structure (Rich & RajBhandary, 1976), they do not have a major role in the formation of the G15·G48 base pair.

Comparison of the sequence of *E. coli* tRNA^{Cys} with all other tRNAs suggests that there are perturbations of the stacking interactions in the D stem and loop of this tRNA (see below). The perturbation is best demonstrated by the reactivity of G15 to DMS in the wild-type tRNA, whereas purine 15 is normally unaccessible to chemical probes in other tRNAs. Introduction of U13 and A21 shifts the accessible G15. One likely consequence of this shift is that G15 would stack with A14. On the basis of the DMS reaction, the level of stacking would be within 95% of that in the yeast tRNA^{Phe}. The U13A21 mutant has a D4V4 configuration, which is one nucleotide short of the D4V5 configuration of yeast tRNA^{Phe} in the variable loop. Addition of G47 in the variable loop does not further enhance the stacking interaction between

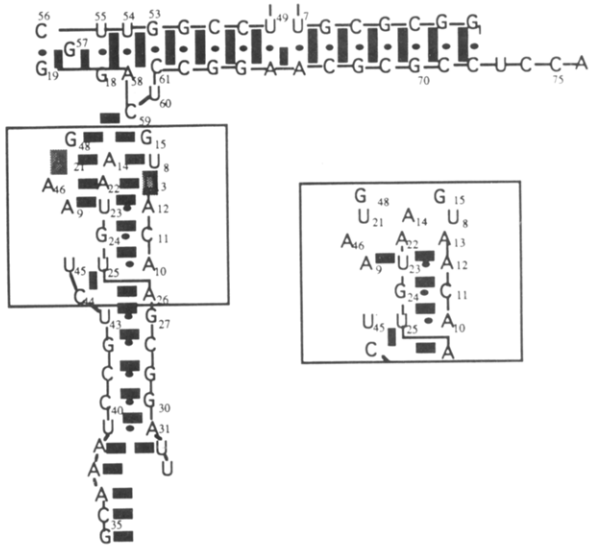

FIGURE 4: Proposed stacking interactions between various nucleotides in the U13A21 mutant of *E. coli* tRNA^{Cys}, where nucleotides U13 and A21 are shaded. The region of the D stem–loop that differs in stacking interactions between the mutant and the wild type is indicated by a box. The proposed perturbation of the stacking interactions in the wild type is shown in the insert. The stacking interactions that are predicted to preserve as in the analogous positions in the crystal structure of yeast tRNA^{Phe} are shown by black bars. Only nucleotides that are involved in the stacking interactions are shown. The connectivity of the nucleotide sequence is indicated by the number.

G15 and A14. In the crystal structure of yeast tRNA^{Phe}, nucleotide 47 is not involved in the tertiary hydrogen or stacking interactions, and is projected away from the center of the tRNA. If the reduced accessibility at G15 reflects enhanced stacking interaction, it is likely that the U13A21 mutant of *E. coli* tRNA^{Cys} has acquired most, or all, of the stacking interactions in the D stem–loop that are observed in yeast tRNA^{Phe}.

Figure 4 shows the proposed stacking interactions in *E. coli* tRNA^{Cys} and in the U13A21 mutant. The figure is drawn on the basis of the stacking interactions in yeast tRNA^{Phe}, but with substitution of the nucleotide sequence for *E. coli* tRNA^{Cys}. The U13A21 mutant shares the composition of A21, U8, and A14 with yeast tRNA^{Phe} and therefore can be proposed to establish a hydrogen bond between the N1 of A21 and the 2′-OH of ribose 8 as is observed in yeast tRNA^{Phe} (Kim *et al.*, 1974a,b; Robertus *et al.*, 1974). The A21·U8·A14 tertiary interaction in yeast tRNA^{Phe} forms a plane, which enables A21 to stack under the Levitt base pair (Kim *et al.*, 1974b; Ladner et al., 1975). If the proposed model is correct, A21 in the U13A21 mutant would also stack under the Levitt-like G15·G48. Below this A21·U8·A14 tertiary interaction in yeast tRNA^{Phe} is a C13·G22 base pair that forms two hydrogen bonds in the major groove between G22 and a positively charged m^{7}G46 (Kim *et al.*, 1974a,b; Robertus *et al.*, 1974). This C13·G22·G46 tertiary interaction contributes further to the stacking interactions in the D stem. A similar tertiary interaction of U13·A22·A46 can be proposed for the U13A21 mutant, whereby the N1 and N6 of A46 would form a hydrogen bond, respectively, with the N6 and N7 of A22 (Kim *et al.*, 1974b). In fact, the combination of A46 and U13·A22 is found in the sequence of yeast tRNA^{Arg}, which also has A21 and U8·A14 (Sprinzl *et al.*, 1991). This suggests that the proposed hydrogen and stacking interactions in the U13A21 mutant are represented in a naturally existing tRNA.

In contrast, the wild-type tRNA^{Cys} contains a U21, which is modified as dihydrouridine (D) in the native tRNA.

Although U21 (or D21) in principle can form a hydrogen bond with the 2′-OH of ribose 8, it is not known if this hydrogen bond would maintain U21 on the same plane of U8·A14. Considerable variation in the ribose phosphate backbone at U21 can be envisaged that can interfere with the stacking interaction between U8·A14 and G15·G48. Conversely, the mismatched A13·A22 does not mean that nucleotides 22 and 46 cannot be stacked. All of the D3V4 tRNAs have mismatched nucleotides at 13 and 22, yet they maintain a Levitt base pair. For example, the crystal structure of *E. coli* $tRNA^{Gln}$ shows that the mismatched A13·A22, which pairs with U46, is stacked under A21·U8·A14 while maintaining a normal Levitt G15·C48 base pair (Rould *et al.*, 1989). It is possible that the bulkier A at positions 13, 22, and 46 cannot be easily accommodated in the same plane. Introduction of a complementary U13 may remove some of the constraints and enhance the stacking interaction at 13·22·46. Thus, installation of both A21·U8·A14 and a U13·A22 base pair that could stabilize the stacking interaction at 13·22·46 is necessary to maintain a Levitt-like G15·G48 base pair.

Examination of the DMS chemical probe data (Figure 3) suggests that, except for the switch at G15·G48, all tRNA mutants that were investigated here maintain an overall tertiary structure similar to that of the wild type. This is indicated by their relative reactivities to DMS at various positions. For example, phosphorimager analysis of band intensity shows that G24 in the wild type reacts to DMS almost twice as strongly as G42. This ratio of 2 for G24 vs G42 is preserved in all four mutants under the native conditions. However, it is fair to say that the U13A21 and U13A21/+G47 mutants may have acquired additional structural changes from the wild type at positions outside of G15·G48. These changes are reflected by the enhanced DMS reactivities at G24 and G34 under semidenaturing conditions. Because these changes are not as significant as the changes at G15 for these mutants, they are probably minor. It is possible that the additional minor changes are brought about by the switch at G15·G48.

Inspection of tRNA sequences shows that, besides *E. coli* $tRNA^{Cys}$, only three other tRNAs have a pyrimidine at position 21. All these tRNAs have an unusual nucleotide composition at positions 15 and 48; e.g., U15·A48 for *Aedes albopictus* $tRNA^{Gly}$ that has U21, A15·A48 for yeast $tRNA^{Pro}$ that has C21, and U15·C48 for a bovine $tRNA^{Ser}$ that has U21 (Sprinzl *et al.*, 1991). Although the detailed structure of these tRNAs is not known, the presence of pyrimidine 21 appears to promote variations from the normal Levitt base pair. Thus, the use of G15·G48 to elucidate U8·A14·A21 as one of the structural elements that contribute to the Levitt base pair has useful applications. It will be interesting to establish the structural requirements in a tRNA that contribute to other tertiary interactions. The understanding of these requirements would ultimately assist in our ability to design and predict RNA tertiary structure.

ACKNOWLEDGMENT

I thank Dr. H. Gamper for critically reading the manuscript, and M. Jansen and C. Slavinsky for discussion.

REFERENCES

Behlen, L. S., Sampson, J. R., DiRenzo, A. B., & Uhlenbeck, O. C. (1990) *Biochemistry 29*, 2515–2523.
Ehresmann, C., Baudin, P., Mougel, M., Romby, P., Ebel, J.-P., & Ehresmann, B. (1987) *Nucleic Acids Res 15*, 9109–9128.
Hou, Y.-M. (1993) *Trends Biochem. Sci. 18*, 362–364.
Hou, Y.-M., Shiba, K., Mottes, C., & Schimmel, P. (1991) *Proc. Natl. Acad. Sci. U.S.A. 88*, 976–980.
Hou, Y.-M., Westhof, E., & Giege, R. (1993) *Proc. Natl. Acad. Sci. U.S.A. 90*, 6776–6780.
Kim, S. H., Suddath, F. L., Quigley, G. J., McPherson, A., Sussman, J. L., Wang, A. H. J., Seeman, N. C., & Rich, A. (1974a) *Science 185*, 435–440.
Kim, S. H., Sussman, J. L., Suddath, F. L., Quigley, G. J., McPherson, A., Wang, A. H. J., Seeman, N. C., & Rich, A. (1974b) *Proc. Natl. Acad. Sci. U.S.A. 71*, 4970–4974.
Klug, A., Ladner, J., & Robertus, J. D. (1974) *J. Mol. Biol. 89*, 511–516.
Ladner, J. E., Jack, A., Robertus, J. D., Brown, R. S., Rhodes, D., Clark, B. F. C., & Klug, A. (1975) *Proc. Natl. Acad. Sci. U.S.A. 72*, 4414–4418.
Levitt, M. (1969) *Nature 224*, 759–763.
Pan, T., & Uhlenbeck, O. C. (1992) *Biochemistry 31*, 3887–3895.
Peattie, D. A., & Gilbert, W. (1980) *Proc. Natl. Acad. Sci. U.S.A. 77*, 4679–4782.
Puglisi, J. D., Putz, J., Florentz, C., & Giege, R. (1993) *Nucleic Acids Res. 21*, 41–49.
Putz, J., Puglishi, J. D., Florentz, C., & Giege, R. (1991) *Science 252*, 1696–1699.
Quigley, G. J., & Rich, A. (1976) *Science 194*, 796–806.
Rich, A., & RajBhandary, U. L. (1976) *Annu. Rev. Biochem. 45*, 805–860.
Robertus, J. D., Ladner, J. E., Finch, J. T., Thodes, D., Brown, R. S., Clark, B. F. C., & Klug, A. (1974) *Nature 250*, 546–551.
Rould, M. A., Perona, J. J., Söll, D., & Steitz, T. A. (1989) *Science 246*, 1135–1142.
Sampson, J. R., & Uhlenbeck, O. C. (1988) *Proc. Natl. Acad. Sci. U.S.A. 85*, 1033–1037.
Sampson, J. R., DiRenzo, A. B., Behlen, L. S., & Uhlenbeck, O. C. (1990) *Biochemistry 29*, 2523–2532.
Schreier, A. A., & Schimmel, P. (1972) *Biochemistry 11*, 1582–1589.
Sprinzl, M., Hartmann, T., Webber, J., Blank, J., & Zeidler, R. (1991) *Nucleic Acids Res. 17*, r1–r172.
Theobald, A., Springer, M., Grunberg-Manago, M., Ebel, J.-P., & Giege, R. (1988) *Eur. J. Biochem. 175*, 511–524.
Wakao, H., Romby, P., Westhof, E., Laalami, S., Grunberg-Manago, M., Ebel, J.-P., Ehresmann, C., & Ehresmann, B. (1989) *J. Biol. Chem. 264*, 20363–20371.

Structural Characteristics of the Nucleotide-Binding Site of *Escherichia coli* Primary Replicative Helicase DnaB Protein. Studies with Ribose and Base-Modified Fluorescent Nucleotide Analogs†

Wlodzimierz Bujalowski* and Malgorzata Maria Klonowska‡

Department of Human Biological Chemistry & Genetics, The University of Texas Medical Branch at Galveston, Galveston, Texas 77555-0653

Received January 5, 1994; Revised Manuscript Received February 15, 1994®

ABSTRACT: Structural characteristics of the base- and ribose-binding regions of the high-affinity noninteracting nucleotide-binding site of *Escherichia coli* primary replicative helicase DnaB protein have been studied, using the base-modified fluorescent nucleotide analog 1, N^6-ethenoadenosine diphosphate (ϵADP) and the ribose-modified fluorescent analogs 3′(2′)-*O*-(*N*-methylantraniloyl)adenosine 5′-diphosphate (MANT-ADP), 3′-*O*-(*N*-methylantraniloyl)deoxyadenosine 5′-diphosphate (MANT-dADP), 3′-*O*-(*N*-methylantraniloyl)-deoxyadenosine 5′-triphosphate (MANT-dATP), and 2′(3′)-*O*-(2,4,6-trinitrophenyl)adenosine 5′-diphosphate (TNP-ADP). The obtained data indicate contrasting differences between these two regions. Binding of ϵADP to the DnaB helicase causes only ~21% increase of the nucleotide fluorescence intensity and no shift of the emission spectrum maximum. The fluorescence of bound ϵADP is characterized by a single lifetime of 24.2 ± 0.6 ns, only slightly shorter than the fluorescent lifetime of the free ϵADP in solution (25.5 ± 0.6 ns). Solute-quenching studies of bound ϵADP, using different quenchers, acrylamide, I^-, and Tl^+, indicate limited accessibility of ethenoadenosine to the solvent. These results strongly suggest that the base-binding region of the DnaB nucleotide-binding site is located in the polar cleft on the enzyme's surface. Moreover, the limiting emission anisotropy of bound ϵADP is 0.21 ± 0.02, compared to the anisotropy of 0.3 of completely immobilized ϵADP at the same excitation wavelength (λ_{ex} = 325 nm, λ_{em} = 410 nm), indicating that the adenine preserves substantial mobility when bound in the base-binding site. In contrast, fluorescence intensity at the emission maximum of TNP-ADP and MANT-ADP, which has modifying groups attached to the 2′ and/or 3′ oxygens of the ribose, increases upon binding to DnaB by factors of ~4.7 (λ_{ex} = 408 nm) and ~2.6 (λ_{ex} = 356 nm), respectively. Moreover, the maximum of emission spectrum of bound TNP-ADP is blue-shifted by ~11 nm and that of MANT-ADP by ~12 nm. Comparisons between spectral properties of TNP-ADP and MANT-ADP bound to DnaB and in different solvents suggest that the ribose-binding region of the DnaB nucleotide-binding site has relatively low polarity. Solute quenching studies of MANT-ADP fluorescence, using acrylamide, I^-, and Tl^+, indicate that the MANT group has very little accessibility to the solvent when bound to DnaB. Taken together, these results suggest that the ribose-binding region constitutes a hydrophobic cleft, or pocket, with very limited, if any, contact with the solvent. Moreover, fluorescence anisotropy of bound TNP-ADP and MANT-ADP is 0.32 ± 0.02 and 0.33 ± 0.02, respectively. These values are very close to the fundamental anisotropies of TNP-ADP and MANT-ADP, indicating that the fluorophores attached to the ribose have very restricted motional freedom. Fluorescence of MANT-ADP free in solution decays with a nearly homogenous single lifetime of 3.9 ± 0.2 ns. However, upon binding, the emission is characterized by two components (τ_1 = 13.1 ± 0.5 ns, amplitude = 0.76, and τ_2 = 6.0 ± 0.2 ns, amplitude = 0.24). Very similar double-exponential fluorescence decays have been obtained with bound MANT-dADP and MANT-dATP. The data indicate that the chromophores attached to the ribose experience two different environments when bound to the DnaB helicase, which may reflect the existence of two different conformations of the ribose-binding region of the DnaB helicase nucleotide-binding site. This result is in contrast to a single environment and probably a lack of discrete conformational heterogeneity at the base-binding region, as probed by ϵADP fluorescence. Thus, the data indicate that conformational heterogeneity is localized around the ribose and not transmitted to the base-binding region, suggesting limited communication between base- and ribose-binding sites. The reported results provide the first insight into the nature of the significant structural differences between base- and ribose-binding regions of the nucleotide-binding site of the DnaB helicase. The importance of these differences, in terms of the biological functioning of the DnaB protein, is discussed.

The DnaB protein is a key replication protein in *Escherichia coli* (Kornberg & Baker, 1992), which is involved both in initiation and elongation stages of DNA replication and also plays a fundamental role in the replication of phage and plasmid DNA (McMacken et al., 1977; Ueda et al., 1978; Kaguni et al., 1982; Matson & Kaiser-Rogers, 1990). The protein is the *E. coli* primary replicative helicase, i.e., the factor responsible for unwinding the DNA duplex in front of

† This work was supported by NIH Grant R01 GM-46679 (to W.B.).

* Send correspondence to this author at Department of Human Biological Chemistry & Genetics, The University of Texas Medical Branch Galveston, 301 University Boulevard, Galveston, TX 77555-0653.

‡ On leave from Laboratory of Physical Chemistry, Drug Science Institute, Department of Pharmacy, Warsaw Medical School, Banacha 1, Warsaw, Poland.

® Abstract published in *Advance ACS Abstracts*, April 1, 1994.

0006-2960/94/0433-4682$04.50/0

the replication fork (LeBowitz & McMacken, 1986; Baker et al., 1987). DnaB protein is the only helicase required to reconstitute DNA replication *in vitro* from the chromosomal origin of replication (oriC). In its role as a "mobile replication promoter", DnaB protein binds to ssDNA.[1] The nucleoprotein complex is then specifically recognized by the primase (Arai & Kornberg, 1981b).

DnaB protein displays multiple activities *in vitro* which reflect its interactions with different ingredients in the primosome and the protein–nucleic acid complexes formed at the origins of bacterial and phage DNA replication. These activities include (1) binding of rNTPs (particularly ATP) and dNTPs (Arai et al., 1981a; Arai & Kornberg, 1981a–c; Reha-Krantz & Hurwitz, 1978b; Bujalowski & Klonowska, 1993), (2) ATPase and ribonucleotide triphosphatase activities (Arai & Kornberg, 1981a–c; Reha-Krantz & Hurwitz, 1978b; Bujalowski & Klonowska, 1993), (3) binding to ss- and dsDNA (Arai & Kornberg, 1981a,b; Reha-Krantz & Hurwitz, 1978b; LeBowitz & McMacken, 1986), (4) interactions with DnaC protein (Wahle et al., 1989a,b; Allen & Kornberg, 1991), primase (DnaG protein) (Arai & Kornberg, 1981b; LeBowitz & McMacken, 1986), phage λ-encoded P protein (Wickner, 1978; Mallory et al., 1990), and phage P1-encoded ban protein (Lanka et al., 1978), and (5) possible interactions with single-stranded binding (SSB) protein which strongly stimulates DnaB helicase activity (LeBowitz & McMacken, 1986).

In solution, the native DnaB protein exists as a stable hexamer composed of six identical subunits with a monomeric molecular weight of 52 265. The hexamer is most probably the species active *in vivo* (Arai et al., 1981a; Reha-Krantz & Hurwitz, 1978a; Bujalowski and Klonowska, submitted).

The binding, or binding and hydrolysis, of ATP is the key element regulating DnaB protein activities, including affinity toward nucleic acids and other components of the replication apparatus (Arai & Kornberg, 1981a–c; Arai et al., 1981b; Reha-Krantz & Hurwitz, 1978b; LeBowitz & McMacken, 1986). It has been proposed that ATP acts as a very specific positive allosteric effector which induces a conformational change in the protein and increases its affinity for ss nucleic acids. Moreover, the unwinding of duplex DNA by the DnaB helicase is fueled by the hydrolysis of ribonucleoside triphosphates, with ATP being the most efficient (LeBowitz & McMacken, 1986; Matson & Kaiser-Rogers, 1990).

It is clear that understanding the nucleotide interactions with DnaB protein, and its regulatory role, is indispensable for understanding different activities of the enzyme. Although the importance of the control and regulation of the DnaB protein functions by nucleotide phosphates has been recognized, the mechanism and the nature of this control still remain unknown at the molecular level.

Quantitative studies of the nucleotide binding to the DnaB helicase have established that the hexamer has six nucleotide-binding sites, presumably one on each protomer (Arai & Kornberg, 1981b; Bujalowski & Klonowska, 1993). On the basis of thermodynamically rigorous fluorescence titrations, we have determined that the binding process is biphasic, with the first three nucleotide molecules binding in the high-affinity step and the next three nucleotides binding in the low-affinity step. The biphasic behavior of binding isotherms results from the negative cooperative interactions among binding sites. The physiological role of the high- and low-affinity binding sites is still unknown. The statistical thermodynamic model, the hexagon, in which the negative cooperativity is limited to neighboring subunits, provides an excellent description of the binding process of nucleotides to the DnaB helicase (Bujalowski & Klonowska, 1993).

Early steady-state enzyme kinetic studies suggested significant differences between the base- and ribose-binding regions of the DnaB nucleotide-binding site in affecting the enzyme activities. Thus, the hydrolysis of nucleoside triphosphates, as well as the helicase activity, was relatively independent of the nature of the base (Arai & Kornberg, 1981a; LeBowitz & McMacken, 1986). On the other hand, DnaB could not hydrolyze either deoxynucleoside triphosphates or TNP-ATP, with a fluorescent group (TNP) attached to the 2′ and 3′ oxygens of the ribose (Arai & Kornberg, 1981a; Bujalowski & Klonowska, 1993). Also, the enzyme could not unwind duplex DNA in the presence of only deoxynucleotides, indicating intimate involvement of the sugar moiety of the nucleotide in the enzyme catalysis (LeBowitz & McMacken, 1986). Both γ-phosphate and intact ribose, but not the base moiety, appeared to be decisive elements in inducing allosteric interactions between the nucleotide and the ssDNA-binding site (Arai & Kornberg, 1981b; Bujalowski and Klonowska, manuscript in preparation). Clearly, different structural regions of the bound nucleotide molecule seem to be able to act either independently, triggering specific responses of the DnaB helicase through highly localized conformational changes, or together in a concerted way. In order to understand these complex interactions, the structure of the DnaB helicase nucleotide-binding site has to be determined.

In this communication, we describe the systematic studies of the structural characteristics of both the base- and ribose-binding regions of the high-affinity noninteracting nucleotide-binding site of the *E. coli* DnaB helicase, using different fluorescent nucleotide analogs: 1,N^6-ethenoadenosine diphosphate (εADP), 3′(2′)-*O*-(*N*-methylantraniloyl)adenosine 5′-diphosphate (MANT-ADP), 3′-*O*-(*N*-methylantraniloyl)-deoxyadenosine 5′-diphosphate (MANT-dADP), 3′-*O*-(*N*-methylantraniloyl)deoxyadenosine 5′-triphosphate (MANT-dATP), and 2′(3′)-*O*-(2,4,6-trinitrophenyl)adenosine 5′-diphosphate (TNP-ADP). These analogs differ by type and location of the modifying groups. In the case of TNP and MANT derivatives, the fluorescent groups are located on the ribose, while in the etheno derivative, the fluorescent modification is on the adenine residue (Bujalowski & Klonowska, 1993).

The obtained results provide the first characterization of the structural differences between the base- and ribose-binding regions of the nucleotide-binding site of the DnaB helicase. While the data indicate that the base is located in a rather polar environment and has relatively high motional freedom, the ribose is located in a hydrophobic region and has strongly constrained mobility. Solute quenching studies suggest that the base is significantly shielded but still has some access to the solvent. However, analogous studies suggest, within experimental accuracy, inaccessibility of the ribose-attached fluorophores to the solvent molecules. Moreover, fluorescence lifetime measurements of the MANT group indicate that the fluorophore senses two different environments, possibly two different conformations of the ribose-binding region. Only a single fluorescence lifetime was detected for the bound εADP,

[1] Abbreviations: TNP-ADP, 2′(3′)-*O*-(2,4,6-trinitrophenyl)adenosine 5′-diphosphate; εADP, 1,N^6-ethenoadenosine diphosphate; MANT-ADP, 3′(2′)-*O*-(*N*-methylantraniloyl)adenosine 5′-diphosphate; MANT-dADP, 3′-*O*-(*N*-methylantraniloyl)deoxyadenosine 5′-diphosphate; MANT-dATP 3′-*O*-(*N*-methylanttraniloyl)deoxyadenosine 5′-triphosphate; SSB, *E. coli* single-stranded binding protein; Tris, tris(hydroxymethyl)-aminomethane; ssDNA, single-stranded deoxyribonucleic acid; dsDNA, double-stranded deoxyribonucleic acid.

suggesting that the conformational heterogeneity around the ribose is not transmitted to the base-binding region of the nucleotide-binding site of the DnaB helicase.

MATERIALS AND METHODS

Reagents and Buffers. All chemicals were reagent grade. All solutions were made with distilled and deionized 18 MΩ (Milli-Q) water. The standard buffer (T2) was 50 mM Tris adjusted to pH 8.1 at appropriate temperatures with HCl, 5 mM $MgCl_2$, and 10% glycerol. The temperatures and the concentrations of NaCl in the buffer are indicated in the text.

Nucleotides. TNP-ADP was from Molecular Probes (Eugene, OR). The nucleotide was additionally purified, as described by Hiratsuka and Uchida (1973). εADP, from Sigma, was used without further purification. MANT-ADP, MANT-dADP, and MANT-dATP were synthesized by the method of Hiratsuka (1983). All nucleotides used in the binding studies were >95% pure as judged by TLC on silica.

DnaB Protein. The *E. coli* DnaB protein was purified from overproducing strain RLM1038, generously provided by Dr. Roger McMacken (Johns Hopkins University), using a slightly modified Arai–Kornberg procedure (Arai et al., 1981a; Bujalowski & Klonowska, 1993). The protein was >97% pure as judged by SDS polyacrylamide gel electrophoresis with Coomassie Brilliant Blue staining. The concentration of the protein was determined spectrophotometrically using the extinction coefficient $\epsilon_{280} = 1.85 \times 10^5$ cm^{-1} M^{-1} (hexamer) (Bujalowski and Klonowska, submitted).

Steady-State Fluorescence Measurements. All steady-state fluorescence measurements were performed using the SLM 48000S spectrofluorometer as we previously described (Bujalowski & Porschke, 1988a,b; Bujalowski & Klonowska, 1993). In the fluorescence intensity measurements, to avoid possible artifacts due to the fluorescence anisotropy of the sample, polarizers were placed in excitation and emission channels and set at 90° and 55° (magic angle), respectively. All steady-state intensity data were corrected, if necessary, for dilution and inner filter effects, using the following formula (Parker, 1968; Lakowicz, 1983)

$$F_{cor} = (F - B)(V/V_0)10^{0.5b(A_{\lambda ex})} \quad (1)$$

where F_{cor} is the corrected value of the fluorescence intensity, F is the experimentally measured fluorescence intensity, B is the background, V is the volume of the sample, V_0 is the initial volume of the sample, b is the total length of the optical path in the cuvette expressed in centimeters, and $A_{\lambda ex}$ is the absorbance of the sample at excitation wavelengths. The temperature of all measurements was controlled to ±0.1 °C.

Steady-State Fluorescence Anisotropy Measurements. All steady-state fluorescence anisotropy measurements were performed in L format using Glan-Thompson polarizers placed in the excitation and emission channel of the SLM 48000S spectrofluorometer. The fluorescence anisotropy of the sample was calculated using eq 2

$$r = (I_{VV} - GI_{VH})/(I_{vv} + 2GI_{VH}) \quad (2)$$

were I is the fluorescence intensity and the first and second subscripts refer to vertical (V) polarization of the excitation and vertical (V) or horizontal (H) polarization of the emitted light (Bujalowski & Lohman, 1989a,b). The factor $G = I_{HV}/I_{HH}$ corrects for the different sensitivity of the emission monochromator for vertically and horizontally polarized light (Azumi & McGlynn, 1962; Lakowicz, 1983).

Quantum Yield Determination. The quantum yields of free and bound nucleotide analogs, q_s, were determined by the comparative method of Parker and Reese (Parker & Reese, 1960) using the following relationship

$$q_S = q_R[(\int F_S \partial\lambda)10^{0.5b(A_S)}/(\int F_R \partial\lambda)10^{-0.5b(A_R)}](A_R/A_S) \quad (3)$$

where q_R is the quantum yield of a standard, $(\int F_S \partial\lambda)10^{0.5b(A_S)}$ and $(\int F_R \partial\lambda)10^{0.5b(A_R)}$ are the areas under the corrected emission spectra, corrected for inner filter effects of the standard and the fluorophore, respectively, A_S and A_R are the absorbances of the standard and the studied fluorophore at a given excitation wavelength, respectively, and b is the optical path in centimeters. Quinine bisulfate in 0.1 N H_2SO_4 was used as a reference for the excitations between 300 and 360 nm (absolute quantum yield $q_R = 0.7$; Scott et al., 1970), and fluorescein in 0.1 N NaOH was used for the excitation wavelength above 400 nm (absolute quantum yield $q_R = 0.92$; Weber & Teale, 1957).

Solute Accessibility Studies. Collisional, or dynamic, quenching of fluorescence results from random collisions between the quenching ligand Q and the fluorophore during the excited-state lifetime of the fluorophore (Parker, 1968; Lakowicz, 1983). If only the dynamic quenching process is present, the deactivation of the excited state of the fluorophore is described by eq 4 (Stern & Volmer, 1919)

$$F_0/F = 1 + K_{SV}[Q] \quad (4)$$

where F_0 and F are the steady-state fluorescence intensities in the absence and presence of the quenching ligand at concentration [Q]. K_{SV} is the Stern–Volmer quenching constant and is related to the bimolecular quenching rate constant k_q and to the fluorescence lifetime of the fluorophore τ by the relationship $K_{SV} = k_q\tau$.

The simultaneous presence of static and dynamic quenching processes may lead to the deviation from ideal Stern–Volmer behavior and can be closely approximated by (Lakowicz, 1983; Eftink, 1991)

$$F_0/F = (1 + K_{SV}[Q])\exp(V[Q]) \quad (5)$$

where V is the static quenching constant.

The efficiency of the solute quenching, γ, is a measure of the exposure of the bound fluorescent ligand and is defined as

$$\gamma = k_q^b/k_q^f \quad (6)$$

where k_q^b and k_q^f are the bimolecular quenching rate constants for bound and free fluorophores.

To obtain information about the accessibility and nature of the microenvironment surrounding different regions of the bound fluorescent nucleotide, quenchers having different physical properties have been selected. The quenching studies have been performed with neutral acrylamide, negatively charged iodide, I^-, and positively charged thallium, Tl^+ (Robbins et al., 1985; Philips et al., 1987; Eftink, 1991). As a control, titrations with ionic quenchers have also been performed in the presence of higher NaCl concentrations (~80 mM). No significant effect of the increased salt concentrations on determined quenching parameters has been observed.

Fluorescence Lifetime Measurements. Fluorescence lifetime determinations of nucleotide analogs, free and bound to

DnaB protein, have been performed using a SLM 48000S multifrequency, lifetime spectrofluorometer. Excitation was produced using a 450-W mercury–xenon lamp. The emission was detected through a Schott KV399-nm filter. To avoid fluorescence anisotropy artifacts in the phase-modulation measurements, Glan-Thompson polarizers were placed in excitation and emission channels and set at 90° and 55° (magic angle), respectively (Spencer & Weber, 1970). The modulation frequency was varied between 10 and 100 MHz at 1- and 2-MHz intervals. Usually, the data were collected for at least 50 different frequencies in a single experiment. The fluorescence lifetimes have been calculated from the phase shifts and demodulations of the emitted light from the sample with respect to scattered light from glycogen as a standard (τ = 0). The dependences of the phase shift and demodulation, as a function of the modulation frequency, were fitted to single or multiexponential decay functions, using the nonlinear least-squares fit routine provided by the manufacturer.

Determination of the Average Number of the Nucleotide Molecules Bound to DnaB Helicase. Studies described in this work focus on the structural characteristics of the high-affinity noninteracting nucleotide-binding site of the DnaB helicase (Bujalowski & Klonowska, 1993). In order to eliminate the interference of the free nucleotide on the fluorescence properties of the bound molecule, the concentrations of the protein and the nucleotide have to be selected to assure that the concentration of bound nucleotide [N_b] is practically equal to its total concentration [N_t]. Moreover, the average number of nucleotide analog molecules $(\sum\nu_i)_H$ bound per DnaB hexamer should not exceed 1.5–2.0 (see below). We previously described thermodynamic studies of the stoichiometries and the mechanism of nucleotide binding to the DnaB protein hexamer using fluorescent nucleotide analogs (Bujalowski & Klonowska, 1993). Using the rigorous thermodynamic method (Bujalowski & Lohman, 1987a,b), the absolute binding isotherms have been determined from fluorescence titrations, independent of the assumption of strict proportionality between the observed quenching of the protein fluorescence and the number of bound nucleotides (Bujalowski & Klonowska, 1993). The exact average number of given nucleotide analog molecules bound to DnaB protein $(\sum\nu_i)_H$ and the concentration of the bound nucleotide [N_b] used in this work have been calculated according to the hexagon model, using the intrinsic binding constants K's and the cooperativity parameters σ's, previously determined, according to the following equations (Bujalowski & Klonowska, 1993)

$$(\sum\nu_i)_H = (6x + 6(3 + 2\sigma)x^2 + 6(1 + 6\sigma + 3\sigma^2)x^3 + 12(3\sigma^2 + 2\sigma^3)x^4 + 30\sigma^4x^5 + 6\sigma^6x^6)/Z_H \quad (7a)$$

$$Z_H = 1 + 6x + 3(3 + 2\sigma)x^2 + 2(1 + 6\sigma + 3\sigma^2)x^3 + 3(3\sigma^2 + 2\sigma^3)x^4 + 6\sigma^4x^5 + \sigma^6x^6 \quad (7b)$$

$$[N_b] = (\sum\nu_i)H[\mathrm{DnaB}]_{total} \quad (7c)$$

where $x = K[N_f]$ and [N_f] is the free nucleotide concentration. $[\mathrm{DnaB}]_{total}$ is the total DnaB protein concentration in the sample. The quantity Z_H is the partition function of the DnaB hexamer–nucleotide system (Bujalowski & Klonowska, 1993).

RESULTS

Base-Binding Region of the Nucleotide-Binding Site of E. coli DnaB Protein. As we mentioned above, the subject of the studies in this work is the structural characterization of the high-affinity noninteracting nucleotide-binding site of the DnaB helicase. Binding of six nucleotides to the DnaB hexamer is described by a statistical thermodynamic model, the hexagon, in which the cooperative interactions are limited to neighboring binding sites (Bujalowski & Klonowska, 1993). Due to negative cooperativity, the binding process is biphasic, i.e., three molecules bind in the high-affinity step, and the subsequent three nucleotides bind in the low-affinity step.

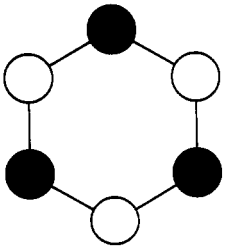

FIGURE 1: Schematic diagram showing the configuration of the hexagon with three high-affinity noninteracting sites of the DnaB hexamer saturated with ligand (closed circles). The statistical weight of this configuration is $2x^3$ (see eq 7b in the text).

This behavior of the binding process results from the fact that in the hexagon model, due to the low density of cooperative interactions, there will be a configuration with three nucleotide molecules bound which has much lower free energy than others with three nucleotides bound (see eq 7b; Bujalowski & Klonowska, 1993). This configuration is schematically presented in Figure 1 and corresponds to the situation where all three bound molecules are separated by an empty binding site (subunit), and hence, there are no cooperative interactions in this particular configuration of the hexamer–nucleotide system. If the degree of binding is low ($(\sum\nu_i)_H < 2$), then only the first terms in eq 7b, which do not contain σ, will have any significant contribution to the partition function of the system. Therefore, to eliminate possible interference of cooperative interactions, and to exclusively examine noninteracting high-affinity nucleotide-binding sites, all studies of bound nucleotides were performed on samples with the average number of nucleotide molecules bound per DnaB hexamer significantly lower than 2 (see below).

Corrected fluorescence emission spectra (λ_{ex} = 325 nm) of ϵADP free and bound to the DnaB helicase in buffer T2 (20 mM NaCl, pH 8.1, 20 °C) are shown in Figure 2a. In applied DnaB protein and nucleotide concentrations, >97% of ϵADP is bound. The average number of the bound nucleotide molecules $(\sum\nu_i)_H$ is ~0.11, thus assuring that, in the case of a protein–nucleotide complex, fluorescence properties of bound ϵADP in a noninteracting nucleotide-binding site are being examined. Binding of ϵADP to DnaB is accompanied by only a ~21% increase of the nucleotide fluorescence intensity, and there is no detectable shift of the maximum of the fluorescence spectrum, suggesting that the ethenoadenine-binding region has polarity similar to the bulk solvent (Sencrist et al., 1972; Spencer et al., 1974). This conclusion is further strongly supported by fluorescence lifetime measurements of the free and bound ϵADP. The emission of free ϵADP in buffer T2 (20 mM NaCl, pH 8.1, 20 °C) is characterized by a single lifetime, τ = 25.5 ± 0.6 ns (Table 1). The emission of ϵADP bound to DnaB is also characterized by a single lifetime, only ~5% shorter (τ = 24.2 ± 0.6 ns). Thus, binding of ϵADP to the DnaB helicase has little effect on the nucleotide fluorescence lifetime. This is in striking contrast to the effect of placing ϵADP in nonpolar solvents which causes a dramatic change in τ. The lifetime decreases from ~24 ns in water solution to ~15 ns in dioxane (Spencer et al., 1974). Thus, lack of a substantial change in ϵADP's lifetime, when bound

Table 1: Stern–Volmer Quenching Constants K_{SV}, Bimolecular Quenching Rate Constants k_q, Fluorescence Lifetimes τ, and Solute Quenching Efficiencies γ of εADP Free and Bound to DnaB Helicase in Buffer T2 (20 mM NaCl, pH 8.1, 20 °C)

nucleotide	quencher	quencher concentration (mM)	F_o/F	τ (ns)	τ_o/τ[a]	K_{SV} (M^{-1})	k_q[b] (M^{-1} s^{-1})	γ[c]
εADP (free)	acrylamide	0	1	25.5	1			
		30	2.43	11.2	2.28	47.7	2.19×10^9	
	I^-	0	1	25.5	1			
		30	5.10	6.2	4.10	136.5	5.3×10^9	
	Tl^+	0	1	25.5	1			
		30	3.84	6.7	3.8	94.7	4.8×10^9	
εADP (bound)	acrylamide	0	1	24.2	1			
		30	1.19	20.7	1.17	6.3	0.31×10^9	0.14
	I^-	0	1	24.2	1			
		30	1.71	14.8	1.64	23.5	1.16×10^9	0.22
	Tl^+	0	1	24.2	1			
		30[d]	1.75	14.0	1.73	24.9	1.32×10^9	0.28

[a] τ_o corresponds to the εADP lifetime determined in the absence of the quencher. [b] The values of k_q have been calculated using lifetime quenching data and corrected for the viscosity of the solvent (10% glycerol). [c] γ is defined by eq 6 (see text). [d] Because TlCl precipitates in our standard buffer (T2) at concentrations above ~8 mM, the titrations with Tl^+ have been performed in two buffer systems; in buffer T2 with Tl^+ concentration up to 5–6 mM and as a control in buffer (50 mM Tris/acetate, pH 8.1, 20 mM sodium acetate, 5 mM magnesium acetate, and 10% glycerol, 20 °C) with Tl^+ up to 35 mM. In the range of Tl^+ concentration from 0 to 6 mM, the quenching parameters as well as the fluorescence lifetimes were identical in both buffer systems. Binding of εADP is unaffected by the exchange of Cl^- for acetate in the buffer in the studied salt concentration range.

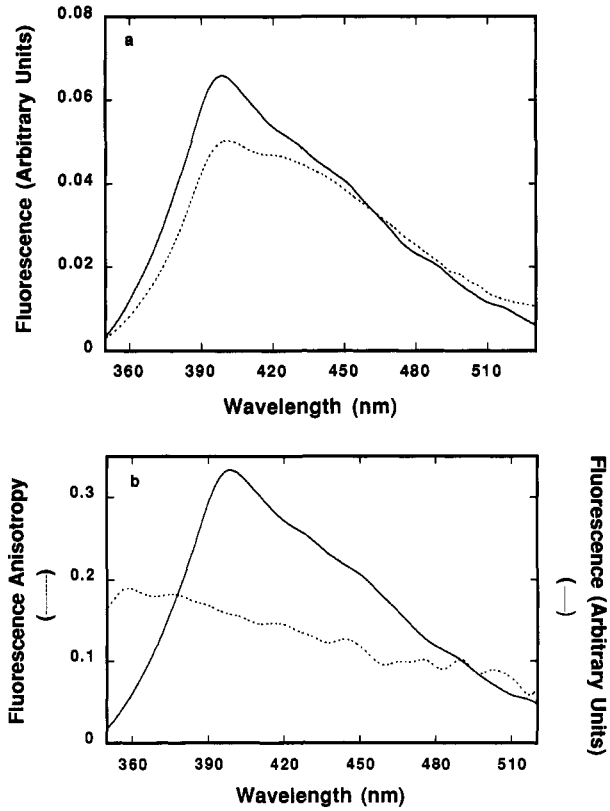

FIGURE 2: (a) Corrected fluorescence emission spectra of εADP (1.1×10^{-6} M) (– – –) free and bound (—) to DnaB helicase in buffer T2 (20 mM NaCl, pH 8.1, 20 °C); λ_{ex} = 325 nm. DnaB concentration is 1.0×10^{-5} M (hexamer). (b) Fluorescence anisotropy of εADP bound to DnaB helicase (– – –) as a function of emission wavelength; λ_{ex} = 325 nm, buffer T2 (20 mM NaCl, pH 8.1, 20 °C). The DnaB protein and εADP concentrations are 1.0×10^{-5} (hexamer) and 1.2×10^{-6} M, respectively. The emission spectrum (—) of the bound εADP recorded at the same excitation wavelength is also included.

to DnaB, strongly suggests polar character of the base-binding region in the nucleotide-binding site of the DnaB helicase.

Emission anisotropy of εADP bound to DnaB, as a function of emission wavelength, with the excitation at the red edge of the nucleotide absorption spectrum (λ_{ex} = 325 nm), is shown in Figure 2b. Although the accurate measurement of the anisotropy at both the blue and red sides of the emission spectrum is difficult, due to the low signal level in these regions, it is clear that the anisotropy varies significantly across the emission band, ranging from 0.18 ± 0.02 at 360 nm to 0.1 ± 0.02 at 500 nm (0.16 ± 0.01 at the maximum) (Figure 2b). Although this phenomenon has been observed before, it is still not completely understood (Gafni et al., 1979; Perkins et al., 1984). The fluorescence anisotropy of such a system is operationally defined by its value around the emission maximum (Sencrist et al., 1972; Perkins et al., 1984; Cheung & Liu, 1984). In the case of εADP bound to the DnaB helicase, the anisotropy at the emission maximum (~400–410 nm) r = 0.16 ± 0.01 is much lower than the anisotropy r_o = 0.3 ± 0.01 of completely immobilized εA at the same excitation and emission wavelengths (Sencrist et al., 1972; Cheung & Liu, 1984). However, it should be pointed out that bound εADP has a fluorescence lifetime of τ = 24.2 ns, which provides a long enough time window to observe rotational diffusion of the whole DnaB hexamer with a molecular weight of 313 590 (Nakayama et al., 1984a; Bujalowski & Klonowska, 1993). Thus, due to the rotation of the protein molecule, the observed anisotropy of bound εADP can be lower than its true limiting anisotropy. The effect of the protein rotational diffusion on the depolarization of bound εADP fluorescence can be estimated using the Perrin equation (Lakowicz, 1983)

$$r_{lim}/r = 1 + (\tau/\phi) \quad (8)$$

where r_{lim} is the limiting anisotropy of the bound εADP and $\phi = \eta V/RT$ is the rotational correlation time, η is the viscosity of the bulk solvent, R is the gas constant, and V is the volume of the protein molecule. Extrapolation of the Perrin plot (λ_{ex} = 325 nm, λ_{em} = 410 nm) to infinite viscosity, at constant temperature (20 °C), provides the limiting anisotropy of bound εADP r_{lim} = 0.21 ± 0.02 (plot not shown) (Table 3). As we mentioned above, the anisotropy of completely immobilized εA is r_0 = 0.3 ± 0.01 (λ_{ex} = 325 nm, λ_{em} = 410 nm), indicating that ethenoadenosine has substantial mobility when εADP is bound to the DnaB nucleotide-binding site (Sencrist et al., 1972; Cheung & Liu, 1984).

Solute Accessibility of the Adenine Ring in DnaB Helicase Nucleotide-Binding Site. Acrylamide, I^-, and Tl^+ are very effective quenchers of ethenoadenosine fluorescence (Ando & Asai, 1980; Perkins et al., 1984), differing dramatically in their physical properties. Acrylamide is a neutral molecule, while I^- and Tl^+, being significantly smaller than acrylamide, are negatively and positively charged, respectively. Fluorescence quenching studies using these quenchers should provide

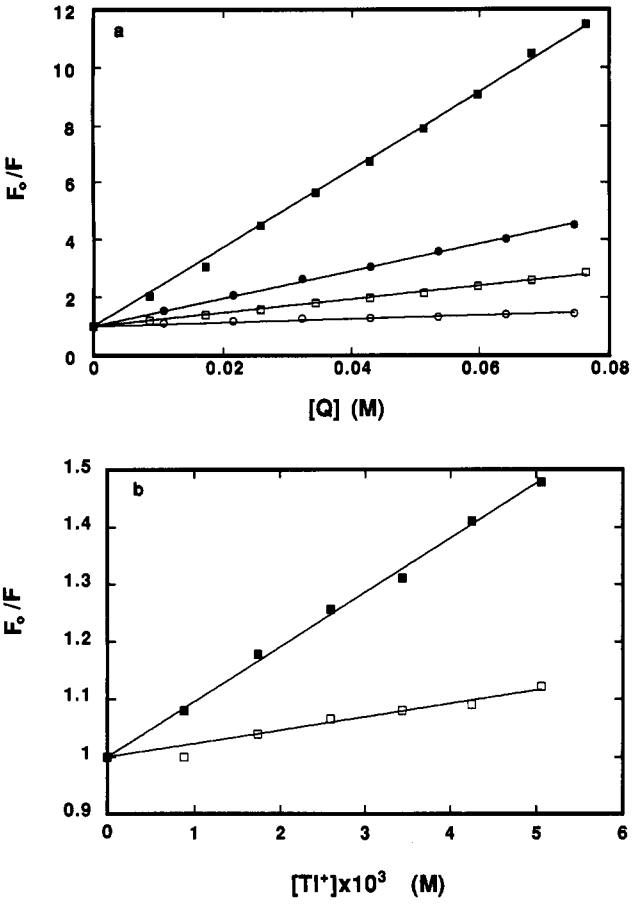

FIGURE 3: (a) Stern–Volmer plots of iodide and acrylamide quenching of the fluorescence of ϵADP free and bound to DnaB helicase in buffer T2 (20 mM NaCl, pH 8.1, 20 °C); λ_{ex} = 325 nm, λ_{em} = 450 nm. Iodide quenching: (■) free ϵADP and (●) bound ϵADP. Acrylamide quenching: (□) free ϵADP and (○) bound ϵADP. Solid lines are linear least-squares fits of Stern–Volmer equation (eq 4 in text) to the data points using the parameters included in Table 1; DnaB and ϵADP concentrations are 4.8×10^{-6} (hexamer) and 1.6×10^{-6} M, respectively. (b) Stern–Volmer plots of Tl^+ quenching of the fluorescence of ϵADP free and bound to DnaB helicase in buffer T2 (20 mM NaCl, pH 8.1, 20 °C); λ_{ex} = 325 nm, λ_{em} = 450 nm; (■) free ϵADP and (□) bound ϵADP. Solid lines are linear least-squares fits of Stern–Volmer equation (eq 4 in text) to the data points using the parameters included in Table 1; DnaB and ϵADP concentrations are 4.8×10^{-6} (hexamer) and 1.6×10^{-6} M, respectively.

the information not only on the accessibility of the adenine ring but also on the environment of the base location in the nucleotide-binding site (Eftink & Ghiron, 1981; Eftink, 1991; Robbins et al., 1985; Philips et al., 1987).

Stern–Volmer plots of fluorescence quenching of ϵADP, free and bound, in DnaB nucleotide-binding sites, as a function of acrylamide, I^-, and Tl^+ concentrations, are shown in Figure 3a,b. Fluorescence intensities and lifetimes of ϵADP in the presence of different quenchers, together with Stern–Volmer quenching constants K_{SV} and bimolecular quenching rate constants k_q, are included in Table 1. Stern–Volmer quenching constant K_{SV}, as well as bimolecular quenching rate constant k_q, for acrylamide is significantly lower than that determined for I^- and Tl^+. This is an expected result because of the larger size and slower diffusion of the acrylamide molecule compared to I^- and Tl^+. The lower values of K_{SV} and k_q may also reflect lower quenching efficiency of ethenoadenosine fluorescence compared to that of I^- and Tl^+, as previously indicated (Ando & Asai, 1980; Perkins et al., 1984). The bimolecular quenching rate constants for I^- and Tl^+ are close to the diffusion limits, with I^- being slightly more efficient.

In the case of acrylamide and I^-, the ratio of intensities F_o/F at a given quencher concentration is slightly higher than the corresponding ratio of lifetimes (Table 1). This result indicates that collisional quenching is predominant, as shown by the linear character of Stern–Volmer plots in Figure 3a. However, there is a small static component in the quenching mechanism of the fluorescence of free ϵADP by both quenchers.

Binding of ϵADP to the DnaB helicase nucleotide-binding site causes a dramatic decrease in the solute quenching efficiency of ϵADP fluorescence by studied quenchers as shown by Stern–Volmer plots in Figure 3 and quenching parameters included in Table 1. This effect is particularly pronounced in the case of acrylamide with K_{SV} and k_q values decreasing by a factor of ~7 compared to their values obtained for free ϵADP in solution. The corresponding quenching constants for I^- and Tl^+ decrease by factors of ~4.5 and ~3.6, respectively (Table 1). Linear Stern–Volmer plots (Figure 3), as well as $F_o/F \approx \tau_o/\tau$, indicate the collisional mechanism of the quenching processes of the bound nucleotide fluorescence.

The quenching data indicate that the solvent accessibility of the base's location in the DnaB nucleotide-binding site is limited. However, the fact that I^- and Tl^+, which are preferentially quenching surface-located chromophores, can still significantly quench the fluorescence of bound ϵADP suggests that the base is located in a cleft on the surface of the enzyme and preserves some limited access to the solvent (Lakowicz, 1983; Eftink, 1991).

It is interesting that I^- and Tl^+ both have very similar bimolecular quenching rate constants for bound ϵADP (Table 1). This result suggests that although the base binding site is polar, as indicated by fluorescence emission spectra and lifetime studies (see above), the distribution of the charges does not induce significant preference for quenchers having positive or negative charges.

Ribose-Binding Region of the Nucleotide-Binding Site of E. coli DnaB Helicase. To probe the structural environment around ribose-binding regions in the nucleotide-binding site of the DnaB helicase, we used ribose-modified fluorescent nucleotide analogs having TNP or MANT groups attached to the 2′ and/or 3′ oxygen of ribose rings (Bujalowski & Klonowska, 1993). Corrected fluorescence emission spectra (λ_{ex} = 408 nm) of TNP-ADP free and bound to a high-affinity noninteracting nucleotide-binding site of the DnaB helicase in buffer T2 (20 mM NaCl, pH 8.1, 20 °C) are shown in Figure 4a. Binding of the nucleotide analog is accompanied by a strong increase (by a factor of ~4.7) of its fluorescence intensity and quantum yield (Table 3). The emission spectra of free and bound TNP-ADP, normalized at the maximum, are shown in Figure 4b. The emission maximum shifts by ~11 nm from 563 nm for free to 552 nm for DnaB bound TNP-ADP.

The fluorescence properties of TNP nucleotide analogs are very sensitive to the solvent polarity and are suitable as reporters of the physical nature of the binding site (Hiratsuka, 1976). To obtain more information about the physical character of the ribose-binding region, as sensed by bound TNP-ADP, we recorded corrected fluorescence emission spectra of TNP-ADP, in solution, containing different concentrations of ethanol (Figure 5a). As the concentration of the ethanol in solution increases, the fluorescence intensity of the nucleotide analog strongly increases with concomitant shift of the emission maximum toward shorter wavelengths. It should be noted that both the intensity and the maximum of the emission spectrum change gradually with the change

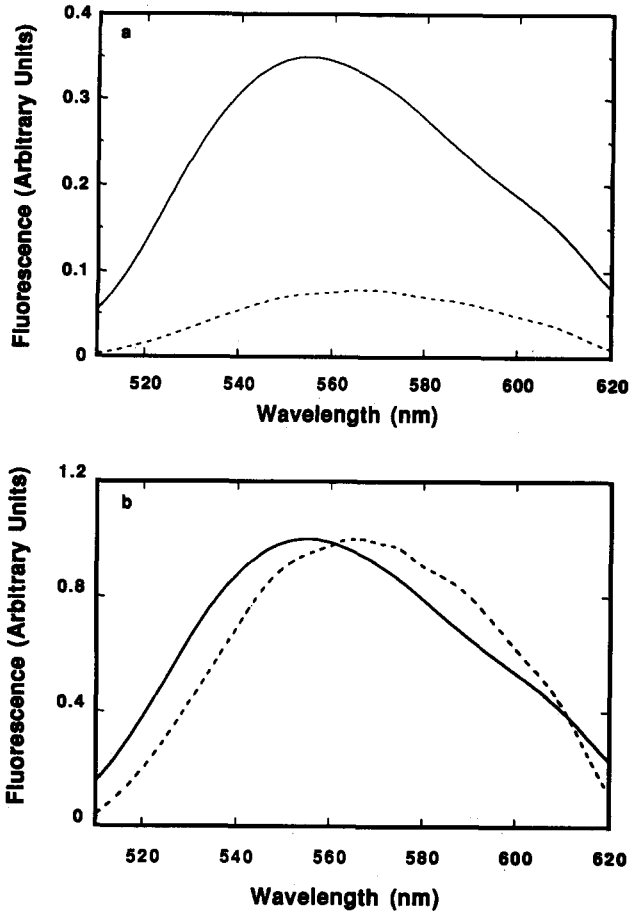

FIGURE 4: (a) Corrected fluorescence emission spectra of TNP-ADP (3.8×10^{-6} M) (– – –) free and bound (—) to DnaB helicase in buffer T2 (20 mM NaCl, pH 8.1, 20 °C); λ_{ex} = 408 nm. DnaB concentration is 4.8×10^{-6} M (hexamer). (b) Normalized corrected fluorescence emission spectra of TNP-ADP (3.8×10^{-6} M) (– – –) free and bound (—) to DnaB helicase in buffer T2 (20 mM NaCl, pH 8.1, 20 °C); λ_{ex} = 408 nm. DnaB concentration is 4.8×10^{-6} M (hexamer).

of the composition of the solvent, and there is no significant change in the shape of the emission spectrum, indicating that the general solvent effect is observed (Hiratsuka, 1976; Lakowicz, 1983). The dependence of the emission maximum and relative fluorescence intensity of TNP-ADP upon solvent polarity is shown in Figure 5b. The solvent polarity has been expressed, using Kosower's empirical polarity Z scale (Kosower, 1958; Turner & Brand, 1968). Both the location of the emission maximum and the emission intensity of the fluorescent analog show very good correlation with the Z value.

Although direct comparison should be treated with caution, the plot in Figure 5b may be used to estimate the Z value for the microenvironment surrounding the ribose-attached TNP group. The data for TNP-ADP bound to the DnaB helicase are included in Figure 5b (closed symbols). It should be noted that both the intensity and the emission maximum correspond to the very similar value of Z (90–90.8). The strong increase of TNP-ADP's fluorescence intensity and the blue shift of the emission maximum upon binding to DnaB protein strongly suggest that the ribose-binding site has a predominantly hydrophobic character which corresponds to a Z at ~90–90.8 on Kosower's empirical polarity scale.

Emission anisotropy of TNP-ADP bound to DnaB in buffer T2 (20 mM NaCl, pH 8.1, 20 °C), as a function of emission wavelength, with excitation at the red edge of the nucleotide absorption spectrum (λ_{ex} = 490 nm), is shown in Figure 6. The anisotropy is relatively constant throughout the spectrum,

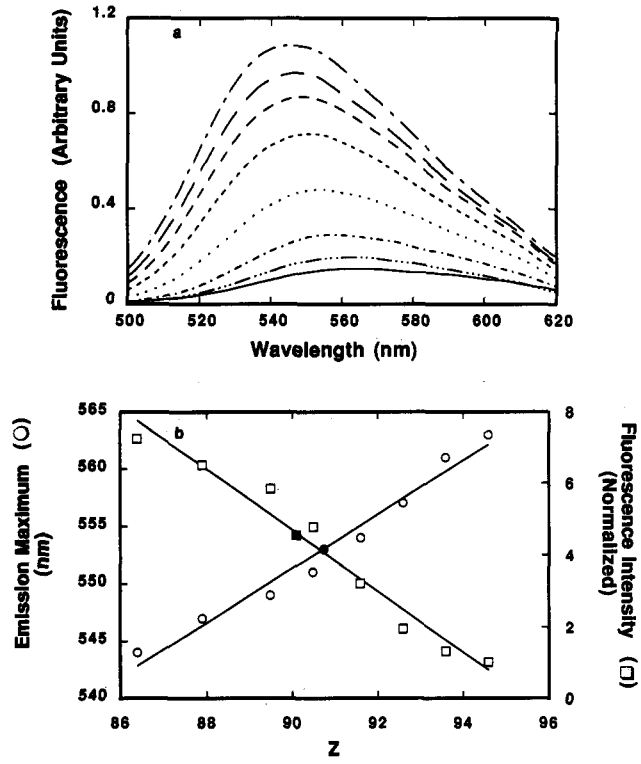

FIGURE 5: (a) Corrected fluorescence emission spectra of TNP-ADP in water solutions (1 mM Tris/HCl, pH 8.1, 25 °C) containing different concentrations of ethanol; λ_{ex} = 408 nm. TNP-ADP concentration is 1.96×10^{-5} M. Ethanol concentrations are (—) 0%, (—·—) 10%, (—··—) 20%, (···) 30%, (– – –) 40%, (– – –) 50%, (— — —) 60%, and (— – —) 70%. (b) Dependence of the position of the emission maximum (○) and the relative fluorescence intensity at the maximum (□) of TNP-ADP as a function of the solvent polarity expressed using Kosower's empirical polarity scale Z (Kosower, 1958; Turner & Brand, 1968). Solid lines are the linear least-squares fits to the data points. Closed symbols are the data obtained for TNP-ADP bound to DnaB protein (see Figure 4a,b).

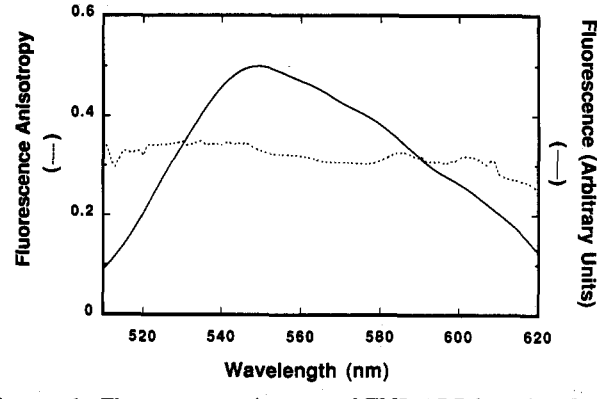

FIGURE 6: Fluorescence anisotropy of TNP-ADP bound to DnaB helicase (– – –) as a function of emission wavelength; λ_{ex} = 490 nm, buffer T2 (20 mM NaCl, pH 8.1, 20 °C). The DnaB protein and TNP-ADP concentrations are 4.8×10^{-6} (hexamer) and 3.8×10^{-6} m, respectively. The emission spectrum (—) of the bound TNP-ADP recorded in the same buffer conditions is also included.

although the error in this measurement is higher than in the case of ϵADP or MANT-ADP (see below), due to the low fluorescence intensity of the TNP-ADP. The emission anisotropy of the bound TNP-ADP, $r = 0.32 \pm 0.02$, is very close to its fundamental anisotropy, $r_o = 0.35$, at the same excitation wavelength (Moczydlowski & Fortes, 1981). This result indicates that when TNP-ADP is bound in the DnaB nucleotide-binding site, the ribose-attached TNP group has very limited motional freedom.

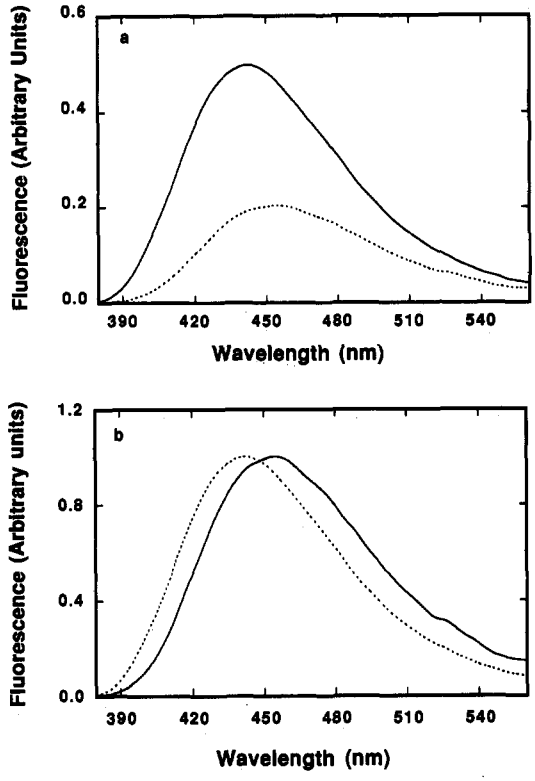

FIGURE 7: (a) Corrected fluorescence emission spectra of MANT-ADP (1.1×10^{-6} M) (- - -) free and bound (—) to DnaB helicase in buffer T2 (20 mM NaCl, pH 8.1, 20 °C); λ_{ex} = 356 nm. The DnaB concentration is 1.0×10^{-5} M (hexamer). (b) Normalized corrected fluorescence emission spectra of MANT-ADP (1.1×10^{-6} M) (—) free and bound (- - -) to DnaB helicase in buffer T2 (20 mM NaCl, pH 8.1, 20 °C); λ_{ex} = 356 nm. DnaB concentration is 1.0×10^{-5} M (hexamer).

The fluorescence properties of bound MANT-ADP corroborate well with the results obtained for TNP-ADP, described above. Corrected fluorescence emission spectra (λ_{ex} = 356 nm) of MANT-ADP free and bound to the DnaB helicase in buffer T2 (20 mM NaCl, pH 8.1, 20 °C) are shown in Figure 7a. As in the case of TNP-ADP, binding of the analog is accompanied by a dramatic increase in the fluorescence intensity (by a factor of ~2.7; see Table 3) and a large (~12 nm) blue shift of the emission spectrum (Figure 7b). These data indicate that, upon binding to DnaB, the MANT group has been placed in a hydrophobic environment (Hiratsuka, 1983; Cremo et al., 1990). The correlation between MANT-ADP fluorescence intensity and the position of the emission maximum with solvent polarity is similar to the one observed for TNP-ADP (data not shown). However, we could not follow the effect of solvent polarity on MANT-ADP fluorescence at higher (>50%) ethanol concentrations due to the significant propensity of this nucleotide analog to precipitate in these solution conditions.

Excitation fluorescence anisotropy spectra (λ_{em} = 450 nm) of MANT-ADP free and bound to the DnaB helicase in buffer T2 (20 mM NaCl, pH 8.1, 20 °C) are shown in Figure 8. Clearly, there is a dramatic change in the MANT-ADP fluorescence anisotropy accompanying the binding. For excitation in the region above 355 nm, anisotropy of the free MANT-ADP has a constant value of 0.015 ± 0.005. In the same excitation region, the anisotropy of the MANT-ADP bound to DnaB reaches the constant value of 0.33 ± 0.02. This value is close to the fundamental anisotropy of MANT-ADP, 0.35–0.4 (Cremo et al., 1990), indicating that the ribose-attached fluorophore has very constrained mobility.

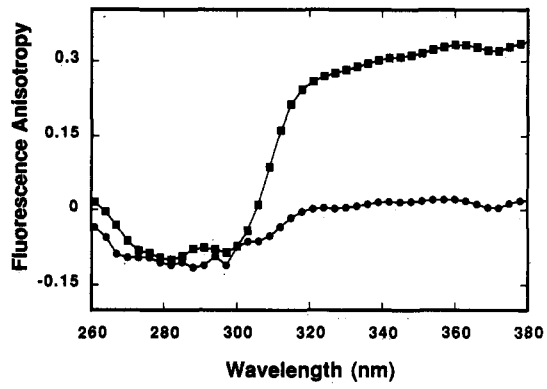

FIGURE 8: Excitation fluorescence anisotropy spectra of MANT-ADP free (●) and bound (■) to DnaB helicase in buffer T2 (20 M NaCl, pH 8.1, 20 °C); λ_{em} = 450 nm. The DnaB and MANT-ADP concentrations are 4.8×10^{-6} (hexamer) and 1.5×10^{-6} M, respectively.

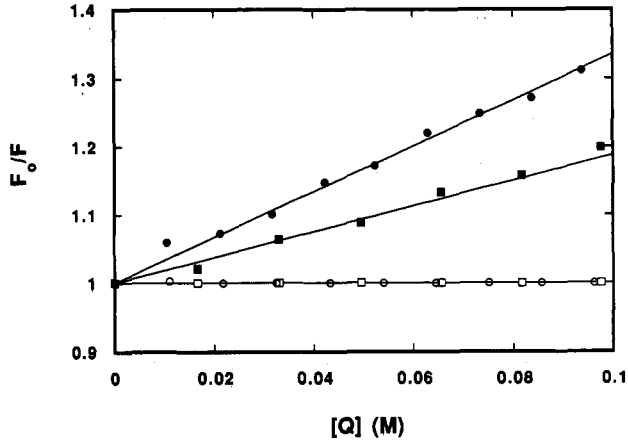

FIGURE 9: Stern–Volmer plots of iodide and acrylamide quenching of the fluorescence of MANT-ADP free and bound to DnaB helicase in buffer T2 (20 mM NaCl, pH 8.1, 20 °C); λ_{ex} = 356 nm, λ_{em} = 450 nm. Iodide quenching: (■) free MANT-ADP and (□) bound MANT-ADP. Acrylamide quenching: (●) free MANT-ADP and (○) bound MANT-ADP. DnaB and MANT-ADP concentrations are 4.8×10^{-6} (hexamer) and 1.0×10^{-6} M, respectively. Solid lines are linear least-squares fits of Stern–Volmer equation (eq 4 in text) to the data points using the parameters included in Table 2.

Solute Accessibility of the Ribose-Binding Region in DnaB Helicase Nucleotide-Binding Site. Accessibility of the ribose-attached fluorophore, free and bound to the DnaB nucleotide-binding site, to different solute quenchers has been determined using MANT-ADP. The analogous studies with TNP-ADP were hindered by the fact that the fluorescence lifetime of the TNP group is in the range of tens of picoseconds (Nakamoto & Inesi, 1984). This fluorescence lifetime is too short for solute quenching studies in the concentration ranges of the quenchers which do not perturb the equilibrium of nucleotide–DnaB protein interaction and/or the conformation of the enzyme (~0.08–0.1 M).

Stern–Volmer plots of the fluorescence quenching of MANT-ADP free and bound to DnaB nucleotide-binding sites as a function of acrylamide and KI concentrations are shown in Figure 9. The plots are linear within the range of acrylamide and KI concentrations studied, indicating the collisional character of the quenching process. The collisional mechanism of the quenching process is fully confirmed by the fluorescence lifetime studies of MANT-ADP in the presence of the studied quenchers (Table 2). The Stern–Volmer quenching constants obtained from steady-state intensity measurements are, within experimental error, identical to the quenching constants determined in lifetime experiments. This is expressed by the

Table 2: Stern–Volmer Quenching Constants K_{SV}, Bimolecular Quenching Rate Constants k_q, Fluorescence Lifetimes τ, and Solute Quenching Efficiencies γ of MANT-ADP Free and Bound to DnaB Helicase in Buffer T2 (20 mM NaCl, pH 8.1, 20 °C)

nucleotide	quencher	quencher concentration (mM)	F_0/F	τ (ns)	τ_0/τ[a]	K_{SV} (M^{-1})	k_q[b] (M^{-1} s^{-1})	γ[c]
MANT-ADP (free)	acrylamide	0	1.0	3.90	1.0			
		30	1.1	3.58	1.09	3.30	0.77×10^9	
	I^-	0	1.0	3.90	1.0			
		30	1.06	3.71	1.05	1.9	0.57×10^9	
	Tl^+	0	1.0	3.90	1.0			
		30	1.4	2.6	1.5	13.3	5.6×10^9	
MANT-ADP (bound)	acrylamide	0	1.0	6.0/13.1	1.0			
		30	1.0	6.0/13.1	1.0	~0	~0	~0
	I^-	0	1.0	6.0/13.1	1.0			
		30	1.0	6.0/13.1	1.0	~0	~0	~0
	Tl^+	0	1.0	6.0/13.1	1.0			
		30[d]	1.04	5.7/12.6	1.05/1.04	1.3	$0.27/0.14 \times 10^9$	0.05/0.030

[a] τ_0 corresponds to the MANT-ADP lifetime determined in the absence of the quencher. [b] The values of k_q have been calculated using lifetime quenching data and corrected for the viscosity of the solvent (10% glycerol). [c] γ is defined by eq 6 (see text). [d] Because TlCl precipitates in our standard buffer (T2) at concentrations above ~8 mM, the titrations with Tl^+ have been performed in two buffer systems; in buffer T2 with Tl^+ concentration up to 5–6 mM and as a control in buffer (50 mM Tris/acetate, pH 8.1, 20 mM sodium acetate, 5 mM magnesium acetate, and 10% glycerol, 20 °C) with Tl^+ up to 35 mM. In the range of Tl^+ concentration from 0 to 6 mM, the quenching parameters as well as the fluorescence lifetimes were identical in both buffer systems. Binding of MANT-ADP is unaffected by the exchange of Cl^- for acetate in the buffer in the studied salt concentration range.

Table 3: Fluorescence Properties of the Fluorescence Analogs ϵADP, MANT-ADP, MANT-dADP, and TNP-ADP Free and Bound to DnaB Helicase in Buffer T2 (20 mM NaCl, pH 8.1, 20 °C)

	ϵADP		MANT-ADP		MANT-dADP		TNP-ADP	
property	free	bound	free	bound	free	bound	free	bound
quantum[a] yield	0.53 ± 0.03	0.59 ± 0.03	0.22 ± 0.02	0.61 ± 0.03	0.27 ± 0.02	0.86 ± 0.05	$(7 \pm 2) \times 10^{-4}$	$(3.8 \pm 0.4) \times 10^{-3}$
limiting anisotropy	$(7 \pm 2) \times 10^{-3}$	0.21 ± 0.02[b]	0.015 ± 0.005	0.33 ± 0.02	0.016 ± 0.005	0.33 ± 0.02		0.32 ± 0.02
emission[a] maximum (nm)	400	400	453	441	452	442	563	552

[a] Excitation wavelengths for ϵADP, MANT-ADP, MANT-dADP, and TNP-ADP were 325, 356, 356 and 408 nm, respectively. [b] Determined from the extrapolation of isothermal Perin plot to infinite viscosity. The viscosity of the solvent has been changed using buffer T2 (20 mM NaCl, pH 8.1, 20 °C) containing different concentrations of glycerol (see eq 8 and the text for details). The controls have been performed to test that the increased glycerol concentration does not perturb DnaB–nucleotide equilibrium. The errors associated with the determination of quantum yields and limiting anisotropies are standard deviations obtained from three to four repeated measurements.

same value of the intensity F_0/F and lifetime τ_0/τ ratios at the corresponding quencher concentration (Table 2). It should be pointed out that the values of bimolecular quenching rate constants of free MANT-ADP fluorescence for all quenchers studied (acrylamide, I^-, and Tl^+) are lower than predicted by diffusion control quenching, an indication of the quenching process's low efficiency.

In contrast to the fluorescence of ϵADP bound to DnaB, which is still significantly quenched, particularly by I^- and Tl^+ (see Figure 3 and Table 1), within experimental accuracy, there is no detectable quenching of the MANT-ADP fluorescence bound to DnaB by acrylamide and I^-. In the case of Tl^+, the Stern–Volmer quenching constant is decreased by a factor of ~10 and the quenching efficiency by a factor of ~21, compared to the corresponding factor of ~3.6 for Tl^+ quenching of the bound ϵADP (Table 2). The larger drop of the quenching efficiency results from the fact that the lifetime of the bound MANT-ADP is significantly longer than that of free MANT-ADP (see below). Thus, these data strongly suggest that the accessibility of the ribose-binding region of the DnaB helicase nucleotide-binding site is significantly lower when compared to the solute accessibility of the base-binding region.

Fluorescence Lifetime of MANT-ADP Free and Bound to DnaB Helicase. Frequency–domain data of fluorescence decays of MANT-ADP free (closed symbols) and bound (open symbols) to DnaB protein in buffer T2 (20 mM NaCl, pH 8.1, 20 °C) are shown in Figure 10. As the modulation frequency increases, the phase angle increases and the modulation decreases. The data have been analyzed using the exponential decay laws, assuming ground-state heterogeneity (Lakowicz, 1983). The emission of free MANT-ADP

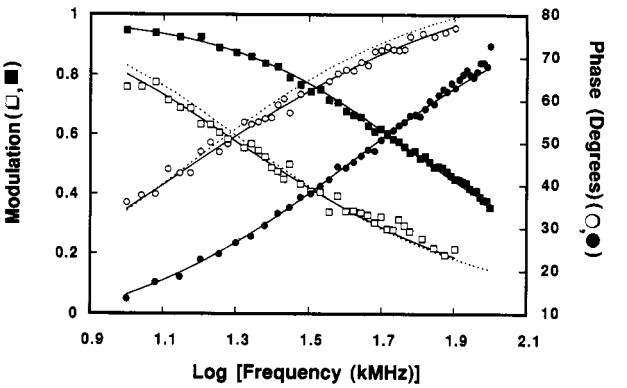

FIGURE 10: Frequency–domain, phase–modulation data for the fluorescence intensity decay of MANT-ADP free (closed symbols) and bound (open symbols) to DnaB helicase in buffer T2 (20 mM NACl, pH 8.1, 20 °C): (●) free MANT-ADP phase, (■) free MANT-ADP modulation, (○) bound MANT-ADP phase, and (□) bound MANT-ADP modulation. λ_{ex} = 356 nm (see Materials and Methods for experimental details). The solid lines are nonlinear double-exponential least-squares fits to the phase and modulation data using τ_1 = 3.9 ns, α_1 = 0.98, $\tau_2 > 20$ ns, and α_2 = 0.02 for free MANT-ADP and τ_1 = 6.0 ns, α_1 = 0.24, τ_2 = 13.1 ns, and α_2 = 0.76 for bound MANT-ADP, respectively (see Table 4). Dashed line represents a single exponential fit to phase–modulation data for bound MANT-ADP (τ = 10.5 ns); DnaB and MANT-ADP concentrations are 4.6×10^{-6} (hexamer) and 1.0×10^{-6} M, respectively.

in solution is almost exclusively characterized by a single lifetime, $\tau = 3.9 \pm 0.2$ ns (amplitude ~0.98). This value is in very good agreement with the previously determined 3.8 ns (Hiratsuka, 1984) and 4.06 ns (Cremo et al., 1990). Less than 2% of the total amplitude required a longer lifetime (>20 ns), which probably results from the presence of small buffer

Table 4: Fluorescence Lifetimes τ and Fractional Amplitudes α of MANT-ADP, MANT-dADP, and MANT-dATP Free and Bound to DnaB Protein Nucleotide-Binding Site (λ_{ex} = 356 nm) in Buffer T2 (20 mM NaCl, pH 8.1, 20 °C)[a]

	free				bound			
nucleotide	τ_1 (ns)	α_1	τ_2 (ns)	α_2	τ_1 (ns)	α_1	τ_2 (ns)	α_2
MANT-ADP	3.9 ± 0.2	0.97 ± 0.01	>20	0.03 ± 0.01	6.0 ± 0.2	0.24 ± 0.01	13.1 ± 0.5	0.76 ± 0.01
MANT-dADP	4.1 ± 0.2	0.98 ± 0.01	>20	0.02 ± 0.01	6.3 ± 0.2	0.27 ± 0.02	12.9 ± 0.5	0.73 ± 0.02
MANT-dATP	4.2 ± 0.2	0.97 ± 0.02	>20	0.03 ± 0.01	6.5 ± 0.2	0.28 ± 0.02	12.8 ± 0.5	0.72 ± 0.02

[a] The errors associated with the determination of lifetimes and amplitudes are standard deviations obtained from four to five repeated experiments.

impurities (Table 4). Binding of MANT-ADP to DnaB dramatically changes fluorescence lifetime characteristics of the nucleotide. The fluorescence decay of the bound nucleotide becomes biexponential with the shorter component characterized by τ_1 = 6.0 ± 0.2 ns and amplitude α = 0.24 and the longer component characterized by τ_2 = 13.1 ± 0.5 ns and α_2 = 0.76, respectively (see Figure 10 and Table 4). Including a third component did not significantly improve the statistics of the fit. For comparison, the fit with only a single decay time (τ = 10.5 ns) has been included (dashed line in Figure 10). We also performed phase–modulation studies of the fluorescence lifetime characteristics of MANT-dADP and MANT-dATP free and bound to the DnaB helicase. Within experimental accuracy, the lifetime characteristics of all studied MANT derivatives are very similar. The fluorescence of free nucleotide is characterized by a nearly homogeneous lifetime of ~4 ns, while, when bound to DnaB, the nucleotide emission is characterized by two decay times, ~6 and ~13 ns (Table 4).

The presence of two decay times in the emission of the bound nucleotides indicates that the MANT groups attached to the ribose sense two different environments, suggesting that the ribose-binding region of the nucleotide-binding site exists in two different conformations. Both lifetimes are much longer than the fluorescence lifetime obtained for free MANT derivatives (Table 4). This is in contrast to the result obtained for the base-binding region, where the single fluorescence lifetime of ϵADP very close to the lifetime of the free ϵADP was detected, indicating a lack of discrete conformational heterogeneity in the base-binding region. Thus, the data suggest that conformational heterogeneity of the ribose-binding region is not transferred to the base-binding site (see Discussion).

On the basis of chemical studies, MANT-ATP and MANT-ADP were originally postulated to exist solely as 3′ isomers (Hiratsuka, 1983). Recent NMR studies indicate that MANT-ATP and MANT-ADP may exist as a mixture of 2′ and 3′ isomers, with the 3′ isomer being predominant (Cremo et al., 1990). The single lifetime for this analog could result exclusively from the fraction of analog existing as the 3′ isomer with the 2′ isomer fraction being completely quenched. To test this possibility, we determined the quantum yield of MANT-ADP, MANT-dADP, and MANT-dATP. If there is a significant fraction of nonfluorescent 2′ isomer, the quantum yield of MANT-ADP should be lower when compared to the quantum yield of deoxy analogs by this fraction. The obtained data indicate that the quantum yield of MANT-ADP is indeed lower than that of MANT-dADP and MANT-dATP by ~19% (Table 3). Thus, it is possible that a lower quantum yield of MANT-ADP by ~19% compared to those of MANT-dADP and MANT-dATP reflects the existence of part of MANT-ADP in solution as a nonfluorescent 2′ isomer, as proposed originally by Cremo et al. (1990).

DISCUSSION

Binding of small ligands to biological macromolecules plays a crucial role in macromolecular activities (Schellman, 1975). In the case of proteins and nucleic acids, ligand binding can regulate both the thermodynamics and kinetics of the conformational stability and interactions (Bujalowski et al., 1986a,b; Bujalowski & Porschke, 1984, 1988a,b; Wong & Lohman, 1992). Regulation and control of multiple activities and interactions of *E. coli* DnaB protein are realized through binding and/or hydrolysis of nucleoside triphosphate molecules (Arai & Kornberg, 1981a,b; LeBowitz & McMacken, 1986; Wahle et al., 1989a,b; Bujalowski & Klonowska, 1993). Allosteric interactions between nucleotide-binding sites and different parts of the DnaB protein are the key elements in the enzyme action. It is clear that understanding the function of the DnaB protein requires understanding of the nature and structure of the nucleotide-binding sites and the conformation of the bound nucleotide.

Although treated as a "small" ligand, the nucleotide is a complex molecule with distinctive structural regions (base, ribose, phosphates), each of which can be responsible for triggering specific responses of the DnaB hexamer and control its activities either independently or in a concerted way. Thus, it has been shown that hydrolysis of nucleoside triphosphate is relatively independent of the nature of the base; however, the DnaB protein could not hydrolyze deoxynucleotides or the ribose-modified nucleotide TNP-ATP (Arai & Kornberg, 1981a; Bujalowski & Klonowska, 1993). Moreover, the presence of the γ-phosphate and the ribose is indispensable in inducing allosteric interactions between nucleotide- and ssDNA-binding sites. In the presence of ATP, or nonhydrolyzable ATP analogs, the affinity of DnaB for ssDNA is increased significantly, while no such effect has been observed in the presence of ADP or dATP (Arai & Kornberg, 1981a).

Application of fluorescent analogs can provide information about the binding mechanism, nature, structure, and dynamics of the nucleotide-binding site, unavailable by other approaches (Moczydlowski & Fortes, 1981; Perkins et al., 1984; Aguirre et al., 1989; Nakamoto & Inesi, 1984; Cremo et al., 1990; Bujalowski & Klonowska, 1993).

In this report, we probed the structural characteristics of the base- and ribose-binding regions of the high-affinity noninteracting nucleotide-binding site of the DnaB helicase, using fluorescent nucleotide analogs, which differ by type and location of the modifying group. To characterize the base-binding region, etheno-ADP, which has a modified adenine ring, has been used (Sencrist et al., 1972; Leonard, 1984, and references therein). To probe the region near the ribose-binding site, TNP-ADP and MANT-ADP, which have fluorescent groups trinitrophenyl (TNP) and methylantraniloyl (MANT) attached to the ribose 2′ and/or 3′ oxygens, have been selected.

The experiments reported in this work provide first insight into the nature of significant structural differences between base- and ribose-binding regions of the DnaB helicase's

nucleotide-binding site. Emission spectrum of εADP bound to a noninteracting binding site of the DnaB helicase shows only a slight increase in the nucleotide fluorescence intensity (~21%) and no detectable change in the position of the emission maximum as compared to that of free εADP in solution. Also, the fluorescence of the bound nucleotide is characterized by a single lifetime of 24.2 ± 0.6 ns, which is only ~5% shorter than the single lifetime of the free nucleotide (25.5 ± 0.6 ns; see Table 1). The effect of solvent polarity on fluorescence properties of ethenoadenosine derivatives has been intensively studied by Leonard and collaborators (Sencrist et al., 1972; Spencer et al., 1974; Leonard, 1984). In solvents of low polarity (e.g., dimethylformamide, dioxane), the fluorescence quantum yield decreases by ~15% with concomitant blue shift of the emission maxima. Moreover, the fluorescence lifetime of ethenoadenosine decreases significantly from 24 ns in H_2O (pH 7.0) to 15 ns in dioxane (Spencer et al., 1974).

Thus, the fluorescence properties of bound εADP strongly suggest that the base-binding region of the DnaB nucleotide-binding site has relatively high polarity, similar to the polarity of the bulk solvent. However, solute accessibility studies, using acrylamide, I^-, and Tl^+, indicate that bound adenine is significantly shielded from the solvent. Both Stern–Volmer quenching constants K_{SV} and bimolecular quenching rate constants k_q, for studied quenchers, are strongly decreased for bound εADP, compared to free nucleotide in solution. Within experimental accuracy, the quenching mechanism of bound εADP fluorescence is collisional. The lowest efficiency of quenching (0.14) is observed for neutral acrylamide, while negatively charged I^- and positively charged Tl^+ show similar quenching efficiency (0.22 and 0.28, respectively).

I^- and Tl^+ are similar in size and diffusion coefficients (Ando & Asai, 1980); thus, any significant difference in collisional quenching efficiency between these two ionic quenchers would result from differences in electrostatic interactions with the chromophore environment. Lack of significant differences between I^- and Tl^+ quenching efficiencies of bound εADP fluorescence suggests that the polar environment of the base-binding site has charge distribution, which does not provide strong preference for negatively or positively charged quenchers. The data indicate that a substantial decrease of the quenching constants of I^- and Tl^+ for bound εADP results from steric constraints at the adenine-binding site and, in effect, limited accessibility to the solvent. It should be pointed out that both ionic quenchers, I^- and Tl^+, are incapable of penetrating the protein matrix; hence, they preferentially quench surface-located chromophores (Lakowicz, 1983; Eftink, 1991). The fact that the fluorescence of bound εADP is still quenched by I^- and Tl^+ indicates that the adenine is located in the cleft on the surface of the enzyme and preserves some contact with the solvent. In this context, the lowest accessibility of bound εADP observed for acrylamide is expected because it has larger dimensions than I^- and Tl^+; thus, it should experience more steric constraints.

It is interesting that the adenine of bound εADP, although significantly shielded from the solvent, still retains substantial mobility as indicated by fluorescence anisotropy data. The limiting anisotropy r_{lim} of εADP bound to the DnaB helicase obtained from the isothermal Perrin plot is 0.21 ± 0.02 (λ_{ex} = 325 nm, λ_{em} = 410 nm). This value is significantly lower than the fundamental anisotropy, $r_o = 0.3 \pm 0.01$, characteristic for completely immobilized ethenoadenine at the same excitation and emission wavelengths (Sencrist et al., 1972; Cheung & Liu, 1984). If one assumes that this depolarization results from a motion of emission dipole over a surface of a cone, the half angle of the cone, $\Theta_c \approx 27°$, can be calculated, using the relationship $r_{lim}/r_o = [\cos \Theta_c(1 + \cos \Theta_c)]^2/2$, as derived by Kinosita et al. (1977). The fact that, when bound, the adenine retains significant mobility suggests the lack of short-range specific interactions between the protein matrix and the base in the base-binding site. Also, nucleotides having different base residues bind with similar intrinsic affinity to the DnaB helicase (Bujalowski and Klonowska, manuscript in preparation). Thus, the data indicate that the interactions in the base-binding site of the DnaB helicase are not unique for a specific base, which corroborates well with experimentally observed low base specificity of ATPase and helicase activities of the DnaB protein (Arai & Kornberg, 1981a; LeBowitz & McMacken, 1986).

As we mentioned above, the importance of the ribose region of the DnaB protein nucleotide-binding site for the enzyme catalysis was indicated in the early studies of DnaB activities (Arai & Kornberg, 1981a; LeBowitz & McMacken, 1986). Structural characteristics of the ribose region of the DnaB nucleotide-binding site have been probed using two different fluorescent nucleotide analogs, TNP-ADP and MANT-ADP (Hiratsuka & Uchida, 1973; Hiratsuka, 1983). There are contrasting differences between ribose- and base-binding regions of the DnaB helicase nucleotide-binding site. Fluorescence intensity of bound TNP-ADP increases by a factor of ~4.7 (λ_{ex} = 408 nm), and the maximum of the emission spectrum is blue-shifted by ~11 nm compared to that of free TNP-ADP in solution (see Figure 4 and Table 3). In the case of MANT-ADP, the corresponding increase of the fluorescence intensity is by a factor of ~2.6 and the blue shift of emission spectrum is by ~12 nm. Both TNP-ADP and MANT-ADP show good correlation between their fluorescence intensity and the positions of emission maximum with the solvent polarity, using the empirical solvent polarity Z scale as defined by Kosower (Kosower, 1958; Turner & Brand, 1968). Thus, these results indicate that the environment near the ribose-binding site has a predominantly hydrophobic character.

Solvent accessibility studies indicate that the MANT group attached to the ribose has very little, if any, solvent accessibility when MANT-ADP is bound in the DnaB helicase nucleotide-binding site. In the case of acrylamide and I^-, the Stern–Volmer quenching constant K_{SV} is ~0 (Table 2). Quenching efficiency for Tl^+ is detectable (~0.05), suggesting the presence of negatively charged amino acid groups near the ribose-binding region. At this point, it should be noted that solute quenching studies of the fluorescence of DnaB tryptophans, which are located in/close to the nucleotide-binding site, also show strong preferential quenching by Tl^+, compared to I^- (Bujalowski and Klonowska, submitted). Thus, the data suggest that protein tryptophans may constitute part of the hydrophobic microenvironment around the ribose-binding region.

Fluorescence anisotropy of MANT-ADP and TNP-ADP bound to DnaB is 0.33 ± 0.02 and 0.32 ± 0.02, respectively. The values are very close to the fundamental anisotropies of these nucleotide analogs, ~0.35–0.4, indicating that both fluorophores attached to the ribose have very limited motional freedom (Moczydlowski & Fortes, 1981; Cremo et al., 1990). These results are particularly interesting in the case of MANT-ADP, whose major emission component (fractional amplitude = 0.76) decays with a lifetime of 13.1 ± 0.5 ns (Table 4). This is a time window long enough to sense rotational motion with correlation time up to ~50 ns (Lakowicz, 1983). Thus, the data strongly suggest that the entire ribose-binding region

has substantially limited mobility with respect to the protein matrix.

Fluorescence of MANT-ADP, free in solution, decays with a nearly homogeneous single lifetime of 3.9 ± 0.2 ns (buffer T2, 20 mM NaCl, pH 8.1, 20 °C) which is very similar to the values previously obtained by Cremo et al. (4.06 ns) and Hiratsuka (3.8 ns) (Cremo et al., 1990; Hiratsuka, 1983). Very similar values of fluorescence lifetimes have been obtained for MANT-dADP and MANT-dATP (Table 4). Binding to the DnaB helicase induces dramatic changes in the MANT-ADP emission decay characteristics. The decay becomes heterogeneous and is described by two components, $\tau_1 = 6.0 \pm 0.2$ ns (amplitude 0.24) and $\tau_2 = 13.1 \pm 0.5$ ns (amplitude 0.76). Thus, both fluorescence lifetimes are increased with respect to the lifetime of free MANT-ADP. The presence of two lifetimes is not a result of the possible different locations of the MANT group in 2′ and 3′ isomers in the ribose-binding region. Both MANT-dADP and MANT-dATP, which have a MANT group attached exclusively to the 3′ oxygen show, within experimental accuracy, the presence of the same two decay components (Table 4). The fluorescence lifetime is a very sensitive measure of the heterogeneity of the environment surrounding the fluorophore (Lakowicz, 1983). The presence of two lifetimes for the MANT-ADP, MANT-dADP, and MANT-dATP bound to the DnaB helicase strongly suggests that the chromophore experiences two different environments, possibly two different conformations, of the ribose-binding region of the DnaB helicase nucleotide-binding site. This result is in contrast to a single environment and probably to a lack of discrete conformational heterogeneity at the base-binding region, as probed by ϵADP fluorescence. The data indicate that conformational heterogeneity is localized in the ribose-binding region and that it is not transmitted to the base-binding region, suggesting limited communication between base- and ribose-binding sites.

DnaB helicase is a free-energy transducing enzyme which can catalyze the unwinding of duplex DNA fueled by ATP hydrolysis (LeBowitz & McMacken, 1986; Baker et al., 1987). A common feature of such enzymes is that they undergo a conformational transition in their active sites during the catalysis (Hill, 1977). To our knowledge, no data are available on the nature and conformation of the nucleotide-binding sites of other helicases. Therefore, comparison of results obtained in this work on the DnaB helicase to the functionally and/or structurally homologous enzymes is not possible at this time. However, the energetics of the two-state conformational transition of the ATP-binding site have been characterized in the case of the other free-energy transducing system, the myosin subfragment S-1, and were proposed to be involved in the "power stroke" of the contractile cycle (Shriver & Sykes, 1982; Aguirre et al., 1989; Lin & Cheung, 1990). It is possible that conformational heterogeneity in the ribose-binding region of the DnaB helicase nucleotide-binding site, described in this work, reflects conformational changes involved in the "power stroke" in the DnaB helicase action (Hill & Tsuchiya, 1982).

ACKNOWLEDGMENT

We would like to thank Drs. D. Wayne Bolen and Edmund W. Czerwinski for careful reading and comments on the manuscript. We would also like to thank Mrs. Gloria Drennan Davis for help in preparing the manuscript.

REFERENCES

Aguirre, R., Lin, S. H., Gonsoulin, F., Wang, C. K., & Cheung, H. C. (1989) *Biochemistry 28*, 799–807.

Allen, G. C., & Kornberg, A. (1991) *J. Biol. Chem. 266*, 22096–22101.

Ando, T., & Asai, H. (1980) *J. Biochem. 88*, 255–264.

Arai, K., & Kornberg, A. (1981a) *J. Biol. Chem. 256*, 5253–5259.

Arai, K., & Kornberg, A. (1981b) *J. Biol. Chem. 256*, 5260–5266.

Arai, K., & Kornberg, A. (1981c) *J. Biol. Chem. 256*, 5267–5272.

Arai, K., Yasuda, S., & Kornberg, A. (1981a) *J. Biol. Chem. 256*, 5247–5252.

Arai, K., Low, R., Kobori, J., Shlomai, J., & Kornberg, A. (1981b) *J. Biol. Chem. 256*, 5273–5280.

Azumi, T., & McGlynn, S. P. (1962) *J. Chem. Phys. 37*, 2413–2420.

Baker, T. A., Funnell, B. E., & Kornberg, A. (1987) *J. Biol. Chem. 262*, 6877–6885.

Bujalowski, W., & Porschke, D. (1984) *Nucleic Acids Res. 12*, 7549–7563.

Bujalowski, W., & Lohman, T. M. (1987a) *Biochemistry 26*, 3099–3106.

Bujalowski, W., & Lohman, T. M. (1987b) *J. Mol. Biol. 195*, 897–907.

Bujalowski, W., & Porschke, D. (1988a) *Biophys. Chem. 30*, 151–157.

Bujalowski, W., & Porschke, D. (1988b) *Z. Naturforsch. 43c*, 91–98.

Bujalowski, W., & Lohman, T. M. (1991a) *J. Biol. Chem. 266*, 1616–1626.

Bujalowski, W., & Lohman, T. M. (1991b) *J. Mol. Biol. 217*, 63–74.

Bujalowski, W., & Klonowska, M. M. (1993) *Biochemistry 32*, 5888–5900.

Bujalowski, W., Greaser, E., McLaughlin, W., & Porschke, D. (1986a) *Biochemistry 25*, 6365–6371.

Bujalowski, W., Jung, M., McLaughlin, W., & Porschke, D. (1986b) *Biochemistry 25*, 6372–6378.

Cheung, H. C., & Liu, B. M. (1984) *J. Muscle Res. Cell Motil. 5*, 65–80.

Cheung, H. C., Gonsoulin, F., & Garland, F. (1985) *Biochim. Biophys. Acta 832*, 52–62.

Cremo, C. R., Neuron, J. M., & Yount, R. G. (1990) *Biochemistry 29*, 3309–3319.

Eftink, M. R. (1991) in *Biophysical and Biochemical Aspects of Fluorescence Spectroscopy* (Dewey, T. C., Ed.) Chapter 1, Plenum Press, New York, London.

Eftink, M. R., & Ghiron, C. A. (1981) *Anal. Biochem. 114*, 199–227.

Gafni, A., Schlessinger, J., & Steinberg, I. Z. (1979) *J. Chem. Soc. 101*, 463–467.

Hill, T. L. (1977) *Free Energy Transduction in Biology*, Academic Press, New York.

Hill, T. L., & Tsuchiya, T. (1981) *Proc. Natl. Acad. Sci. U.S.A. 78*, 4796–4800.

Hiratsuka, T. (1983) *Biochim. Biophys. Acta 742*, 496–508.

Hiratsuka, T. (1984) *J. Biochim. 96*, 155–162.

Hiratsuka, T., & Uchida, K. (1973) *Biochim. Biophys. Acta 320*, 635–647.

Kaguni, J. M., Fuller, R. S., & Kornberg, A. (1982) *Nature 296*, 623–626.

Kinosita, K., Jr., Kawato, S., & Ikegami, A. (1977) *Biophys. J. 20*, 289–305.

Kornberg, A., & Baker, T. A. (1992) *DNA Replication*, Freeman, San Francisco.

Kosower, E. M. (1958) *J. Am. Chem. Soc. 80*, 3253–3260.

Lakowicz, J. R. (1983) *Principle of Fluorescence Spectroscopy*, Chapter 10, Plenum Press, New York, London.

Lanka, E., Geschke, B., & Schuster, H. (1978) *Proc. Natl. Acad. Sci. U.S.A. 75*, 799–803.

LeBowitz, J. H., & McMacken, R. (1986) *J. Biol. Chem. 261*, 4738–4748.

Leonard, N. J. (1984) *Crit. Rev. Biochem. 15*, 125–199.

Lin, S. H., & Cheung, H. C. (1989) *Biochemistry 30*, 4317–4322.
Mallory, J. B., Alfano, C., & McMacken, R. (1990) *J. Biol. Chem. 265*, 13297–13307.
Matson, S. W., & Kaiser-Rogers, K. A. (1990) *Annu. Rev. Biochem. 59*, 289–329.
McMacken, R., Ueda, K., & Kornberg, A. (1977) *J. Biol. Chem. 253*, 3313–3319.
Moczydlowski, E. G., & Fortes, P. A. G. (1981) *J. Biol. Chem. 256*, 2346–2356.
Nakamoto, R. K., & Inesi, G. (1984) *J. Biol. Chem. 259*, 2961–2970.
Nakayama, N., Arai, N., Kaziro, Y., & Arai, K. (1984a) *J. Biol. Chem. 259*, 88–96.
Nakayama, N., Arai, N., Bond, M. W., Kaziro, Y., & Arai, K. (1984b) *J. Biol. Chem. 259*, 97–101.
Parker, C. A. (1968) *Photoluminescence of Solutions*, Elsevier Publishing Co., Amsterdam.
Parker, C. A., & Reese, W. T. (1960) *Analyst 85*, 587–592.
Perkins, W. J., Wells, J. A., & Yount, R. G. (1984) *Biochemistry 23*, 3994–4002.
Philips, A. V., Robbins, D. J., Coleman, M. S., & Barkley, M. D. (1987) *Biochemistry 26*, 2893–2903.
Reha-Krantz, L. J., & Hurwitz, J. (1978a) *J. Biol. Chem. 253*, 4043–4050.
Reha-Krantz, L. J., & Hurwitz, J. (1978b) *J. Biol. Chem. 253*, 4051–4057.
Robbins, D. J., Deibel, M. R., Jr., & Barkley, M. D. (1985) *Biochemistry 24*, 7250–7257.
Schekman, R., Weiner, A., & Kornberg, A. (1974) *Science 186*, 987–993.
Schekman, R., Weiner, J. H., Weiner, A., & Kornberg, A. (1975) *J. Biol. Chem. 250*, 5859–5865.
Schellman, J. (1975) *Biopolymers 14*, 999–1018.
Scott, T. G., Spencer, R. D., Leonard, N. J., & Weber, G. (1970) *J. Am. Chem. Soc. 92*, 687–695.
Secrist, J. A., Bario, J. R., Leonard, N. J., & Weber, G. (1972) *Biochemistry 11*, 3499–3506.
Shriver, J. W., & Sykes, B. D. (1982) *Biochemistry 21*, 3022–3028.
Spencer, R. D., & Weber, G. (1970) *J. Chem. Phys. 52*, 1654–1663.
Spencer, R. D., Weber, G., Tolman, G., Barrio, J. R., & Leonard, N. J. (1974) *Eur. J. Biochem. 45*, 425–429.
Stern, O., & Volmer, M. (1919) *Phys. Z. 20*, 183–188.
Tanford, C. (1961) *Physical Chemistry of Macromolecules*, J. *Wiley*, New York.
Turner, D. C., & Brand, L. (1968) *Biochemistry 10*, 3381–3390.
Ueda, K., McMacken, R., & Kornberg, A. (1978) *J. Biol. Chem. 253*, 261–269.
Wahle, E., Lasken, R. S., & Kornberg, A. (1989a) *J. Biol. Chem. 264*, 2463–2468.
Wahle, E., Lasken, R. S., & Kornberg, A. (1989b) *J. Biol. Chem. 264*, 2469–2475.
Weber, G., & Teale, F. W. J. (1957) *Trans. Faraday Soc. 53*, 646–655.
Wickner, S. H. (1978) *Cold Spring Harbor Symp. Quant. Biol. 43*, 303–310.
Wickner, S., Wright, M., & Hurwitz, J. (1973) *Proc. Natl. Acad. Sci. U.S.A. 71*, 783–787.
Wong, I., & Lohman, T. M. (1992) *Science 256*, 350–355.

DNA Replication Fidelity with 8-Oxodeoxyguanosine Triphosphate†

Youri I. Pavlov,‡ Dana T. Minnick,§ Shunji Izuta,§ and Thomas A. Kunkel*,§

Laboratory of Molecular Genetics, National Institute of Environmental Health Sciences, Research Triangle Park, North Carolina 27709, and Department of Genetics, St. Petersburg University, Universitetskaya emb. 7/9, St. Petersburg 199034, Russia

Received November 12, 1993; Revised Manuscript Received January 10, 1994®

ABSTRACT: Oxidative metabolism is known to generate mutagenic compounds within cells, among which is 8-oxodeoxyguanosine. Here the mutagenic potential of the triphosphate form of this base analog (8-O-dGTP) is investigated during replication *in vitro* of the *lacZ* α-complementation sequence in M13mp2 DNA. Adding 8-O-dGTP at equimolar concentration with the normal dNTPs to polymerization reactions decreases the fidelity of DNA synthesis by exonuclease-deficient Klenow, T4, and *Thermus thermophilus* DNA polymerases. Sequence analysis of mutants suggests that 8-O-dGMP is misincorporated opposite template adenines, yielding A → C transversions. The degree of polymerase selectivity against this error is enzyme-dependent, with rates varying by >25-fold. To determine if the A·8-O-dGMP mispair is proofread, a direct comparison of the fidelity of proofreading-proficient and proofreading-deficient Klenow and T4 DNA polymerases was made. Although the exonuclease activity of Klenow polymerase did not substantially reduce overall misincorporation of 8-O-dGMP, misincorporation was lower for the proofreading-proficient T4 enzyme as compared to its proofreading-deficient derivative. These data suggest that the A·8-O-dGMP mispair can be proofread. The mutagenic potential of 8-O-dGTP with eukaryotic systems was also examined. Misincorporation of 8-O-dGTP opposite adenine was observed during SV40 origin-dependent replication of double-stranded DNA in HeLa cell extracts. When present during replication at a concentration equal to the four normal dNTPs, 8-O-dGTP was at least 13-fold more mutagenic for A·T → C·G transversions than was a 100-fold excess of normal dGTP. These data suggest that 8-O-dGTP could be highly mutagenic during nuclear genomic replication in eukaryotes, with a specificity similar to that in *Escherichia coli*. DNA polymerase γ, the replicative polymerase for mitochondrial DNA, also readily misincorporated 8-O-dGMP opposite adenine despite the presence of a highly active proofreading exonuclease activity. Given the amount of oxidative metabolism occurring in mitochondria, this result has implications for the stability of the mitochondrial genome and for the origin of degenerative diseases resulting from mitochondrial mutations.

Certain analogs of the four bases normally found in DNA are capable of provoking mutations during DNA synthesis due to their ambivalent pairing capacity (Freese, 1959). For many years they have been used as tools to examine DNA replication fidelity and the genetic consequences of inaccurate replication (Drake & Greening, 1970; Bessman *et al.*, 1974; Pavlov *et al.*, 1991). Interest in base analogs also stems from recent evidence that they are formed *in vivo* under both normal and abnormal physiological conditions and, thus, are a potential source of spontaneous mutations.

One process known to produce a base analog *in vivo* is oxidative metabolism, which generates reactive oxygen species that damage a variety of macromolecules. Among the many byproducts of oxidative metabolism, one that has received considerable recent attention is 8-oxodeoxyguanine, the so-called "GO"[1] lesion [Kasai & Nishimura, 1984; for reviews, see Kasai and Nishimura (1991) and Michaels and Miller (1992)]. A series of studies in *Escherichia coli* have demonstrated that this modified guanine nucleotide can be mutagenic by base pairing with either cytosine or adenine, the latter possibly occurring when GO is in the *syn* conformation (Kouchhakdjian *et al.*, 1991). Thus, *E. coli* strains defective in repair of the GO lesion are among the strongest mutators known. For example, the products of the *mutM* and *mutY* genes are involved in repair of base pairs containing the GO lesion, and the double mutant is a >10000-fold mutator for G → T transversions (Michaels *et al.*, 1992a). These result when the modified guanine is present as a template base and mispairs with incoming dATP (Wood *et al.*, 1990; Shibutani *et al.*, 1991: Moriya *et al.*, 1991; Moriya, 1993).

Alternatively, as a triphosphate precursor for synthesis by *E. coli* DNA polymerases (Maki & Sekiguchi, 1992; Cheng *et al.*, 1992), 8-O-dGTP is incorporated opposite template adenine, leading to A·T → C·G transversions. The product of the *mutT* gene has nucleoside triphosphatase activity (Bhatnagar & Bessman, 1988; Akiyama *et al.*, 1989) that hydrolyzes 8-O-dGTP to 8-O-dGMP (Maki & Sekiguchi, 1992). Because a *mutT*⁻ strain is a 100–10000-fold mutator for A·T → C·G transversions (Yanofsky *et al.*, 1966) that result from misincorporation of some form of dGTP opposite template A (Schaaper & Dunn, 1987; Akiyama *et al.*, 1989), Maki and Sekiguchi (1992) suggested that the 8-O-dGTPase activity eliminates this potentially mutagenic base analog from the dNTP precursor pool used for DNA replication.

We initiated the present study of the fidelity of DNA synthesis *in vitro* in the presence of 8-O-dGTP to address

† This work was supported in part by a Central and Eastern European Initiative Grant from the Fogarty International Center.

* Author to whom correspondence should be addressed [phone (919) 541-2644; fax (919) 541-7613].

‡ St. Petersburg University.

§ National Institute of Environmental Health Sciences.

® Abstract published in *Advance ACS Abstracts,* April 1, 1994.

[1] Abbreviations: GO, 8-oxodeoxyguanine; 8-O-dGTP, 8-oxodeoxyguanosine triphosphate; 8-O-dGMP, 8-oxodeoxyguanosine monophosphate; dNTPs, deoxyribonuclotide triphosphates; *Tth*, *Thermus thermophilus*.

0006-2960/94/0433-4695$04.50/0

three unresolved issues. First, we wanted to quantitatively establish the mutagenic potential of 8-O-dGTP in model polymerization reactions. In a previous study (Cheng *et al.*, 1992), 8-O-dGTP was shown to be incorporated opposite template adenine by the exonuclease deficient large fragment of *E. coli* DNA polymerase I. However, this was detected only when the analog was substituted completely for dGTP and in 10–100-fold excess over the other three normal dNTPs. Likewise, the catalytic subunit of *E. coli* DNA polymerase III also incorporated 8-O-dGTP opposite template adenine (Maki & Sekiguchi, 1992), but that study examined insertion (but not mispair extension) at a single template site in a reaction containing only dATP and 8-O-dGTP. Given the potential importance of this analog *in vivo* and the lack of information on its possible concentration relative to the four normal dNTPs, we wanted to extend the earlier studies to establish mutagenic potential in quantitative terms in reactions in which the analog was present in equimolar concentration with all four normal dNTPs. The fidelity assay used here also permits an examination of the effects of local sequence context on misincorporation.

Second, we wanted to determine if, once formed by a DNA polymerase, the A·8-O-dGMP mispair was subject to exonucleolytic proofreading. In a study of the miscoding potential of 8-O-dG as a template nucleotide during DNA synthesis *in vitro*, Shibutani *et al.* (1991) concluded that misinsertions of dAMP opposite template 8-O-G were not proofread by the 3′ → 5′ exonuclease of *E. coli* DNA polymerase I. They suggested that this is because the exonuclease does not recognize the 8-O-dG·dAMP mispair as a substrate. However, the situation in the present study is different in that the modified nucleotide is the incoming dNTP. It is well-known that DNA polymerases discriminate to different extents against substitutions involving the same two nucleotides depending on which is the template and which is the incoming triphosphate [for a review, see Kunkel and Bebenek (1988)]. This could result in differential proofreading. In fact, from a more recent study of revertants at *trpA* sites using mutator strains of *E. coli*, Fowler *et al.* (1992) suggested that proofreading by the *dnaQ* gene product (the 3′ → 5′ exonuclease subunit of DNA polymerase III holoenzyme) does reduce the frequency of A·T → C·G transversions in *mutT* strains *in vivo*. Because these transversions have been suggested to result from misincorporation of 8-O-dGTP opposite template adenine (Maki & Sekiguchi, 1992), we wanted to determine whether 8-O-dGMP, once inserted opposite adenine, would be removed by the exonucleolytic proofreading activity associated with DNA polymerases. This determination is made possible by the availability of mutant DNA polymerases that have normal DNA polymerase activity but lack proofreading activity due to amino acid substitutions within the exonuclease active sites [*e.g.*, Derbyshire *et al.* (1988) and West Frey *et al.* (1993)].

The identification of a human enzyme functionally equivalent to the MutT protein (Mo *et al.*, 1992) and the recent cloning and expression of its cDNA (Sakumi *et al.*, 1993) suggest that eukaryotes may need protection against mutagenic forms of dGTP generated by oxidative stress. Since the mutagenic potential of 8-O-dGTP has not been examined beyond the studies in the powerful *E. coli* genetic system, we wanted to determine whether 8-O-dGTP is mutagenic during eukaryotic DNA replication. To do so, we performed reactions with proteins involved in replication of either of two genomes. The first uses the well-characterized *in vitro* model for duplication of nuclear DNA, the SV40 origin-dependent replication system (Kelly, 1988); Stillman, 1989; Hurwitz *et al.*, 1990). Here circular, double-stranded DNA can be completely replicated in a series of complex reactions catalyzed by a number of host cell proteins. We have previously found that such replication in HeLa cell extracts is accurate for base substitution errors (Roberts & Kunkel, 1988; Thomas *et al.*, 1991), including the A·T → C·G substitutions characteristic of 8-O-dGTP misincorporation. This provides a low background, such that analog-induced errors can be readily detected. The second is gap-filling, single-stranded DNA synthesis catalyzed by DNA polymerase γ, the central enzyme for replication of mitochondrial DNA. DNA polymerase γ is normally very accurate for substitution errors due to the presence of a highly active proofreading exonuclease (Kunkel & Soni, 1988). This determination is particularly intriguing because oxygen radicals are a natural byproduct of the extensive oxidative phosphorylation that occurs in mitochondria and hence might generate mutagenic nucleotide precursors in this organelle. Mutagenesis induced by 8-O-dGTP during mitochrondrial DNA replication could contribute to the degenerative diseases associated with mitochondrial DNA mutations [for a review, see Wallace (1992)].

EXPERIMENTAL PROCEDURES

Bacterial Strains and Reagents. *E. coli* strains CSH50, NR9099, NR9162, and MC1061 were as described (Kunkel & Soni, 1988). *E. coli* strain CC104 *mutM*⁻ (*ara* Δ(*gpt-lac*)$_5$ *rpsL* [*F′lacI378 lacZ461 proA*⁺*B*⁺] *mutM*) was from Jeffrey H. Miller (UCLA). NR9373 (*ara thi* Δ(*pro-lac*) *mutY*::*Tn5*) was provided by Roel M. Schaaper (NIEHS). A mutant strain deficient in both *mutM* and *mutY* was made by P1 transduction of *mutM* with a P1 lysate grown on NR9373, selecting for tetracycline and kanamycin resistance. Resulting transductants were colony-purified and tested for spontaneous mutation rate, which was found to be 1000-fold higher than in the parent strain, in agreement with a previous study (Michaels *et al.*, 1992a). The 8-O-dGTP was prepared as described (Mo *et al.*, 1992) using a 4-μm Waters Radial NovaPack column instead of a Spherisorb SAX column. The sources of all other reagents and the preparation of DNA substrates were as described (Kunkel & Soni, 1988; Roberts & Kunkel, 1993).

DNA Polymerases. The wild-type large (Klenow) fragment of *E. coli* DNA polymerase I and its exonuclease-deficient variant (D355A, E357A changes; Derbyshire *et al.*, 1988) were from U.S. Biochemical Corp. (Cleveland, OH). The thermostable DNA polymerase from *Thermus thermophilus* (Bechtereva *et al.*, 1989) was from Biomaster (Moscow, Russia) or Amersham. Wild-type T4 DNA polymerase and its exonuclease-deficient derivative (containing a D219A change; West Frey *et al.*, 1993) were gifts from Michelle West Frey and Stephen J. Benkovic (Pennsylvania State University). Chick embryo DNA polymerase γ was described previously (Kunkel & Soni, 1988). For replication studies, HeLa cell cytoplasmic extract was prepared according to the method of Li and Kelly (1985). SV40 T antigen was purchased from Molecular Biology Resources.

DNA Synthesis Reactions. Reactions (25 μL) contained equimolar concentrations of dATP, dGTP, dCTP, TTP, and 8-O-dGTP, either 50 μM (for Klenow, T4, and *Tth* polymerases) or 100 μM (for pol γ and SV40 replication reactions). DNA polymerase reactions contained 150 ng (~67 fmol) of gapped M13mp2 DNA; the replication reaction contained 40 ng of double-stranded M13mp2 SV DNA. Other reaction components, incubation temperatures, and time were as follows. Klenow polymerase: 20 mM Hepes (pH 7.8), 2 mM

Table 1: Fidelity of Exonuclease-Deficient Klenow Polymerase in the Presence of 8-O-dGTP[a]

strain	8-O-dGTP	plaques total	plaques mutant	mutant freq ($\times 10^{-4}$)
wild-type	–	12570	116	92
	+	2152	107	500
mutM$^-$	–	7250	53	73
	+	2387	96	400
mutM$^-$*Y*$^-$	–	4215	39	93
	+	2923	47	160

[a] Reactions, electroporations, and platings were performed as described under Experimental Procedures.

dithiothreitol, 10 mM $MgCl_2$, and 0.7 pmol of polymerase; 37 °C; 10 min. T4 DNA polymerase: 67 mM Tris-HCl (pH 8.8), 10 mM β-mercaptoethanol, 5 mM $MgCl_2$, 60 mM NaCl, and 0.9 pmol of polymerase; 37 °C; 30 min. *Tth* polymerase: 20 mM Tris-HCl (pH 8.0), 2 mM dithiothreitol, 10 mM $MgCl_2$, and 0.2 pmol of polymerase; 70 °C; 10 min. DNA polymerase γ: 20 mM Tris-HCl (pH 8.0), 2 mM dithiothreitol, 10 mM $MgCl_2$, and 5 units of polymerase; 37 °C; 30 min. Replication reaction: 30 mM Hepes (pH 7.8), 7 mM $MgCl_2$, 4 mM ATP, 200 μM CTP, GTP, and UTP, [α-^{32}P]dCTP (4000 cpm/pmol), 40 mM creatine phosphate, 100 μg of creatine phosphokinase/mL, 15 mM sodium phosphate (pH 7.5), 1 μg of SV40 T antigen, and 10 μL of extract; 37 °C; 6 h.

Product Analysis. Polymerase reactions were terminated with EDTA, and a portion of each reaction was analyzed by agarose gel electrophoresis (Kunkel, 1985a) to monitor the extent of synthesis. In all cases, the products migrated coincident with the full-length circular DNA standard, indicating that the 390-nucleotide gap molecules had been filled. Replication reaction products were analyzed by diagnostic restriction endonuclease digestion and agarose gel electrophoresis as described (Roberts & Kunkel, 1993). Aliquots of each reaction were used for electroporation of competent cells as described (Roberts & Kunkel, 1993).

Fidelity Assay. The assay scores errors during synthesis of the minus-strand of the wild-type *lacZ*α gene sequence in M13mp2. Correct polymerization during gap-filling synthesis by purified polymerases or during SV40 origin-dependent replication of double-stranded DNA produces DNA that yields dark blue M13 plaques upon transfection of an appropriate *E. coli* host strain followed by plating on indicator plates. Errors are scored as lighter blue or colorless plaques. All possible types of substitutions as well as frameshifts at many different sites can be scored (Roberts & Kunkel, 1993).

RESULTS

Misincorporation of 8-O-dGTP during Synthesis by Exonuclease-Deficient Klenow Polymerase. To examine the mutagenic potential of 8-O-dGTP during DNA synthesis *in vitro*, we began with the well-defined enzyme studies by Cheng *et al.* (1992) of the Klenow fragment of *E. coli* DNA polymerase I. This polymerase (Table 1) is devoid of exonucleolytic proofreading activity by virtue of the double amino acid change D355A,E357A within the exonuclease active site. The enzyme is otherwise normal both structurally and kinetically (Derbyshire *et al.*, 1988), and its fidelity with normal dNTP substrates has been extensively characterized (Bebenek *et al.*, 1990; Joyce *et al.*, 1992; Eger & Benkovic, 1992).

In reactions using M13mp2 DNA with a 390-nucleotide single-stranded gap containing the *lacZ* α-complementation sequence, gap-filling DNA synthesis with the D355A,E357A Klenow polymerase and normal dNTPs generates reaction products that, upon electroporation of a wild-type *E. coli* α-complementation strain, yield a mutant frequency of 92×10^{-4} (Table 1). Sequence analysis of over 100 independent mutants demonstrated that none contained an A → C transversion. Thus, this polymerase rarely misincorporates dGTP opposite template A.

In a parallel reaction, inclusion of 8-O-dGTP at a concentration equal to that of the four normal dNTPs yielded a 5-fold increase in mutant frequency (Table 1). Sequence analysis of 19 mutants demonstrated that 17 contained one or more A → C substitutions. These data are consistent with formation of A·8-O-dGMP mispairs during synthesis *in vitro*. They also demonstrate that the mispair survived transfection and was expressed, *i.e.*, that the newly incorporated 8-O-dGMP templated the incorporation of dCTP during subsequent replication *in vivo*. These data are completely consistent with observations reported by Cheng *et al.* (1988).

At least two repair activities in *E. coli* could influence recovery of mutants. The *MutM* gene encodes a glycosylase that removes 8-O-dGMP from a C·8-O-dGMP pair (Tchou *et al.*, 1991). The *MutY* gene encodes an adenine glycosylase (Au *et al.*, 1988) that removes the adenine from a A·8-O-dGMP mispair (Michaels *et al.*, 1992a,b; Moriya & Grollman, 1993). Introduction of aliquots of the polymerase reaction products into a *mutM*$^-$ strain yielded mutant frequencies that were similar to those obtained with the wild-type strain (Table 1). Thus, the MutM gene product does not substantially affect the ability to score mutants originating from misincorporation of 8-O-dGTP during synthesis *in vitro*. Introduction of an aliquot of the 8-O-dGTP-containing reaction products into a *mutM*$^-$*mutY*$^-$ double-mutant strain yielded mutant frequencies lower than those obtained with the wild-type strain (Table 1, compare 160×10^{-4} to 500×10^{-4}). This antimutator effect is consistent with the possibility that, upon transfection of DNA into a wild-type strain, the glycosylase removes the "correct" (*i.e.*, adenine) nucleotide from the A·8-O-dGMP mispair made *in vitro*, which is then replaced by dCMP during repair synthesis *in vivo*. Thus, *MutY* action in the wild-type strain actually enhances the ability to score misincorporation of 8-O-dGTP *in vitro*.

Incorporation of 8-O-dGTP opposite template C during DNA synthesis *in vitro*, followed by misincorporation of dAMP opposite template 8-O-dGMP during subsequent replication *in vivo*, would yield C·G → A·T transversions. When the products of the Klenow polymerase reactions were used to transfect the wild-type *E. coli* strain and DNAs from 40 independent mutants were sequenced, none contained C·G → A·T transversions. This does not exclude the possibility that 8-O-dGTP may be incorporated opposite template C, since this base pair could be converted to a normal C·G pair *in vivo* by MutM action or by replication. Alternative approaches will be required to study misincorporation of 8-O-dGTP opposite template C. Nonetheless, the data with the exonuclease-deficient Klenow polymerase validate the M13mp2 forward mutation assay for addressing several issues on misincorporation of 8-O-dGMP opposite adenine.

Contribution of Base Selectivity to 8-O-dGTP Misincorporation Error Rate. We first wanted to examine the role of DNA polymerase selectivity in determining the degree of 8-O-dGTP-induced infidelity, in the absence of proofreading activity. To do so, we performed reactions with and without 8-O-dGTP using three different proofreading-deficient DNA polymerases, the 3′ → 5′ exonuclease-deficient mutant forms

Table 2: Differential Mutagenic Potential of 8-O-dGTP with Prokaryotic DNA Polymerases[a]

DNA polymerase	mutant frequency ($\times 10^{-4}$)			
	exonuclease-deficient		exonuclease-proficient	
	− 8-O-dGTP	+ 8-O-dGTP	− 8-O-dGTP	+ 8-O-dGTP
Klenow	92	500	27	340
T4 (expt 1)	70	120	7	22
(expt 2)	46	120	8	19
Tth	73	1100		

[a] Reactions were performed as described under Experimental Procedures. All frequencies are derived from scoring several thousand plaques per variable. The data in Table 1 represent typical results.

of Klenow polymerase and bacteriophage T4 DNA polymerase, and the normally exonuclease-deficient thermostable *Tth* DNA polymerase. All three enzymes generate higher mutant frequencies in reactions containing the base analog than in reactions that do not (compare the second and third columns in Table 2). The differences were 5.4- and 15-fold for Klenow and *Tth* polymerases, respectively. Since the difference was only 1.7-fold in the initial experiment with T4 DNA polymerase (120×10^{-4} vs 70×10^{-4}), a second experiment was performed. This experiment (T4 experiment 2 in Table 2) confirmed the small 8-O-dGTP-dependent effect. It also illustrates, as in a number of previous studies [see Thomas *et al.* (1991)], that M13-based transfection assays are reproducible, with repeat experiments seldom varying by more that 50% and multiple determinations yielding standard deviations less than 20% of mean values.

Previous studies have shown that DNA polymerases generate a variety of errors during synthesis with normal dNTPs. To quantitatively establish the full miscoding potential of 8-O-dGTP, sequence analysis of mutants obtained from reactions with and without the analog was performed. The results (Table 3) revealed that the increases resulted predominantly from A → C substitutions. The analog-dependent increases in error rate were ≥600-, ≥70-, and ≥730-fold for the exonuclease-deficient Klenow, T4, and *Tth* polymerase, respectively. Thus, these three DNA polymerases all misincorporate 8-O-dGTP opposite template adenine. However, they do so at rates that vary by more than 25-fold, ranging from 2.8×10^{-4} for exonuclease-deficient T4 DNA polymerase to 73×10^{-4} for *Tth* DNA polymerase (Table 3). In this type of fidelity assay, these rates reflect the probability of misinsertion followed by successful extension to fix the mispair. Thus, the observed enzyme-dependent differences could result from rate differences at one or both steps in the reaction.

As of this writing, there are 25 template adenines in the *lacZ* α-complementation reporter gene used in this study at which A → C substitutions can be detected as a mutant plaque phenotype. The sequence analysis of mutants from reactions containing 8-O-dGTP revealed a distinctly nonrandom distribution of misincorporation of the base analog. For example, 4 of the 17 A → C substitutions (24%) recovered from reactions with the exonuclease-deficient Klenow polymerase were at one position, a template adenine at position 109 (where +1 is the first transcribed nucleotide of the gene). Similarly, 4 of the 16 A → C substitutions (25%) recovered from reactions with the exonuclease-deficient T4 DNA polymerase were at a single site. However, this was a different nucleotide, a template adenine at position 130.

Contribution of Exonucleolytic Proofreading to 8-O-dGTP Misincorporation Error Rate. We next wanted to use this model system to determine whether 8-O-dGMP, once inserted opposite adenine, would be removed by the exonucleolytic proofreading activity associated with DNA polymerases. To examine this possibility, we made pairwise comparisons using two different wild-type DNA polymerases and their exonuclease-deficient counterparts. For the first comparison we used the Klenow polymerase, where the proofreading deficiency of the mutant enzyme results from two amino acid differences in the exonuclease active site. Since these changes affect neither the structure of the polymerase active site nor polymerization activity (Derbyshire *et al.*, 1988), any differences in fidelity are interpreted as reflecting the proofreading defect rather than altered base selectivity, although the latter cannot be completely excluded.

Using identical reaction conditions, both wild-type and exonuclease-deficient Klenow polymerases yield a high rate of A → C errors in reactions performed with 8-O-dGTP (Tables 2 and 3). However, the rate is only slightly higher for the exonuclease-deficient enzyme (compare 19×10^{-4} to 30×10^{-4} in Table 3), suggesting that proofreading of A·8-O-dGMP mispairs by the exonuclease activity of Klenow polymerase is inefficient.

The second comparison uses T4 DNA polymerase. The wild-type enzyme has a 3′ → 5′ exonuclease, while its mutant counterpart does not (West Frey *et al.*, 1993) as a result of a change of an amino acid (D219A) that is highly conserved among DNA polymerases containing associated 3′ → 5′ exonuclease activity. Under identical reaction conditions, both forms of the T4 polymerase yield A → C errors in reactions performed with 8-O-dGTP (Table 3). However, the rate with the mutant polymerase is 4.5-fold higher than for the wild-type enzyme (compare 0.6×10^{-4} to 2.7×10^{-4} in Table 3). This suggests that more than 80% of misinsertions of 8-O-dGMP opposite template adenine by the T4 DNA polymerase are proofread by its associated exonuclease activity. (Again, this interpretation assumes no difference in polymerase base selectivity between the wild-type and mutant enzyme.) However, even in a polymerization reaction where proofreading would contribute greatly to accuracy for mispairs involving normal dNTPs, 8-O-dGTP retains a high mutagenic potential.

8-O-dGTP Misincorporation Error Rates during Eukaryotic Replication. To examine whether 8-O-dGTP is mutagenic during eukaryotic DNA replication, we used the simian virus 40 (SV40) replication system. Inclusion of 8-O-dGTP in a replication reaction at a concentration equal to that of the other dNTPs reduces replication efficiency by less than 2-fold, as measured by incorporation of radiolabeled dCTP. When analyzed by agarose gel electrophoresis, the products of reactions containing 8-O-dGTP (not shown) are indistinguishable from those obtained with normal dNTPs [e.g., see Figure 1 in Roberts and Kunkel (1988)]. The monomer-length circular products are resistant to digestion by the restriction endonuclease *DpnI* and are thus inferred to be the hemimethylated products of semiconservative replication.

The results of transfection of these products are shown in Table 4. In the first experiment, the mutant frequency is 2.8-fold higher for products of reactions containing 8-O-dGTP than for replication with normal dNTPs (compare 23×10^{-4} to 8.2×10^{-4} in Table 4). This 8-O-dGTP-dependent increase is T antigen-dependent (not shown), demonstrating that it reflects replication errors. We had previously found that replication using normal dNTPs is accurate for base substitution errors (Roberts & Kunkel, 1988; Thomas *et al.*, 1991), including the A·T → C·G substitutions characteristic of misincorporated 8-O-dGTP. In contrast, sequence analysis of mutants from reactions containing 8-O-dGTP suggests that

Table 3: Error Rates for A→C Transversions with Several DNA Polymerases

	without 8-O-dGTP			with 8-O-dGTP		
	mutants sequenced			mutants sequenced		
DNA polymerase	total	A→C	error rate[a] for A→C (×10⁻⁴)	total	A→C	error rate[a] for A→C (×10⁻⁴)
wild-type Klenow	ND[b]	ND		20[c]	17	19
exo⁻ Klenow	118	0	≤0.05	19[c]	17	30
wild-type T4	13	0	≤0.04	32	15	0.6
exo⁻ T4	104	0	≤0.04	47	16	2.7
Tth	50	0	≤0.10	20[c]	20	73
poly γ	162[d]	1[d]	~0.01	20[c]	20	37

[a] The error rate was calculated by multiplying the mutant frequencies from Table 2 by the proportion of mutants containing A→C substitutions, dividing by 0.6 to correct for expression of errors in these *E. coli* cells (Kunkel & Soni, 1988), and dividing by 25, the number of sites at which A→C substitutions can be detected. [b] ND, not determined. [c] Because some mutants contained more than one A→C substitution, the error rate is a minimum estimate. [d] From Kunkel (1985b).

Table 4: Mutagenic Potential of 8-O-dGTP during Replication of Double-Stranded DNA

	plaques				
addition	total	mutant	mutant freq (×10⁻⁴)	sequencing (A·T→C·G per total sequenced)	error rate[a] (×10⁻⁶)
expt 1					
normal dNTPs[b]	47 635	39	8.2	2/78	≤0.9[c]
plus 8-O-dGTP	11 988	28	23	13/27	46
100 × dGTP	45 830	79	17	0/20	≤3.5
expt 2					
normal dNTPs	16 699	27	16[d]	ND[e]	
plus 8-O-dGTP	12 802	74	58	25/59[f]	100

[a] Calculated as described in the footnote to Table 3, but expression of errors upon transfection is 50% (Roberts & Kunkel, 1988) and there are 48 detectable sites for A→C errors, 25 on the plus strand and 23 on the minus strand (Roberts & Kunkel, 1993; and this study). [b] From Thomas *et al.* (1991). [c] This is a "≤" value because it differs by less than 2-fold from the background frequency obtained with unreplicated DNA [see Thomas *et al.* (1991)]. [d] This frequency is from an original plating of transfected cells. Typically when mutant candidates are replated, some are found to be plating artifacts. In addition, a few mutants are sequenced and found to have no change in the gene from position −84 to 170. Thus, this frequency may slightly overestimate the actual α-complementation mutant frequency. [e] ND, not determined. [f] Slightly fewer than half the mutants analyzed from 8-O-dGTP-containing replication reactions contained A·T→C·G substitutions. Of the remaining 48 mutants from experiments 1 and 2, 41 had no change within the sequenced analyzed. These could have had A→C substitutions or other changes downstream in the unsequenced region of the *lacZ* α-complementation gene in the vector.

the rate for A·T → C·G substitutions increases at least 50-fold when 8-O-dGTP is present during replication. When the experiment was performed a second time (Table 4, experiment 2), the estimated error rate with 8-O-dGTP was slightly higher. These A·T → C·G substitution rates with equimolar 8-O-dGTP are much higher than that obtained from a reaction containing no 8-O-dGTP but a 100-fold excess of normal dGTP (1000 μM) over the other three normal dNTPs (10 μM each). This illustrates the substantial mutagenic potential of 8-O-dGTP during replication of double-stranded DNA.

Because oxygen radicals are a natural byproduct of the extensive oxidative phosphorylation that occurs in mitochondria and hence might generate mutagenic nucleotide precursors in this organelle, we also inquired whether 8-O-dGTP was mutagenic with the replicative DNA polymerase for the mitochrondrial genome, DNA polymerase γ. Transfection of the DNA products of reactions performed with and without 8-O-dGTP yielded mutant frequencies of 25 × 10^{-4} and 560 × 10^{-4}, respectively. Sequence analysis of mutants (Table 3) indicates that the A → C substitution error rate for chick embryo pol γ is increased more than 1000-fold for synthesis in the presence of the analog at a concentration equal to that of the normal dNTP. This increase occurs despite the presence of an associated proofreading exonuclease (Kunkel & Soni, 1988) which renders the polymerase highly accurate during DNA synthesis with normal dNTPs.

DISCUSSION

The present study addresses several issues regarding the mutagenic incorporation of 8-O-dGTP. First, the data in Tables 2 and 3 extend earlier studies by Cheng *et al.* (1992) and Maki and Sekiguchi (1992) by demonstrating that this modified nucleotide is primarily misincorporated opposite template adenine by a variety of DNA polymerases. The data provide a quantitative estimate of the average rate of stable misincorporation at 25 detectable template adenines, when 8-O-dGTP is present at a concentration equimolar to the four normal dNTPs. This provides a basis for a future estimation of the mutagenic potential of 8-O-dGTP *in vivo* in relation to the concentration of the normal dNTPs, if indeed 8-O-dGTP is found to be stably present in the dNTP pool.

The different error rates obtained with exonuclease-deficient DNA polymerases (Table 3) illustrate that the analog's mutagenic potential in model polymerization reactions depends on the DNA polymerase catalyzing the reaction. The limited error specificity data described above, *i.e.*, the "hot spots" observed with two different DNA polymerases, also suggest that, as for errors with normal dNTPs [e.g., Joyce *et al.* (1992); for reviews, see Kunkel and Bebenek (1988) and Echols and Goodman (1991)], the rate of misincorporation of 8-O-dGTP depends on the surrounding sequence. Extrapolating to the *in vivo* situation, 8-O-dGTP-dependent mutagenesis may vary depending on where it is misincorporated and on which of the several replicative and repair DNA polymerases utilizes it. The unique signature of 8-O-dGTP-dependent mutagenesis, A·T → C·G transversions, makes this compound an ideal choice for model studies to try to understand how sequence context affects base selectivity and perhaps proofreading activity and to examine fidelity during different phases of replication (Kunkel, 1992). The high rate of A·T → C·G transversions generated in reactions catalyzed by the *Tth* DNA polymerase at 72 °C suggests that this base analog may also be useful for

in vitro mutagenesis of genes using the polymerase chain reaction.

The observation that the rate for A·8-O-dGMP errors is 4.5-fold higher for exonuclease-deficient T4 DNA polymerase than for its proofreading-proficient counterpart (Table 3) is consistent with the possibility that 8-O-dGMP misinserted opposite adenine can be excised by the proofreading exonuclease associated with this polymerase. This possibility is also supported by a recent study (Fowler *et al.*, 1992) suggesting that proofreading by the *E. coli dnaQ* gene product (the 3′ → 5′ exonuclease subunit of DNA polymerase III holoenzyme) reduces the frequency of A·T → C·G transversions in *mutT* strains *in vivo*. Comparison of mutant vs wild-type Klenow polymerase, which has a less active 3′ → 5′ exonuclease than does the T4 DNA polymerase, revealed little difference in error rates (Table 3). Interestingly, Shibutani *et al.* (1991) concluded that misinsertions of dAMP opposite template 8-O-G were not proofread by the 3′ → 5′ exonuclease of *E. coli* DNA polymerase I. Perhaps a difference might be observed if the T4 DNA polymerase were used in their approach. However, the situation in the present study is different from their study in that here the modified nucleotide is the incoming dNTP. It is well-known that DNA polymerases can discriminate to different extents against substitutions involving the same two nucleotides depending on which is the template and which is the incoming triphosphate [for a review, see Kunkel and Bebenek (1988)]. Differential polymerase discrimination at the extension step for the two mispairs or different rates of excision of dAMP vs 8-O-dGMP as terminal nucleotide could result in differential proofreading.

The A·T → C·G transversions generated during replication in HeLa cell extracts containing equimolar concentrations of 8-O-dGTP and the four normal dNTPs (Table 4) suggest that it will be mutagenic in human cells if it is indeed stably generated by oxidative stress *in vivo*. The magnitude of the increase shown in Table 4 should not be overinterpreted, because the extract may contain proteins that process the nucleotide analog before or after incorporation. For example, the human protein with 8-O-dGTPase activity (Mo *et al.*, 1992) is likely to be present in HeLa cell extracts and may degrade the analog. Nonetheless, degradation would lead to an underestimate of the mutagenic potential of 8-O-dGTP, and the analog is clearly highly mutagenic during SV40 origin-dependent replication. In fact, at equimolar concentration, it is much more mutagenic for A·T → C·G transversions than is a 100-fold excess of dGTP. This high degree of mutagenesis occurs despite observations suggesting that mispairs involving undamaged nucleotides are efficiently proofread during replication (Roberts & Kunkel, 1991). It remains to be determined whether A·8-O-dGMP mispairs are proofread during replication in human cells.

The 8-O-dGTP-dependent mutagenesis observed during DNA synthesis catalyzed by eukaryotic DNA polymerase γ is consistent with the possibility that 8-O-dGTP is mutagenic during mitochondrial DNA replication *in vivo*. Again, the high rate of A → C transversions is striking in light of the large contribution to fidelity with normal mispairs provided by the 3′ → 5′ exonuclease activity associated with DNA polymerase γ (Kunkel & Soni, 1988). It is also interesting in light of the substantial oxidative metabolism occurring in mitochondria. Mutagenesis resulting from such metabolism has been suggested to contribute to the degenerative diseases associated with mitochondrial DNA mutations [for a review, see Wallace (1992)]. The present study suggests that one route to mitochondrial mutagenesis may be misincorporation of modified dNTPs. This raises the question of whether enzymes exist to sanitize mitochondrial dNTP pools.

ACKNOWLEDGMENT

We thank Jin-Yao Mo for advice and Dinh Nguyen for assistance in the purification of 8-*O*-dGTP. We also thank Michelle West Frey and Steve Benkovic for their generous gift of T4 DNA polymerases, Roel M. Schaaper for the P1 lysate of *E. coli* strain NR9373, and Jeffrey H. Miller for *E. coli* strain CC104. We are grateful to John W. Drake and Jin-Yao Mo for their careful evaluation of the manuscript.

REFERENCES

Akiyama, M., Maki, H., Sekiguchi, M., & Houiuchi, T. (1989) *Proc. Natl. Acad. Sci. U.S.A. 86*, 3949–3952.

Au, K. G., Clark, S., Miller, J. H., & Modrich, P. (1988) *Proc. Natl. Acad. Sci. U.S.A. 85*, 8877–8881.

Bebenek, K., Joyce, C. M., Fitzgerald, M. P., & Kunkel, T. A. (1990) *J. Biol. Chem. 265*, 13878–13887.

Bechtereva, T. A., Pavlov, Y. I., Kramorov, V. I., Migunova, B., & Kiselev, O. I. (1989) *Nucleic Acids Res. 17*, 10507.

Bessman, M. J., Muzycka, N., Goodman, M. F., & Schaar, R. L. (1974) *J. Mol. Biol. 88*, 409–421.

Bhatnagar, S. K., & Bessman, M. (1988) *J. Biol. Chem. 263*, 8953–8957.

Cheng, K. C., Cahill, D. S., Kasai, H., Nishimura, S., & Loeb, L. A. (1992) *J. Biol. Chem. 267*, 166–172.

Derbyshire, V., Freemont, P. S., Sanderson, M. R., Beese, L., Friedman, J. M., Joyce, C. M., & Steitz, T. A. (1988) *Science 240*, 199–201.

Drake, J. W., & Greening, E. O. (1970) *Proc. Natl. Acad. Sci. U.S.A. 66*, 823–829.

Echols, H., & Goodman, M. F. (1991) *Annu. Rev. Biochem. 60*, 477–511.

Eger, B. T., & Benkovic, S. J. (1992) *Biochemistry 31*, 9227–9236.

Fowler, R. G., Amutan, M. V., & Isbell, R. J. (1992) *Mutat. Res. 284*, 307–319.

Freese, E. (1959) *J. Mol. Biol. 1*, 87–105.

Hurwitz, J., Dean, F. B., Kwong, A. D., & Lee, S.-H. (1990) *J. Biol. Chem. 265*, 18043–18046.

Joyce, C. M., Sun, X. C. S., & Grindley, N. D. F. (1992) *J. Biol. Chem. 267*, 24485–24500.

Kasai, H., & Nishimura, S. (1984) *Nucleic Acids Res. 12*, 2137–2145.

Kasai, H. & Nishimura, S. (1991) in *Oxidative Stress: Oxidants and Antioxidants* (Sies, H., Ed.) pp 99–116, Academic Press, London.

Kelly, T. J. (1988) *J. Biol. Chem. 263*, 17889–17892.

Kouchhakdjian, M., Bodepuri, V., Shibutani, S., Eisenberg, M., Johnson, F., Grollman, A. P., & Patel, D. J. (1991) *Biochemistry 30*, 1403–1412.

Kunkel, T. A. (1985a) *J. Biol. Chem. 260*, 5787–5796.

Kunkel, T. A. (1985b) *J. Biol. Chem. 260*, 12866–12874.

Kunkel, T. A. (1992) *BioEssays 14*, 303–308.

Kunkel, T. A., & Bebenek, K. (1988) *Biochim. Biophys. Acta 951*, 1–15.

Kunkel, T. A., & Soni, A. (1988) *J. Biol. Chem. 263*, 4450–4459.

Li, J. J., & Kelly, T. J. (1985) *Mol. Cell. Biol. 5*, 1238–1246.

Maki, H., & Sekiguchi, M. (1992) *Nature 355*, 273–275.

Michaels, M. L., & Miller, J. H. (1992) *J. Bacteriol. 174*, 6321–6325.

Michaels, M. L., Cruz, A. P., Grollman, A. P., & Miller, J. H. (1992a) *Proc. Natl. Acad. Sci. U.S.A. 89*, 7022–7025.

Michaels, M. L., Tchou, J., Grollman, A. P., & Miller, J. H. (1992b) *Biochemistry 31*, 10964–10968.

Mo, J.-Y., Maki, H., & Sekiguchi, M. (1992) *Proc. Natl. Acad. Sci. U.S.A. 89*, 11021–11025.
Moriya, M. (1993) *Proc. Natl. Acad. Sci. U.S.A. 90*, 1122–1126.
Moriya, M., & Grollman, A. P. (1993) *MGG Mol. Gen. Genet. 239*, 72–76.
Moriya, M., Ou, C., Bodepudi, V., Johnson, F., Takeshita, M., & Grollman, A. P. (1991) *Mutat. Res. 254*, 281–288.
Pavlov, Y. I., Noskov, V. N., Lange, E. K., Moiseeva, E. V., Pshenichnov, M. R., & Khromov-Borisov, N. N. (1991) *Mutat. Res. 253*, 33–46.
Roberts, J. D., & Kunkel, T. A. (1988) *Proc. Natl. Acad. Sci. U.S.A. 85*, 7064–7068.
Roberts, J. D., & Kunkel, T. A. (1993) in *Methods in Molecular Genetics* (Adolph, K. W., Ed.) Vol. 2, pp 295–313, Academic Press, Orlando, FL.
Sakumi, K., Furuichi, M., Tsuzuki, T., Kakuma, T., Kawabata, S., Maki, H., & Sekiguchi, M. (1993) *J. Biol. Chem. 268*, 23524–23530.
Schaaper, R. M., & Dunn, R. L. (1987) *J. Biol. Chem. 262*, 16267–16270.
Shibutani, S., Takeshita, M., & Grollman, A. P. (1991) *Nature 349*, 431–434.
Stillman, B. (1989) *Annu. Rev. Cell Biol. 5*, 197–245.
Tchou, J., Kasai, H., Shibutani, S., Chung, M.-P., Laval, J., Grollman, A. P., & Nishimura, S. (1991) *Proc. Natl. Acad. Sci. U.S.A. 88*, 4690–4694.
Thomas, D. C., Roberts, J. D., Sabatino, R. D., Myers, T. W., Downey, K. M., So, A. G., Bambara, R. A., & Kunkel, T. A. (1991) *Biochemistry 30*, 11751–11759.
Wallace, D. (1992) *Science 256*, 628–632.
West Frey, M., Nossal, N. G., Capson, T. L., & Benkovic, S. J. (1993) *Proc. Natl. Acad. Sci. U.S.A. 90*, 2579–2583.
Wood, M. L., Dizdaroglu, M., Gajewski, E., & Essigmann, J. M. (1990) *Biochemistry 29*, 7024–7032.
Yanofsky, C., Cox, C., & Horn, V. (1966) *Proc. Natl. Acad. Sci. U.S.A. 53*, 274–281.

Selective Inhibition of Mammalian Lanosterol 14α-Demethylase by RS-21607 in Vitro and in Vivo

David C. Swinney,*,‡ On-Yee So,‡ David M. Watson,‡ Pamela W. Berry,‡ Austin S. Webb,‡ Denis J. Kertesz,§ Emma J. Shelton,§ Pamela M. Burton,‖ and Keith A. M. Walker§

Syntex Discovery Research, S3-1, 3401 Hillview Avenue, Palo Alto, California 94304

Received December 28, 1993⊛

ABSTRACT: The discovery of selective lanosterol 14α-demethylase inhibitors may lead to novel hypolipidemic drugs. RS-21607, (2*S*,4*S*)-*cis*-2[(1*H*-imidazol-1-yl)methyl]-2-[2-(4-chlorophenyl)ethyl]-4-[[(4-aminophenyl)thio]methyl]-1,3-dioxolane, was characterized as a tight-binding, competitive inhibitor of lanosterol 14α-demethylase purified from rat liver. The apparent K_i was determined to be 840 pM and found to be similar in hepatic microsomes from human, rat, and hamster. RS-21607, which contains two chiral centers, was a more effective lanosterol 14α-demethylase inhibitor than its three stereoisomers. In vitro, RS-21607 had a greater affinity for lanosterol 14α-demethylase than the other cytochromes P450 evaluated: CYP7, CYP27, CYP11A1, CYP19, CYP17, CYP11B1, CYP21, CYP3A4, CYP4A, CYP2D6, CYP1A2, CYP2C9, and 27-hydroxycholesterol 7α-hydroxylase. The other stereoisomers were not as selective as RS-21607. Doses of 3–30 mg/kg RS-21607 given orally to hamsters caused a dose-dependent decrease in cholesterol biosynthesis with a corresponding accumulation of 24,25-dihydrolanosterol. RS-21607 inhibited the enzyme and cholesterol biosynthesis in hamster liver by 50% at 18 h following a 30 mg/kg oral dose. This was interpreted to indicate that RS-21607 is able to distribute to the site of action in hamsters and inhibit the target enzyme. In the same dose range, the plasma concentrations of testosterone, corticosterone, and progesterone, the endpoints for the cytochromes P450 involved in steroid biosynthesis, were relatively unaffected. These data show RS-21607 to be an effective and selective inhibitor of lanosterol 14α-demethylase, both in vivo and in vitro. RS-21607 interacted with the purified enzyme to produce a type II binding spectrum, consistent with an interaction between the imidazole moiety and the heme. The electrostatic contribution of the imidazole binding was investigated using the desimidazole analog of RS-21607. The apparent K_i for the desimidazole compound (65 μM) was similar to the apparent K_m for the substrate DHL (79 μM). Together, these data confirm that the ligand attached to the imidazole in RS-21607 is a good non-sterol substitute for DHL, i.e., binding to the enzyme with similar affinity, and that the coordination of the imidazole to the heme provides a major electrostatic contribution for the inhibition of lanosterol 14α-demethylase by RS-21607. RS-21607 was also observed to increase the accumulation of 3β-hydroxy-24,25-dihydrolanost-8-en-32-al, the second intermediate in the multistep oxidation, but not the first intermediate, 24,25-dihydrolanost-8-ene-3β,32-diol. The accumulation of this regulatory oxysterol indicates that RS-21607 inhibits both the first and third steps in the multistep reaction sequence.

Elevated serum cholesterol is implicated in many cardiovascular diseases including atherosclerosis (Anderson et al., 1987). Therapies which reduce serum cholesterol have been shown to reduce the incidence of the disease (Lipid Research Clinics Program, 1984). Blocking the synthesis of cholesterol with HMG-CoA reductase inhibitors has proven to be effective in lowering serum cholesterol (Endo, 1985; Wangworth & Bacon, 1987). There are numerous other enzymatic reactions of cholesterol biosynthesis which have the potential to be therapeutic targets. One such enzyme is lanosterol 14α-demethylase (LDM)[1] which catalyzes the first modification of the sterol nucleus in mammals and yeast. Demethylation of lanosterol by LDM occurs via three successive oxidations at the C-32 methyl group resulting in loss of formic acid and formation of 4,4-dimethyl-5α-cholesta-8,14,24-trien-3β-ol (Figure 1)[2] (Yoshida & Aoyama, 1984; Aoyama et al., 1984; Trzaskos et al., 1986a). Inhibition of any of these three oxidation steps should result in a block of cholesterol biosynthesis.

Many antifungal azole compounds including ketoconazole, clotrimazole, fluconazole, and miconazole have been found to interact with fungal LDM (Vanden Bossche, 1988). It has been determined that these compounds cause fungal cell death by blocking the biosynthesis of ergosterol at the lanosterol 14α-demethylation step. Upon the approval of the orally active antifungal agent ketoconazole, the interaction with lanosterol 14α-demethylase in humans could be investigated. Keto-

* To whom correspondence should be addressed.
‡ Department of Drug Metabolism.
§ Institute of Organic Chemistry.
‖ Institute of Biochemistry and Cell Biology.
⊛ Abstract published in *Advance ACS Abstracts,* April 1, 1994.

[1] Abbreviations: LDM, lanosterol 14α-demethylase; DHL, 24,25-dihydrolanosterol; 8,14-diene, 4,4-dimethyl-5α-cholesta-8,14-dien-3β-ol; 32-alcohol, 24,25-dihydrolanost-8-ene-3β,32-diol; 32-aldehyde, 3β-hydroxy-24,25-dihydrolanost-8-en-32-al; RS-21607, (2*S*,4*S*)-*cis*-2-[(1*H*-imidazol-1-yl)methyl]-2-[2-(4-chlorophenyl)ethyl]-4-[[(4-aminophenyl)-thio]methyl]-1,3-dioxolane; desimidazole or *trans*-2*R*,4*S*-DI, (2*R*,4*S*)-*trans*-[2-(4-chlorophenyl)ethyl]-2-methyl-4-[[(4-aminophenyl)thio]methyl]-1,3-dioxolane; *cis*-2*S*,4*S*-DI, (2*S*,4*S*)-*cis*-[2-(4-chlorophenyl)ethyl]-2-methyl-4-[[(4-aminophenyl)thio]methyl]-1,3-dioxolane; DTT, dithiothreitol; EDTA, ethylenediaminetetraacetic acid; BHT, butylated hydroxytoluene; ^{T}V = tritium isotope effect upon V_{max}; $^{T}(V/K)$ = tritium isotope effect upon V_{max}/K_m.

[2] Dihydrolanosterol is used instead of lanosterol as the enzyme substrate in this study because it is similar to lanosterol in enzyme activity (Trzaskos et al., 1986b) and dihydrolanosterol, not lanosterol, primarily accumulates after RS-21607 treatment to hamsters. The accumulation of DHL is thought to result from the shunting of lanosterol to the side-chain reductase pathway when oxidation by LDM is blocked.

0006-2960/94/0433-4702$04.50/0

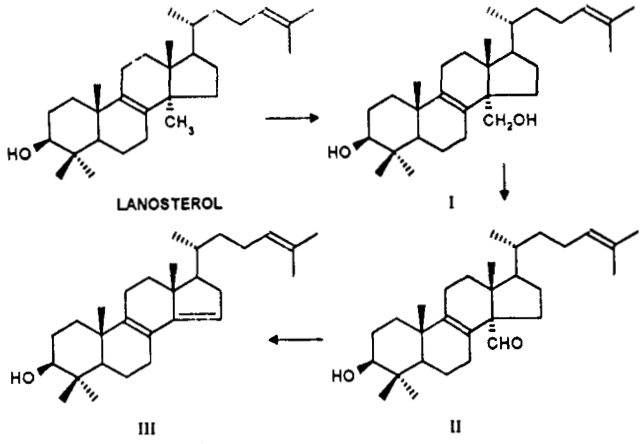

FIGURE 1: Mechanism of lanosterol demethylation.

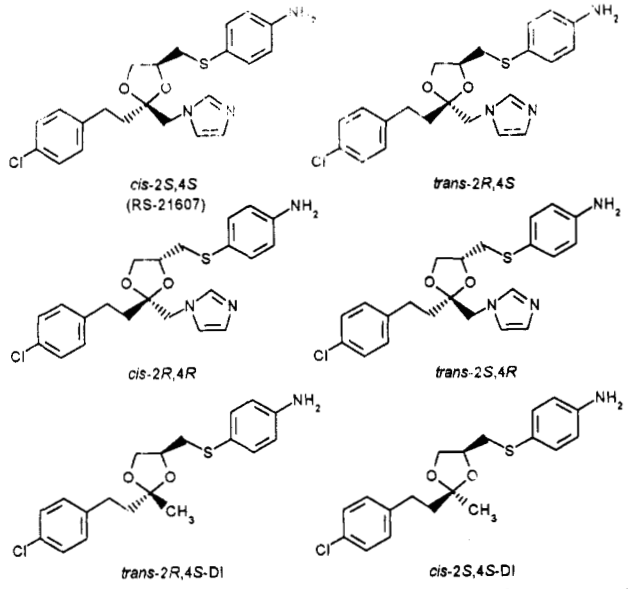

FIGURE 2: Structures of the stereoisomers of RS-21607 and desimidazoles.

conazole has been shown to reduce serum total cholesterol by approximately 30% in humans, with a corresponding increase in serum lanosterol concentrations (Kraemer & Pont, 1986; Miettinen, 1988; Gylling et al., 1991). However, ketoconazole is a relatively nonspecific cytochrome P450 inhibitor in that at therapeutic doses it interferes with the synthesis of adrenal steroid hormones and testosterone (Feldman, 1986).

We report here the details of the interactions of another azole, RS-21607, and its three stereoisomers (Figure 2) with mammalian lanosterol 14α-demethylase. The results obtained show the 2*S*,4*S*-diastereomer, RS-21607, to be a potent and selective non-steroidal inhibitor of mammalian lanosterol 14α-demethylase. This compound has also been found to effectively lower cholesterol in hamster (Walker et al., 1993) and man (Dr. K. Schwartz, personal communication).

MATERIALS AND METHODS

Materials. RS-21607 and its stereoisomers were prepared as previously described (Walker et al., 1993) as were [32-$^3H_3$]DHL, the 8,14-diene (DeKeczer et al., 1993), the 32-alcohol (Takano & Morisaki, 1991), and nafimidone (Walker et al., 1980; Rush et al., 1987). The radiochemicals with the exception of [24,25-$^3H_2$]DHL and [7β-^{3}H]-7α-hydroxycholesterol were purchased from New England Nuclear (Boston, MA). [16,22-^{3}H]-27-Hydroxycholesterol was prepared from krypotogenin by the method of Scheer et al. (1956). Steroids and sterols were purchased from Steraloids (Wilton, NH) or Research Plus (Bayonne, NJ). Debrisoquine and 4-hydroxydebrisoquine were obtained from Biomol (Plymouth. Meeting, PA), and 1-heptanesulfonic acid sodium salt, 1-hydrate was obtained from Eastman Kodak (Rochester, NY). All other chemicals were obtained from Aldrich Chemical Co. (Milwaukee, WI) and Sigma Chemical Co. (St. Louis, MO). RIA kits for progesterone and testosterone were supplied by Diagnostic Products Corporation (Los Angeles, CA), and the kits for corticosterone were purchased from ICN Biomedicals, Inc. (Costa Mesa, CA).

Enzyme Source. Tissues were minced with a Brinkman polytron and then homogenized in 3–5 mL/g of tissue of 50 mM Tris buffer (0.25 M sucrose, 1.15% KCl, pH 7.5, at 4 °C). The homogenate was centrifuged at 1000*g* for 10 min at 5–10 °C. The pellet was discarded, and the supernatant was centrifuged at 9000*g* for 20 min at 5–10 °C. The resulting mitochondrial pellet was resuspended in at least 10 pellet volumes of homogenizing buffer and recentrifuged at 9000*g* for 10 min. The final mitochondrial pellet was suspended in one to two pellet volumes of 0.25 M sucrose and stored at −80 °C. Microsomes were prepared from the initial 9000*g* supernatant which was centrifuged at 100000*g* for 80 min. The resulting microsomal pellet was washed by suspension in 10 mM EDTA (pH 7.4, 1.15% KCl) and recentrifugation at 100000*g* for 80 min. The final microsomal pellet was suspended and stored as described for mitochondria. Samples stored at −80 °C retained catalytic activity for up to 3 years. When microsomes were prepared without concurrent mitochondria preparation, the 0.25 M sucrose was omitted from the homogenization buffer.

NADPH–cytochrome P450 reductase was purified from phenobarbital-treated rats to a specific activity of >65 000 units/mg of protein by a combination of the methods of Dignam and Strobel (1975) and Yasukochi and Masters (1976). One unit of reductase catalyzes the reduction of 1 nmol of cytochrome *c*/min at 22 °C in 0.3 M potassium phosphate buffer (pH 7.7) containing 0.1 mM EDTA and 0.1 mM NADPH. Cytochrome b_5 was purified from rat liver microsomes by the method of Spatz and Strittmatter (1971) to a specific activity of 19.8 nmol/mg of protein.

Purification of Lanosterol 14α-Demethylase. LDM was purified from the livers of cholestyramine-treated rats by a modification of the procedures of Trzaskos et al. (1986a). Male rats (strain Crl:CD-BR VAF+, Charles River Labs, Wilmington, DE, 200 g) on a reverse-light cycle were treated with 4% cholestyramine resin in the diet for 1 week and livers removed at the middle of the dark cycle. Approximately 6.5 g of microsomal protein was diluted to 4 mg/mL with PEDG buffer (100 mM potassium phosphate, pH 7.4, 0.1 mM EDTA, 0.1 mM DTT, 20% glycerol) containing 0.6% sodium cholate (w/v) and stirred for 2 h. The supernatant isolated by centrifugation (105000*g* for 1 h) was treated with 50% polyethyleneglycol to a final percentage of 16%. The pellet was isolated (0–16% PEG) and dissolved in PEDG, pH 7.25, containing 0.6% sodium cholate. This was applied to four *n*-octylamine columns (2.6 cm × 30 cm) (Sigma Co., St. Louis). Each column was previously equilibrated with 300 mL of PEDG, pH 7.25, containing 0.6% sodium cholate and washed with 340 mL of the equilibration buffer. The protein eluted with PEDG, pH 7.25, containing 0.2% Triton N-101. The pooled *n*-octylamine fractions were concentrated against an Amicon YM-30 membrane to a final volume of 100 mL. This was dialyzed overnight against 4 L of 5 mM PEDGT,

pH 7.8, diluted to 260 mL with a solution of 0.1 mM EDTA, 0.1 mM DTT, 20% glycerol, and 0.2% Triton N-101, and applied to a DEAE Sephacel column (2.6 × 25 cm) (Pharmacia, Uppsala, Sweden) previously equilibrated with 250 mL of 5 mM PEDGT, pH 7.8. The column was washed with 100 mL of 5 mM PEDGT, pH 7.8, followed by 200 mL of 10 mM PEDGT, pH 7.8. The column was eluted with a 600-mL linear gradient of 10 mM PEDGT to 100 mM PEDGT, both pH 7.8. Fractions containing lanosterol demethylase activity were pooled and dialyzed against 10 mM PEDGT, pH 6.8, overnight. These fractions (approximately 200 mL) were applied to an S-Sepharose fast flow column (1.5 cm × 7 cm) (Pharmacia, Uppsala, Sweden) previously equilibrated with the same buffer. The column was washed with 50 mL of equilibration buffer and eluted with a 300-mL linear gradient from 0 to 0.2 M KCl in equilibration buffer. Fractions showing a single band on 7.5% SDS-PAGE gel and having lanosterol demethylase activity were pooled, concentrated with an Amicon centricon-10 concentrator, and dialyzed against 50 mM PEDG, pH 7.4. Triton N-101 was removed using a course Sephadex G-25 gel filtration column (1.5 × 10 cm) (Pharmacia, Uppsala, Sweden). The column was equilibrated with 200 mL of 50 mM PEDG, pH 7.4, and the concentrated protein was loaded on to the column and eluted with the same buffer. The fractions absorbing at 280 nm were pooled and concentrated with an Amicon centricon-10 concentrator.

Enzymatic Activities. Unless stated otherwise, inhibitors and substrates were added in methanol to a final concentration of methanol of not greater than 2%. Control incubations not containing inhibitor contained 2% methanol. Final incubation volumes were 1 mL, and all reactions were carried out at 37 °C.

Lanosterol 14α-Demethylase. Microsomal activity was determined in 30-min incubations containing potassium phosphate buffer (0.2 M, pH 7.0), dithiothreitol (0.3 mM), EDTA (0.1 mM), magnesium chloride (3 mM), glucose-6-phosphate (5 mM), glucose-6-phosphate dehydrogenase (1 unit), NADPH (1 mM), microsomal protein (1 mg/mL, unless otherwise stated), and [32-$^3H_3$]DHL (40 μM, unless otherwise stated). Both tritium-labeled and unlabeled DHL were purified by HPLC prior to use. Substrate was added in tyloxapol (1:75 w/w ratio) as described by Trzaskos et al. (1986a). The incubations were terminated using 250 μL of a 40% trichloroacetic acid solution. The activity was determined from the radioactivity not retained on activated 1-mL C-18 Bond-Elut extraction columns (Varian, Harbor City, CA). The columns were activated with methanol (1 × 1 mL) followed by deionized water (2 × 1 mL). In incubations using [24,25-$^3H_2$]DHL as substrate, AY-9944 (50 μM) and potassium cyanide (5 mM) were included to inhibit the further metabolism of 4,4-dimethyl-5α-cholesta-8,14-dien-3β-ol to cholesterol. These reactions were stopped with 1 mL of 15% potassium hydroxide in 95% methanol and the mixtures heated at 60 °C for 30 min and extracted with petroleum ether. The product of the reaction, 4,4-dimethyl-5α-cholesta-8,14-dien-3β-ol, was separated from substrate with a Jones analytical 5-μm Apex ODS column (4.6 cm × 25 cm), eluted with a 45/45/10 mixture of isopropyl alcohol/acetonitrile/water isocratically at a flow rate of 1 mL/min (Trzaskos et al., 1984), and quantitated by radiochemical detection. The product eluted at 17 min and substrate at 21.5 min. The products of the studies investigating the accumulation of 32-oxylanosterols were separated isocratically at 1 mL/min with a 65/10/25 mixture of isopropyl alcohol/acetonitrile/water. The 32-alcohol eluted at 15 min, the 32-aldehyde at 17 min, the diene at 33 min, and DHL at 40 min. Experiments with reconstituted enzyme used 10 000 units/mL cytochrome P450 reductase. Additional lipid was omitted as dilauroylphosphatidylcholine did not stimulate catalytic activity (1–20 μg/mL).

CYP7—Cholesterol 7α-Hydroxylase. Incubations containing hepatic microsomes from cholestyramine-treated rats (2 mg/mL protein; 0.14 μmol of endogenous cholesterol substrate), magnesium chloride (3 mM), EDTA (0.1 mM), cysteamine hydrochloride (20 mM), and potassium phosphate buffer, pH 7.4 (0.1 M), were agitated for 10 min following addition of NADPH (1 mM). Inhibitors were added to the incubation tubes, and solvent was evaporated prior to addition of the other components. After the 10-min incubation period, the NADPH-dependent reactions were stopped by the addition of sodium cholate (5 mg) to solubilize the membranes and products were converted to their respective 4-cholesten-3-ones by the addition of cholesterol oxidase (0.23 unit dissolved in 100 μL of 10 mM potassium phosphate buffer containing 20% glycerol and 1 mM dithiothreitol) and agitation for 20 min. All reactions were terminated by addition of 1 mL of methanol followed by 5 mL of petroleum ether. The extracts were analyzed using HPLC and the products detected at 240 nm. Separation of products was achieved with two 5-μm, 25-cm silica columns (Dupont Zorbax Sil or Beckman Ultrasphere Sil) preceded by a silica-packed 3-cm guard column. The columns were eluted with hexane/isopropyl alcohol at 1 mL/min under the following conditions: 12 min isocratic at 95/5; 5 min with a linear gradient to 70/30; and 23 min isocratic at 70/30. 7α-Hydroxy-4-cholesten-3-one eluted at 26 min.

27-Hydroxycholesterol 7α-Hydroxylase. Incubations containing hepatic microsomes from male hamsters (0.1 mg/mL protein), [16,22-$^3H_2$]-27-hydroxycholesterol, NADPH (2 mM), magnesium chloride (3 mM), calcium chloride (2 mM), EDTA (0.1 mM), and potassium phosphate buffer, pH 7.4 (100 mM), were agitated for 10 min. The reactions were stopped by the addition of 7.5 mL of acetone (containing 0.02% BHT). Following separation and evaporation, the residues were dissolved in acetonitrile:isopropyl alcohol (50:50, containing 0.02% BHT, 200 μL), sonicated for 5 min, filtered through 4.5-μm filters (Gelman Acrodisc 3CR), and analyzed by HPLC (75-μL injection volume). Separation of products was achieved on a 5-μm, 25-cm C-18 column (Jones Apex or Partisil-ODS 3) preceded by a Newguard C18 guard column. The column was eluted at 1 mL/min with acetonitrile/isopropyl alcohol/water under the following conditions: 2 min isocratic at 32.5/24/43.5; 10 min with a linear gradient to 48/32/20; 15 min isocratic at 48/32/20; 5 min with a linear gradient to 9/90/1; and 15 min isocratic at 9/90/1. 7α,27-Dihydroxycholesterol eluted at 16 min and 27-hydroxycholesterol at 25 min. The kinetic constants associated with product formation were V_{max}, 260 pmol/min/mg, and K_m, 8.9 μM.

CYP27—Cholesterol 27-Hydroxylase. Incubations contained hepatic mitochondria from hamster (2 mg/mL protein), [^{3}H]cholesterol in tyloxapol (1:75 w/w ratio) (diluted by endogenous cholesterol), NADPH (2 mM), glucose-6-phosphate (5 mM), glucose-6-phosphate dehydrogenase (1 unit/mL), magnesium chloride (3 mM), calcium chloride (2 mM), EDTA (1 mM), nafimidone (25 μM), and potassium phosphate buffer, pH 7.4 (100 mM). Following a 1-h incubation, the reaction products were processed and analyzed as described for 27-hydroxycholesterol 7α-hydroxylase.

CYP11A1—Cholesterol Side-Chain Cleavage. [26-^{3}H]-Cholesterol in tyloxapol (1:75 w/w ratio) was incubated with bovine adrenal cortex mitochondria (1 mg/mL), bovine adrenal cytosol (1 mg/mL), bovine serum albumen (0.25 mg/mL), potassium phosphate, pH 7.4 (20 mM), calcium chloride (0.5 mM), magnesium chloride (4 mM), EDTA (0.5 mM), glucose-6-phosphate dehydrogenase (2 units/mL), glucose-6-phosphate (5 mL), and NADPH (1.0 mM) for 1 h. The reactions were quenched with 2 mL of methanol and the products applied to 3-mL C-18 Bond Elut extraction columns previously activated with methanol (3 mL) and water (2 × 3 mL). The amount of [^{14}C]isocaproic acid formed was determined from the radioactivity in the aqueous eluent.

CYP19—Aromatase. The microsomal incubations contained potassium phosphate buffer (pH 7.4, 5 mM), dithiothreitol (0.3 mM), microsomal protein from human placenta (0.1 mg), [1β,2β-^{3}H$_2$]androstenedione, and NADPH (0.01 M). Following incubation for 10 min, the reactions were terminated with 25 μL of 40% trichloroacetic acid. The activity was determined from the radioactivity not retained on activated 1-mL C-18 Bond-Elut extraction columns as described for the DHL assay. The apparent K_m for product formation was 9 nM, and the V_{max} was approximately 200 pmol/min/mg of protein.

CYP17—Progesterone 17α/20-Lyase. Reaction mixtures with microsomes from the testes of neonatal pigs contained protein (0.025 mg/mL), NADPH (1 mM), magnesium chloride (3 mM), potassium phosphate buffer, pH 7.25 (100 mM), and 17α-hydroxyprogesterone. All reactions were terminated after 10 min by addition of 6 mL of methylene chloride followed immediately by 1 nmol of internal standard (11β-hydroxytestosterone in 50 μL of methanol). The residues from the organic phase were dissolved in 200 μL of methanol, sonicated, and analyzed by HPLC. Separation of substrate (17α-hydroxyprogesterone), product (androstenedione), and internal standard was achieved with a Jones chromatography 5-μm, 25-cm ODS column. The column was eluted isocratically with a 42/20/38 ratio of methanol/acetonitrile/water. The internal standard, detected at 254 nm, eluted with a retention time of 6.6 min, androstenedione at 10.7 min, and 17α-hydroxyprogesterone at 12.9 min. The apparent K_m was observed to be 4 μM and V_{max} 2.1 nmol/min/mg.

Progesterone Hydroxylase—CYP21 and CYP3A4. The progesterone assay was conducted as previously reported (Swinney, 1990). Briefly, mixtures containing either bovine adrenal microsomes (0.1 mg/mL) for determining activity associated with CYP21 or microsomes from human liver (1 mg/mL) for determining activity associated with CYP3A4, NADPH (1 mM), magnesium chloride (3 mM), potassium phosphate buffer, pH 7.4 for human liver and pH 7.25 for bovine adrenal (50 mM), and progesterone were incubated for 10 min. All reactions were terminated by addition of 6 mL of methylene chloride followed immediately by 1 nmol of internal standard (11β-hydroxytestosterone in 50 μL of methanol). The residues from the organic phase were dissolved in 200 μL of methanol, sonicated, and analyzed by HPLC. Separation was achieved with a Jones chromatography 5-μm, 25-cm ODS column at a flow rate of 2 mL/min. The column was eluted with tetrahydrofuran/methanol/acetonitrile/water under the following conditions: 3 min isocratic at 4/5/6/85; 25 min with a 0.5 convex gradient to 8/13/11/68; 10 min with linear gradient to 11/17/14.5/57.5; and a 5-min ramp to 4/3/3/90. Products detected at 254 nm had the following retention times: internal standard, 18 min; 16α-hydroxyprogesterone, 21 min; 6β-hydroxyprogesterone, 31 min; 21-hydroxyprogesterone, 35 min; and progesterone, 45 min. The kinetic constants associated with human hepatic 6β-hydroxyprogesterone formation were V_{max}, 714 pmol/min/mg, and K_m, 171 μM, and those with human hepatic 16α-hydroxyprogesterone formation were V_{max}, 125 pmol/min/mg, and K_m, 132 μM.

CYP11B1—11β-Hydroxylase. Incubations with bovine adrenal mitochondria containing protein (0.05 mg/mL), NADPH (1 mM), magnesium chloride (3 mM), potassium phosphate buffer, pH 7.4 (100 mM), and deoxycorticosterone were agitated for 10 min. Mitochondria were sonicated 5 min on ice before addition to the incubation mixture. The workup and analysis of the reaction mixture were the same as those for progesterone hydroxylations. The retention time for the product, corticosterone, was 22 min, and the kinetic constants associated with its formation were V_{max}, 2 nmol/min/mg, and K_m, 0.4 μM.

CYP1A2. The 3-demethylation of caffeine associated with CYP1A2 was determined in reaction mixtures (200-μL final volume) containing hepatic microsomes from human (0.4 mg), potassium phosphate buffer (50 mM, pH 8.0), magnesium chloride (2 mM), potassium chloride (0.23%), glucose-6-phosphate (5 mM), NADPH (10 mM), glucose-6-phosphate dehydrogenase (2 units/mL), and [^{14}C]caffeine, and they were incubated for 120 min at 37 °C. The reactions were stopped by the addition of 200 μL of pH 3.0 buffer containing 80 mM phosphoric acid and 5 mM heptanesulfonic acid. Following centrifugation, the supernatants were injected directly into the HPLC system and eluted isocratically with 80 mM phosphoric acid, 5 mM heptane sulfonic acid, pH 3.0, and 1% tetrahydrofuran at a flow rate of 1.5 mL/min. Radiolabeled product, paraxanthine, eluted at 9.2 min and caffeine at 18.5 min. The apparent K_m associated with the 3-demethylation was 184 μM and the V_{max} 4.6 pmol/min/mg of protein.

CYP2D6. The 4-hydroxylation of debrisoquine associated with CYP2D6 was determined in reaction mixtures (200-μL final volume) containing hepatic microsomes from human (0.5 mg), potassium phosphate buffer (50 mM, pH 8.0), magnesium chloride (3 mM), EDTA (0.5 mM), dithiothreitol (0.5 mM), debrisoquine, and NADPH (10 mM). The samples were incubated for 30 min and the reactions stopped by the addition of methanol (500 μL). The eluates from activated C-18 Bond Elut were evaporated, reconstituted in HPLC buffer, injected on to the HPLC system, and eluted isocratically with 13% acetonitrile in 80 mM phosphoric acid and 5 mM heptanesulfonic acid, pH 3.0, at a flow rate of 2 mL/min. 4-Hydroxydebrisoquine (retention time 5.5 min) was detected at 210 nm and quantitated with external standards. The apparent K_m was observed to be 82 μM and the V_{max} 57 pmol/min/mg of protein.

CYP4A1. Lauric acid 12-hydroxylation was measured as previously reported (Swinney et al., 1991). Briefly, reactions contained microsomal protein (0.1 mg) from clofibrate-treated rats (400 mg/kg in corn oil, ip, once daily for 3 days), potassium phosphate buffer (50 mM, pH 7.4), magnesium chloride (3 mM), EDTA (0.5 mM), NADPH (1 mM), and [^{14}C]lauric acid. The 10-min incubations were terminated and samples prepared as for the progesterone assay (without internal standard). Radiochemical detection following HPLC separation on a 5-μm, 25-cm C-18 column eluted at 1 mL/min with 1% acetic acid and acetonitrile (38% acetonitrile for 14 min, increased to 90% over the next 8 min and then held constant) showed 12-hydroxylauric acid eluting at 15 min and lauric acid at 31 min. The apparent K_m for the reaction was 4.2 μM and the V_{max} 7.6 nmol/min/mg of protein.

CYP2C9. The incubations contained potassium phosphate buffer (100 mM, pH 7.4), magnesium chloride (6 mM), EDTA (0.05 mM), glucose-6-phosphate (10 mM), NADPH (1 mM), and 0.4 unit of glucose-6-phosphate dehydrogenase, tolbutamide, and hepatic microsomes from human (1 mg/mL) in a final volume of 200 μL. After 120 min, the reactions were stopped by the addition of an equal volume of 80 mM phosphoric acid and 5 mM heptanesulfonic acid, pH 3.0, and 1 nmol of the internal standard, chlorpropamide, was added. The samples were injected directly on to the HPLC system following the separation of protein by centrifugation and eluted isocratically with 20% acetonitrile in 80 mM phosphoric acid and 5 mM heptanesulfonic acid, pH 3.0. The flow rate was maintained at 1 mL/min and monitored at a wavelength of 230 nm. Retention times for 4-hydroxybutamide, chlorpropamide, and tolbutamide were 7.0, 23.0, and 36.3 min, respectively. The apparent K_m was observed to be 246 μM, and the V_{max} was 126 pmol/min/mg of protein.

General Methods. Protein concentration was determined by the method of Lowery et al. (1951). Cytochrome P450 determinations were by the method of Omura and Sato (1964) in potassium phosphate (10 mM), DTT (0.1 mM), EDTA (0.1 mM), glycerol (20%), emulgen 911 (0.2%), and sodium cholate (0.5%).

Determination of Kinetic Constants. Tight-binding inhibition kinetics were evaluated with the linear equations described by Henderson (1972). The apparent K_i values associated with inhibition of the various cytochromes P450 were determined by Dixon analysis and/or Lineweaver–Burk analysis or from an extrapolation of IC_{50} data by Dixon analysis (cholesterol 7α-hydroxylase, CYP7). The need for the extrapolation was due to the fact that substrate concentrations (cholesterol) could not be adequately varied as a result of the high endogenous concentrations. For a Dixon plot, $1/v$ versus [I] gives an x-intercept of $-K_i([S]/K_m + 1)$. Via a substrate concentration determined from total microsomal cholesterol concentration and a K_m value determined from partially purified cholesterol 7α-hydroxylase (36 μM), the apparent K_i values were determined. Analysis of data only in the log linear portion of the IC_{50} determinations was used to calculate apparent K_i values by the method of Dixon (10–90% control activity). All K_i values associated with LDM activity were determined from a plot of K/V (determined from a $1/v$ versus $1/[S]$ plot) versus $[I](V_o/K_o)$. The r^2 values of the line (four to seven points) were always greater than 0.96. Standard deviations were calculated from multiple ($n \geq 3$) determinations.

In Vivo Assays. Hepatic dihydrolanosterol accumulation and cholesterol depletion were determined in male Syrian hamsters (LAK:LVG(SYR)VAF+, 90–110 g, Charles River Labs, MA). Groups of five to seven animals were administered the dihydrochloride salt of RS-21607 dissolved in water or water (vehicle) orally by gavage. At 90 min prior to sampling, the hamsters received an ip dose of approximately 10 μCi of [^{14}C]mevalonate in 0.5 mL of isotonic saline. At sampling time, livers were removed, rinsed in saline, blotted, weighed, minced, and immersed in 40 mL of acetone containing 0.5 μCi of [32-^{3}H$_3$]dihydrolanosterol and 0.5 μCi of [^{3}H]-cholesterol. The samples were homogenized with a Brinkman polytron and frozen overnight. The precipitated protein was then removed by filtration and the acetone evaporated under a stream of nitrogen. The residue was reconstituted in a 50/50 mixture of isopropyl alcohol/acetonitrile containing 0.02% BHT, and the sterols analyzed were separated and quantitated by HPLC. Dihydrolanosterol was separated from lanosterol and cholesterol with the HPLC analysis used for determining lanosterol demethylase activity. Cholesterol was separated from the methyl sterols on a Beckman 5-μm Ultrasphere silica column (4.6 cm × 25 cm) with a 97/3 ratio of hexane to isopropyl alcohol isocratically at 1 mL/min. For both analyses, the flow rate of the scintillation cocktail through the radioflow detector was 3 mL/min. The values are presented as dpms of [^{14}C]dihydrolanosterol or -cholesterol formed from [^{14}C]-mevalonic acid administered 90 min prior to sampling, normalized to the dpm's of the internal standards, [^{3}H]-dihydrolanosterol or -cholesterol, [^{14}C]mevalonic acid added, and liver weight.

The effect of RS-21607 upon plasma steroid concentrations was determined in male Sprague–Dawley rats (Crl:CD-BR-VAF+, 200 g, Charles River Labs, MA). Groups of seven animals were administered the dihydrocholoride salt of RS-21607 dissolved in water or water (vehicle) orally by gavage. At 60 min prior to sampling, the hamsters received an im dose of 0.5 μg of LHRH and 25 μg of ACTH in isotonic saline. To avoid stress, the animals were also sedated with an ip dose of nembutal (33 mg/kg). At the appropriate sampling time, the animals were anesthetized with halothane and blood was collected by cardiac puncture into heparinized tubes. Plasma testosterone, progesterone, and corticosterone concentrations were determined using radioimmunoassay.

Chemistry. [24,25-$^3H_2$]Dihydrolanosterol. [24,25-^{3}H$_2$]-DHL was synthesized as described previously with minor modifications (Nicolas et al., 1978). A 10-mL side-arm septum flask containing a stirring magnet and 5% Pt/carbon (5 mg) was connected to a high-vacuum line and evacuated. A solution of lanosterol (4.25 mg, 0.01 mmol) in ethyl acetate was injected into the flask. The mixture was degassed and then frozen in liquid nitrogen. Tritium gas (10 Ci, 58 Ci/mmol carrier-free) was transferred into the reaction flask via a Toepler pump, and the reaction mixture was allowed to stir overnight at ambient temperature. Unused tritium gas and most of the solvent were transferred into a liquid-nitrogen-cooled waste bulb connected to the vacuum line. After removal of the flask from the line, the residue was dissolved in ethyl acetate (5 mL) and filtered through a Gelman 0.45-μm nylon filter. To remove any labile radioactivity, the filtrate was concentrated three times from ethanol/ethyl acetate and then dissolved in ethyl acetate (10 mL) to give 350 μCi at a purity of 60%. Purification by flash chromatography (10- × 120-mm column; 90:10 hexanes:ethyl acetate) gave 201.4 mCi at >99% radiochemical purity.

(2R,4S)-trans-2-[2-(4-Chlorophenyl)ethyl]-2-methyl-4-[[(4-aminophenyl)thio]methyl]-1,3-dioxolane, Hydrogen Oxalate Salt (trans-2R,4S-DI). A solution of *p*-toluenesulfonic acid monohydrate (570 mg, 3.0 mmol) in toluene (10 mL) was dried by refluxing through a bed of 4-Å sieves in a Dean-Stark side-arm apparatus for 1.5 h. The solution was cooled, and a separate solution of 4-(4-chlorophenyl)-2-butanone (274 mg, 1.5 mmol), *S*-solketal tosylate (640 mg, 2.25 mmol), and *n*-butanol (0.275 mL, 3 mmol) in toluene (3 mL) was added. The mixture was allowed to reflux through a bed of 4-Å molecular sieves for 5 h and then cooled and poured into aqueous sodium bicarbonate. Extraction of the aqueous mixture with ethyl acetate followed by removal of the solvent by evaporation under reduced pressure gave the crude product as a yellow oil (1.25 g). Separation of the mixture by flash chromatography (45- × 240-mm silica gel, 75:25 hexanes/ethyl acetate) afforded pure less polar isomer as an oil (154 mg, 25.0% yield) and impure more polar isomer. Rechromatography of the more polar isomer (32- × 240-mm silica

gel, 65:35 hexanes/diethyl ether) gave pure material as an oil (164 mg, 29.9% yield). Nuclear Overhauser effect (NOE) difference experiments with ^{1}H NMR spectra of the isomers demonstrated that the less polar isomer had 2*R*,4*S*-*trans*-stereochemistry (wherein the 2-methyl group and the 4-tosylate side chain are *cis*), while the more polar isomer possessed 2*S*,4*S*-*cis*-stereochemistry. Thus, irradiation of the 2-methyl protons of the more polar *cis*-isomer resulted in enhancement of the resonance of the 4-proton, whereas no similar effect was noted with the less polar *trans*-isomer.

Less polar isomer (2*R*,4*S*)-*trans*-2-[2-(4-chlorophenyl)-ethyl]-2-methyl-4-[[(*p*-toluenesulfonyl)oxy]methyl]-1,3-dioxolane was an oil: $[\alpha]^{20}_D = -3.2°$ (c = 0.4, $CHCl_3$); ^{1}H NMR (300 MHz, $CDCl_3$) δ 1.33 (s, 3H, 2-CH_3), 1.86 (m, 2H, CH_2), 2.46 (s, 3H, $ArCH_3$), 2.62 (m, 2H, $ArCH_2$), 3.79 (dd, 1H, J = 6.1, 8.7 Hz) and 4.07 (dd, 1H, J = 6.3, 8.7 Hz) (CH_2O), 4.02 (m, 2H, CH_2OS), 4.27 (m, 1H, CHO), 7.09 (d, 2H, J = 8.4 Hz, H-2, H-6 of C_6H_4Cl), 7.23 (d, 2H, J = 8.4 Hz, H-3, H-5 of C_6H_4Cl), 7.36 (d, 2H, J = 8.0 Hz, H-3, H-5 of C_6H_4S), 7.81 (d, 2H, J = 8.4 Hz, H-2, H-6 of C_6H_4S); MS m/e 410 (M^+).

More polar isomer (2*S*,4*S*)-*cis*-2-[2-(4-chlorophenyl)ethyl]-2-methyl-4-[[(*p*-toluenesulfonyl)oxy]methyl]-1,3-dioxolane was also an oil: $[\alpha]^{20}_D = -1.8°$ (c = 0.4, $CHCl_3$); ^{1}H NMR (300 MHz, $CDCl_3$) δ 1.31 (s, 3H, 2-CH_3), 1.88 (m, 2H, CH_2), 2.40 (s, 3H, $ArCH_3$), 2.58 (m, 2H, $ArCH_2$), 3.56 (dd, 1H, J = 5.6, 8.6 Hz) and 4.08 (dd, 1H, J = 6.7, 8.7 Hz) (CH_2O), 4.04 (m, 2H, CH_2OS), 4.35 (m, 1H, CHO), 7.06 (d, 2H, J = 8.5 Hz, H-2, H-6 of C_6H_4Cl), 7.22 (d, 2H, J = 8.4 Hz, H-3, H-5 of C_6H_4Cl), 7.31 (d, 2H, J = 8.0 Hz, H-3, H-5 of C_6H_4S), 7.78 (d, 2H, J = 8.3 Hz, H-2, H-6 of C_6H_4S); MS m/e 410 (M^+).

To a solution of the (2*R*,4*S*)-*cis*-tosylate (95 mg, 0.23 mmol) prepared as above and 4-aminobenzenethiol (95 mg, 0.76 mmol) in acetone (5 mL) was added solid potassium carbonate (125 mg, 0.9 mmol), and the mixture was heated under reflux for 4 h. The mixture was cooled, and an additional quantity of thiol (80 mg, 0.64 mmol) was added and the mixture refluxed another 4 h. The mixture was cooled, poured into water, and extracted into ethyl acetate. The extracts were washed with H_2O, dried (Na_2SO_4), and evaporated under reduced pressure to give a residue which was purified by flash chromatography (22- × 215-mm silica gel, 75:25 hexanes/ethyl acetate), affording the pure title compound as an oil (70 mg, 83.3% yield). The hydrogen oxalate salt was formed by treating an ethereal solution of the compound with ethereal anhydrous oxalic acid. Recrystallization of the salt from ethyl acetate–hexane afforded an off-white solid: mp 130.5–131.3 °C; $[\alpha]^{20}_D = -2.0°$ (c = 0.3, $CHCl_3$); ^{1}H NMR (300 MHz, DMSO-d_6) δ 1.31 (s, 3H, 2-CH_3), 1.79 (m, 2H, CH_2), 2.57 (m, 2H, $ArCH_2$), 2.81 (dd, 1H, J = 7.5, 13.3 Hz) and 2.96 (dd, 1H, J = 5.2, 13.4 Hz) (CH_2S), 3.58 (m, 1H) and 4.00 (m, 1H) (CH_2O), 4.07 (m, 1H, CHO), 6.55 (d, 2H, J = 8.5 Hz, H-3, H-5 of C_6H_4N), 7.14 (d, 2H, J = 8.5 Hz, H-2, H-6 of C_6H_4N), 7.20 (d, 2H, J = 8.5 Hz, H-2, H-6 of C_6H_5Cl), 7.28 (d, 2H, J = 8.4 Hz, H-3, H-5 of C_6H_5Cl); MS m/e 363 (M^+). Anal. Calcd for $C_{21}H_{24}ClNO_6S$: C, 55.56; H, 5.33; N, 3.09. Found: C, 55.70; H, 5.16; N, 3.18.

(2S,4S)-cis-2-[2-(4-Chlorophenyl)ethyl]-2-methyl-4-[[(4-aminophenyl)thio]methyl]-1,3-dioxolane, Hydrogen Oxalate Salt (cis-2S,4S-DI). This compound was prepared from the (2*S*,4*S*)-*cis*-tosylate as described for the *trans*-isomer. Recrystallization from ethyl acetate–hexane gave a pale yellow solid: mp 129.2–131.8 °C; $[\alpha]^{20}_D = -3.4°$ (c = 0.3, $CHCl_3$); ^{1}H NMR (300 MHz, DMSO-d_6) δ 1.25 (s, 3H, 2-CH_3), 1.85 (m, 2H, CH_2), 2.61 (m, 2H, $ArCH_2$), 2.82 (dd, 1H, J = 7.4, 13.3 Hz) and 2.95 (dd, 1H, J = 5.2, 13.3 Hz) (CH_2S), 3.56 (dd, 1H, J = 6.5, 8.0 Hz) and 4.03 (dd, 1H, J = 6.2, 8.2 Hz) (CH_2O), 4.14 (m, 1H, CHO), 6.55 (d, 2H, J = 8.5 Hz, H-3, H-5 of C_6H_4N), 7.14 (d, 2H, J = 8.5 Hz, H-2, H-6 of C_6H_4N), 7.21 (d, 2H, J = 8.5 Hz, H-2, H-6 of C_6H_5Cl), 7.30 (d, 2H, J = 8.5 Hz, H-3, H-5 of C_6H_5Cl); MS m/e 363 (M^+). Anal. Calcd for $C_{21}H_{24}ClNO_6S$: C, 55.56; H, 5.33; N, 3.09. Found: C, 55.85; H, 5.41; N, 3.10.

3β-Hydroxy-24,25-dihydrolanost-8-en-32-al. Prepared from the previously reported 3β-hydroxy-32-(benzyloxy)-24,25-dihydrolanost-8-ene (Takano et al., 1991) by modification of the procedures reported by the same authors. Thus, to an ice-cooled solution of the 32-benzyl ether (125 mg, 0.23 mmol) and collidine (0.062 mL, 0.47 mmol) in methylene chloride (6 mL) was added *tert*-butyltrimethylsilyl (TBDMS) triflate (0.065 mL, 0.27 mmol). The ice bath was removed, and the mixture was stirred for 2 h, after which it was poured into a 1 *N* aqueous solution of $NaHSO_4$. Extraction with a 2:1 hexane/methylene chloride mixture followed by evaporation of solvents under reduced pressure gave the crude 3β-TBDMS ether. To this material in absolute ethanol (10 mL) was added 10% palladium on carbon catalyst (25 mg), and the mixture was stirred under a hydrogen atmosphere for 16 h. After filtration through a pad of Celite, evaporation of solvent under reduced pressure gave a residue which was then recrystallized from methanol–methylene chloride affording pure 3β-[(*tert*-butyltrimethylsilyl)oxy]-32-hydroxy-24,25-dihydrolanost-8-ene, mp 157–160 °C (103 mg, 78.8% yield for two steps).

To an ice-cooled solution of the above 32-alcohol (84 mg, 0.15 mmol) in acetone (10 mL) was added Jones reagent (0.1 mL, 0.21 mmol of chromic acid in acetone), and the mixture was stirred for 1 h. The mixture was then poured into water and extracted with ethyl acetate, after which concentration of the extracts under reduced pressure gave a residue consisting of crude 3β-TBDMS ether 32-aldehyde. This material was dissolved in THF (10 mL), and 2 *N* aqueous H_2SO_4 (8 mL) was then added, after which the mixture was heated at 40 °C for 28 h. The mixture was poured into water and extracted into ethyl acetate, the extracts then being concentrated under reduced pressure. The residue was further purified by flash chromatography (175- × 16-mm silica gel, 88:12 hexanes/acetone), which afforded the title compound (40 mg, 60.1% yield). Recrystallization from acetone–hexane provided an analytical sample, mp 178–181 °C [lit. mp 177–179 °C, Takano et al. (1991); 177–179 °C, Trzaskos et al., (1987)]. All other physical data agreed with that reported by Trzaskos et al. (1987).

[7β-^{3}H]-7α-Hydroxycholesterol. A freshly prepared solution of [^{3}H]sodium borohydride (100 mCi, 58.1 Ci/mmol, 0.0017 mmol) in aqueous 0.01 N sodium hydroxide (0.1 mL) was added to 7-ketocholesterol (3β-hydroxycholest-5-en-7-one) (3.1 mg, 0.0077 mmol) in a small screw-cap vial. Ethanol (0.3 mL) was added, and the reaction mixture was allowed to stir at room temperature. After 2 days, acetone (0.3 mL) was added to quench the reaction followed by 10% aqueous hydrogen chloride (0.002 mL), and the solvent was removed by evaporation under a nitrogen stream. The residue was dissolved in ethyl acetate (10 mL) to determine the amount of activity (104 mCi). Radio-TLC (silica gel, 50:50 hexane/isopropyl acetate, three passes) showed a 1:7 mixture of [7β-^{3}H]-7α-hydroxycholesterol and [7α-^{3}H]-7β-hydroxycholesterol. The solution was concentrated, taken up in toluene (1.0 mL), and purified three times by flash chromatography (10- × 120-mm column; 80:20 hexanes/ethyl acetate) to give

Table 1: Kinetic Constants Associated with Microsomal Metabolism of Dihydrolanosterol[a]

species	substrate	$K_{m,app}$ (μM)	V_{max} (pmol/min/mg)
human ♂	[32-$^3H_3$]DHL	10.3 ± 4.7	21.5 ± 10.2
human ♀	[32-$^3H_3$]DHL	10.3	46.5
hamster ♂	[32-$^3H_3$]DHL	34.2 ± 5.1	233 ± 28
rat ♂	[24,25-$^3H_2$]DHL	181 ± 123	1553 ± 925
rat ♂	[32-$^3H_3$]DHL	79.0 ± 25.2	766 ± 311
purified rat	[32-$^3H_3$]DHL	36.7 ± 8.4	3.41 ± 1.05 min^{-1}

[a] Rate constants were determined from Lineweaver–Burk analysis of product formation at substrate concentrations ranging from 5 to 50 μM (higher substrate concentrations had very limited solubility). When [32-$^3H_3$]dihydrolanosterol was used as substrate, the rate of product formation was determined from the amount of tritium soluble in water. The amount of 4,4-dimethyl-5α-cholesta-8,14-dien-3β-ol formed from [24,25-$^3H_2$]dihydrolanosterol in the presence of AY-9944 was determined by HPLC.

2.78 mCi of [7β-^{3}H]-7α-hydroxycholesterol at >99% radiochemical purity.

RESULTS

Lanosterol Demethylase Activity. Lanosterol 14α-demethylase activity was determined utilizing either [24,25-$^3H_2$]-DHL or [32-$^3H_3$]DHL as substrate. The rates of reaction following incubation with [32-$^3H_3$]DHL were associated with the rate of tritium release into the aqueous media. The rates following incubation with [24,25-$^3H_2$]DHL were determined using HPLC with a radioflow detector as described by Trzaskos and co-workers (1984). Further metabolism of the demethylation product, 4,4-dimethyl-5α-cholesta-8,14-dien-3β-ol (8,14-diene), was blocked by the addition of AY-9944, a Δ^{14}-reductase inhibitor. The formation of the products by both methods was comparable and linear with time and protein.

The kinetic constants associated with microsomal lanosterol demethylation as monitored by the tritium release assay are shown in Table 1. The apparent K_m associated with the human was lower than those of rat and hamster (10.3 ± 4.7, 79.0 ± 25.2, and 34.2 ± 5.1 μM, respectively). The rat enzyme was purified to apparent homogenity as determined by SDS–polyacrylamide gel electrophoresis. The specific activities of two separate preparations were 2.35 and 5.00 nmol of P450/mg of protein. The reason for the low specific activity is unknown. The activity in a system reconstituted with cytochrome P450 reductase was unaffected by cytochrome b_5 (0.5–1.0 nmol) or dilauroylphosphatidylcholine (1–20 μg/mL). The apparent K_m for the partially pure enzyme was 36.7 ± 8.4 μM, and the V_{max} was 3.41 ± 1.05 min^{-1} (Table 1); accordingly, the second-order rate constant for the reaction, V/K, is approximately 1550 M^{-1} s^{-1}.

Inhibition of Lanosterol Demethylase. The inhibition of LDM purified from rat by RS-21607 showed that under the conditions employed (5 and 10 nM LDM), RS-21607 acted kinetically as tight-binding inhibitor with an apparent K_i of 840 pM (Figure 3). The increase in slope with an increase in substrate concentration in the $I_t/1 - (v_i/v_o)$ versus v_o/v_i plot (Figure 3A) is consistent with a competitive inhibition mechanism (Henderson, 1972).

RS-21607 and its three stereoisomers were also observed to be competitive inhibitors of microsomal LDM. The apparent K_i values for the four stereoisomers of RS-21607 associated with the inhibition of LDM in microsomes from cholestyramine-treated rats are shown in Table 2. The *cis*-2*S*,4*S*-compound (RS-21607, apparent K_i = 2.5 ± 1.5 nM) was approximately 50-fold more effective than its *trans*-2*R*,4*S*-diastereomer. Both the 2*S*-enantiomers were over an order of magnitude more effective than the corresponding 2*R*-enantiomers, and, consistent with related antifungal agents, the *cis*-diastereomers were more effective than the *trans*-diastereomers. Ketoconazole, a *cis*-dioxolane racemic mixture,

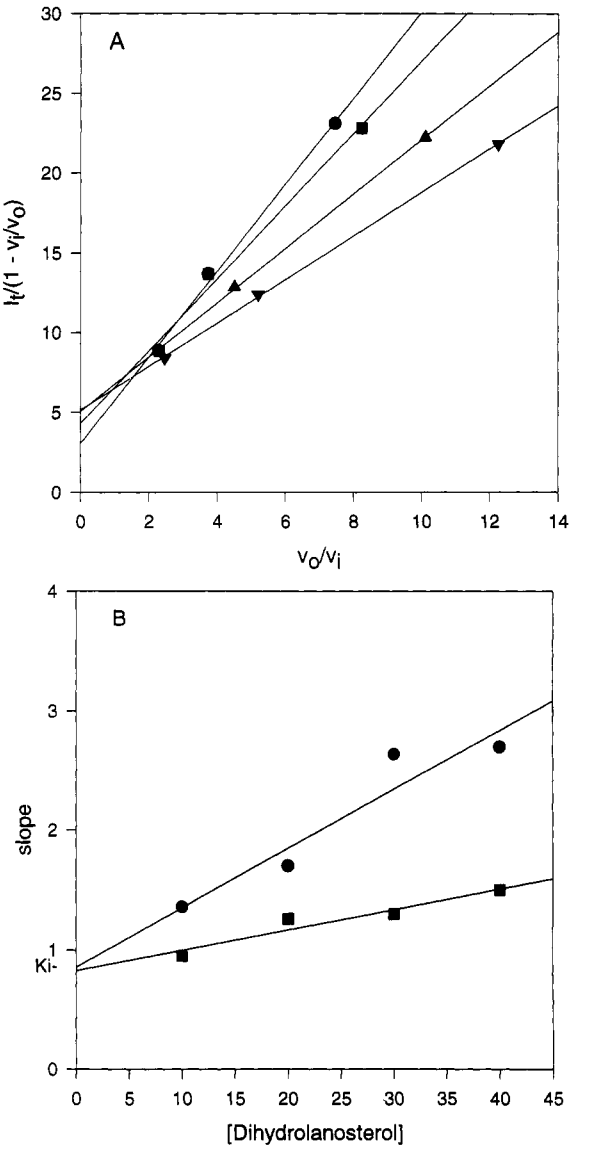

FIGURE 3: Tight-binding inhibition of purified rat lanosterol demethylase by RS-21607. (A) Relationship of dose–response curves to changes in inhibitor concentration with 10 nM LDM analyzed by the method of Henderson (1971): (●) 40 μM DHL, (■) 30 μM DHL, (▲) 20 μM DHL, and (▼) 10 μM DHL. (B) Replot of slopes of (A): (●) 10 nM LDM and (■) 5 nM LDM. The data from the dose–response curves with 5 nM LDM were similar to those shown with 10 nM LDM and also intercepted the y-axis at approximately 5. I_t is total concentration of inhibitor; v_i is velocity in the presence of inhibitor; and v_o is velocity without inhibitor.

Table 2: Inhibition of Rat Microsomal Lanosterol Demethylase

compound	K_i (nM)
cis-2*S*,4*S* (RS-21607)	2.5 ± 1.5
cis-2*R*,4*R*	37 ± 11
trans-2*S*,4*R*	11.0
trans-2*R*,4*S*	117
cis-2*S*,4*S* + 2*R*,4*R*	11.5 ± 8.5
ketoconazole	64, 67
trans-2*R*,4*S*-DI[a]	64800
cis-2*S*,4*S*-DI[a]	10400

[a] DI is the abbreviation for desimidazole.

Table 3: Inhibition of Lanosterol Demethylase in Hepatic Microsomes from Human, Rat, and Hamster[a]

	human K_i (nM)		rat K_i	hamster K_i
	male	female	(nM)	(nM)
cis-2*S*,4*S* (RS-21607)	0.85, 0.35	0.82, 1.17	2.5 ± 1.5	1.4
cis-2*R*,4*R*	17.7		37 ± 11	40.4
cis-2*S*,4*S* + cis-2*R*,4*R*	1.24		6.3 ± 4	2.5
ketoconazole	63.5		64, 67	24.5

[a] Data from Lineweaver–Burk analysis of the rate of tritium release from [$^3H_3$]dihydrolanosterol.

Table 4: Selective Inhibition of Cytochrome P450 Activity[a]

	inhibitor	
cytochrome P450	RS-21607	keto-conazole
Sterol Hydroxylases		
lanosterol 14α-demethylase (human)	0.80 ± 0.34	66
cholesterol 7α-hydroxylase (CYP7)	1625 ± 784	334
cholesterol 27-hydroxylase (CYP27)	71%[b]	32%[b]
27-hydroxycholesterol 7α-hydroxylase	66%[b]	45%[b]
cholesterol side-chain cleavage (CYP11A1)	18400 ± 800	1400 ± 0
Steroid Hydroxylases		
aromatase (CYP19)	7.6 ± 1.3	103%[b]
progesterone 17α,20-lyase (CYP17)	446, 448	38, 29
corticoid 11β-hydroxylase (CYP11B1)	27, 42	81
progesterone 21-hydroxylase (CYP21)	51%[b]	92%[b]
Xenobiotic Hydroxylases		
hepatic progesterone hydroxylases		
6β-hydroxylase (human CYP3A)	33.0 ± 10.2	140
16α-hydroxylase (human)	35.6 ± 12.4	80
lauric acid 12-hydroxylase (rat CYP4A)	NI	NI
debrisoquine (human CYP2D6)	17500 ± 9300	NI
caffeine (human CYP1A2)	3100 ± 1500	100000
tolbutamide (human CYP2C9)	7170	27330

[a] Data are expressed as apparent K_i in nM. NI, no inhibition at 100 μM. [b] Percent control at inhibitor concentration of 5 μM.

was approximately 6-fold less effective than the racemic *cis*-RS-21607.

RS-21607 was at least as potent in hepatic microsomes from male and female human and male hamster as in microsomes from male rat (Table 3) with an apparent K_i value at least an order of magnitude lower than that of the *cis*-2*R*,4*R*-enantiomer. This implies that the intrinsic affinity of these compounds for LDM is independent of the enzyme source and suggests that the nature of the active site is conserved across these species.

Cytochrome P450 in Vitro Selectivity. The high affinity of imidazoles for cytochromes P450 can result in undesired interactions with nontarget cytochromes P450. RS-21607 was selected for further study as a potential cholesterol-lowering agent, based on selective inhibition of LDM relative to the other sterol hydroxylases, steroid hydroxylases, or xenobiotic hydroxylases (Tables 4 and 5). RS-21607 was a minimum of 10-fold more active against LDM than the other cytochromes P450 investigated (Table 5).

The importance of resolving racemic mixtures is emphasized by comparing the activities of RS-21607 and its enantiomer *cis*-2*R*,4*R*. RS-21607 is a much better LDM inhibitor than the *cis*-2*R*,4*R*-enantiomer; however, the *cis*-2*R*,4*R*-enantiomer was a considerably more effective inhibitor of CYP7, CYP17, and CYP11B1, the enzymes responsible for degradation of cholesterol and synthesis of androgens and corticoids, respectively. The apparent K_i values associated with inhibition of LDM, CYP7, CYP17, and CYP11B1 by the *cis*-2*R*,4*R*-enantiomer were 37, 109, 55, and 16 nM, respectively. Accordingly, the difference in K_i values between LDM and CYP7, CYP17, and CYP11B1 was only 2.9, 1.5, and 0.4, respectively, as compared to 559, 2031, and 44 for RS-21607 (Table 5). Strong interactions with these other cytochromes P450 would have been expected if the activity of the two enantiomers had not been separated by preparation of the individual enantiomers. Ketoconazole, a *cis*-dioxolane racemic mixture, is relatively nonselective for the cytochromes P450 (Tables 4 and 5). We have previously prepared the individual enantiomers of ketoconazole and also found differential activities in the separate enantiomers (Rotstein, 1992). These data show RS-21607 to be a selective inhibitor of LDM in vitro, with a much better selectivity profile than ketoconazole.

Table 5: Relative Selectivity of Cytochrome P450 Inhibition[a]

	inhibitor	
cytochrome P450	RS-21607	ketoconazole
Sterol Hydroxylases		
lanosterol demethylase	1	1
cholesterol 7α-hydroxylase (CYP7)	2031	5
cholesterol side-chain cleavage (CYP11A1)	23000	22
Steroid Hydroxylases		
aromatase (CYP19)	10	>1560
progesterone 17α,20-lyase (CYP17)	559	0.5
corticoid 11β-hydroxylase (CYP11B1)	44	1.2
Xenobiotic Hydroxylases		
hepatic progesterone hydroxylases		
6β-hydroxylase (human CYP3A)	41	2.2
16α-hydroxylase (human)	45	1.3
lauric acid 12-hydroxylase (rat CYP4A)	>125000	>1560
debrisoquine (human CYP2D6)	21875	>1560
caffeine (human CYP1A2)	3875	1560
tolbutamide (human CYP2C9)	8963	427

[a] Data are extrapolated from Table 4.

Cytochrome P450 Activities in Vivo. The interaction of RS-21607 with LDM in vivo was investigated by measuring the accumulation of newly synthesized hepatic DHL and the depletion of newly synthesized cholesterol following oral administration of RS-21607. RS-21607 was given to hamsters as the dihydrochloride salt dissolved in water; 90 min prior to sampling, approximately 10 μCi of [^{14}C]mevalonic acid was administered intraperitoneally. At the appropriate time, livers were removed and extracted with acetone, and the sterols were separated by HPLC and their levels determined by radiochemical detection. It is important to note that this method provides information only for the 90-min period prior to sampling. Figure 4A shows that administration of RS-21607 caused a large accumulation (>10-fold) of newly synthesized DHL in somewhat of a dose-responsive fashion. At all the doses of RS-21607, DHL accumulation reached a maximum around 10 dpm of [^{14}C]DHL/dpm of [^{3}H]DHL/μCi of mevalonic acid/g of liver. At later time points, the accumulation of DHL decreases in a dose-dependent fashion, presumably as a result of drug clearance. RS-21607 caused a dose-responsive decrease in hepatic cholesterol biosynthesis with the greatest inhibition between 5 and 8 h (Figure 4B). Cholesterol biosynthesis 18 h postdose was unaffected by 3 mg/kg RS-21607, inhibited by 25% at 10 mg/kg, and inhibited by 52% and 54% by 30 mg/kg (two separate experiments). Accordingly, RS-21607 has an 18-h ED_{50} for cholesterol lowering of 30 mg/kg. *These data indicate that RS-21607 can effectively reach the target enzyme in vivo and inhibit DHL turnover and cholesterol synthesis.*

The in vitro cytochrome P450 selectivity data predicts that RS-21607 should selectively inhibit LDM and cholesterol biosynthesis with minimal effects upon other cytochrome-P450-dependent reactions. This assumption was evaluated

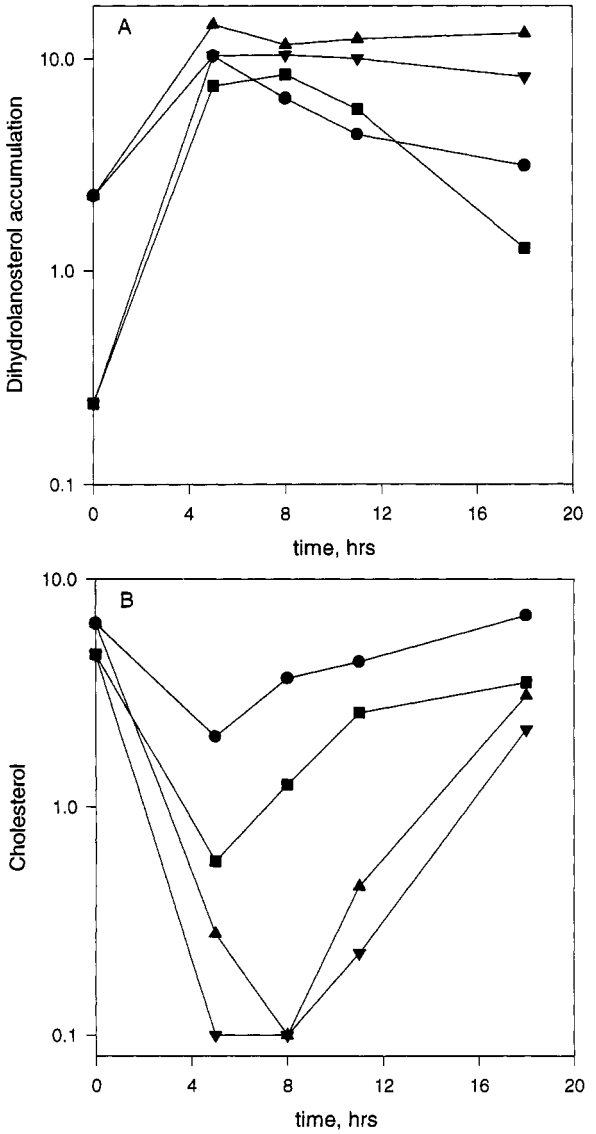

FIGURE 4: Effect of RS-21607 upon lanosterol demethylase activity in hamster. A single oral dose of RS-21607 was given to hamsters and the ability to inhibit lanosterol demethylase determined by the accumulation of hepatic dihydrolanosterol (A) and the depletion of cholesterol (B). The values are presented as dpms of [^{14}C]-dihydrolanosterol or -cholesterol formed from [^{14}C]mevalonic acid administered 90 min prior to sampling, normalized to the dpm's of the internal standards, [^{3}H]dihydrolanosterol or -cholesterol, [^{14}C]-mevalonic acid added, and liver weight, and are plotted against the time after the initial dose of drug. The data represent groups of five animals, and the standard errors are all less than 10% of the final value. Animals were dosed with 3 mg/kg (●), 10 mg/kg (■), or 30 mg/kg (▲) and (▼) (two separate experiments).

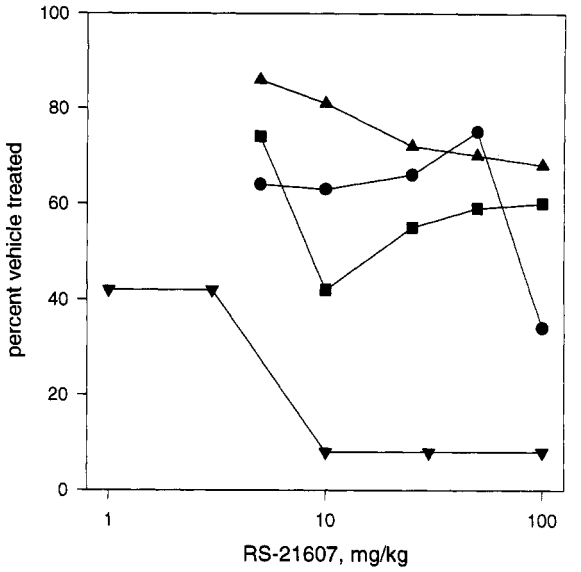

FIGURE 5: Comparison of ability of RS-21607 to inhibit hepatic cholesterol biosynthesis versus its effect upon cytochrome-P450-dependent steroid formation. Inhibition of cholesterol biosynthesis (▼) was determined in hamsters 5 h following a single dose of RS-21607. Cholesterol levels were determined from the dpm's of [^{14}C]-cholesterol formed from [^{14}C]mevalonic acid administered 90 min prior to sampling, normalized to the dpm's of the internal standards, [^{3}H]cholesterol, [^{14}C]mevalonic acid added, and liver weight. Plasma steroid concentrations were measured in LHRH/ACTH-primed male rats (N = 7) 2 h following a single oral dose of RS-21607. The steroid concentrations in untreated animals were 19.9 ng/mL for testosterone (●), 7.15 ng/mL for progesterone (■), and 964 ng/mL for corticosterone (▲). Standard errors were all less than 20% of final values.

by comparing the ability of RS-21607 to lower cholesterol biosynthesis in hamster to its effects upon steroid hormone levels in rat (Figure 5). These data show that RS-21607 is a much more effective inhibitor of cholesterol biosynthesis than of the biosynthesis of testosterone, corticosterone, or progesterone. These steroids are formed by the CYP17, CYP11B1, and CYP11A1, respectively. The effect of RS-21607 upon the plasma concentrations of these compounds was determined after oral administration of 5–100 mg/kg to male rats stimulated with ACTH and LHRH. Corticosterone levels decreased from 964 ± 70 ng/mL with no RS-21607 to 655 ± 54 ng/mL following a 100 mg/kg dose (32% decrease). A single 100 mg/kg dose of ketoconazole reduced corticosterone levels 86% (from 1054 ± 66 mg/mL to 147 ± 13 ng/mL). While testosterone levels were reduced only slightly after doses of 5–50 mg/kg of RS-21607 (from 19.9 ± 2.4 to 12.7 ± 1.9 and 14.9 ± 1.9 ng/mL, respectively), they dropped to 6.75 ± 1.25 ng/mL after the 100 mg/kg dose. This was a 66% decrease as compared to untreated rats. In contrast, ketoconazole decreased testosterone levels 73% following a 25 mg/kg dose and 94% following a 50 mg/kg dose. Progesterone plasma concentrations dropped from 7.15 ± 0.94 ng/mL in untreated animals to 2.99 ± 0.41 ng/mL in animals treated with 10 mg/mL RS-21607. However, this effect on progesterone was not related to dose since the plasma concentration of progesterone was 4.26 ± 0.39 ng/mL at 100 mg/kg RS-21607. These data support the conclusions of the in vitro studies.

Mechanism of Inhibition. Azoles are known to competitively inhibit cytochromes P450 in part by coordination to the heme, resulting in a type II binding spectrum, characterized by an absorption peak at 425–435 nm and an absorption minimum at 390–405 nm (Schenkman, 1981). As expected, RS-21607 interacted with the purified LDM to produce a type II binding spectrum with an absorption maximum of approximately 432 nm and a minimum of 412 nm (Figure 6). At the concentrations of enzyme needed to observe the inhibitor-induced spectrum (100–250 pmol/mL), RS-21607 appeared to bind stoichiometrically to the enzyme (data consistent with tight-binding inhibition), precluding the determination of the apparent K_d.

The relative importance of the imidazole upon binding to the rat enzyme was investigated with the desimidazole analogs of *cis*-2*S*,4*S* (RS-21607) and *trans*-2*R*,4*S*, *trans*-2*R*,4*S*-DI, and *cis*-2*S*,4*S*-DI, respectively. (The change from 2*S* to 2*R* and from *cis* to *trans* in going to the corresponding desimidazole analogs is due to a reversal of the Cahn–Ingold–Prelog priority sequence in the desimidazole compounds.) As expected, the

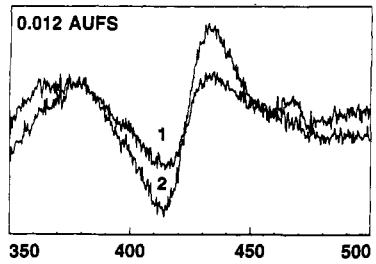

FIGURE 6: Binding spectrum of the interaction of RS-21607 with LDM purified from rat. RS-21607 was added to a sample cuvette containing LDM (200 pmol/mL) and the spectrum recorded between 350 and 500 nm with a SLM Aminco UV spectrophotometer in the split-beam mode. The reference cuvette contained only pure LDM and RS-21607 vehicle. Full-scale absorbance on the *y*-axis is 0.012. Spectra 1 and 2 were recorded following the addition of 50 and 150 pmol/mL RS-21607, respectively. Addition of more RS-21607 resulted in no increased absorbance. Background absorbance was automatically subtracted from the recorded spectra.

imidazole greatly increases the ability of these compounds to inhibit LDM (Table 2), presumably as a result of its ability to coordinate directly with the heme. In contrast to the imidazole compounds, the *cis*-2*S*,4*S*-desimidazole analog (in which the methyl group and side chain are *trans*) had a higher affinity for the enzyme than its *trans*-analog (methyl group and side chain are *cis*). Another interesting observation from these data is that the desimidazole analogs bind with a similar affinity to LDM as does the substrate DHL (assuming k_{-1} is much greater than k_2, making K_i and K_m values comparable). Together, these data confirm that the ligand attached to the imidazole in RS-21607 is a good non-sterol substitute for DHL and that coordination of the imidazole to the heme provides the major contributing factor for the inhibition of LDM by RS-21607.

The 32-oxysterol intermediates (32-alcohol and 32-aldehyde) formed in the demethylation of DHL accumulate under conditions of low metabolism, presumably as a result of competition for further oxidation with excess substrate (Trzaskos et al., 1986b). Ketoconazole was observed by these investigators to increase the accumulation of the 32-oxy intermediates. We also found that as the percent metabolism decreased, the ratio of accumulated oxylanosterol to demethylated product increased (Figure 7). The results shown in Figure 7 were obtained with 40 μM DHL incubated from 2 to 30 min. Addition of RS-21607 (5–30 nM) to the 20-min reactions caused a decreased in the percent metabolism as compared to control (11%), as expected. However, the percent of accumulated oxylanosterols in the products was greater than expected if the decrease in metabolism was simply a result of inhibition of the enzyme at only the first step of the reaction. If this had been the case, the inhibited profile should have had an identical slope to that without inhibitor. The increase in accumulation with increasing inhibitor and decreasing metabolism can only be interpreted to indicate that *RS-21607 inhibits more than one step in the demethylation reaction.* Other studies showed that the profiles for RS-21607 and ketoconazole (100–800 nM) were nearly identical (data not shown) and the primary oxysterol accumulated with both inhibitors was the 32-aldehyde. Similar results were obtained in experiments using 80 μM DHL. These data are interpreted to indicate that the relative affinities of RS-21607 and ketoconazole for the different steps in the sequential oxidation of DHL by LDM are similar and that both preferentially inhibit third oxidation relative to second, resulting in an accumulation of the 32-aldehyde. The difference between the two inhibitors is that 10–20 times more

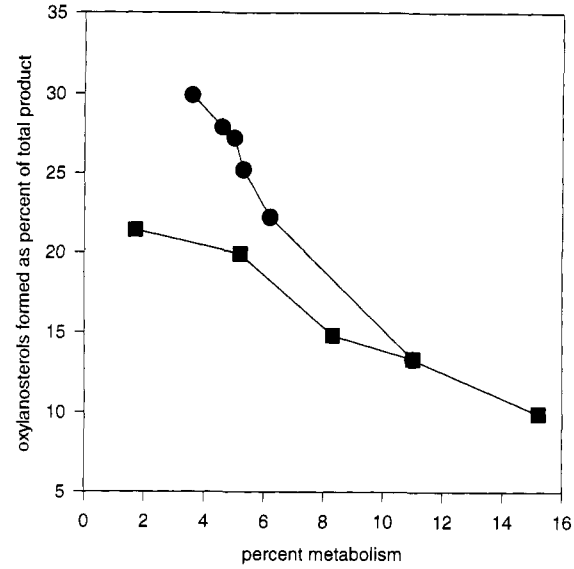

FIGURE 7: Accumulation of oxylanosterols. DHL (40 μM) was incubated with 1 mg/mL microsomal protein from cholestyramine-treated rats. The percent of 32-oxysterol formation was determined from the HPLC analysis of 32-alcohol, 32-aldehyde, and diene formation. The change in percent metabolism in the absence of RS-21607 (■) was obtained by changing the incubation time from 5 to 30 min. The data with RS-21607 (●) was obtained by changing the inhibitor concentration in 20-min incubations. RS-21607 concentration was varied from 5 to 30 nM. An example of the acutal amount of product formed per 1 mL of incubation is the 20-min incubation without inhibitor; 11% of the DHL was metabolized to 3.99 nmol of diene, 0.398 nmol of 32-alcohol, and 0.212 nmol of 32-aldehyde. Addition of 20 nM RS-21607 decreased the conversion of DHL to 4.6%; 1.328 nmol of diene, 0.172 nmol 32-alcohol, and 0.344 nmol of 32-aldehyde were formed. Similar ratios of products were observed at other concentrations of inhibitors. Individual data points represent the mean of duplicate incubations. The data presented in this figure are representative of three separate studies, two using 40 μM DHL and one using 80 μM DHL.

ketoconazole was needed to achieve the same results as those observed for RS-21607.

DISCUSSION

These studies were initiated to determine if mammalian LDM could be selectively inhibited both in vitro and in vivo. Methods were established to monitor in vitro LDM inhibition and interactions with other known cytochromes P450, as well as methods to measure endpoints of specific in vivo enzyme chemistry.

The synthesis of [32-$^3H_3$]DHL made possible the development of a rapid and convenient method for evaluating lanosterol demethylase activity (DeKeczar et al., 1993). The label incorporated at the C-32 position is lost the aqueous environment during the oxidation process. This is easily separated from unreacted product and quantitated. Evaluation of LDM activity by this procedure could be complicated by kinetic isotope effects. The breaking of a C–T bond during a catalytic event should proceed much more slowly than for a C–H bond due to the lower zero-point energy; accordingly, DHL labeled with three tritiums on the C-32 methyl group might be thought to be oxidized much more slowly than unlabeled enzyme. However, the rate of demethylation from [32-$^3H_3$]DHL was very similar to that observed with [24,25-$^3H_2$]DHL which has an unlabeled C-32 methyl group (Table 1). A ^TV isotope effect of 2.03 was observed in microsomes from cholestyramine-treated rats, while no significant isotope effect associated with $^T(V/K)$ was observed (Table 1). The lack of a large isotope effect upon this reaction allows us to

reliably determine the kinetic constants associated with the inhibition of lanosterol demethylase using [32-$^3H_3$]DHL as the substrate. It also suggests that the demethylation chemistry is not rate limiting in the enzymatic reaction.[3]

RS-21607, a *cis*-2*S*,4*S*-stereoisomer, was determined to be the most effective and selective non-sterol, mammalian LDM inhibitor yet described. It was characterized against LDM purified from rat as a competitive tight-binding inhibitor with an apparent K_i of 840 pM (Figure 2). Its ability to block LDM activity was similar in microsomes from all the species studied (human, rat, and hamster) (Table 2). The ability to inhibit the enzyme appears to be largely a result of the electrostatic contribution of the imidazole binding to the heme. Removal of the imidazole from the substrate dramatically decreased the apparent K_i, data consistent with the observation of a type II binding spectrum (Figure 7). RS-21607 also had a higher affinity for LDM than the other cytochromes P450 involved in sterol, steroid, and xenobiotic oxidations. Since all cytochromes P450 have a protoporphyrin IX heme prosthetic group, an azole has the potential to bind with high affinity to all these enzymes. Therefore, the apparent selectivity of RS-21607 suggests that it interacts with the apoprotein of LDM with a much higher affinity than it interacts with the apoprotein of the other cytochromes P450. RS-21607 was also found to block the biosynthesis of cholesterol in hamsters in a dose-dependent manner with a corresponding accumulation of dihydrolanosterol. This was interpreted to indicate that RS-21607 is able to distribute to the site of action in hamsters and inhibit the target enzyme. At the same doses in rat testosterone, corticosterone, and progesterone plasma concentrations, endpoints of the enzymes involved in steroid biosynthesis were relatively unaffected. These data show RS-21607 to be an effective and selective inhibitor of LDM in vitro and in vivo.

It is well established that for many racemic compounds, one enantiomer interacts with biological systems in a manner distinct from its antipode. For example, we have previously shown that the *cis*-2*S*,4*R*-enantiomer of ketoconazole is approximately 3-fold more effective than the *cis*-2*R*,4*S*-enantiomer for inhibition of LDM (Rotstein et al., 1992). In contrast, the *cis*-2*R*,4*S*-enantiomer is an order of magnitude more effective as an inhibitor of CYP7. Therefore, the *cis*-2*S*,4*R*-enantiomer has a much more desirable profile for cholesterol lowering than its antipode. However, most studies with ketoconazole have been undertaken with the racemic mixture, i.e., a mixture of two compounds with distinctly different biological profiles. Upon investigating the profile of the four stereoisomers of RS-21607 against various cytochromes P450, we also observed the different diastereomers to have different interactions. Fortunately, the stereoisomer with the best activity for LDM, RS-21607, also had the least activity against CYP7, CYP17, and CYP11B1. Obviously, inhibition of cholesterol degradation (CYP7) should decrease the ability of the compounds to lower cholesterol in vivo. This translates to an overall maximal effect on cholesterol biosynthesis by RS-21607, with minimal effects upon cholesterol degradation and androgen and corticoid formation.

The 32-aldehyde of dihydrolanosterol has been reported to accumulate under a variety of conditions including high DHL concentration and the presence of ketoconazole (Trzaskos et al., 1986b, 1987; Saucier et al., 1987). We observed a similar accumulation with RS-21607. The accumulation of this oxysterol has been associated with a suspension of HMG-CoA reductase activity. Recently, Trzaskos and co-workers (1993) used the lanosterol analog 15α-fluorolanost-7-en-3β-ol to generate a stable sterol 32-aldehyde analog. They observed this compound to supress HMG-CoA reductase activity by reducing the translational efficiency of the reductase mRNA. They proposed that the "accumulation of the 32-aldehyde *in situ* may be the result of a designed integrated regulatory process which serves to control endogenous cholesterol biosynthesis under normal physiological fluxes of carbon flow through the sterol pathway". Accordingly, an inhibitor which increases the accumulation of the 32-aldehyde of DHL, such as RS-21607, may decrease cholesterol biosynthesis by two mechanisms, inhibition of lanosterol 14α-demethylase and feedback suppression of HMG-CoA reductase. This proposal is supported by the observation that RS-21607 suppresses the post-translational activity of HMG-CoA reductase activity in hamsters and HEP G2 cells (Dr. Pamela M. Burton, personal communication).

In this report, we have presented the methodology used to rationally evaluate an inhibitor for an enzyme of cholesterol biosynthesis. RS-21607 was characterized to be a high-affinity, tight-binding, competitive inhibitor of LDM. It inhibited the enzyme and cholesterol biosynthesis in hamster liver for at least 18 h following a 30 mg/kg oral dose. RS-21607 had minimal effects against the other cytochromes P450 investigated both in vivo and in vitro. It also caused an increase in the accumulation of the 32-aldehyde oxysterol intermediate. Therefore, as a result of its effectiveness as a LDM inhibitor and its selectivity against other cytochromes P450, RS-21607 has the potential to be a novel therapy for the treatment of hypolipidemic disorders. Preliminary results indicate that RS-21607 effectively lowers LDL cholesterol in mildly hypolipidemic patients without serious side effects (Dr. Ken Schwartz, personal communication).

[3] The intrinsic isotope effect for an enzymatic reaction can be masked by other enzymatic steps in the reaction sequence. Northrup (1977) has shown that masking of the V isotope effect is a result of the "ratio of catalysis" and represents the ratio of the rate of the catalytic step to the rate of the other forward steps contributing to the maximal velocity, whereas masking of the V/K isotope effect is a result of the "commitment to catalysis" and represents the tendency of the enzyme–substrate complex to go forward through catalysis as opposed to its tendency to break down to free enzyme and substrate. The observation of the lower V/K isotope effect with lanosterol demethylase suggests that steps preceeding the catalytic event, such as substrate binding or enzyme reduction, may be rate limiting.

ACKNOWLEDGMENT

The authors wish to thank Dr. Melvin D. Chaplin for his constant support throughout this project.

REFERENCES

Anderson, K. M., Castelli, W. P., & Levy, D. (1987) *JAMA, J. Am. Med. Assoc. 257*, 2176–2180.
Aoyama, Y., Yoshida, Y., & Sato, R. (1984) *J. Biol. Chem. 259*, 1661–1666.
DeKeczer, S., Kertesz, D., & Parnes, H. (1993) *J. Labelled Compd. Radiopharm. 33*, 219–231.
Dignam, J. D., & Strobel, H. W. (1975) *Biochem. Biophys. Res. Commun. 63*, 845–852.
Endo, A. (1985) *J. Med. Chem. 28*, 401–405.
Feldman, D. (1986) *Endocr. Rev. 7*, 409–420.
Gylling, H., Vanhanen, H., & Miettinen, T. A. (1991) *Metabolism 40*, 35–41.
Henderson, P. J. F. (1972) *Biochem. J. 127*, 321–333.
Kramer, F. B., & Pont, A. (1986) *Am. J. Med. 80*, 616–620.
Lipid Research Clinics Program (1984) *JAMA, J. Am. Med. Assoc. 251*, 351–374.

Lowery, O. H., Rosegrough, N. J., Farr, A. L., & Randall, R. J. (1951) *J. Biol. Chem. 193*, 265–275.
Miettinen, T. A. (1988) *J. Lipid Res. 29*, 43–51.
Northrup, D. B. (1977) in *Isotope Effects on Enzyme-Catalyzed Reactions* (Cleland, W. W., O'Leary, M. H., & Northrup, D. B., Eds.) pp 121–151, University Park Press, Baltimore.
Omura, T., & Sato, R. (1964) *J. Biol. Chem. 239*, 2379–2385.
Romano, M. C., Straub, K. M., Yodis, L. A. P., Eckardt, R. D., & Newton, J. F. (1988) *Anal. Biochem. 170*, 83–93.
Rotstein, D. M., Kertesz, D. J., Walker, K. A. M., & Swinney, D. C. (1992) *J. Med. Chem. 35*, 2818–2825.
Rush, W. R., Smith, S. A., Mulvey, J. H., Graham, D. J. M., & Chaplin, M. D. (1987) *Drug Metab. Dispos. 15*, 571–578.
Saucier, S. E., Kandutsch, A. A., Phinwa, S., & Spencer, T. A. (1987) *J. Biol. Chem. 262*, 14056–14062.
Scheer, I., Thompson, M. J., & Mosettig, E. (1956) *J. Am. Chem. Soc. 78*, 4733–4737.
Schenkman, J. B., Sligar, S. G., & Cinti, D. L. (1981) *Pharmacol. Ther. 12*, 43–71.
Shaw, R., & Elliot, W. H. (1979) *J. Biol. Chem. 254*, 7177–7182.
Sono, H., Sonoda, Y., & Sato, Y. (1991) *Biochim. Biophys. Acta 1078*, 388–394.
Spatz, L., & Stritmatter, P. (1971) *Proc. Natl. Acad. Sci. U.S.A. 68*, 1042–1046.
Swinney, D. C. (1990) *Drug Metab. Dispos. 18*, 859–865.
Swinney, D. C., Webb, A. S., & Freedman, R. (1991) *Biochem. Pharm. 42*, 2341–2349.
Takano, Y., & Morisaki, M. (1991) *Chem. Pharm. Bull. 39*, 1647–1648.
Trzaskos, J. M., Bowen, W. D., Shafiee, A., Fisher, R. T., & Gaylor, J. L. (1984) *J. Biol. Chem. 259*, 13402–13412.
Trzaskos, J. M., Kawata, S., & Gaylor, J. L. (1986a) *J. Biol. Chem. 261*, 14651–14657.
Trzaskos, J. M., Fisher, R. T., & Favata, M. F. (1986b) *J. Biol. Chem. 261*, 16937–16942.
Trzaskos, J. M., Favata, M. F., Chen, H. W., Fisher, R. T., & Greenberg, R. S. (1987) *J. Biol. Chem. 262*, 12261–12269.
Trzaskos, J. M., Magolda, R. L., Favata, M. F., Fisher, R. T., Johnson, P. R., Chen, H. W., Ko, S. S., Leonard, D. A., & Gaylor, J. L. (1993) *J. Biol. Chem. 268*, 22591–22599.
Vanden Bossche, H. (1988) in *Sterol Biosynthesis Inhibitors* (Berg, D., & Plempel, M., Eds.) pp 79–119, Ellis Horwood Ltd., Chichester, England.
Walker, K. A. M., Kertesz, D. J., Rotstein, D. M., Swinney, D. C., Berry, P. W., So, O. Y., Webb, A. W., Watson, D. M., Mak, A. Y., Burton, P. M., Mills-Dunlap, B., Chiou, M. Y., Tokes, L. G., Kurz, L. J., Kern, J. R., Chan, K. W., Salari, A., & Mendizabal, G. R. (1993) *J. Med. Chem. 36*, 2235–2237.
Walker, K. A. M., Wallach, M. B., & Hirschfeld, D. R. (1980) *J. Med. Chem. 24*, 67–74.
Wangworth, D. R., & Bacon, S. (1987) *Am. J. Cardiol. 60*, 339–429.
Yasukochi, Y., & Masters, B. S. S. (1976) *J. Biol. Chem. 251*, 5337–5344.
Yoshida, Y., & Aoyama, Y. (1984) *J. Biol. Chem. 259*, 1655–1660.

Mechanism for the Desulfurization of L-Cysteine Catalyzed by the *nifS* Gene Product†

Limin Zheng, Robert H. White, Valerie L. Cash, and Dennis R. Dean*

Departments of Anaerobic Microbiology and Biochemistry, Virginia Polytechnic Institute and State University, Blacksburg, Virginia 24061

Received December 2, 1993; Revised Manuscript Received February 10, 1994®

ABSTRACT: The *nifS* gene product (NIFS) is a pyridoxal phosphate binding enzyme that catalyzes the desulfurization of L-cysteine to yield L-alanine and sulfur. In *Azotobacter vinelandii* this activity is required for the full activation of the nitrogenase component proteins. Because the nitrogenase component proteins, Fe protein and MoFe protein, both contain metalloclusters which are required for their respective activities, it is suggested that NIFS participates in the biosynthesis of the nitrogenase metalloclusters by providing the inorganic sulfur required for Fe–S core formation [Zheng, L., White, R. H., Cash, V. L., Jack, R. F., & Dean, D. R. (1993) *Proc. Natl. Acad. Sci. U.S.A. 90*, 2754–2758]. In the present study the mechanism for the desulfurization of L-cysteine catalyzed by NIFS was determined in the following ways. First, the substrate analogs, L-allylglycine and vinylglycine, were shown to irreversibly inactivate NIFS by formation of a γ-methylcystathionyl or cystathionyl residue, respectively, through nucleophilic attack by an active site cysteinyl residue on the corresponding analog–pyridoxal phosphate adduct. Second, this reactive cysteinyl residue, which is required for L-cysteine desulfurization activity, was identified as Cys^{325} by the specific alkylation of that residue and by site-directed mutagenesis experiments. Third, the formation of an enzyme-bound cysteinyl persulfide was identified as an intermediate in the NIFS-catalyzed reaction. Fourth, evidence was obtained for an enamine intermediate in the formation of L-alanine. All of these results support a mechanism for NIFS-catalyzed desulfurization of L-cysteine which involves formation of a substrate cysteine–pyridoxal phosphate ketimine adduct and subsequent nucleophilic attack by the thiolate anion of Cys^{325} on the sulfur of the substrate cysteine. These events result in formation of a protein-bound persulfide, which is the proposed sulfur donor in Fe–S core formation, and a pyridoxal phosphate-bound enamine which is ultimately released as L-alanine.

Nitrogenase is a two-component metalloenzyme that catalyzes the MgATP-dependent reduction of dinitrogen. During catalysis, an Fe protein component sequentially delivers single electrons to a MoFe protein component upon which the substrate reduction site is located [reviewed by Burgess (1990)]. A feature common to both the Fe protein and the MoFe protein is that they contain metalloclusters comprised of Fe–S cores (Georgiadis *et al.*, 1992; Kim & Rees, 1992). These metalloclusters are necessary for nitrogenase activity, and they appear to participate in various aspects of electron transfer or substrate reduction. In *Azotobacter vinelandii*, the genes that encode the nitrogenase structural components (*nifH*, Fe protein subunit; *nifDK*, MoFe protein subunits) are contiguous and arranged *nifHDK* (Brigle *et al.*, 1985). However, the primary translation products of the nitrogenase structural genes are not active. Rather, immature forms of the nitrogenase component proteins are activated through the formation and insertion of their complementary metalloclusters in processes that require the activities of a consortium of associated *nif*-specific gene products [see Dean and Jacobson (1992) for a review]. One such processing step must include the mobilization of the inorganic sulfide required for formation of the Fe–S cores. We have recently demonstrated (Zheng *et al.*, 1993) that the *A. vinelandii nifS* gene product, which is required for the full *in vivo* activation of both the Fe protein and the MoFe protein (Jacobson *et al.*, 1989), is a pyridoxal phosphate (PLP)[1] enzyme that catalyzes the desulfurization of L-cysteine to yield L-alanine and elemental sulfur. On the basis of these results we proposed that NIFS catalyzes the release of sulfur from L-cysteine in a pathway which ultimately provides the sulfide present in the metalloclusters of the nitrogenase component proteins. Because the catalytic activity of NIFS is extremely sensitive to alkylating reagents, such as *N*-ethylmaleimide, a reactive cysteine was proposed to be involved in catalysis. We also suggested that an intermediate step in Fe–S core assembly includes the formation of a NIFS-bound cysteinyl persulfide. Such a cysteinyl persulfide could be formed through nucleophilic attack by the active site cysteinyl thiolate on the cysteine–PLP ketimine adduct. In the present study we have tested this possible mechanism for the mobilization of sulfur by identifying the active site cysteinyl residue located on NIFS and by demonstrating the formation of an enzyme-bound cysteinyl persulfide at that site.

EXPERIMENTAL PROCEDURES

Materials. γ-Methylcystathionine, prepared by the condensation of L-allylglycine with L-cysteine catalyzed by cystathionine γ-synthase from *Escherichia coli* (Brzović *et al.*, 1990), was kindly supplied by Dr. Peter Brzović, Department of Biochemistry, University of California at Riverside. Homocystathionine, *S*-(4-amino-4-carboxybutyl)-cysteine,

† This work was supported by National Science Foundation Grant MCB930800.

* Author to whom correspondence should be addressed.

® Abstract published in *Advance ACS Abstracts*, April 1, 1994.

[1] Abbreviations: DTT, dithiothreitol; GC–MS, gas chromatography–mass spectroscopy; HPLC, high-pressure liquid chromatography; 1,5-I-AEDANS, *N*-(iodoacetyl)-*N'*-(5-sulfo-1-naphthyl)ethylenediamine; NIFS, *nifS* gene product; PLP, pyridoxal phosphate; SDS–PAGE, sodium dodecyl sulfate–polyacrylamide gel electrophoresis.

0006-2960/94/0433-4714$04.50/0

was synthesized in the following manner. Diethyl acetamidomalonate was condensed with 1,3-dibromopropane in ethanol containing sodium ethoxide to form 1-acetamido-1,1-bis(carboxyethoxy)-4-bromobutane. This product was then condensed with cysteine under basic conditions to generate *S*-(4-acetamido-4,4-dicarbethoxybutyl)cysteine, which was subsequently converted into the desired product after saponification with NaOH, decarboxylation, and hydrolysis with HCl.

Wild-type NIFS and NIFS–Ala^{325} were hyperexpressed in *E. coli* cells and purified as described before (Zheng *et al.*, 1993). The K_M was determined using the hydrogen sulfide assay described previously (Zheng *et al.*, 1993). The cysteine concentrations used were 0.2, 0.5, 1.0, 2.0, 4.0, and 9.0 mM. Because cysteine interferes with the hydrogen sulfide assay, separate sodium sulfide standard curves were respectively obtained in the presence of each cysteine concentration used to determine the K_M. It should be noted that NIFS activity is highly sensitive to pH and temperature, so the K_M observed might depend on the condition used. Ammonia was assayed according to the method of Dilworth *et al.* (1992). The reagents L-cysteine, allylglycine, vinylglycine, and *N*-(iodoacetyl)-*N'*-(5-sulfo-1-naphthyl)ethylenediamine (1,5-I-AEDANS) were freshly prepared in water and adjusted to pH 8.0, if necessary. All of the reactions described below were performed at ambient temperature unless specifically noted otherwise.

Isolation and Identification of the Protein-Bound γ-Methylcystathionine. Purified NIFS (5 mg, 110 nmol) was inactivated by incubation with 5 μmol of L-allylglycine in 1 mL of 50 mM Tris·HCl buffer, pH 8.0, for 2 h. After this treatment the excess unreacted amino acid analog was separated from the protein fraction by three cycles of centrifugal ultrafiltration using an Amicon Centricon 30 device. The isolated protein was then hydrolyzed under N_2 in 1 mL of 6 M HCl at 110 °C for 21 h in the presence of 5 μL of mercaptoethanol. After evaporation of the HCl, the resulting amino acids were dissolved in 0.5 mL of water, applied to a Dowex 50W-8X H+ column (1 × 0.6 cm), and eluted with an HCl gradient consisting of 3 mL of 1 M HCl, 0.5 mL of 2 M HCl, and finally 3 mL of 3 M HCl. Under this condition authentic γ-methylcystathionine was eluted in the 3 M HCl fraction. The amino acids present in the 3 M HCl eluant fraction were then converted into their *n*-butyl trifluoroacetyl derivatives as previously described (White & Rudolph, 1978) and were separated by gas chromatography–mass spectroscopy (GC–MS) on a DB-5 column (30 m × 0.32 mm, J&W Scientific Co.) programmed from 175 to 300 °C at 10 °C/min. Under these conditions the γ-methylcystathionine derivative eluted after 8.3 min. The mass spectra were obtained at 70 eV using a VG-70-70EHF mass spectrometer.

Isolation and Identification of the Protein-Bound Cystathionine. Vinylglycine-inactivated NIFS was prepared by incubation of 17 nmol of NIFS with two additions of 5 μmol of L-vinylglycine in a total volume of 1 mL of 50 mM Tris·HCl buffer, pH 8.0, for 8 h. NIFS-bound cystathionine was identified using the same procedures described above for the identification of γ-methylcystathionine. Authentic cystathionine was used as standard.

Separation and Identification of the Peptide Containing the Active Site Cysteinyl Residue. NIFS (120 μg, 2.7 nmol) was incubated with 6.5 nmol of the dansylated alkylating reagent 1,5-I-AEDANS for 12 h. After the excess of 1,5-I-AEDANS was removed by three cycles of ultrafiltration, as described above, NIFS was denatured in 1 mL of 4.8 M Gdn·HCl, 80 mM Tris·HCl, pH 8.0, and 50 mM dithiothreitol (DTT) buffer and the three remaining cysteinyl residues were alkylated with a 1.1 molar excess of iodoacetamide. The protein treated in this way was then extensively dialyzed against water and dried in a speed vacuum apparatus. The resulting pellet was dissolved in 0.5 mL of 100 mM $(NH_4)_2CO_3$ buffer, pH 7.7, and digested with 2.4 μg of trypsin for 18 h at 37 °C. The separation of the resulting peptides was by HPLC using an Axxion octadecylsilane column (5 μm, 4.6 × 250 mm) equilibrated with 0.1% (v/v) trifluoroacetic acid in water. Elution was with a 20–40% gradient of 0.075% (v/v) trifluoroacetic acid in acetonitrile at a flow rate of 1 mL/min. The elution was monitored both by UV absorbance (220 nm) and by fluorescence (excitation at 340 nm; emission at 500 nm; Gorman *et al.*, 1987). The peak having the highest fluorescence was collected and sequenced on an Applied Biosystems protein sequencer (Model 477A) operated by the Virginia Tech sequencing facility.

Site-Directed Mutagenesis and Gene Replacement. Methods for site-directed mutagenesis and gene replacement were the same as previously described for the analysis of the *nifD* gene from *A. vinelandii* (Brigle *et al.*, 1987). The template used for mutagenesis was an *Xba*I fragment containing the entire *nifS* gene from pDB551 (Zheng *et al.*, 1993) cloned into the M13mp18 *Xba*I site. The codon for Cys^{325}, UGC, was changed to GCC. The oligonucleotide primer used for mutagenesis had the following sequence: 5'GGTTCGGCCGCCACCTCCGG3'.

Identification of the NIFS-Bound Persulfide. The procedure for the identification of a NIFS-bound persulfide is outlined in Figure 1. In a typical experiment 4.4 mg (100 nmol) of NIFS was incubated with or without 100 nmol of L-cysteine (substrate-treated enzyme, as in the left route, or untreated enzyme, as in the right route, respectively) in 50 mM Tris·HCl buffer, pH 8.0, for 10 s (step 1 in Figure 1) before 300 nmol of 1,5-I-AEDANS was added (step 2 in Figure 1). The reaction was allowed to proceed for 30 min before the excess of the 1,5-I-AEDANS was removed by washing three times with the above buffer using ultrafiltration. The protein samples were then brought to 2 mL with the buffer and equally divided. An aliquot of 1 M DTT was added to one sample to give a final concentration of 5 mM to reduce any disulfide bond formed between NIFS and the fluorescent compound (step 3 in Figure 1). The other half was not reduced and served as a control. After incubation for 30 min, small molecules were separated from protein by washing twice using a ultrafiltration Centricon 30 device. All of the samples were then brought to 2 mL with Tris·HCl buffer and the relative concentrations of the 1,5-I-AEDANS derivatives determined spectrofluorometrically. The *N*-(thioacetyl)-*N'*-(5-sulfo-1-naphthyl)ethylenediamine produced by reductive cleavage of the disulfide adduct with DTT was identified by its quantitative methylation to *N*-[(methylthio)acetyl]-*N'*-(5–sulfo-1-naphthyl)ethylenediamine using excess methyl iodide in diluted aqueous ammonia and comparing the R_f of this methylated product with that of a synthetic sample of *N*-[(methylthio)-acetyl]-*N'*-(5-sulfo-1-naphthyl)ethylenediamine. The authentic sample of *N*-[(methylthio)acetyl]-*N'*-(5-sulfo-1-naphthyl)ethylenediamine was prepared by reacting 1,5-AEDANS with an excess of methylthiol in aqueous ammonia. In each case, the methylated products were separated from the salts by retention on a Sep-Pak C_{18} cartridge (Waters Associates, Milford, MA), the column was washed with water, and the compounds were eluted with 60% acetonitrile in water. The fluorescent compounds were then analyzed by TLC using

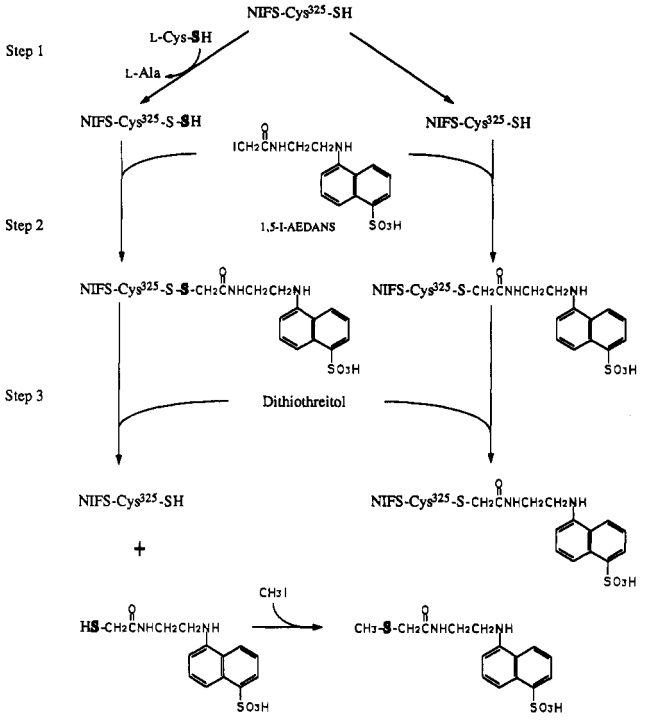

FIGURE 1: Scheme for the identification of a NIFS-bound persulfide. The left route shows the formation of a persulfide on NIFS when incubated in the presence of the substrate L-cysteine (step 1), the alkylation of this persulfide by 1,5-I-AEDANS (step 2), and the reduction of the disulfide bond between the NIFS and the fluorescent complex (step 3). The right route shows the control experiment in which the substrate cysteine was omitted. Under this condition 1,5-I-AEDANS reacts directly with Cys^{325} to form a stable enzyme-bound thioether and, thus, no fluorescent group should be released from the enzyme by reduction with DTT. The total fluorescence bound to NIFS at step 2 was approximately equal for both samples. Quantitation of the relative amounts of the fluorescent compound released in these schemes gave the following results: 81% of the total fluorescent compound bound to NIFS was released by DTT treatment in the left route, whereas only 1.4% of the fluorescent compound bound to NIFS was released by DTT treatment in the right route. The alkylation step used to identify the fluorescent compound released by DTT treatment is shown at the bottom of the scheme.

two different solvent systems, acetonitrile–water–formic acid (180:20:10 v/v/v) and acetonitrile. 1,5-I-AEDANS had R_f values of 0.63 in the first solvent system and 0.175 in the second, whereas the methylated product had R_f values of 0.59 in the first solvent system and 0.11 in the second. The compounds were readily visualized on the TLC plate as bright blue fluorescent bands when the plate was exposed to UV light.

NIFS Desulfuration Reaction in ^2H_2O. L-Alanine, L-cysteine, and Tris·HCl buffer were prepared in ^2H_2O and titrated to pH 8.0 using HCl or NaOH. NIFS was transferred to 50 mM Tris·HCl prepared in ^2H_2O and equilibrated by repetitive dilution and ultrafiltration using the deuterated buffer. Following this treatment the $^1H/^2H$ ratio was calculated to be less than 1/30. L-Alanine (20 μmol) or L-cysteine (1 μmol) was incubated with 0.5 mg of NIFS in a 1-mL reaction mixture containing 50 mM Tris·HCl buffer for 2 h. After the reaction, the amino acids were separated from NIFS by ultrafiltration and analyzed by GC–MS as described above in the analysis of γ-methylcystathionine.

RESULTS

Allylglycine and Vinylglycine Are Suicide Inhibitors of NIFS-Catalyzed Cysteine Desulfurization Activity. Olefinic

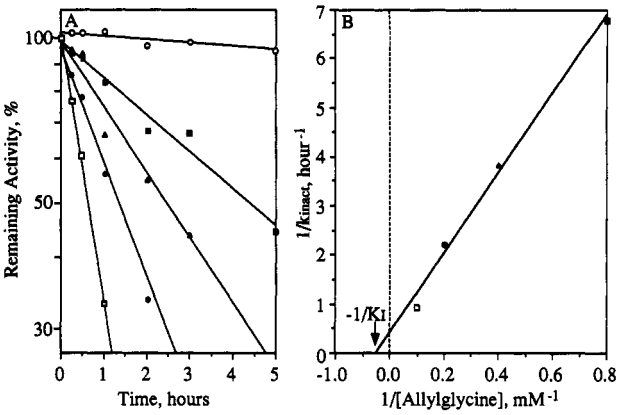

FIGURE 2: Inhibition of NIFS activity by L-allylglycine. (A) Time-dependent loss of NIFS activity by incubation with no (○), 1.25 mM (■), 2.5 mM (▲), 5.0 mM (●) and 10 mM (□) allylglycine. (B) Double-reciprocal plots of the observed rate constant vs the concentration of allylglycine using the data in panel A. $k_{inact} = \ln 2/T_{1/2}$, where $T_{1/2}$ is the half-life of the NIFS activity under a certain concentration of allylglycine.

amino acids are often used as mechanism-based suicide inhibitors of PLP enzymes (Cooper, 1983; Walsh, 1986). In this study L-allylglycine and L-vinylglycine were used to investigate the mechanism of NIFS-catalyzed cysteine desulfurization. Incubation of NIFS with allylglycine resulted in a time-dependent loss of cysteine desulfurase activity (Figure 2A). Such inhibition was not reversed by addition of the substrate L-cysteine, nor was it reversed by addition of PLP or DTT. Furthermore, extensive dialysis of the allylglycine-inhibited enzyme did not result in its reactivation. DL-Allylglycine, at a concentration twice as great, inactivated NIFS-catalyzed cysteine desulfurase activity at the same rate as L-allylglycine. These results indicate that allylglycine inhibition of NIFS activity requires an enzymatic reaction that is specific for the L-form of the olefinic amino acid which is consistent with the requirement of L-cysteine as substrate in the desulfurization reaction (Zheng *et al.*, 1993). A kinetic analysis showed that NIFS inactivation by allylglycine is a pseudo-first-order reaction (Figure 2A) having an apparent K_I of 20 mM (Figure 2B). In contrast, the apparent K_M for L-cysteine is about 75 μM.

To test whether or not NIFS can use L-allylglycine as substrate to catalyze formation of a product, we searched for product formation following the co-incubation of NIFS and L-allylglycine. On the basis of thin-layer chromatography using ninhydrin detection, such incubation of NIFS and L-allylglycine did not lead to formation of a product that could be distinguished from the substrate L-allylglycine. Because allylglycine irreversibly inactivates NIFS, it seemed more likely that a protein-bound covalent adduct was formed during the inactivation. Two possible routes for allylglycine inactivation of NIFS can be considered. One route could involve a mechanism-based suicide inactivation in which the enzyme tautomerizes the terminal double bond of allylglycine followed by nucleophilic attack by the proposed active site cysteinyl at the γ-carbon (Scheme 1). This mechanism has precedence in cystathionine γ-synthase which is able to catalyze the condensation of a PLP–allylglycine adduct and L-cysteine to form γ-methylcystathionine (Brzović *et al.*, 1990). It should be noted here that the protonation of the quinonoid form of PLP and the deprotonation of the reactive cysteine are not necessarily coupled as shown in Scheme 1 but are presented in this way for convenience. Also, the L-structure of the final product shown in Scheme 1 was not determined experimentally

Scheme 1: Proposed Mechanism of NIFS Inhibition by L-Allylglycine

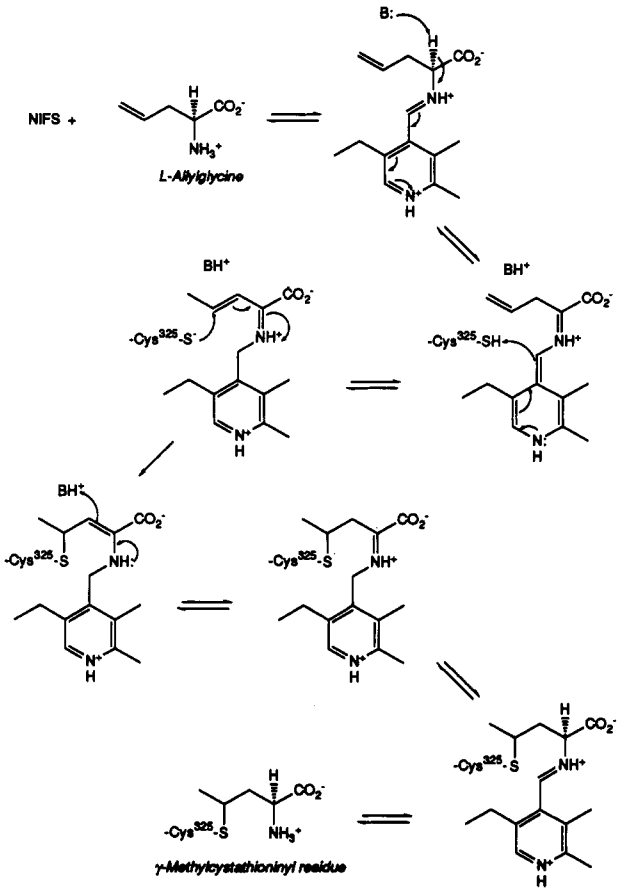

but was inferred from the fact that L-alanine is the product of the NIFS-catalyzed cysteine desulfuration reaction (Zheng *et al.*, 1993). An alternative possibility is that the inactivation is not mechanism based but involves a simple addition reaction which occurs by nucleophilic attack at the δ-carbon to form homocystathionine. Of the two possible mechanisms, the former was confirmed by the identification of γ-methylcystathionine as one of the amino acids produced by the acid hydrolysis of the allylglycine inactivated enzyme (Figure 3). γ-Methylcystathionine was identified in the acid hydrolysate of the L-allylglycine-treated enzyme by comparing the gas chromatographic retention time and the mass spectra of the *n*-butyl trifluoroacetyl derivative of isolated and known compounds (Figure 3). The known compounds used in the analysis were γ-methylcystathionine and homocystathionine, the corresponding products expected by attack at either the γ- or δ-carbon of allylglycine, respectively, and these were readily distinguished by their mass spectroscopic fragmentation pattern (Figure 3) and gas chromatographic retention times (data not shown).

The pattern of inhibition by L-vinylglycine on cysteine desulfurase activity catalyzed by NIFS was more complicated because vinylglycine serves as both a substrate and a suicide inhibitor. In our initial experiments, approximately equimolar amounts of vinylglycine and NIFS were co-incubated, which resulted in deamination of vinylglycine to yield ammonia and an α-keto compound, most likely α-ketobutyrate. Thus, NIFS and cystathionine γ-synthase share another feature in that both are able to catalyze deamination of vinylglycine (Brzović *et al.*, 1990). Under these conditions there was no apparent inactivation of the NIFS-catalyzed cysteine desulfurase activity. In contrast, NIFS lost all cysteine desulfurase activity

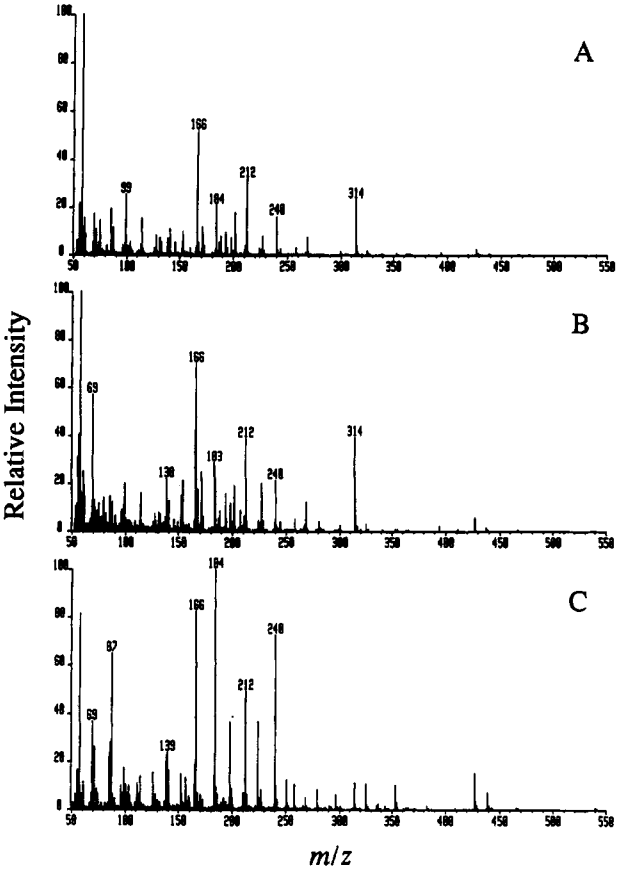

FIGURE 3: 70-eV mass spectra of *n*-butyl trifluoroacetyl derivatized samples. (A) The complex isolated from hydrolysis of L-allylglycine inactivated NIFS; (B) γ-methylcystathionine; (C) homocystathionine. The preparation of the samples is described under Experimental Procedures.

when incubated with a large molar excess of vinylglycine. Using the same methods decribed above for the allylglycine-inactivated enzyme, it was shown that vinylglycine inactivation occurred through formation of a cystathionyl residue. The vinylglycine deamination reaction catalyzed by NIFS apparently does not require participation of the reactive cysteinyl residue because allylglycine-treated NIFS, vinylglycine-treated NIFS, and an altered form of NIFS that has an alanyl substitution for the active site cysteinyl residue (discussed below) were all able to catalyze the deamination reaction at rates comparable to that of the native enzyme. The mechanisms for the deamination of L-vinylglycine catalyzed by NIFS and the vinylglycine-directed suicide inactivation of NIFS cysteine desulfurase activity are presented in Scheme 2.

Identification of the Reactive Cysteinyl Residue in NIFS. From the above experiments and our previous results (Zheng *et al.*, 1993) it is known that NIFS has a reactive cysteinyl residue that is necessary for cysteine desulfurase activity. Blocking of a reactive thiolate group located on NIFS by using either a thiol-specific alkylating reagent or an olefinic amino acid analog results in irreversible inactivation of NIFS activity. Like *N*-ethylmaleimide, 1,5-I-AEDANS is able to react stoichiometrically with NIFS to effect greater than 90% loss of enzymatic activity (results not shown). Thus, the fluorescent property of 1,5-I-AEDANS was used to identify the reactive cysteinyl residue located on NIFS. In these experiments native NIFS was first alkylated by treatment with 1,5-I-AEDANS and subsequently denatured, alkylated with iodoacetamide, and digested with trypsin. After digestion, the resultant peptides were separated by reversed phase HPLC

Scheme 2: Proposed Mechanism of NIFS Inhibition by L-Vinylglycine

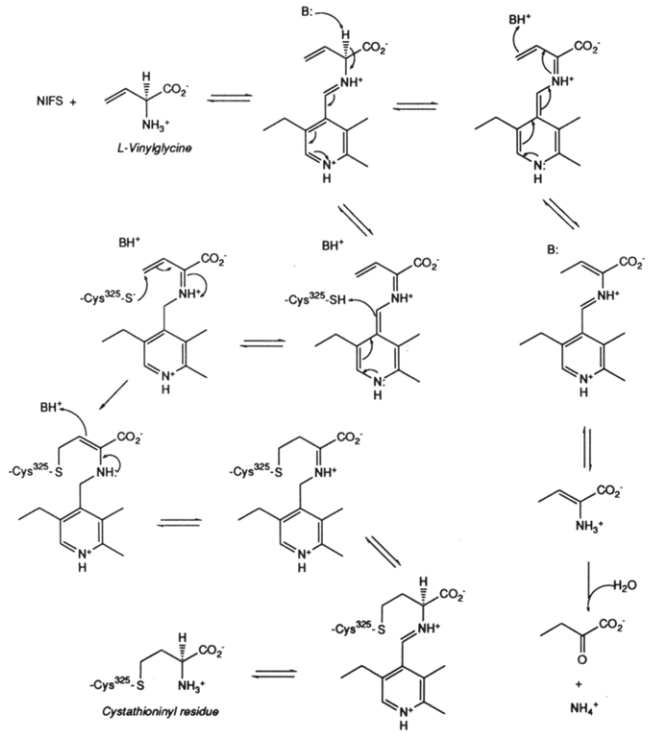

and the elution position of the dansylated peptide was determined by simultaneously monitoring the HPLC profile at 220 nm and the fluorescence emission at 500 nm (Figure 4). The major fluorescent peptide peak was eluted at ~25 min, and this fraction was collected and its sequence determined by automated amino acid sequence analysis. In this way the dansylated peptide was shown to have the N-terminal sequence Val-Gly-Ile-Ala-Ala-Ser-Ser-Gly-Ser-Ala-X-Thr, where the Val residue and the unidentified residue (X) respectively correspond to the Val^{315} and Cys^{325} positions in the NIFS primary sequence. On the basis of the primary sequence of NIFS deduced from the gene sequence (Beynon *et al.*, 1987; see Figure 4, top panel), formation of a peptide having this N-terminal sequence upon tryptic digestion of NIFS was expected. Also, Cys^{325} is the only cysteinyl residue expected to be present in this peptide.

That the hyperreactive Cys^{325} is, in fact, located at the active site was also shown by a site-directed mutagenesis experiment in which the Cys^{325} codon was substituted by an alanine codon. When this mutation was transferred to the *A. vinelandii* chromosome, it conferred the same diazotrophic growth characteristics previously reported for *nifS* deletion mutants (Jacobson *et al.*, 1989). In addition, the purified NIFS–Ala^{325} protein was shown to be inactive in the cysteine desulfurase assay but active in the vinylglycine deamination reaction. In another series of experiments NIFS, vinylglycine-treated NIFS, allylglycine-treated NIFS, and NIFS–Ala^{325} were individually incubated with 1,5-I-AEDANS. The NIFS proteins treated in this way were then separated from the excess of the fluorescent alkylating reagent by SDS–PAGE and analyzed by fluorography and Coomassie staining. The results of these experiments (Figure 5) show that substitution of an alanyl residue for Cys^{325} eliminates reactivity of NIFS toward alkylation. There are three other cysteinyl residues within the NIFS primary sequence (Beynon *et al.*, 1987), and therefore, these results confirm that Cys^{325} provides the only reactive thiolate in the native protein and agree well with the

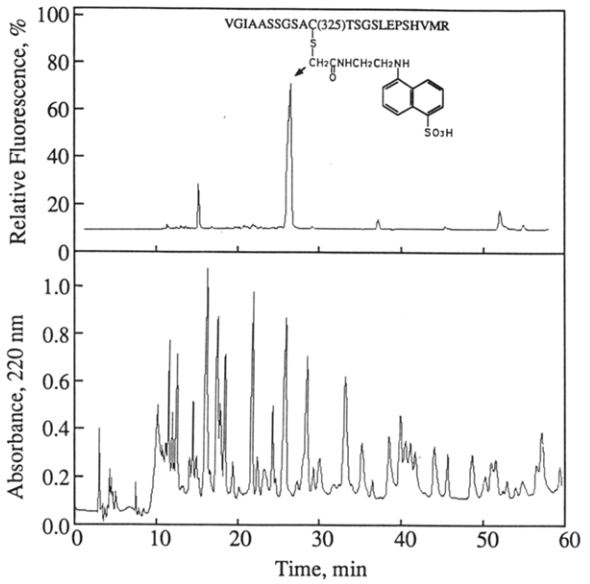

FIGURE 4: Reversed phase HPLC profiles of the tryptic digests of NIFS. Native NIFS (120 μg) was labeled with 1,5-I-AEDANS, then denatured, alkylated, digested with trypsin, and separated by HPLC with a gradient from 20 to 40% acetonitrile in water (v/v) from 5 to 55 min. The elution was monitored at 220 nm and fluorescence emission at 500 nm. The sequence of the peak with highest fluorescence was identified by automated amino acid sequencing. The structure of the peptide–1,5-I-AEDANS adduct is as shown in the upper panel. A time course of trypsin digestion revealed that the leftward fluorescent peak in the upper panel respresents a product of incomplete digestion.

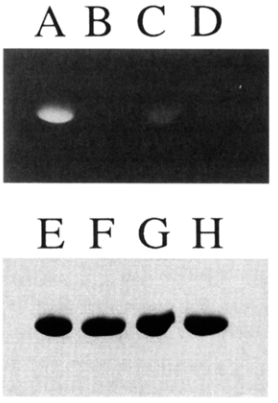

FIGURE 5: SDS–PAGE of modified NIFSs. NIFS, vinylglycine-inactivated NIFS, allylglycine-inactivated NIFS, or NIFS-Ala^{325} (20 μg each) was incubated with an equal molar amount of 1,5-I-AEDANS in 20 μL of 50 mM Tris·HCl buffer, pH 8.0, at ambient temperature for 60 min. The samples were then loaded onto an SDS–PAGE. After electrophoresis, the gel was visualized first by fluorography and then by Coomassie staining. Lanes A, B, C, and D, fluorography of NIFS, vinylglycine-treated NIFS, allylglycine-treated NIFS, and NIFS-Ala^{325}, respectively. Lanes E, F, G, and H, Coomassie stain of the same samples as shown in lanes A, B, C, and D, respectively.

observation that NIFS activity can be quantitatively inhibited by treatment with an equimolar amount of an alkylating reagent (Zheng *et al.*, 1993). Also, when an excess of 1,5-I-AEDANS was reacted with NIFS and the unreacted alkylating reagent subsequently removed by dialysis, it was found, on the basis of the extinction coefficient of cysteine-treated 1,5-I-AEDANS, that 1,5-I-AEDANS reacted with NIFS monomers at a 1.1 to 1 molar ratio. Finally, neither vinylglycine- nor allylglycine-treated NIFS could be effectively labeled with the fluorescent alkylating reagent when compared to alkylation of the native enzyme. This result indicates that Cys^{325} provides the thiolate which reacts with the respective

Scheme 3: Proposed Mechanism of NIFS Desulfuration Reaction

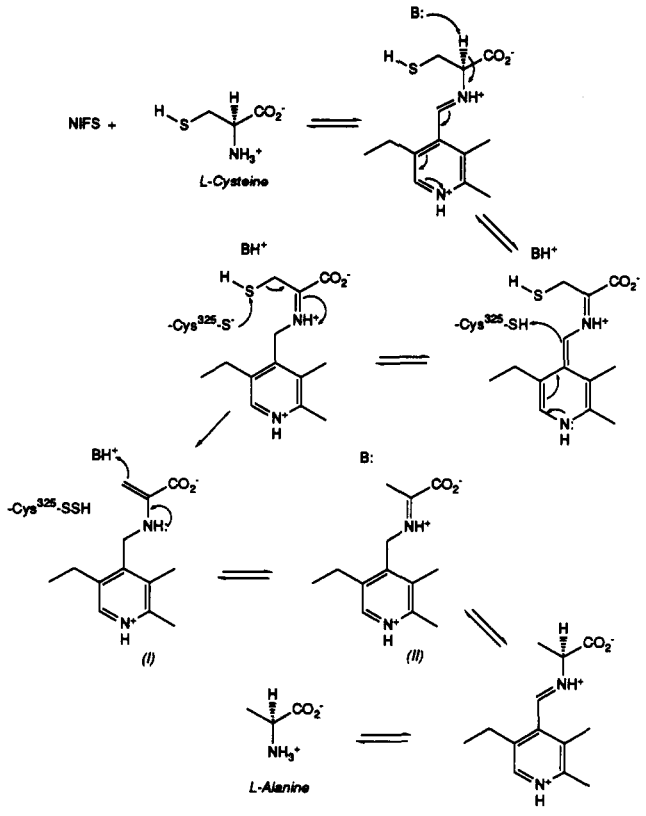

enzyme-bound analog adducts to form either a γ-methylcystathionyl or a cystathionyl residue.

Persulfide Formation Is an Intermediate in NIFS-Catalyzed Desulfuration of L-*Cysteine.* In Scheme 3 a mechanism for NIFS is proposed in which L-cysteine desulfurization occurs by nucleophilic attack of the active site Cys^{325} thiolate on the substrate cysteine PLP adduct. If correct, this mechanism predicts the formation of an enzyme-bound persulfide as an intermediate in the reaction. We therefore tested for the formation of such a persulfide during NIFS catalysis by reacting the substrate-treated enzyme with the alkylating reagent 1,5-I-AEDANS and asking if a disulfide linkage was formed from an enzyme-bound persulfide and the alkylating reagent. In a separate control experiment the untreated enzyme was also reacted with 1,5-I-AEDANS to form the stable thioether derivative. The rationale and results of these experiments are presented in Figure 1. The results show that reaction of 1,5-I-AEDANS with the substrate-treated form of NIFS results in formation of a DTT-reducible disulfide bond in more than 80% of the enzyme. The fluorescent species released from the substrate-treated enzyme by reducing this disulfide bond was shown to be *N*-(thioacetyl)-*N'*-(5-sulfo-1-naphthyl)ethylenediamine. In contrast, the fluorescent NIFS derivative obtained by reacting the untreated enzyme with 1,5-I-AEDANS could not be released by treatment with DTT.

Evidence for the Reversible Formation of an Enamine Intermediate during L-*Cysteine Desulfurization Catalyzed by NIFS.* To further characterize the mechanism by which NIFS catalyzes the desulfurization of L-cysteine, the reaction was carried out in the presence of ^2H_2O and the deuterium incorporated into the reactants and products was determined by GC–MS analysis of their *n*-butyl trifluoroacetyl derivatives. Under these reaction conditions it was found that alanine generated by desulfurization of L-cysteine was completely deuterated. Thus, during the formation of the alanine product, the α- and β-hydrogens are all readily exchanged. The observed complete exchange of the β-hydrogens can be explained by the rapid equilibration of the enamine form of the product (compound **I**, Scheme 3) with the ketimine form of the product (compound **II**, Scheme 3) before rearrangement and separation of the alanine from the enzyme. It was observed that the α-hydrogen of all the cysteine remaining in the reaction mixture had been exchanged as well. Thus, it appears that the slow step in the reaction involves displacement of the sulfur from the bound cysteine.

It was also found that the α-hydrogen and all three β-hydrogens of a small fraction of L-alanine became deuterated when NIFS was incubated with L-alanine in ^2H_2O. Thus, exchange occurred at all four positions or not at all. This result indicates that L-alanine reacts slowly with the enzyme but once the alanine–PLP adduct is formed there is rapid exchange of all four hydrogens. The mechanism for the rapid exchange of the β-hydrogens is most likely explained as discussed above for the rapid equilbration of compounds **I** and **II** shown in Scheme 3. The exchange of the α-hydrogen would occur during the rearrangement of compound **II** to alanine. These results are similar to those of Babu and Johnston, who reported the complete exchange of the α- and β-hydrogens of alanine catalyzed by glutamic-pyruvic transaminase and glutamic-oxaloacetic transaminase (Babu & Johnston, 1976). Our results and the observation that millimolar amounts of L-alanine do not significantly inhibit NIFS-catalyzed cysteine desulfurase activity thus reflect a rather slow binding/dissociation of L-alanine with NIFS relative to formation of the enamine intermediate.

DISCUSSION

We have previously shown that the product of the *nifS* gene is an L-cysteine desulfurase which catalyzes the removal of cysteine sulfur to form L-alanine and elemental sulfur (Zheng *et al.*, 1993). Our current hypothesis is that the reaction catalyzed by NIFS represents a step in the formation of the Fe–S cores contained within the nitrogenase component proteins. In particular, we have suggested that NIFS catalyzes formation of an enzyme-bound persulfide which is the active species for providing the inorganic sulfide necessary for Fe–S cluster biosynthesis. In Scheme 3 a model that describes the proposed mechanism for the formation of an enzyme-bound persulfide using PLP chemistry and cysteine substrate is shown. The salient and novel feature of the model is nucleophilic attack by an active site cysteinyl thiolate anion on the sulfur of a cysteine–PLP adduct. This nucleophilic attack results in formation of a cysteinyl persulfide and an enamine derivative of alanine. In the present study, three basic features predicted by such a mechanism were experimentally confirmed: An essential active site cysteinyl thiolate (Cys^{325}) was identified, formation of an enzyme-bound persulfide was demonstrated, and indirect evidence for formation of an enamine intermediate during L-alanine formation was obtained. Furthermore, derivatization of the active site cysteinyl residue by incubation of NIFS with the mechanism-based inhibitors, allylglycine or vinylglycine, to form an enzyme-bound γ-methylcystathionyl or cystathionyl residue, respectively, clearly demonstrates that a cysteinyl thiolate is poised for nucleophilic attack at the appropriate substrate position (see Schemes 1–3). The observation that treatment of NIFS with L-allylglycine or L-vinylglycine specifically blocks alkylation of the Cys^{325} residue and the results of site-directed mutagenesis experiments, which show that Cys^{325} is required for cysteine desulfurase activity, also support this conclusion.

To our knowledge the cleavage of L-cysteine to yield L-alanine and sulfur by the mechanism presented in Scheme 3 represents a PLP-based biochemical reaction not previously described. It involves cleavage of a C–S bond by nucleophilic attack of a substrate cysteine sulfur by a protein cysteinyl anion with the expulsion of a stabilized β-carbanion of alanine. Although cleavage of a C–S bond by an attacking thiolate anion has not been described for biological systems, there is chemical precedence for such a reaction. One example is the thioalkylation of a thiocyanate to generate an unsymmetrical disulfide (Wijers *et al.*, 1969). This reaction proceeds by the nucleophilic attack of a thiolate anion at the sulfur of thiocyanate with the consequent expulsion of cyanide as the leaving group. Another example is the formation of dimethyl disulfide from the reaction of an α-methylthio ester with methyl thiolate (Trost, 1974). In this reaction the ester-stabilized C-2 anion facilitates the reaction.

The mechanism proposed here for NIFS-catalyzed cysteine desulfurization is different from that proposed for the analogous reaction catalyzed by selenocysteine β-lyase, which cleaves L-selenocysteine to yield L-alanine and elemental selenium (Esaki *et al.*, 1982, 1985). The most significant difference is that an active site cysteinyl is required for elimination of sulfur from L-cysteine in the NIFS-catalyzed reaction and an enzyme-bound persulfide is an intermediate in that process. In contrast, Esaki *et al.* have proposed a two-base mechanism analogous to aspartate β-decarboxylase (Chang *et al.*, 1982) in which selenium is directly released in elemental form from selenocysteine. Another difference is that NIFS is able to catalyze both the desulfurization of L-cysteine and removal of selenium from selenocysteine, whereas selenocysteine β-lyase is reported to be specific for selenocysteine. Although the NIFS-catalyzed elimination of selenium from selenocysteine has not been characterized in detail, this reaction is probably mechanistically similar to the cysteine desulfurase reaction because Cys^{325} is required for both activities. It is unlikely that elimination of selenium from selenocysteine catalyzed by NIFS is a physiologically relevant reaction, however, because Se is not required for biological nitrogen fixation.

In summary, the requirement of NIFS for the full activation of the nitrogenase component proteins, both of which require the formation of Fe–S cores for their respective activities, and the cysteine desulfurase activity exhibited by NIFS indicate a role for NIFS in the activation of the inorganic sulfide required for Fe–S core formation. Results of the present work which demonstrate the formation of an enzyme-bound persulfide as an intermediate in the desulfurization of L-cysteine provide evidence for this idea. It is of particular interest that NIFS-like proteins have also been recently identified in non-nitrogen fixing organisms (Sun & Setlow, 1993; Kolman & Söll, 1993). These findings, and the strong sequence conservation among NIFS and NIFS-like proteins in the region surrounding and including the active site cysteinyl residue identified for NIFS (Zheng *et al.*, 1993), suggest that the mechanism determined here for NIFS activity could represent a global mechanism for the mobilization of the inorganic sulfide required for Fe–S cluster biosynthesis.

ACKNOWLEDGMENT

We thank Dr. Jiann-Shin Chen for discussions, Dr. Robert S. Phillips for comments on the manuscript, and Kim C. Harich for technical assistance.

REFERENCES

Babu, U. M., & Johnston, R. B. (1976) *Biochemistry 15*, 5671–5678.

Beynon, J., Ally, A., Cannon, M., Cannon, F., Jacobson, M., Cash, V., & Dean, D. R. (1987) *J. Bacteriol. 169*, 4024–4029.

Brigle, K. E., Newton, W. E., & Dean, D. R. (1985) *Gene 37*, 37–44.

Brigle, K. E., Setterquist, R. A., Dean, D. R., Cantwell, J. S., Weiss, M. C., & Newton, W. E. (1987) *Proc. Natl. Acad. Sci. U.S.A. 84*, 7066–7069.

Brzović, P., Holbrook, E. L., Greene, R. C., & Dunn, M. F. (1990) *Biochemistry 29*, 442–451.

Burgess, B. K. (1990) *Chem. Rev. 90*, 1377–1406.

Chang, C., Laghai, A., O'Leary, M. H., & Floss, H. G. (1982) *J. Biol. Chem. 257*, 3564–3569.

Cooper, A. J. L. (1983) *Annu. Rev. Biochem. 52*, 187–222.

Dean, D. R., & Jacobson, M. R. (1992) in *Biological nitrogen fixation* (Stacey, G., Burris, R. H., & Evans, H. J., Eds.) pp 763–834, Chapman and Hall, New York.

Dilworth, M. J., Eldridge, M. E., & Eady, R. R. (1992) *Anal. Biochem. 207*, 6–10.

Esaki, N., Nakamura, T., Tanaka, H., & Soda, K. (1982) *J. Biol. Chem. 257*, 4386–4391.

Esaki, N., Karai, N., Nakamura, T., Tanaka, H., & Soda, K. (1985) *Arch. Biochem. Biophys. 238*, 418–423.

Georgiadis, M. M., Komiya, H., Chakrabarti, P., Woo, D., Kornuc, J. J., & Rees, D. C. (1992) *Science 257*, 1653–1659.

Gorman, J. J., Corino, G. L., & Mitchell, S. J. (1987) *Eur. J. Biochem. 168*, 169–179.

Jacobson, M. R., Cash, V. L., Weiss, M. C., Laird, N. F., Newton, W. E., & Dean, D. R. (1989) *MGG, Mol. Gen. Genet. 219*, 49–57.

Kim, J., & Rees, D. C. (1992) *Science 257*, 1677–1682.

Kolman, C., & Söll, D. (1993) *J. Bacteriol. 175*, 1433–1442.

Sun, D., & Setlow, P. (1993) *J. Bacteriol. 175*, 1423–1432.

Trost, B. M. (1974) in *Organic sulphur chemistry, structure, mechanism and synthesis* (Stirling, C. J. M., Ed.) pp 237–264, Butterworth, London.

Walsh, C. T. (1986) in *Vitamin B6, pyridoxal phosphate, chemical, biological and medical aspects* (Dolphin, D., Poulson, R., & Avramovic, O., Eds.) Part B, pp 43–70, Wiley, New York.

White, R. H., & Rudolph, F. B. (1978) *Biochim. Biophys. Acta 542*, 340–347.

Wijers, H. E., Boelens, H., & Van der Gen, A. (1969) *Recl. Trav. Chim. Pays-Bas 88*, 519–529.

Zheng, L., White, R. H., Cash, V. L., Jack, R. F., & Dean, D. R. (1993) *Proc. Natl. Acad. Sci. U.S.A. 90*, 2754–2758.

Two Crystal Structures of the B1 Immunoglobulin-Binding Domain of Streptococcal Protein G and Comparison with NMR†,‡

Travis Gallagher,* Patrick Alexander, Philip Bryan, and Gary L. Gilliland*

Center for Advanced Research in Biotechnology, University of Maryland Biotechnology Institute, and the National Institute of Standards and Technology, 9600 Gudelsky Drive, Rockville, Maryland 20850

Received November 24, 1993; Revised Manuscript Received January 28, 1994®

ABSTRACT: The structure of the 56-residue B1 immunoglobulin-binding domain from streptococcal protein G has been determined in two different crystal forms. The crystal structures were deduced by molecular replacement, based on the structure of the B2 domain (Brookhaven accession code 1PGX). Final R values are 0.174 and 0.198 for orthorhombic and trigonal forms, for diffraction data from 6.0 to 2.07 Å and from 6 to 1.92 Å, respectively. The orthorhombic crystals have an unusually high packing density for protein crystals, with V_m = 1.66 and a solvent content of 26%. The protein structure is found to be very similar (rms deviation 0.25 Å for 56 Cα's) in the two crystal forms, with an efficiently packed hydrophobic core between a four-stranded β-sheet and a four-turn α-helix. The B1 domain has the same fold and general structure as the B2 domain (rms deviations 0.36 and 0.39 Å), despite the six residue differences between them. The crystallographic models differ from NMR-derived models in several local regions, primarily in the loop involving residues 46–51; other significant variations are observed in the helix and in the structure of bound water. The primary crystal contact is the same in both crystal forms, involving both sheet edges to form extended β-sheets throughout the crystals.

Many infectious bacteria display surface proteins that bind tightly to immunoglobulins and other host proteins, and some of these bacterial proteins have found useful roles in the laboratory and clinic. The most familiar example is protein A from *Staphylococcus*, whose affinity for IgG confers wide utility in antibody separation procedures. Protein G from *Streptococcus*, Lancefield group G, also binds human IgG in the Fc region (Myhre & Kronvall, 1977). This protein consists of a series of small binding domains separated by linkers, and a cell-wall anchor near the C-terminus. Two (in some strains, three) of the domains bind IgG; another two or three domains bind serum albumin. The binding interactions are believed to help the pathogen evade the host's immune response by mimicking the "self"-markers commonly displayed by host cells. The IgG-binding domains of protein G are of increasing interest due to their broad biomedical utility (e.g., in purifying antibodies) and for studies of folding and stability. They are minimal folding units of high thermostability, without disulfides or cofactors. The domains are also remarkable for their sequence parsimony: they are devoid of serine, cysteine, arginine, proline, histidine, and, in the native form, methionine.

The IgG-binding domains of protein G are identified as B1, B2, etc., numbering from the N-terminus of the native protein G molecule. The subject of the present study, B1, is identical to the B1 domain in strain GX7809 (Fahnestock et al., 1986), wherein there are six residue differences between domains B1 and B2. These six, with the B1 residue given first, are 16V,[1] L7I, E19K, A24E, V29A, and E42V. The melting temperatures of B1 and B2 at pH 5.4 are 87.5 and 79.4 °C, respectively (Alexander et al., 1992). Protein G, proteolytically released from streptococci, binds human IgG with an association constant of 6.7×10^{10} M^{-1} (Akerstrom & Bjork, 1986). The B1 and B2 domains bind to the Fc fragment of IgG with association constants of 3×10^6 and 1×10^7 M^{-1}, respectively, as determined by titration calorimetry (Alexander, unpublished data). The isoelectric points for the two domains are 4.0 and 4.7, respectively (Alexander et al., 1992a). The three-dimensional structure of the B1 domain was first determined by NMR techniques (Gronenborn et al., 1991). The fold was shown to consist of a four-stranded sheet and a helix. Both sheet and helix are strongly amphipathic, with a hydrophobic core between them. The five secondary structure elements are connected by four loops, L1, L2, L3, and L4 (see Table 1 for sequence and secondary structure information). The structures of both domains, from a different bacterial strain in which B1 contains the I6V and L7I substitutions, were determined by NMR (Lian et al., 1992). The crystal structure of the B2 domain has also been reported (Achari et al., 1992), as has a complex of a B3 domain and an Fab fragment (Derrick & Wigley, 1992). While the domains consist of 56 residues, some of these studies involve constructs with extra lengths of polypeptide at either end, with the result that residues are numbered differently. In the present paper, residue numbers are identical to those used by Gronenborn et al. (1991), 5 less than those used by Lian et al. (1992), and 13 less than those of Achari et al. (1992).

Table 1: Amino Acid Sequence and Locations of Loops in the B1 Domain of Protein G

```
          L1          L2    (..helix..)     L3        L4
        ** **       * **                  *** *     ****
MTYKLILNGK TLKGETTTEA VDAATAEKVF KQYANDNGVD GEWTYDDATK TFTVTE
         10          20        30          40          50    56
```

[†] This work was supported in part by NSF Grant MCB-92-19309.

[‡] The refined models have been submitted to the Brookhaven Protein Data Bank under filenames 1PGA and 1PGB.

* To whom correspondence should be addressed at the Center for Advanced Research in Biotechnology. Phone: (301) 738-6272. FAX: (301) 738-6255.

® Abstract published in *Advance ACS Abstracts*, March 15, 1994.

[1] Abbreviations: A, Ala; C, Cys; D, Asp; E, Glu; F, Phe; G, Gly; H, His; I, Ile;, K, Lys; L, Leu; M, Met; N, Asn; P, Pro; Q, Gln; R, Arg: S, Ser; T, Thr; V, Val; W, Trp; Y, Tyr; rms, root mean square; NMR, nuclear magnetic resonance. Single-site mutations are denoted by the sequence number preceded by the original amino acid (using the one-letter abbreviation) and followed by the substituted amio acid.

0006-2960/94/0433-4721$04.50/0

The NMR structure of the B1 domain and the crystal structure of the B2 domain were compared by Achari et al. (1992). The structures were found to be similar (rms coordinate shift for Cα's 1.13 Å), with the main differences in the loops connecting secondary structure elements. Also noted was a difference of 10° in the angle of the helix relative to the sheet, and a variation in the structure of the C-terminal portion of the helix. A subsequent NMR investigation of ordered water in the solution structure has provided evidence for two specific found water sites, one of which is postulated to correlate with a distortion in the helix by involvement with the helix hydrogen bond 29O–33N (Clore & Gronenborn, 1992). Alexander et al. (1992) have investigated the unfolding and refolding of B1 and B2, providing measurements of the relevant thermodynamic and kinetic parameters. Their studies have been applied toward an explanation of the cooperative folding/unfolding transition and the high melting temperatures of IgG-binding domains, which are characteristic of small folding units and do not necessarily imply extreme stability at physiological temperatures. In addition, NMR sequence assignments and preliminary amide exchange studies have also been carried out on the B2 domain (Orban et al., 1992).

In order to provide a diffraction-based structural model of the B1 domain, for comparison with the B2 domain and for the assessment of differences in the results of NMR and X-ray methods, we undertook crystallographic studies of protein G, domain B1. Crystals in two different space groups were suitable for diffraction analysis and provided data for the two independent structure determinations described below. These structures are compared with each other and with those reported by Gronenborn et al. (1991), Lian et al. (1992), and Achari et al. (1992).

MATERIALS AND METHODS

The B1 domain was engineered for production as a 56-residue protein with N-terminal methionine (this position was threonine in the wild type). The sequences of B1 and B2 correspond to amino acids 228–282 and 298–352 of the gene sequence given by Fahnestock et al. (1986). Aspects of the cloning, expression, and purification of the domain are detailed by Alexander et al. (1992). Protein for crystallization was kept in 50 mM NaOAc, pH 4.5, and stored at 4 °C. Crystals were grown in 10-μL hanging drops by the vapor diffusion technique, using Linbro 24-well tissue culture plates. Crystal conditions were sought in the pH range 3.8–5.0 due to the domain's low p*I*. The only successful crystallization agent found was 2-methyl-2,4-pentanediol, in the range of 50–80%. Many crystal forms were observed from combinations of 2-methyl-2,4-pentanediol and various salts, although few crystals achieved sufficient size and diffraction quality. Crystals grew best at 18 °C, and required several weeks to grow. See Table 2 for crystal conditions.

Diffraction data were collected using X-rays generated by a Siemens rotating anode, operated at 40 kV and 70 mA. A Siemens focusing mirror system was utilized. A Siemens electronic area detector was positioned 100 mm from the crystal, and at a 2θ angle of 24°. Diffraction data collected with the area detector were recorded as a series of discrete frames or electronic images, each comprising a 0.2° scan in ω counted for 90 s. The temperature of data collection was 20 °C. The determination of crystal orientation and the integration of reflection intensities were performed with the XENGEN program system (Howard et al., 1987). Unweighted R_{sym} values were 0.070 and 0.068 for intensities in the orthorhombic and trigonal reduced data sets, respectively. See Table 2 for diffraction statistics.

Table 2: Crystallographic Data for the B1 IgG-Binding Domain in Two Crystal Forms

	orthorhombic	trigonal
crystal conditions	50% MPD[a] 50 mM NaCl 25 mM NaOAc pH 4.5 20% IPA[a] T = 18 °C	70% MPD 300 mM $MgSO_4$ 25 mM NaOAc pH 4.0 T = 18 °C
protein concentration (mg L^{-1})	10	10
crystal size (mm)	0.1 × 0.1 × 0.8	0.3 × 0.4 × 0.4
growth time (weeks)	4	2
habit	rectangular rod	irregular block
space group	$P2_12_12_1$	$P3_121$
a (Å)	37.04	36.63
b (Å)	25.08[b]	36.63
c (Å)	51.28	79.25
V_m	1.66	2.14
diffraction data		
reflections	2701	5014
resolution (Å)	2.04	1.86
R_{sym}[c]	0.070	0.068
$\langle I/\sigma \rangle$ in high-resolution shell	6.4	4.9

[a] Abbreviations: MPD, 2-methyl-2,4-pentanediol; IPA, 2-propanol. [b] The usual convention of naming orthorhombic cell edges in increasing order was broken to facilitate comparison with a monoclinic crystal form with a = 37.9 Å, b = 26.3 Å, c = 50.1 Å, and β = 100° (refinement in progress). [c] $R_{sym} = \sum_{hkl}|I_{ij} - \langle I \rangle_j G_{ij}|/\sum I_{ij}$.

Table 3: Refinement Data for the B1 IgG-Binding Domain in Two Crystal Forms

crystal	orthorhombic	trigonal
refinement		
resolution (Å)	6–2.07	6–1.92
reflections ($I > \sigma_I$[a])	2567	4493
data completeness (%)	85	93
final model		
protein atoms	436	436
solvent molecules	20	24
refined R[b]	0.174	0.198
deviations, rms[c,d]		
bonds (Å)	0.020	0.020
angles (deg)	1.970	2.045

[a] I = intensity. [b] $R = \sum_{hkl}||F_o| - |F_c||/\sum_{hkl}|F_o|$. [c] rms = root mean square. [d] Although the final refinement used PROLSQ, the rms deviations given are from the ideal parameters in XPLOR 3.1 parameter sets tophcsdx.pro and parhcsdx.pro (see Materials and Methods).

The structures were solved by molecular replacement using a suite of programs implemented in XPLOR 3.1 (Brunger et al., 1987). The search probe was a partially refined model of a mutant of the B2 domain (the V21C mutant), a structure currently in refinement that was solved by molecular replacement using the B2 crystal structure 1PGX (Achari et al., 1992) as a search probe. Subsequently, it was found that the 1PGX structure itself would suffice as a probe to solve the present structures. The B1 NMR structure 2GB1.PDB, although chemically identical, gave a weaker signal in the rotation function and hence was not used. The probe was prepared by removing the N- and C-terminal extensions and converting the following residues to alanine: all Glu, Gln, and Lys, both termini, and the seven residues different between B2:V21C and B1. In both cases the stepwise sequence of the molecular replacement method was rotation search, Patterson correlation refinement of rotation function peaks, translation search, rigid body refinement of the whole probe, and rigid body refinement of the probe divided into three parts (1–20, 21–39, 40–56). The resolutions of diffraction data used in

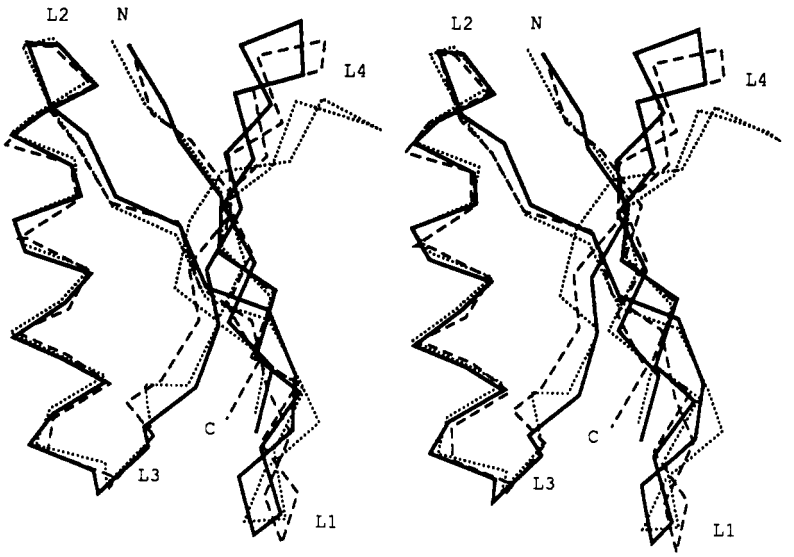

FIGURE 1: Stereo Cα superposition of the trigonal crystal form (solid lines) with the Gronenborn et al. (1991) NMR structure (dashed lines) and the first Lian et al. (1992) NMR structure (dotted lines). The greatest deviations among the models are in the four loops, especially L1 (residues 9–12), L3 (residues 38–41), and L4 (residues 47–50).

the rotation functions were 8.0–3.3 Å (orthorhombic form) and 9.0–3.4 Å (trigonal form). In both cases the solution was among the top three rotation function peaks, and Patterson correlation refinement amplified the solution to a clear maximum. The translation function results were unambiguous, and in the case of the trigonal space group, clearly distinguished between space group $P3_121$ and its enantiomorph $P3_221$. The R values of the translation function solutions were 0.39 and 0.42 for the orthorhombic and trigonal structures, and the corresponding values after rigid body refinement were 0.35 and 0.39.

The two structures were refined independently, in parallel, without reference to each other. Atomic positions and thermal parameters were initially refined using XPLOR, in a series of steps at increasing resolution. The topology and parameter sets used were tophcsdx.pro and parhcsdx.pro, respectively. Diffraction data with $I > \sigma(I)$ and with d spacings under 6 Å were included. Each step typically involved a round of simulated annealing and/or Powell minimization, followed by examination of electron-density maps to check progress, guide the building of the missing residues, and search for waters. Simulated annealing temperatures ranged from 4500 °C in early rounds to 1500 °C in late rounds. The program FRODO (Jones, 1987) was used on an Evans and Sutherland PS300 graphics system for inspection of electron-density maps and adjustment of the model. When nearly all the reflections had been included, several rounds of additional refinement were carried out by the restrained parameter least-squares procecedure of PROLSQ (Hendrickson & Konnert, 1980), which has been modified by Sheriff (1987) to restrain contacts between different molecules. Thermal parameters, which had been released in the late rounds of XPLOR refinement, were now refined to convergence under the least-squares restraints of PROLSQ.

To reduce bias to the probe structure and intermediate phasing models, annealed omit maps were used throughout refinement to guide manual refitting. About half the side chains were rebuilt or manually adjusted at least once in each refinement. This fact, and the large number of passes of simulated annealing (at least 20 for each structure), helps to ensure the independence of the final models. In a final test, atoms were deliberately mispoisitioned (to incorrect rotamers) and Fourier maps calculated. The R value invariably increased in such experiments, and the maps contained new peaks reflective of the displacements. The refinements of both structures are summarized in Table 3. The refined models are in the Brookhaven Protein Data Bank (Bernstein et al., 1977) under filenames 1PGA (orthorhombic) and 1PGB (trigonal).

Hydration of the protein was determined by examination of difference maps, with new water molecules being added to the model at chemically reasonable sites as indicated by electron-density maxima. Waters whose temperature factors refined to exceed 40 Å^2 or whose omit-map electron density dropped below the 3σ level were removed from the model. Finally waters were ranked by occ$^2/B$ (James & Sielecki, 1983). Crystal packing was analyzed as follows. First, atoms within 3.8 Å of another protein molecule were determined using the SAM CONTACTS routine in FRODO (Jones, 1987). These atoms were grouped into contacts (a "contact" was defined as the set of atoms on one molecule that are close to another single molecule). Contacts were ranked according to the number of atom pairs involved.

RESULTS

The two refined structures of the B1 IgG-binding domain from protein G superimpose with a root mean square deviation over 56 Cα positions of 0.25 Å, indicating that the structure of this protein is very similar in the two different crystals. In the core region, the deviations between the two structures are under 0.15 Å. The only differences in rotamers are in the side chains of the following surface residues: Met1, Lys4, Lys10, Glu15, Glu19, Lys28, Lys31, Gln32, Asn35, Glu42, and Lys50. All of these except Lys31 and Asn35 are involved in symmetry contacts in one or both of the crystal forms. The greatest Cα deviation (0.53 Å) is at residue 38 in the loop L3 (see Table 1 for sequence and secondary structure information). Due to the strong consensus between the two structures, the trigonal form will stand for both in most of the following comparisons. The trigonal form is chosen because its diffraction data extend to higher resolution, and because it has fewer crystal contacts.

The NMR structure of the chemically identical molecule (Gronenborn et al., 1991) and the NMR structure of a molecule differing only slightly (Lian et al., 1992) afford good comparisons of the X-ray and NMR methodologies. The Lian et al. (1992) report describes two domains referred to as II

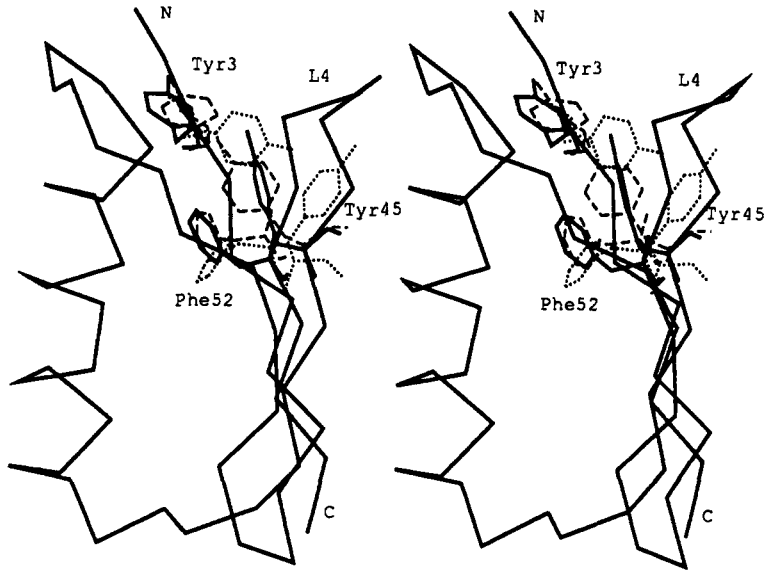

FIGURE 2: Stereogram of the region of the core close to L4, showing differing conformations of three aromatic residues. Solid lines, including the Cα tracing, are from the trigonal crystal structure. Dashed lines are from the NMR model of Gronenborn et al. (1991). Dotted lines are from the first NMR model of Lian et al. (1992).

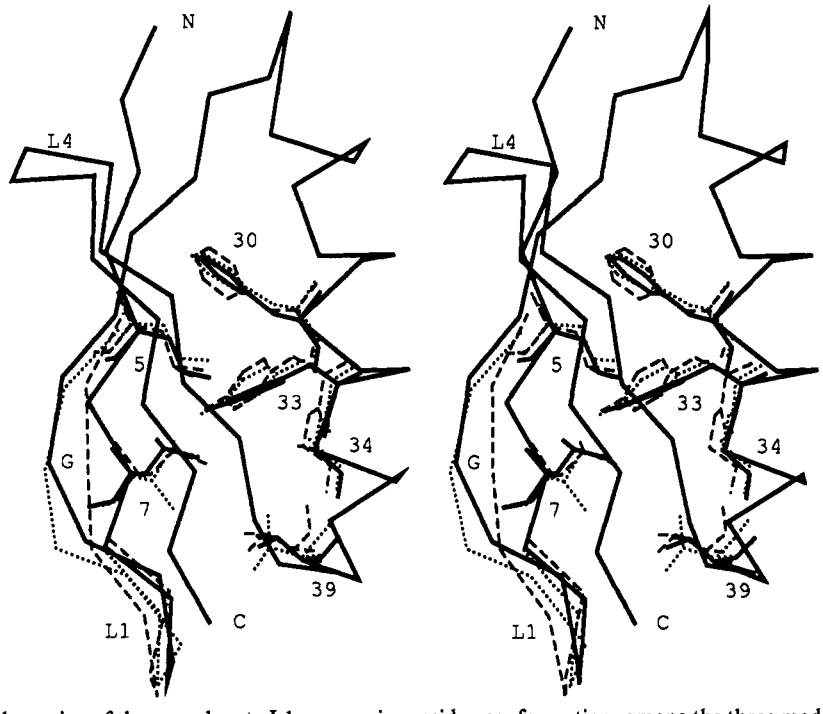

FIGURE 3: Stereogram of the region of the core close to L1, comparing residue conformations among the three models Gronenborn et al. (1991) (dashed lines), Lian et al. (1992) (dotted lines), and the trigonal crystal form (solid lines). Most of the residues are in good agreement. See Table 1 for residue types. Residue 7 is the only nonsolvated mutation site among the reported sequence variants of IgG-binding domains; it is Ile in the Lian et al. (1992) structure and Leu in the others. The letter G indicates that position of Gly14, which has a nearly fully extended conformation in all reported structures, giving the sheet an outward bend.

and III. Except for short extensions at the N- and C-termini, their II domain is very similar to the B1 domain of the present paper. The differences are at positions 6 and 7, where domain II has the same sequence as B2, Val-Ile, instead of Ile-Leu as in B1. Domain II is thus a sequence hybrid of B1 and B2. The rms deviations (Cα) between the present structures and the solution structure of Gronenborn et al. (1991) (Brookhaven accession code 2GB1) are 1.06 and 1.18 Å for the orthorhombic and trigonal forms, respectively. PDB coordinate set 2IGG contains 27 models of domain II resulting from the NMR structure determination by Lian et al. (1992). The average rms deviation (Cα) of these structures from the orthorhombic crystal form of B1 is 1.67 Å; the corresponding figure for the trigonal form is 1.72 Å. In general the Gronenborn structure more closely resembles the X-ray structure than do the Lian structures (see Figure 1). The differences are most significant at L1 and L4. In these regions, the solution structures (and especially the Lian et al. (1992) structures) appear less compact than the X-ray structure. The average rms deviation (Cα) between the Gronenborn structure and the Lian structures is 1.55 Å; thus, the crystal structure agrees with one NMR model better than they agree with each other. The present crystal structures of B1 resemble the B2 crystal structure (Achari et al., 1992) more closely than they resemble either B1 NMR structure. The rms deviations between the B2 structure and the B1 crystal structures are 0.39 and 0.36 Å for the

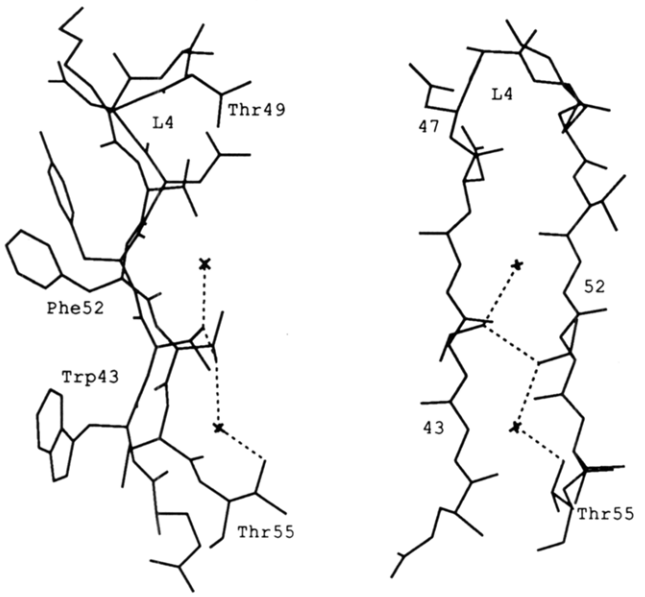

FIGURE 4: Two orthogonal views of the two strongest water sites. These waters are cradled by pleats on the external face of the β-sheet, where most of their neighbors are threonine residues. In addition to the hydrogen bonds indicated by dotted lines, the waters are within H-bonding distance of the peptide carbonyls and amides in the underlying antiparallel β-structure.

orthorhombic and trigonal crystal forms. The only differences in side chain rotamers are for surface residues. The greatest backbone deviations are in the L3 region, especially residues 39–42 and the adjacent residue 56. The mutation at residue 42 may have a role in these structural differences, although the effect is not obvious since the residue projects into the solvent. That this is found to be the region of greatest dissimilarity between the crystal structures of B1 and B2 is consistent with the NMR results of Lian et al. (1992). None of the six residue differences between B1 and B2 has a marked effect on the backbone or on another residue. There are no intraprotein hydrogen bonds involving any of the six side chains in either domain. Thus, there is no immediate explanation for the difference in stability. Most of the residue differences are on the protein surface. Residue 7 contributes to the core; the alternative residues here (Leu/Ile) are found to have similar conformations (i.e., similar χ_1 and χ_2 torsions).

The hydrogen bonding in the present models is basically as described by Gronenborn et al. (1991), with the following elaborations. The first β-ribbon is fully H-bonded, including two bonds between residue 1 and residue 20. The loop L1 is a type I β-turn, but without a hydrogen bond linking the carbonyl of 9 and the amide of 12. The conformational angles of residue 11 incline the 11–12 peptide so as to make the 9O–12N distance about 4.4 Å. This is consistent with amide exchange rates observed by Orban et al. (1992). The present structures concur with the B2 crystal structure of Achari et al. (1992) in this turn. In the helix, hydrogen bonding is normal from 22O through 37N. In particular, the hydrogen bond from 29O to 33N is between 2.9 and 3.0 Å, while the ϕ, ψ angles at Tyr33 are –55°, –52° (orthorhombic form) and –64°, –50° (trigonal form). Although in several instances the O_i–N_{i+3} distances are under 3.3. Å (suggesting a 3–10 helix), the helix is best described as α in its entire length. In its final turn, 34O receives hydrogen bonds from amides 37 and 39; the distance to 38N is suitable for a long H bond, but the angle is poor (the ON vector is over 60° from the peptide plane). The lack of a hydrogen bond 34O–38N is consistent with fast amide exchange observed by Orban et al. (1992). The second β-ribbon has three pairs of H bonds with standard

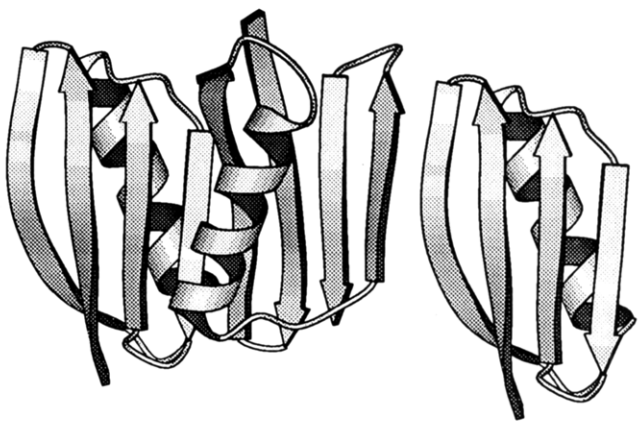

FIGURE 5: Three adjacent G:B1 molecules in the crystal lattice. The sheet–edge contact shown here is the primary crystal contact in both the orthorhombic and trigonal forms. Interacting molecules are related by 2-fold screw symmetry, forming molecular chains with extended β-sheets throughout the crystal. This diagram was produced with the program MOLSCRIPT (Kraulis, 1991).

antiparallel geometry, linking residues 42, 44, and 46 with residues 55, 53, 51, respectively. The central, parallel portion of the β–sheet has six regular hydrogen bonds, from 4N–50O to 8O–56N. In addition to these main chain hydrogen bonds, the following four well-ordered H bonds involving side chains could be important in stabilizing the protein structure. Two pairs of threonines form hydrogen bonds between their hydroxyl groups, 49–51 and 44–53, and the side chain carboxylate of Glu 56 tucks into the space between L1 and L3, uniting them by hydrogen bonding to the amides of residue 10 and residue 40.

The two Phe side chains are completely buried in the core, in van der Waals contact and with the planes of their rings nearly perpendicular in the manner described by Burley and Petsko (1985). The three tyrosine rings and the single Trp side chain are clustered loosely around the phenyl rings, generally with perpendicular or oblique contact geometry of their aromatic systems. The crystal structures [both the present B1 structures and the B2 structure of Achari et al. (1992)] have the same rotamers for all the aromatic side chains. The Gronenborn et al. (1991) structure agrees in every rotamer except χ_2 of Tyr45. The Lian et al. (1992) first model disagrees with the crystal and Gronenborn et al. (1991) models in the χ_1 rotamers for Tyr3, Trp43, and Phe52. While it has the same rotamers as the crystal structures for Tyr45, this residue is in a completely different position in the Lian et al. (1992) model due to the unique open structure of L4 (see Figure 1). The situation of the side chain of Tyr45 is different among the various models. Gronenborn et al. (1991) reported a hydrogen bond between the hydroxyl groups of Tyr3 and Tyr45. In the crystal structures this bond is absent, and Tyr45 is instead H-bonded to the side chain of Asp47. This situation holds also in the first model reported by Lian et al. (1992), despite the overall different structure of L4. In this region, as throughout the core, the B1 crystal structures are in close agreement with the B2 crystal structure of Achari et al. (1992). Figure 2 compares the conformations of the aromatic residues Tyr3, Tyr45, and Phe52 in the present crystal structure and the two NMR structures. The main chain at Lys50 is in the left-handed helical conformation, with ϕ, ψ angles of about +60°, +40° in the present crystal structure. In all reported structures of protein G domains, especially the X-ray structures, Gly14 has an extended, nearly flat conformation with ϕ, ψ angles near 180°, 180°. The effect is to remove a β-pleat, producing a bend in the strand that serves to accommodate the core residues Leu(or Ile)7 and Tyr33 (see Figure 3).

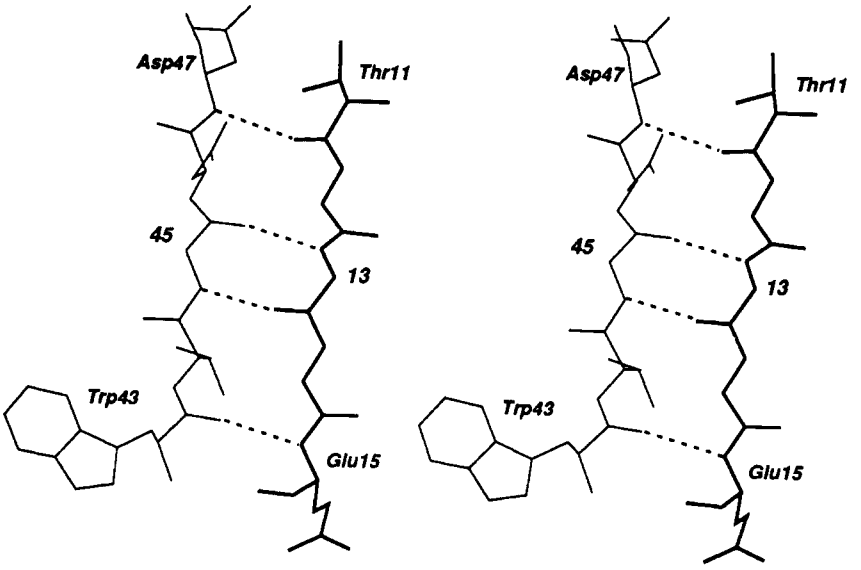

FIGURE 6: Stereogram close-up of the primary crystal contact in both structures. The four hydrogen bonds have standard antiparallel geometry.

Approximately 20 ordered water molecules have been refined with each protein. Their loci are usually not conserved between the two models, often because of adjacency to crystal contacts. However, several strongly occupied waters that interact with only one protein molecule are conserved. Waters have been ranked by "quality", defined as the square of occupancy divided by the thermal parameter (James & Sielecki, 1983). The highest quality water in both structures occupies a distinct location in the threonine-rich outer surface of the β-sheet. This water site is cradled by a pleat of the sheet and surrounded by residues 42, 43, 54, and 55. This location gives the water several polar atoms within hydrogen-bonding distance. The water is close to two hydrogen bonds in an antiparallel β-arrangement, as well as the Oγ atoms of three proximal threonines. A similar site in the adjacent pleat of the sheet holds the second-ranked water in the trigonal structure, and the first water in the B2 structure reported by Achari et al. (1992) (see Figure 4).

In both crystals, the strongest intermolecular contact involves the edges of the four-stranded sheet, effectively forming a continuous sheet, or "β-chain", that runs throughout the crystal. Four hydrogen bonds with typical antiparallel β-geometry give adjacent molecules a 2-fold screw relation, with the screw axis running along the molecular chain. This crystal contact (see Figures 5 and 6) is virtually identical in the orthorhombic and trigonal systems. The contact relates molecules along the **a** lattice direction in the orthorhombic crystals, and along both the **a** and **b** directions in the trigonal crystals. Thus, the **a** lattice constant in both crystals corresponds approximately to twice the width of the β-sheet. [The same contact also occurred in the B2 structure of Achari et al. (1992); see Discussion.] Weaker contacts, involving fewer atoms, interrelate different β-chains to give rise to the crystal symmetry. In the orthorhombic crystals, the chains are all (anti)parallel, producing an unusually high packing density for protein crystals, with a solvent content of only about 26%.

DISCUSSION

The fold, core structure, and overall H-bonding pattern of the IgG-binding domains from protein G are now well established. Among the various structure descriptions from X-ray and NMR, and across several sequence variants, there

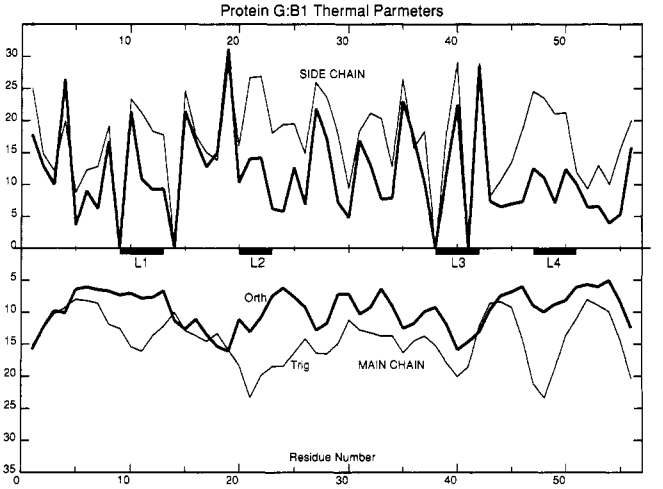

FIGURE 7: Residue-average thermal factors for the two structures for side chains (top half) and the main chain (bottom half) plotted versus sequence: thin lines, trigonal form; thick lines, orthorhombic form. In the side chain (upper) plot, a value of 0 indicates glycine.

is general agreement in the core and backbone hydrogen-bonding pattern, but there remains some question as to the conformation of several regions including the loops. In part, this irresolution results from the greater flexibility of the loops, and it may not be reasonable to expect a precise, unique description of the more mobile components of any protein. While NMR methods may be faithful to the solution "structure" in leaving such regions ambiguous, crystal-based models may give a precise model that is only one of many normal conformations, rigidified by the crystalline environment.

Protein molecules in a crystal must all have a common structure to enable diffraction. Diffraction data report the location of all ordered parts of the protein, without regard for their neighbors. NMR data report interatomic distances. In both methodologies, more observations make a better result, but incomplete data have different effects in the two techniques. While a poorly defined X-ray structure is likely to misconnect its parts and have the correct overall shape, a poorly defined NMR structure is likely to have good local connectivity and the wrong overall shape. In this way, the two methods are complementary. One reason for determining the crystal structure in two different crystal forms is to control for possible

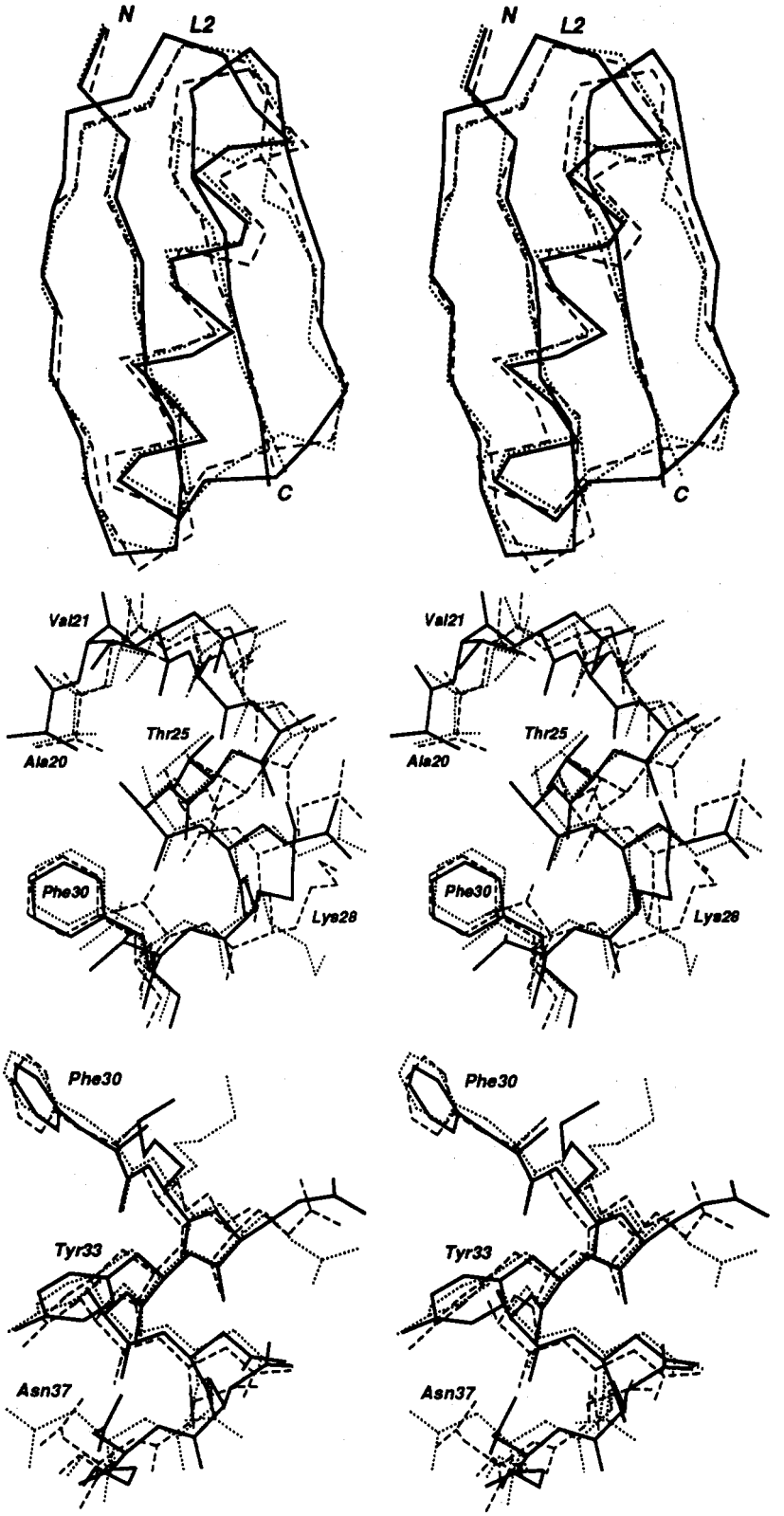

FIGURE 8: Three stereograms of the superposed Cα models in the region of the α-helix: NMR model of Gronenborn et al. (1991), dashed lines; NMR model of Lian et al. (1992), dotted lines; trigonal crystal form, solid lines; (a, top) emphasizing the angular relation of the helix to the sheet; (b, middle) superposed models in the N-terminal half of the helix; (c, bottom) superposed models in the C-terminal half of the helix.

structural perturbations due to crystal packing forces. In the present study, several surface side chains (and water molecules) are affected by the crystal environment, but there is no evidence for a significant effect on the protein backbone. The sheet–edge contact common to both crystal forms does not make the sheet's width or general structure different from those in the NMR models.

In general, the NMR models appear less compact than the X-ray models, as illustrated for loops L1 and L4 in Figure 1. NMR methods require long-range distance restraints to define the relation of loop L4 to the rest of the molecule. The Lian et al. (1992) structure is based on 478 distance restraints, while the Gronenborn et al. (1991) structure utilizes 854 interproton distance restraints. Lian et al. (1992) describe

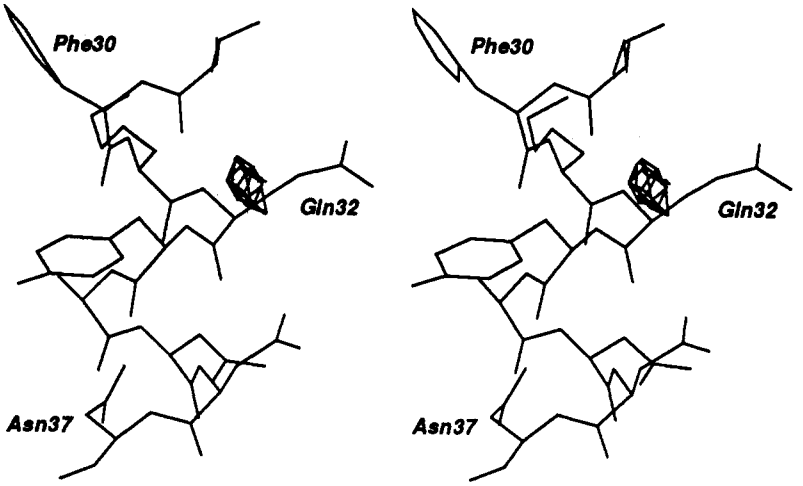

FIGURE 9: Final difference electron density near the helix hydrogen bond 29O–33N. The map is contoured at 1.7σ. This site coincides closely with a water site in the Achari et al. (1992) B2 domain model.

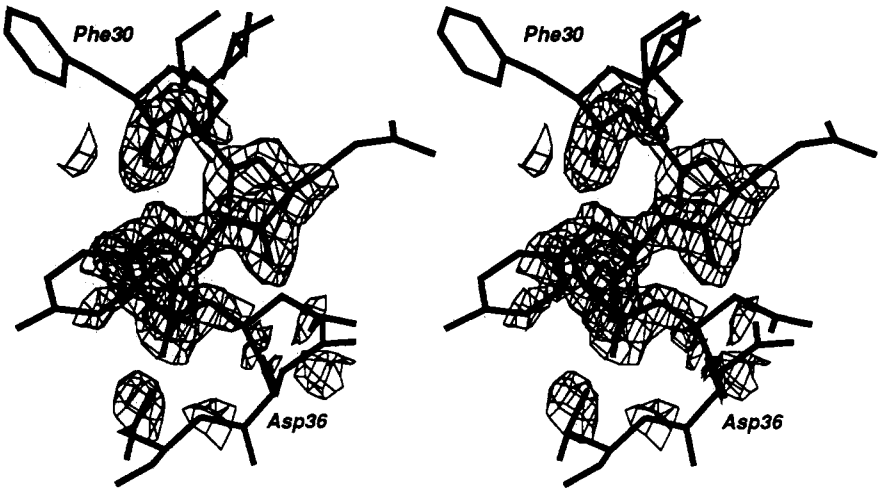

FIGURE 10: Final $2F_o - F_c$ electron density for the helix backbone near Tyr33. The map is contoured at 2σ.

two distinct classes of conformations for L4 among their models, with large differences in the ϕ, ψ angles of residues 47–50, and large differences in local interatomic distances. While the possibility of these alternative conformations and the implied motion between them are interesting, this model is more a result of molecular dynamics simulation than of structure determination. The predominant conformation of L4 described by Lian et al. (1992) is essentially the same as the one in all other reported structures. L4 has the highest main chain thermal parameters in the trigonal crystal structure, and a significant peak in the orthohombic form, indicating that even in the crystal this region is somewhat mobile (see Figure 7).

The variance in the angular relation of the helix to the sheet was at first suspected to be due to the B1/B2 residue substitutions, but it now appears that this is not the case. The model of Gronenborn et al. (1991) is unique in this parameter; in particular it disagrees with other NMR models (see Figure 8a) and with the present X-ray models. Dissecting the correlates of the 8–10° difference at the level of individual amino acids reveals that, because the ends of the helix contribute no large side chains to the core, the rotation does not demand any striking changes in side chain conformation. Thus, the observed main chain displacements on the order of 1 Å at the ends of the helix may involve little energetic cost. The side chains of Asn37 and Leu12 are in van der Waals contact, implying that the apparent rotational mobility of the helix may be dynamically coupled with observed displacements in L1. In addition to its unique rotation with respect to the sheet, the Gronenborn et al. (1991) helix is somewhat distorted, as described in Clore and Gronenborn (1992). Careful consideration must be given to the sample conditions and techniques used in deducing the several models, in an effort to understand the observed differences in helix structure. In comparing the structures of the helix in various models, the following features are noted. Several of the charged residues adopt varying rotamers, as may be expected for solvent-interacting Glu and Lys side chains. Two possibly significant conformational differences are in the Thr25 rotamer (see Figure 8b) and in the torsion for the 36–37 peptide (see Figure 8c). Regarding Thr25, the Gronenborn et al. (1991) rotamer is rare for threonine in α-helices, and unique among the reported models of either domain.

The two water sites deduced from solution NMR data and described by Clore and Gronenborn (1992) were examined in the present structures. Both sites in both structures are sufficiently distant from crystal contacts that normal hydration may be expected. The crystallographically refined water sites do not include waters at these positions, indicating there are no well-ordered waters at these locations. However, some electron density can be observed at these sites at the 2.4σ level (and below) in final difference maps. It thus appears that water does bind at both these positions, but not with sufficient occupancy to warrant inclusion in the refined model. Figure

9 shows the final difference map for the low-density water site near the 29O–33N hydrogen bond, while Figure 10 presents the final $2F_o - F_c$ map in the backbone region of the adjacent helix. Two other hydrogen bonds of the helix, 24O–28N and 32O–36N, do bind water molecules in the crystallographic models. Both models also feature a water site bound to the amide of Thr11 (as does the Achari et al. (1992) B2 model). The waters that appear to bind the tightest are at the two sites described in the previous section, and depicted in Figure 4. These waters refine with full occupancy and thermal parameters comparable to those of the best-ordered protein atoms. Figure 1 in Clore and Gronenborn (1992) shows several resonances attributed to waters near threonines 44, 51, and 55 (with Thr53 conspicuously absent) and likely arising from these crystallographically observed waters.

The higher packing density in the orthorhombic crystals places many more atoms in crystal contacts (118 as opposed to 88, using a 3.8-Å distance cutoff), providing a succinct explanation for the generally lower temperature factors in that structure (the average temperature factor also depends on the resolution and completeness of diffraction data). It is noteworthy that both the present structures, as well as the B2 structure of Achari et al. (1992), feature the same predominant crystal contact, namely, the sheet–edge association. This type of interaction has also been reported in the binding of a protein G domain to Fab (Derrick & Wigley, 1992). The binding of protein G to Fc could also involve a sheet–edge interaction, but this is unlikely, since the known binding site for protein A (Diesenhofer, 1983), with which protein G competes for binding, is not close to a sheer–edge in the Fc. More likely, protein G interacts with Fc by its helix in a manner similar to that of the all-helix protein A. Recent evidence from NMR solution studies supports this hypothesis (Gronenborn & Clore, 1993). The structures of two crystal forms of the B2 domain (consisting of 56 residues, without the N- and C-terminal extensions of the Achari et al. (1992) structure) are currently being refined and lack the sheet–edge contact, proving that it is not universal in protein G crystals.

ACKNOWLEDGMENT

The authors gratefully acknowledge helpful discussions with John Orban and Joseph Nachmann in the development of this paper. Certain commercial equipment, instruments, and materials are identified in this paper in order to specify the experimental procedure. Such identification does not imply recommendation or endorsement by the National Institute of Standards and Technology, nor does it imply that the materials or equipment are necessarily the best available for the purpose.

REFERENCES

Achari, A., Hale, S. P., Howard, A. J., Clore, G. M., Gronenborn, A. M., Hardman, K. D., & Whitlow, M. (1992) *Biochemistry 31*, 10449–10457.
Agarwal, R. C. (1978) *Acta Crystallogr. A34*, 791–809.
Akerstron, B., & Bjork, L. (1986) *J. Biol. Chem. 261*, 10240–10247.
Alexander, P., Fahnestock, S. R., Lee, T., Orban, J., & Bryan, P. N. (1992) *Biochemistry 31*, 3597–3603.
Alexander, P., Orban, J., & Bryan, P. N. (1992) *Biochemistry 31*, 7243–7248.
Bernstein, F. C., Koetzle, T. F., Williams, G. J. B., Meyer, E. F., Jr., Brice, M. D., Rogers, J. R., Kennard, O., Shimanouchi, T., & Tasumi, M. (1977) *J. Mol. Biol. 112*, 535–542.
Brunger, A. T., Kuriyan, J., & Karplus, M. (1987) *Science 235*, 458–460.
Burley, S. K., & Petsko, G. A. (1985) *Science 229*, 23–28.
Clore, G. M., & Gronenborn, A. M. (1992) *J. Mol. Biol. 223*, 853–856.
Cohen, G. H. (1986) *J. Mol. Biol. 190*, 593–604.
Derrick, J. P., & Wigley, D. B. (1992) *Nature 359*, 752–754.
Fahnestock, S. R., Alexander, P., Nagle, J., & Filpula, D. (1986) *J. Bacteriol. 167*, 870–880.
Finzel, B. C. (1987) *J. Appl. Crystallogr. 20*, 53–55.
Gronenborn, A. M., & Clore, G. M. (1993) *J. Mol. Biol. 233*, 331–335.
Gronenborn, A. M., Filpula, D. R., Essig, N. Z., Achari, A., Whitlow, M., Wingfield, P. T., & Clore, G. M. (1991) *Science 253*, 657–661.
Hendrickson, W. A., & Konnert, J. H. (1980) in *Computing in Crystallography* (Diamond, R., Ramaseshan, S., & Venkatesan, K., Eds.) pp 13.01–13.23, Indian Institute of Science, Bangalore.
Howard, A. J., Gilliland, G. L., Finzel, B. C., Poulos, T. L., Ohlendorf, D. H., & Salemme, F. R. (1987) *J. Appl. Crystallogr. 20*, 383–387.
James, M. N. G., & Sielecki, A. R. (1983) *J. Mol. Biol. 163*, 299–361.
Jones, T. A. (1987) *J. Appl. Crystallogr. 11*, 268–272.
Kraulis, P. J. (1991) *J. Appl. Crystallogr. 24*, 946–950.
Lian, L.-Y., Derrick, J. P., Sutcliffe, M. J., Yang, J. C., & Roberts, G. C. K. (1992) *J. Mol. Biol. 228*, 1219–1234.
Myhre, E. B., & Kronvall, G. (1977) *Infect. Immun. 17*, 475–482.
Orban, J., Alexander, P., & Bryan, P. (1992) *Biochemistry 31*, 3604–3611.
Sheriff, S. (1987) *J. Appl. Crystallogr. 20*, 55–57.
Ten Eyck, L. F. (1973) *Acta Crystallogr. A29*, 183–191.

Immunoglobulin-Type Domains of Titin: Same Fold, Different Stability?†

A. S. Politou,*,‡ M. Gautel, M. Pfuhl, S. Labeit, and A. Pastore

EMBL, Meyerhofstrasse 1, W69117 Heidelberg, Germany

Received December 2, 1993; Revised Manuscript Received January 27, 1994®

ABSTRACT: Titin is a 3-MDa protein thought to form a fibrous intracellular system in vertebrate striated muscle and to play an important role in sarcomere alignment during muscle contraction. It has also been implicated as a "molecular ruler", regulating the assembly and the precise length of the thick filaments [Whiting, A. J., Wardale, J., & Trinick, J. (1989) *J. Mol. Biol. 205*, 163–169]. Partial sequencing of titin-encoding cDNAs suggests that the protein is organized in a modular fashion, containing two classes of ~100-residue repeats [Labeit, S., Barlow, D. P., Gautel, M., Gibson, T., Holt, J., Hsieh, C. L., Francke, U., Leonard, K., Wardale, J., Whiting, A., & Trinick, J. (1990) *Nature 345*, 273–276]. These motifs, referred to as type I and type II modules, show sequence homology to the fibronectin III and immunoglobulin C2 superfamilies, respectively. Since the type II modules represent the most widely occurring motifs along the titin molecule, we expressed in *Escherichia coli* three domains of this type spanning different regions of the sarcomere (A-band and M-line) and studied their structure and stability. Using circular dichroism, nuclear magnetic resonance, and fluorescence spectroscopy, we showed that all the fragments examined are independently folded in solution and possess a β-sheet conformation. Furthermore, employing NMR analysis, we identified an overall folding pattern present in all modules and related to the Ig fold, as previously suggested by theoretical predictions. The stability of the modules over a range of conditions was investigated by measuring key thermodynamic parameters for both thermal and chemical denaturation and by monitoring amide proton exchange as a function of time. Despite the overall structural similarity, the stability of the modules seemed to differ; the motif corresponding to the M-line band was significantly more stable than the motifs corresponding to the A-band. Our data provide direct experimental evidence that the titin type II modules possess a β-sheet conformation and further suggest that similarly folded motifs located at different regions of the titin molecule may have distinct molecular properties and stability. As structural analysis of more titin domains is proceeding, these and related observations are expected to establish clear cut structure–function relationships and to unveil the exact cellular role of this protein.

Titin is the largest protein described to date (~3 MDa) and one of the few proteins specific to vertebrate striated muscle (Maruyama et al., 1984; Wang, 1985; Kurzban & Wang, 1988; Fürst et al., 1988). Related giant proteins are found in invertebrates (Benian et al., 1989; Ayme-Southgate et al., 1991). In the mature myofibril, titin is the third most abundant component of the sarcomere, after actin and myosin, comprising about 10% of its mass. Single titin molecules are "string-like" particles, over 1 μm in length, which span half the sarcomere, i.e., from M- to Z-line (Fürst et al., 1988; Nave et al., 1989). The part of the titin molecule located in the I-band appears to make elastic connections with the thick filaments and the Z-disk (Fürst et al., 1988; Horowits et al., 1989; Funatsu et al., 1990, 1993); the A-band region of titin contains a multiplicity of binding sites for myosin and C-protein (Labeit et al., 1992; Fürst et al., 1992); finally, in intimate association with other proteins, titin forms an integral part of the M-line (Vinkemeyer et al., 1993; Gautel et al., 1993). Because of these multiple interactions, titin is thought to play an important role in providing sarcomere alignment during muscle contraction and in regulating the assembly and the precise length of the thick filaments during myofibrillogenesis (Trinick et al., 1984; Whiting et al., 1989; Fulton & Isaacs, 1991; Isaacs et al., 1992; Gautel et al., 1993; Wang et al., 1993).

A detailed structural characterization of the titin molecule had until recently been precluded by its large size. However, the cloning and sequencing of cDNAs coding for an appreciable part of titin showed that this protein is organized in a typically modular fashion and that it contains two classes of repeated ~100-residue motifs (Labeit et al., 1990, 1992; Gautel et al., 1993). These modules, referred to as type I and type II, show sequence homology to the fibronectin III and immunoglobulin C2 superfamilies, respectively (Benian et al., 1989). The arrangement of the repeated sequences along the titin molecule shows considerable variation. In the elastic I-band region of the sarcomere there is an irregular alternation of type I and type II motifs including long stretches of exclusively class II motifs (S. Labeit, unpublished results). In the A-band region the two types of motifs form a very regular 11 domain super-repeat pattern (-II-I-I-II-I-I-I-II-I-I-I-) (Figure 1A). Finally, within the M-line, i.e., C-terminally, class II motifs are separated by nonrepetitive "linker" sequences (Figure 1B).

The modularity implied from the sequence data makes titin an ideal object for NMR[1] studies as the size of the motifs is well within reach of multidimensional NMR spectroscopy. Therefore, a structural study of the individual titin modules

† Supported by grants from the Deutsche Forschungsgemeinschaft (Ga 405/2-1, La 668/2-1), the European Community and the Human Frontiers Science Project.

* To whom correspondence should be addressed.

‡ Recipient of a BRIDGE Fellowship from EC.

® Abstract published in *Advance ACS Abstracts,* March 15, 1994.

[1] Abbreviations: NMR, nuclear magnetic resonance; PCR, polymerase chain reaction; SDS, sodium dodecyl sulfate; PAGE, polyacrylamide gel electrophoresis; CD, circular dichroism; TOCSY, total correlation spectroscopy; TPPI, time-proportional phase incrementation; NOESY, nuclear Overhauser enhancement spectroscopy; DQF-COSY, double quantum filter correlated spectroscopy; HMQC, heteronuclear multiple quantum coherence; HSQC, heteronuclear single quantum coherence; ΔG, Gibbs free energy change; ΔS, entropy change; ΔH, enthalpy change; T_m, melting temperature; MLCK, myosin light chain kinase; NOE, nuclear Overhauser enhancement; UV, ultraviolet.

0006-2960/94/0433-4730$04.50/0

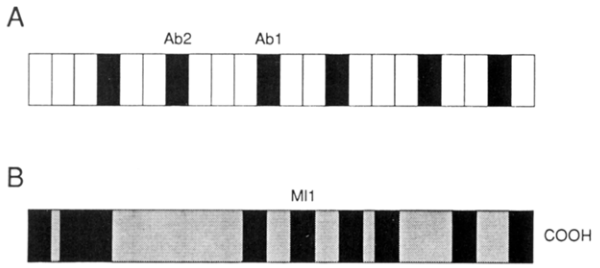

FIGURE 1: Arrangement of modules in the A-band (A) and in the M-line (B) part of the titin molecule. Black boxes indicate the type II and white ones the type I modules. Shaded boxes represent nonrepetitive "linker" sequences separating the type II modules in the M-line. Also indicated are the positions of the modules expressed and studied in the present work.

is both meaningful and feasible because it could eventually address important aspects of the function of titin, such as its elasticity, at the molecular level. Such an approach has been successfully applied to several modular proteins and is by now well established (Baron et al., 1990; Driscoll et al., 1991; Main et al., 1992).

We have undertaken a longterm structural analysis of representative titin modules in solution using a variety of techniques and mainly NMR spectroscopy. The general scope of this type of analysis and the initial data obtained with selected motifs made it obvious that a detailed study of the stability and conformational properties of individual domains is an absolute prerequisite before any rigorous 3D structure determination is attempted. At the present time we have concentrated on the structural analysis of type II modules, mainly for two reasons. First, these modules are present in all regions of the molecule in various combinations with modules of the same class or of class I or with nonrepetitive "linker" sequences. Second, they belong to the Ig superfamily, a diverse structural class which now includes intra- as well as extracellular proteins. The structures of these proteins have been extensively studied, allowing comparison among a large family of evolutionarily related proteins; however, the number of stability studies is rather limited (Buchner et al., 1991).

In this study, we provide experimental evidence showing that individual titin modules possess a predominantly β-sheet secondary structure. We also report the results of a stability survey for selected titin modules of class II from the A-band and the M-line which represents, to the best of our knowledge, the first of this type for single, isolated Ig modules.

EXPERIMENTAL PROCEDURES

Protein Expression and Purification. cDNAs coding for various titin type II domains from the A-band and M-line regions of the molecule were isolated by PCR (Saiki et al., 1985) using the rabbit CE12 and human CH11 (Labeit et al., 1992) and human AB5 (Gautel et al., 1993) clones as templates (Ab2: EMBL data library AC X64698, bp 847–1137; Ml1: AC X69490, bp 11365–11637; Ab1: AC X64696, bp 14404–14685). The DNA fragments obtained were subcloned into the pET8c vector (Studier et al., 1990) and fused N-terminally with an oligonucleotide linker encoding a His_6 tag sequence, introducing an additional two serine residues in the linker. After induction of transformed BL21 [DE3] pLysE cells (Studier & Moffat, 1991) with 0.3 mM IPTG for 4 h, the harvested cell pellet was treated with lysozyme at 20 μg/mL and sonicated in 50 mM sodium phosphate, pH 8.0, 150 mM NaCl, and 0.1% Triton X-100. After centrifugation at 25000g and washing, the insoluble inclusion bodies were dissolved in 8 M urea, 50 mM potassium phosphate, pH 8.0, and 20 mM β-mercaptoethanol. The urea extract was clarified by centrifugation at 25000g and the soluble supernatant fractionated by metal chelate affinity chromatography on Ni^{2+}–NTA agarose (Qiagen) essentially as described (LeGrice & Grueninger-Leitch, 1990). Pure fractions from imidazole gradients were pooled, diluted at 100 μg/mL, and dialyzed against several buffer changes of 20 mM Tris/acetate, pH 8.0, 1 mM EDTA, and 0.5 mM PMSF. Insoluble protein after dialysis was pelleted at 25000g and the supernatant passed over 50 mL of DEAE-Sephacel equilibrated in the dialysis buffer. Unbound fractions contained pure titin domains as judged by SDS–PAGE (Laemmli, 1970) and mass spectrometry and were concentrated by vacuum dialysis against the appropriate assay buffers.

Labeling. Uniformly ^{15}N-labeled samples were obtained from bacteria grown in M9 medium with $^{15}NH_4Cl$ as the sole nitrogen source. For the ^{13}C labeling, a mixture of ^{13}C-labeled saccharides and peptides from an acid hydrolysate was used.

Circular Dichroism–Thermal Unfolding. Circular dichroism (CD) spectra in the far ultraviolet were recorded on a Jasco J-710 spectropolarimeter, fitted with a thermostated cell holder and interfaced with a Neslab RTE-110 water bath. The instrument was calibrated with a 0.10% aqueous solution of d_{10}-camphorsulfonic acid. Quartz, thermostated cuvettes with 1- or 0.2-mm path lengths were used (Hellma). Spectra were typically recorded in 10 mM acetate buffer, pH 4.2, and were baseline corrected by subtraction of the appropriate buffer spectra. The combined absorbance of cell, sample, and solvent was kept less than 1 over the measured range. Thermal denaturation curves were obtained at a heating rate of 20 °C/h. Thermal denaturation curves of at least two different preparations were recorded for each module.

Fluorescence Spectroscopy–Urea Denaturation Studies. Urea denaturation of the titin domains was monitored by measuring the intrinsic fluorescence intensity of solutions containing typically 0.070 mg/mL of protein in 10 mM acetate buffer, pH 4.2, and urea in the concentration range of 0–8 M. At least two different samples of each module were used. Urea stock solutions (10 M) were prepared with "ultrapure" urea purchased from Schwarz/Mann Biotech and were used within 24 h. Fluorescence measurements were made in 1.0-cm quartz cuvettes thermostatted at 25 ± 0.1 °C either with an SLM-Aminco Bowman Series 2 or with an SLM 8000 spectrofluorimeter operating in ratio mode. The slit widths were 4 nm for both excitation and emission. For an excitation wavelength of 293 nm, the maximal change in fluorescence intensity between the folded and the unfolded form was obtained at emission wavelengths of 312 nm for Ab1, 314 nm for Ab2, and 315 nm for Ml1. The solutions were incubated at 25 °C for 10–12 h before the measurement. After the fluorescence measurements, the pH of four solutions near the midpoint of the transition was recorded on a PHM93 Radiometer pH meter after a double buffer adjustment, and the average was considered as the pH of denaturation. The resulting urea denaturation curves were analyzed, and the free energy of folding was determined by the linear extrapolation method (Pace et al., 1989) assuming a two-state mechanism of unfolding and by nonlinear regression analysis.

Nuclear Magnetic Resonance. The samples for NMR measurements typically contained 1–1.5 mM protein in 90% H_2O/10% D_2O and 10 mM deuterated acetate buffer, pH 4.2. Samples for the hydrogen exchange experiments were obtained by first lyophilizing the protein from its aqueous solutions and then redissolving it in 99.5% D_2O. All 2D NMR spectra were acquired on Bruker AMX-500 and AMX-600 spectrometers in the phase-sensitive mode (TPPI) either with preirradiation of the water resonance or with selective

```
          Ab1  A P D I D L D L E L   R K I I N I R A G G   S L R L F V . P I K   G R P T P E V K W G
          Ab2  . P T I V L D P T I   K D G L T I K A G D   T I V L N A I S I L   G K P L P K S S W S
          M11  . . . . R I L T K P   R S . M T V Y E G E   S A R F S C . D T D   G E P V P T V T W L
      Telokin  H V K P Y R T K T I   L D . M D V V E G S   A A R F D C . K V E   G Y P D P E V M W F

          Ab1  K V D G E I R D . .   . . A A I I D S T S   . S F T S L V L D N   V N R Y D S G K I T
          Ab2  K A G K D I R P S D   I T Q I T S T P T .   . . S S M L T I K Y   A T R K D A G E I T
          M11  R K G Q V L S T S A   . . R H Q V T T T K   . Y K S T R E I S S   V Q A S D E G N I S
      Telokin  K D D N P V K E S R   . . H F Q I D Y D E   E G N C S L T I S E   V C G D D D A K Y T

          Ab1  L T L E N S S G T K   S A F V T V R V L D   T
          Ab2  I T A T N P F G T K   V E H V K V T V L D   V
          M11  V V V E N S E G K Q   E A E F T L T I Q K
      Telokin  C K A V N S L G E A   T C T A E L L V E T   M
```

FIGURE 2: Alignment of all three titin modules against telokin.

excitation (WATERGATE pulse sequence; Piotto et al., 1992). Clean-TOCSY spectra (Griesinger et al., 1988) were measured using the MLEV-17 composite pulse cycle (Bax & Davis, 1985) and an optimized "cleaning" delay approximately 1.5 times longer than the low-power 90° pulse. Mixing times used were in the range 30–75 ms for the TOCSY and 50–200 ms for the NOESY spectra. Homonuclear 2D DQF-COSY, clean-TOCSY, and NOESY and heteronuclear ^1H–^{15}N HSQC, ^1H–^{15}N HSQC-TOCSY, and ^1H–^{15}N HSQC-NOESY as well as ^1H–^{13}C HMQC, ^1H–^{13}C HMQC-NOESY, and ^1H–^{13}C HMQC-TOCSY spectra (Bodenhausen & Ruben, 1980; Bax et al., 1990; Norwood et al., 1990) were recorded at 17, 27, and 35 °C, with 2048 data points in the acquisition domain and 512 data points in t_1. Data were processed on a Bruker X-32 data station using UXNMR software. Prior to Fourier transformation, the data were zero filled to 2048 points in the t_1 dimension and weighted with a Gaussian window in t_2 and a cosine window in t_1. A baseline correction was performed in both dimensions using a polynomial.

RESULTS

Selection of Module Boundaries. The precise boundaries of the modules were selected on the basis of an extensive sequence alignment of all type I and type II modules present in the A-band and M-line (70% of the whole titin sequence) (Higgins et al., 1994). The N-terminus of the A-band domains was selected around the well conserved proline. With the M-line domain two slightly different alignments of the N-terminus are possible, because of the lack of the starting proline common to most of the others. We chose the one that aligns the first hydrophobic residue (Ile) to the first Phe of telokin. The choice of the C-terminus was in all cases unambiguous, as it had to include the well conserved Hydrophobic–X–Hydrophobic (Figure 2).

Secondary Structure Deduced by Circular Dichroism. CD spectra of all three titin domains at room temperature (25 °C) are characteristic of a predominantly β-sheet secondary structure (Figure 3). Use of the method described by Chen et al. (1974) to estimate the secondary structure gave identical results for the three modules (52% in β-sheet and 48% in secondary structures other than β-sheet and helix). However, the error associated with the fitting process is large, so that the resulting percentages are only qualitatively significant.

CD spectra recorded in the pH range of 4–7 show the same features, indicating that there is no pH-dependent conformational change. A pH of 4.2 which is more favorable for NMR experiments was chosen for our further work, so that similar conditions could be used in all our studies.

Urea Denaturation. Fluorescence spectroscopy is ideally suited for monitoring of the unfolding, because in all three

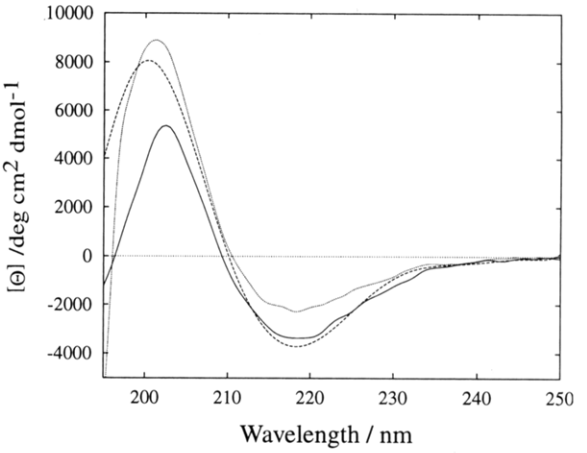

FIGURE 3: CD spectra of Ab1 (dotted line), Ab2 (solid line), and M11 (dashed line) at 25 °C, pH 4.2, in 10 mM acetate buffer.

cases the emission spectra of the denatured material differ significantly from the ones of the native protein both in intensity and in the maximum emission wavelength (21-, 28-, and 30-nm shift upon unfolding of M11, Ab1, and Ab2, respectively). The latter is highly indicative of a tryptophan well buried in the hydrophobic core of the protein (318 nm for Ab1 and 323 nm for Ab2 and M11 in their native forms).

The denaturation curves obtained by monitoring the intrinsic fluorescence of the modules at 312 nm for Ab1, 314 nm for Ab2, and 315 nm for the M11 domain are all characterized by the same sigmoidal shape (see Figure 4A for a representative curve). They can be divided into three regions: (a) the pretransition region that shows the effect of increasing urea concentration on the fluorescence intensity for the folded protein; (b) the transition region, which shows how the same property varies upon progression of unfolding; (c) the posttransition region, which shows the dependence of the fluorescence intensity on the denaturant concentration for the unfolded protein. An appreciable increase in the fluorescence intensity relative to the native state was observed at very low urea concentrations (<0.25 M) only in the case of the Ab1 module; a similar effect has been previously reported with other proteins and mainly in cases of guanidinium-induced unfolding (Pace et al., 1990). These points were not included in our analysis of the curve. There is also a slight linear dependence of fluorescence on urea concentration for urea concentrations higher than 7.5 M, in agreement with previous observations (Schmid et al., 1989; Pace et al., 1992).

A two-state folding mechanism was postulated to analyze the curves. Such an assumption is supported by the single-step shape of the unfolding curve (Figure 4A) and by its subsequent analysis (Figure 4B). On that basis ΔG can be

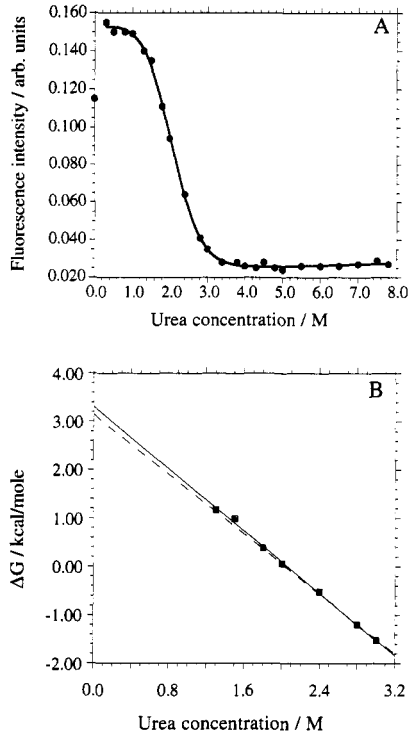

FIGURE 4: (A) Urea unfolding curve for the Ab1 module at pH 4.2, in 10 mM acetate buffer, 25 °C. The intrinsic fluorescence intensity was measured at 312 nm after excitation at 293 nm. The curve of best fit obtained from the nonlinear regression analysis is also shown. (B) ΔG as a function of the urea concentration for the transition region. ΔG was calculated from the data in panel A using eq 1 (points) and linearly extrapolated to zero according to eq 2 (solid line).

calculated as a function of urea concentration from the points in the transition region using

$$\Delta G = -RT \ln K = -RT \ln (f_u/f_f) = -RT \ln [(y_f - y)/(y - y_u)] \quad (1)$$

where R is the gas constant [1.987 calories/(deg·mol)], T is the absolute temperature, K is the equilibrium constant, f_f and f_u represent the fraction of protein present in the folded and unfolded conformation, respectively, y is the observed fluorescence intensity at the selected wavelength, and y_f and y_u are the values of the fluorescence intensities characteristic of the folded and unfolded conformation, respectively (Pace et al., 1989). Values of y_f and y_u were obtained by extrapolation of the pre- and posttransition baselines. A least-squares analysis was used to determine the equations for f_u and f_f in the transition region. In all three cases ΔG was found to vary linearly with urea concentration. Assuming that this linear dependence continues to zero concentration, the data were then fit to

$$\Delta G = \Delta G(H_2O) - m[\text{urea}] \quad (2)$$

where $\Delta G(H_2O)$ is the value of ΔG at 25 °C in the absence of the denaturant, known as conformational stability, and m is a measure of the steepness of the unfolding curves.

In all three cases, a very good fit was found between values of ΔG derived from the experimentally measured fluorescence intensity and those obtained by extrapolation in the transition region (Figure 4B). This lent additional support to our initial assumption of an one-step mechanism of unfolding.

It has been argued before (Santoro & Bolen, 1989) that this method of analysis underestimates the final error in the parameters determined (ΔG and m) because no error is assumed for the pre- and posttransition baselines. The use of a nonlinear regression analysis was suggested to fit the entire unfolding curve, such as that shown in Figure 4A, to

$$y = \{(y_f + m_f[U]) + (y_u + m_u[U])(\exp[-(\Delta G(H_2O))/RT - m[U]/RT)]\}/\{1 + \exp[-(\Delta G(H_2O)/RT - m[U]/RT)]\} \quad (3)$$

where m_f and m_u are the the slopes of the pre- and the posttransition lines, respectively, and [U] is the urea concentration. Using the nonlinear regression analysis program Kaleidagraph (Synergy Software, PCS Inc.), all six parameters of eq 3 were obtained with their standard errors.

Table 1: Thermodynamic Parameters Characterizing the Stability of the Three Titin Modules

module	T_m[a]	$[U]_{1/2}$[b] (M)	m[b] (cal mol^{-1} M^{-1})	$\Delta G(H_2O)$[b,c] (kcal mol^{-1})	ΔH_m[d] (kcal mol^{-1})
Ab1	43.9 (0.1)	2.06	1608 (38)	3.31 (0.15)	45.6 (1.6)
		2.03	1547 (78)	3.15 (0.21)	
Ab2	45.6 (0.3)	3.17	1313 (130)	4.18 (0.13)	61.3 (4.7)
		3.22	1463 (248)	4.71 (0.83)	
Ml1	52.5 (0.2)	4.37	985 (69)	4.31 (0.13)	68.5 (6.7)
		4.03	1445 (235)	5.80 (0.95)	

[a] Calculated from plots of ΔG vs T at $\Delta G = 0$. [b] For each module, the top line gives the results of a least-square analysis of plots of ΔG vs [urea] (eq 2), and the second line gives the results of the nonlinear regression analysis of the entire unfolding curve (eq 3). Errors are given in parentheses. [c] Conformational stability, at 25 °C, pH 4.2. [d] Obtained from the slope of ΔG vs T plots, ΔS_m, and T_m (= $T_m \Delta S_m$).

The results of the urea denaturation study are summarized in Table 1 and clearly show that the Ml1 module is the most stable of the three titin domains examined. For comparison, the results of both the linear least-squares fit and the nonlinear regression analysis are shown.

It should be emphasized at this point that more relevant in the present study is the relative stability of the modules and not the absolute values of $\Delta G(H_2O)$. As there is no single parameter to characterize (and no single method to calculate) differences in conformational stability between structurally related proteins, all relevant parameters are included in the table: (i) The midpoint of urea unfolding curve, $[\text{urea}]_{1/2}$, is the most "objective" parameter, in the sense that it can be determined quite accurately and reproducibly and is almost independent of the unfolding mechanism and the method of analysis used. (ii) m is not directly measured, and its value depends on the unfolding mechanism and the method of analysis; it is nevertheless useful as the only direct measure of the steepness of the unfolding curve. (iii) The values of $\Delta G(H_2O)$ *per se* also depend on the method of analysis used and include the error associated with m to an even larger extent, but they give an overall estimate of the stability of the protein and, as such, are quite useful.

The low values of the conformational stability could be partly due to the method of analysis used which is known to yield the lowest estimates of $\Delta G(H_2O)$ (Pace et al., 1989), but they could also reflect the nature of the proteins studied. It is reasonable to expect that modules cannot be as stable as an intact protein.

Thermal Denaturation Monitored by CD. Thermal denaturation of the three domains was monitored by following the change in the far-UV CD spectrum with increasing temperature. Since the maximal change in ellipticity between the folded and the unfolded conformation was obtained at 201–204 nm, this range of wavelengths was selected to monitor the thermal denaturation of the proteins. With increasing temperature there was a loss of the β-sheet CD pattern occurring at a different temperature for each domain (Table

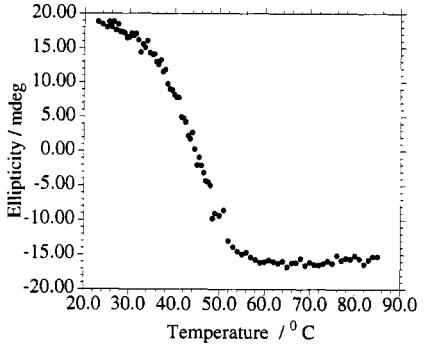

FIGURE 5: Thermal denaturation curve of Ab1 in 10 mM acetate buffer, pH 4.2, monitored by circular dichroism at 203 nm.

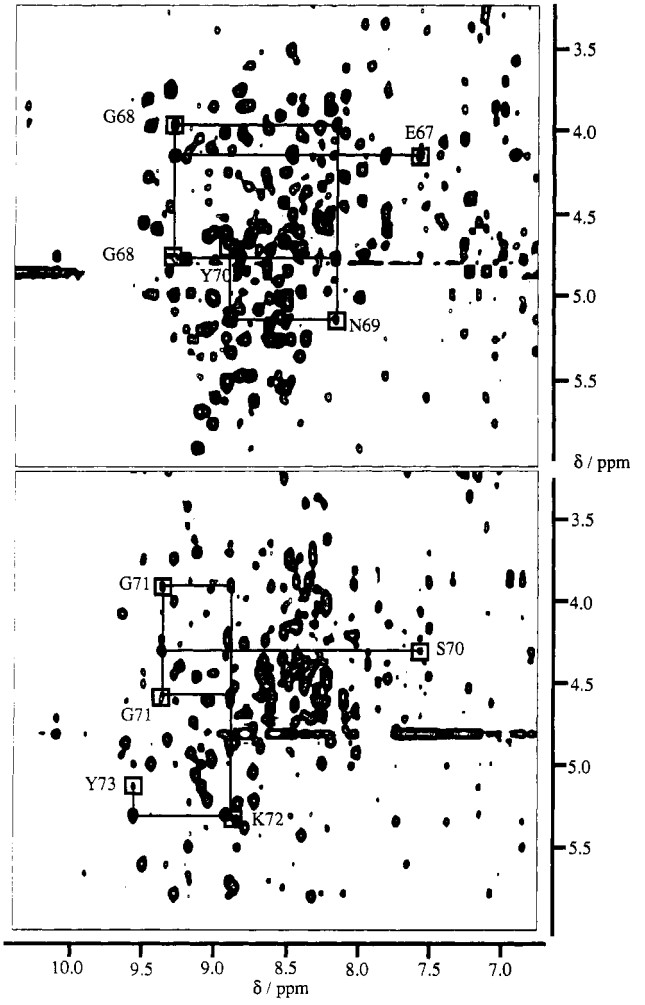

FIGURE 6: Fingerprint regions of NOESY spectra of Ml1 (top) and Ab1 (bottom) acquired under identical conditions (300 K, pH 4.2 in acetate buffer, mixing time = 120 ms). The sequential assignment pathways for a stretch of well-conserved residues are also shown.

1). Thermal denaturation curves (Figure 5) were analyzed in the standard manner, using a two-state approximation (Becktel & Schellman, 1987). Equations 1 and 2 corresponding to thermal denaturation were used to calculate the dependence of ΔG on temperature in the transition region, and subsequently the midpoint of thermal transition, T_m (where $\Delta G = 0$), and the enthalpy change, ΔH_m ($\Delta H_m = T_m \Delta S_m$, where ΔS_m is the slope of ΔG vs T), were determined. Calculation of ΔH_m values from the slope of van't Hoff plots yielded the same results. Data depicted in Table 1, which includes the T_m and ΔH_m values, show that the three titin domains differ in their thermal stability and that Ab1 is unstable relative to the other modules.

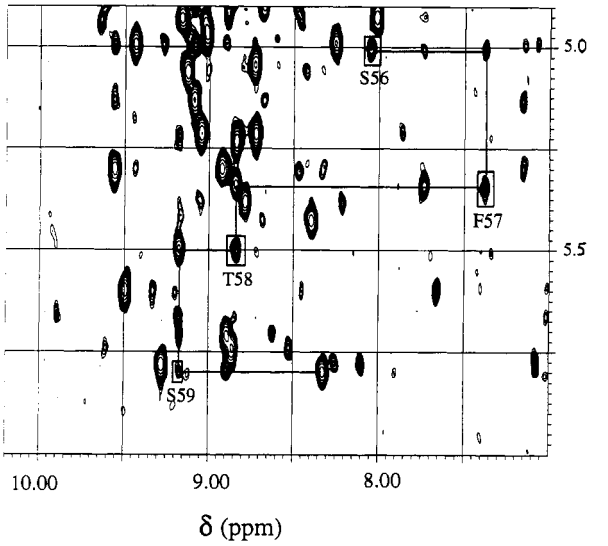

FIGURE 7: Part of the fingerprint region of a NOESY spectrum (mixing time = 120 ms) for Ab1 in acetate buffer, pH 4.2, recorded at 27 °C. The locations of the intraresidual amide proton–α-proton TOCSY cross-peaks are indicated with rectangular frames and the sequential assignment pathway with straight lines.

NMR Assignments. The NMR spectra of the three domains have a striking similarity and are all characteristic of a predominantly β-sheet protein (Figure 6). However, they differ markedly in the overall dispersion. Ml1 gives the best resolved spectra, while the NMR spectra of the Ab1 domain, although in general of a good quality, are characterized by regions of adequate dispersion mixed with regions of extensive overlap which make sequential assignment very difficult. For historical reasons, the NMR data presented here are those derived from the spectra of Ab1.

Initial spin system assignments were obtained from 2D homonuclear TOCSY and DQF-COSY spectra. Additional spin systems were identified in the 2D ^1H–^{15}N HSQC-TOCSY spectrum. Heteronuclear ^{13}C-based experiments proved invaluable; by using them the ambiguity in the aromatic region of the spectrum was completely resolved, and the previous assignments were confirmed.

Sequential assignment of the backbone ^1H and ^{15}N resonances (for the parts of the sequence assigned) was done in the conventional manner (Wüthrich, 1986) using mainly 2D ^1H–^1H NOESY, ^1H–^{15}N HSQC-NOESY, and ^1H–^{13}C HMQC-NOESY spectra to identify short-range through-space connectivities between the previously assigned spin systems. An example is given in Figure 7.

Use of any type of 3D experiment that could resolve the majority of the remaining ambiguities was precluded for the Ab1 module, because of degradation of the protein in the time required for the acquisition of a 3D spectrum. Therefore, we can presently be confident only about the assignment of 60% of the residues in Ab1. NMR work on the Ml1 domain, which shows better spectroscopic behavior, is in progress. A full account of this work will be published elsewhere.

NMR Secondary Structure. It has been widely accepted that secondary shifts, i.e., deviations of the NMR chemical shifts from their random coil values, contain valuable information regarding protein secondary structure (Pastore & Saudek, 1990; Spera & Bax, 1991; Wishart et al., 1991; Ikura et al., 1991). The $^1H_\alpha$ and $^{13}C_\alpha$ secondary shifts are believed to give the best correlation to the secondary structure (Wishart et al., 1991). Helices are characterized by positive $^{13}C_\alpha$ and negative $^1H_\alpha$ secondary shifts; the opposite is true for β-sheets. The magnitude of the deviations from the random

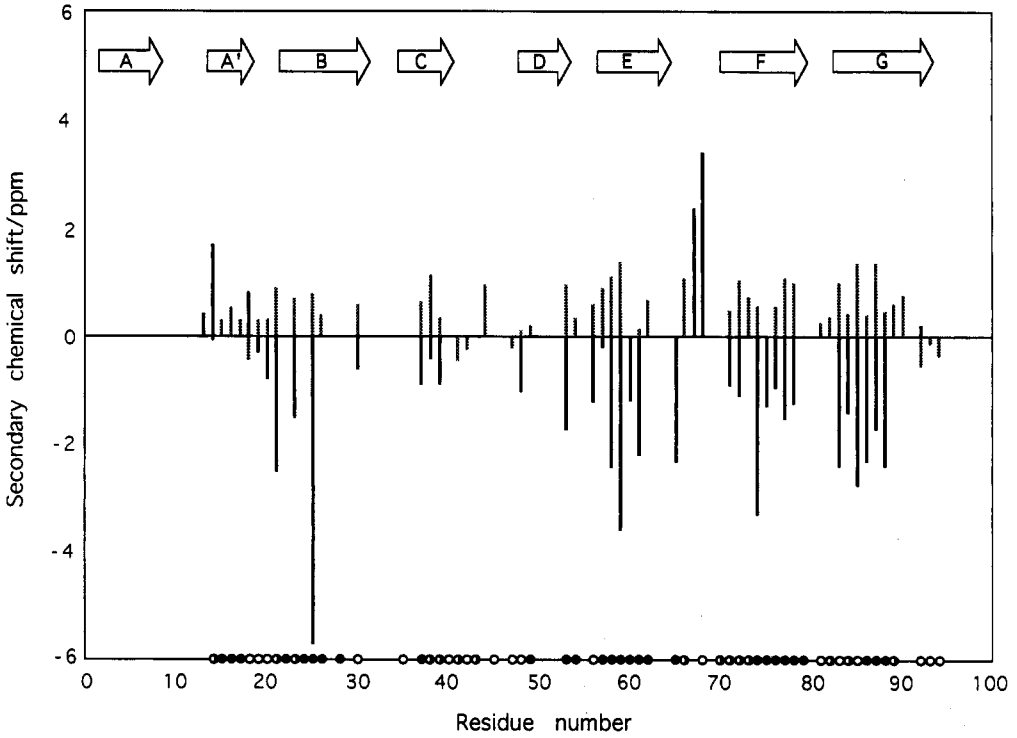

FIGURE 8: NMR secondary shifts and amide proton exchange. Plot of $^{13}C_\alpha$ (black bars) and $^1H_\alpha$ (shaded bars) secondary shifts vs residue number for the assigned part of Ab1. Stretches of negative $^{13}C_\alpha$ (or positive $^1H_\alpha$) shifts indicate the location of β-strands. Qualitative amide proton–deuterium exchange data are also shown: (a) fast exchanging protons (open circles), i.e., those with lifetime less than 4 h; (b) medium (half-filled circles) with lifetime between 4 and 10 h; (c) slow exchanging protons (filled circles), i.e., those with lifetime between 10 and 26 h. No amide protons remained unexchanged after 26 h in D_2O. The putative location of the β-strands for the model used are also indicated and marked by the arrows on the top of the drawing. The residues for which no data are shown are the ones not assigned.

coil values is less pronounced for residues in β-sheets than for α-helix. However, these deviations are still characteristic of the secondary structure, and they can reliably be used for this purpose. In fact, there is evidence that this method of analysis can result, in certain cases, in a clearer definition of the secondary structure elements, such as ends of helices, than the pattern of sequential and medium-range NOEs considered alone (Shirakawa et al., 1993). In deducing the secondary shifts, we used the "coil" values given by Wishart et al. (1991), which represent average values from secondary structures other than β-sheets and α-helices (including random coil). Figure 6 shows secondary shifts for the $^1H_\alpha$ and $^{13}C_\alpha$ of the Ab1 residues assigned. There are clearly present stretches of secondary shifts of the same sign which identify the residues involved in β-strands (55% of the assigned residues).

Amide Proton Exchange. The Ab1 domain was lyophilized once from H_2O and then dissolved in D_2O. 2D TOCSY spectra were acquired at 17 °C starting immediately after dissolution; the acquisition time for each spectrum was 4 h. The majority of the cross-peaks for the amide protons (85%) were absent from the spectrum acquired 4 h following dissolution, while 26 h later there was none detectable. These data are summarized in Figure 8 and clearly show that exchange of most of the amide protons of Ab1 is rather rapid. This was not the case with Ml1; an appreciable number of amide protons (12%) had not exchanged even after 1 month in D_2O.

Modeling of the Tertiary Structure. The structure of type II modules was modeled after telokin according to the alignment shown in Figure 2 and suggested by Y. Harpaz and C. Chothia (personal communication). Telokin is the only member with known 3D structure (Holden et al., 1992) of the intracellular Ig subfamily, and it represents the C-terminal domain of MLCK; for this reason it is the most suitable one for the modeling of titin, despite the relatively low sequence homology. The pairwise identity between telokin and Ab1, Ab2, and Ml1 is 26%, 25%, and 28%, respectively, while, if amino acid similarity is also considered, these numbers become 42%, 40%, and 45%, respectively. The overall fold of telokin is that of a β-sandwich of antiparallel β-sheets (Holden et al., 1992). In Figure 8 the regions where the β-strands are expected on the basis of this model are shown and compared with the experimentally determined locations of the β-strands. In the telokin structure 60% of the residues are located in β-strands, while roughly 55% of the Ab1 residues assigned showed secondary shifts characteristic for amino acids involved in β-strands.

In addition, a network of NH–NH and H_α–H_α NOE connectivities between nonsequential residues that could be confidently determined from our NMR data was compared with the corresponding interstrand contacts expected from the model. This is illustrated in Figure 9. NOE connectivities can de detected by NMR between protons that are less than 4 Å apart in space. Most of the expected NOEs that have not been experimentally detected correspond to residues for which the NMR assignment is not available.

The ^1H, ^{13}C, and ^{15}N chemical shifts of the N-terminally attached His_6 sequence show in all three cases no appreciable dispersion and have values characteristic for random coil conformation. We can confidently conclude, therefore, that the His_6 tag does not participate in any way in the formation of secondary or tertiary structure.

DISCUSSION

The Ig fold, a stable β-sheet sandwich, has been elegantly described as "a stable platform upon which a diversity of sequences are displayed by varying the amino acids that are exposed on the external faces of the β sheets or on the loops of sequence connecting the β strands" (Williams et al., 1989). The wealth of sequences published in recent years has introduced even more variety in the family by including

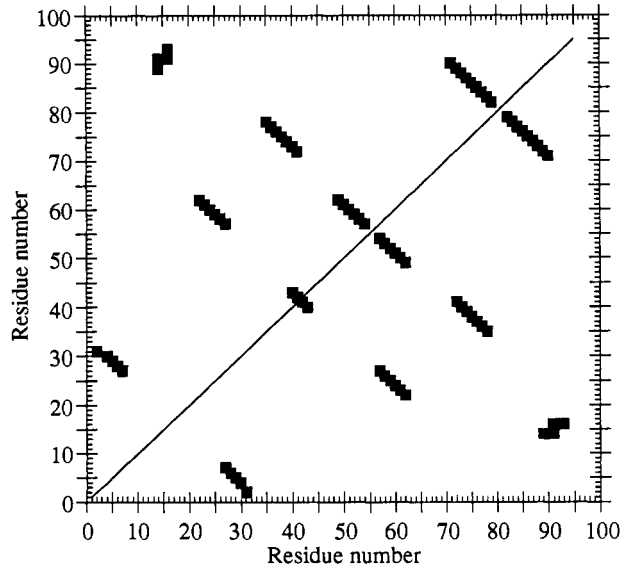

(A)

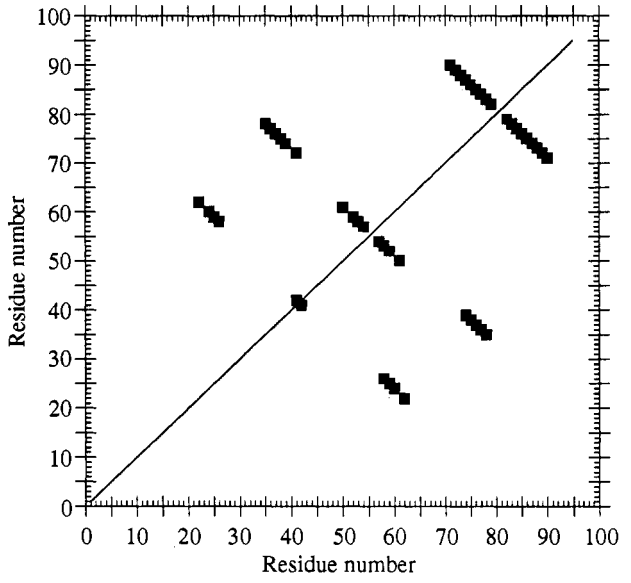

(B)

FIGURE 9: Distance plot (A) derived from the model used and the experimentally determined connectivities (B) for the Ab1 module. In panel A all the interstrand NH–NH and H_α–H_α contacts for the model constructed after telokin are shown. In panel B the NH–NH and H_α–H_α NOE connectivities detected by NMR are indicated.

modules from intracellular proteins and forcing "the abandonment of conserved disulphide bond as the last invariant characteristic of an immunoglobulin-type domain" (Williams, 1987).

Secondary structure predictions and homology searches suggested that type II titin modules belong to the Ig superfamily (Labeit et al., 1990). The fluorescence, CD, and NMR spectra collected in this work provide direct experimental evidence in support of this hypothesis.

The wavelength of the fluorescence maximum shows that the unique tryptophan, the most conserved residue in all titin modules and in all members of the immunoglobulin superfamily (Lesk & Chothia, 1982; Williams & Barklay, 1988; Hsu & Steiner, 1992), is well buried in all three domains. This is consistent with the topology predicted.

The CD patterns obtained are typical of the so-called immunoglobulin fold, rich in β-sheets and in perfect agreement with those reported in the literature for "classical" immunoglobulins [V_{REI} fragment (Brahms & Brahms, 1980); F_c receptor (Gastinel et al., 1992); F_c fragments of IgG molecules (Hobbs et al., 1992); V_H and V_k Ab regions (Ito et al., 1992); mouse IgG (Perczel et al., 1992)] as well as for recent members of the family (single CD2 adhesion domain; Recny et al., 1990). This similarity is very meaningful, given that CD spectra of proteins of high β-pleated content, unlike those of the helical ones, show a large variation in shape and intensity (Perczel et al., 1992). CD spectra of the whole titin molecule have been reported in the past (Maruyama et al., 1986). The differences between those and the ones obtained in the present study could be attributed mainly to the different size of the fragments and the varying contribution of unfolded sequence stretches, as well as nonmodule sequences, in the different preparations of titin.

The NMR-derived plot of $^{13}C_\alpha$ and H_α secondary shifts vs residue number for Ab1 (Figure 8) also indicates the presence of β-sheet secondary structure and identifies the residues involved. There is a good agreement with the predicted location of β-strands in the sequence. Moreover, long-range connectivities (included in the contact map shown in Figure 9), representing interstrand backbone contacts, are identified in the NOESY spectra between protons from residues that are not found in the immediate proximity of each other along the primary sequence. These connectivities are characteristic of a β-sheet folding and agree very well with the fold expected on the basis of the modeling after the telokin structure.

Therefore, we can safely conclude that the three domains studied share a high degree of structural similarity, despite their overall low sequence homology. On the other hand, we should point out the difference in stability, as evidenced by the thermodynamic parameters shown in Table 1 and by the NMR-related spectroscopic behavior: while two modules appear to be quite stable and rigid, the other one, Ab1, was found much less stable and prone to degradation at high temperatures. The higher stability of the M-line domain relative to the others could perhaps be attributed to its position in the titin molecule. Within the M-line, class II motifs are separated by nonrepetitive "linker" sequences, so they could be structurally more "autonomous" than the ones in the A-band, where they are always closely flanked by type I domains (Figure 1). The M-line as a rigid anchoring plane for the thick filaments may also require a higher degree of stability of its constituting modules than along the myosin filaments, where a certain intrinsic elasticity has been demonstrated (Higuchi et al., 1992).

At this point, a word of caution should be added on the potential influence of the boundaries on the stability of isolated modules. Even in extracellular Ig domains, where the intron–exon boundaries are known, domains can be unstable when expressed singly. In the case of intracellular proteins, like titin, the situation is even less clear and that is the reason why our selection of boundaries was based on multiple alignment criteria (as described in detail under Results). We should add that the M-line domain, the one with the least defined boundaries and the shortest length, is the most stable, a fact that could further indicate the stabilizing effect of interdomain interactions.

Could the difference in stability derive from a different functional role? This question can only be answered by a detailed structural and biochemical analysis of motifs spanning a representative range of locations along the whole titin molecule; this analysis is included in the scope of our ongoing work. This type of work is complementary to investigations aiming at the characterization of the whole titin molecule. In a recent publication (Soteriou et al., 1993), CD and fluorescence data collected for the denaturation of the intact titin

molecule indicate a two-step mechanism of unfolding, with Gu-Cl midpoints at 0.1 M and 1.3 M Gu-Cl. The first transition has been interpreted as due to weak interactions between domains, while the second one indicates complete unfolding of titin. The average free energy of unfolding for each domain has subsequently been estimated at ~10 kcal/mol. While our data cannot, at this stage, lead to conclusions about domain interactions, they can yield a more direct estimate of thermodynamic parameters of isolated domains. Furthermore, large, filamentous molecules, such as titin, may collapse in solution producing a series of nonspecific interactions which might lead to artifactual estimates of their stability.

When the whole sequence of the titin molecule becomes available, a more extensive comparison between the structure and stability of modules from different regions will be possible and could explain important properties, such as the elasticity, at the molecular level.

ACKNOWLEDGMENTS

We are grateful to Catherine Joseph for technical assistance with the preparation of the proteins, to Toby Gibson for many helpful discussions, and to Arthur Lesk, Cyrus Chothia, and Spyros Georgatos for critical reading of the manuscript.

REFERENCES

Ayme-Southgate, A., Vigoreaux, Benian, G. M., & Pardue, M. L. (1991) *Proc. Natl. Acad. Sci U.S.A. 88*, 7973–7977.
Baron, M., Norman, D. G., Willis, A., & Campbell, I. D. (1990) *Nature 345*, 642–646.
Bax, A., & Davis, D. G. (1985) *J. Magn. Reson. 63*, 207–212.
Bax, A., Ikura, M., Kay, L. E., Torchia, D. A., & Tschudin, R. (1990) *J. Magn. Reson. 86*, 304–318.
Becktel, W. J., & Schellman, J. A. (1987) *Biopolymers 26*, 1859–1877.
Benian, G. M., Kiff, J. E., Neckelmann, N., Moerman, D. G., & Waterston, R. H. (1989) *Nature 342*, 45–50.
Bodenhausen, G., & Ruben, D. J. (1980) *Chem. Phys. Lett. 69*, 185–189.
Brahms, S., & Brahms, J. (1980) *J. Mol. Biol. 138*, 149–178.
Buchner, J., Lilie, H., Hinz, H. J., Jaenicke, R., Kiefhaber, T., & Rudolph, R. (1991) *Biochemistry 30*, 6922–6929.
Chen, Y. H., Yang, J. T., & Chau, K. H. (1974) *Biochemistry 13*, 3350–3359.
Driscoll, P. C., Cyster, J. G., Campbell, I. D., & Williams, A. F. (1991) *Nature 353*, 762–765.
Fürst, D. O., Osborn, M., Nave, R., & Weber, K. (1988) *J. Cell Biol. 106*, 1563–1572.
Fürst, D. O., Vinkemeier, U., & Weber, K. (1992) *J. Cell Sci. 102*, 769–778.
Fulton, A. B., & Isaacs, W. B. (1991) *BioEssays 13*, 157–161.
Funatsu, T., Higuchi. H., & Ishiwata S. (1990) *J. Cell Biol. 110*, 53–62.
Funatsu, T., Kono, E., & Tsukita, S. (1993) *J. Cell Biol. 120*, 711–724.
Gastinel, L. N., Simister, N. E., & Bjorkman, P. J. (1992) *Proc. Natl. Acad. Sci. U.S.A. 89*, 638–642.
Gautel M., Leonard K., & Labeit S. (1993) *EMBO J. 10*, 3827–3834.
Griesinger, G., Otting, G., Wüthrich, K., & Ernst, R. R. (1988) *J. Am. Chem. Soc. 110*, 7878–7872.
Higgins, D. G., Labeit, S., & Gibson, T., (1994) *J. Mol. Evol.* (in press).
Higuchi, H., Suzuki, T., Kimura, S., Yoshioka, T., Maruyama, K., & Umazume, Y. (1992) *J. Muscle Res. Cell Motil. 13*, 285–294.
Hobbs, S. M., Jackson, L. E., & Hoadley, J. (1992) *Mol. Immunol. 29*, 949–956.
Holden, H. M., Ito, M., Hartshorne, D. J., & Rayment, I. (1992) *J. Mol. Biol. 227*, 840–851.
Horowits, R., Maruyama, K., & Podolsky, R. J. (1989) *J. Cell Biol. 109*, 2169–2176.
Hsu, E., & Steiner, L. A. (1992) *Curr. Opin. Struct. Biol. 2*, 422–431.
Ikura, M., Spera, S., & Bax, A. (1991) *Biochemistry 30*, 9216–9228.
Isaacs, W. B., Kim, I. S., Struve, A., & Fulton, A. B. (1992) *Proc. Natl. Acad. Sci. U.S.A. 89*, 7496–7500.
Kurzban, G. P., & Wang, K. (1988) *Biochem. Biophys. Res. Commun. 155*, 1155–1161.
Labeit, S., Barlow, D. P., Gautel, M., Gibson, T., Holt, J., Hsieh, C. L., Francke, U., Leonard, K., Wardale, J., Whiting, A., & Trinick, J. (1990) *Nature 345*, 273–276.
Labeit, S., Gautel, M., Lackey, A., & Trinick, J. (1992) *EMBO J. 11*, 1711–1716.
Laemmli, U. K. (1970) *Nature 227*, 680–685.
LeGrice, S. F. J., & Grueninger-Leitch, F. (1990) *Eur. J. Biochem. 187*, 307–314.
Lesk, A. M., & Chothia, C. (1982) *J. Mol. Biol. 160*, 325–342.
Main, A. L., Harvey, T. S., Baron, M., Boyd, J., & Campbell, I. D. (1992) *Cell 71*, 671–678.
Maruyama, K., Kimura, S., Yoshidomi, H., Sawada, H., & Kikuchi, K. (1984) *J. Biochem. (Tokyo) 89*, 701–709.
Maruyama, K., Itoh, Y., & Arisaka, F. (1986) *FEBS Lett. 202*, 353–355.
Nave, R., Fürst, D. O., & Weber, K. (1989) *J. Cell Biol. 109*, 2177–2187.
Norwood, T. J., Boyd, J., Heritage, J. E., Soffe, N., & Campbell, I. D. (1990) *J. Magn. Reson. 87*, 488–501.
Pace, C. N., Shirley, B. A., & Thomson, J. A. (1989) in *Protein Structure: A Practical Approach* (Creighton, T. E., Ed.) pp 311–330, IRL Press, Oxford.
Pace, C. N., Laurents, D. V., & Thomson, J. A. (1990) *Biochemistry 29*, 2564–2572.
Pace, C. N., Laurents, D. V., & Erickson, R. E. (1992) *Biochemistry 31*, 2728–2734.
Pastore, A., & Saudek, V. (1990) *J. Magn. Reson. 90*, 165–176.
Perczel, A., Park, K., & Fasman, G. D. (1992) *Proteins 13*, 57–69.
Piotto, M, Saudek, V., & Sklenar, V. (1992) *J. Biomol. NMR 2*, 661–664.
Recny, M. A., Neidhard, E. A., Sayre, P. H., Ciardelli, T. L., & Reinherz, E. L. (1990) *J. Biol. Chem. 265*, 8542–8549.
Saiki, R. K., Scharf, S. J., Faloona, F., Mullis, G. T., & Erlich, H. A. (1985) *Science 230*, 1350–1354.
Santoro, M. M., & Bolen, D. W. (1988) *Biochemistry 27*, 8063–8070.
Schmid, F. X. (1989) in *Protein Structure: A Practical Approach* (Creighton, T. E., Ed.) pp 251–285, IRL Press, Oxford.
Shirakawa, M., Fairbrother, W. J., Serikawa, Y., Okhubo, T., Kyogoku, Y., & Wright, P. E. (1993) *Biochemistry 32*, 2144–2153.
Soteriou, A., Clarke, A., Martin, S., & Trinick J. (1993) *Proc. R. Soc. London B 254*, 83–86.
Spera, S., & Bax, A. (1991) *J. Am. Chem. Soc. 113*, 5490–5492.
Studier, F. W., & Moffat, B. A. (1991) *J. Mol. Biol. 189*, 113–130.
Studier, F. W., Rosenberg, A. H., & Dubendorff, J. W. (1990) *Methods Enzymol. 185*, 62–89.
Trinick, J., Knight, P., & Whiting, A. J. (1984) *J. Mol. Biol. 180*, 331–356.
Vinkemeyer, U., Obermann, W., Weber, K., & Fürst, D. O. (1993) *J. Cell Sci. 106*, 319–330.
Wang, K. (1985) *Cell Muscle Motil. 6*, 315–369.
Whiting, A. J., Wardale, J., & Trinick, J. (1989) *J. Mol. Biol. 205*, 163–169.
Williams, A. F. (1987) *Immunol. Today 8*, 298–303.
Williams, A. F., & Barclay, A. N. (1988) *Annu. Rev. Immunol. 6*, 381–405.
Williams, A. F., Davis, S. J., He, Q., & Barclay, A. N. (1989) *Cold Spring Harbor Symp. Quant. Biol. 54*, 637–647.
Wishart, D. S., Sykes, B. D., & Richards, F. M. (1991) *J. Mol. Biol. 222*, 311–333.
Wüthrich, K. (1986) *NMR of Proteins and Nucleic Acids*, Wiley, New York.

Molecular Basis of the Medium-Chain Fatty Acyl-CoA Dehydrogenase-Catalyzed "Oxidase" Reaction: pH-Dependent Distribution of Intermediary Enzyme Species during Catalysis†

Jeffrey K. Johnson, N. Ravi Kumar, and D. K. Srivastava*

Biochemistry Department, North Dakota State University, Fargo, North Dakota 58105

Received October 27, 1993; Revised Manuscript Received February 14, 1994®

ABSTRACT: In a previous paper, we demonstrated that the medium-chain fatty acyl-CoA dehydrogenase-catalyzed (MCAD-catalyzed) reductive half-reaction of indolepropionyl-CoA proceeds via formation of a chromophoric intermediary species "X" (absorption maximum = 400 nm) and proposed that the decay of this species might limit the overall rate of the "oxidase" reaction [Johnson, J. K., & Srivastava, D. K. (1993) *Biochemistry 32*, 8004–8013]. During this latter reaction, the buffer-dissolved O_2 served as an electron acceptor [Johnson, J. K., Wang, Z. X., & Srivastava, D. K. (1992) *Biochemistry 31*, 10564–10575]. To ascertain whether the intrinsic stability of X influences the oxidase activity, we undertook a detailed kinetic investigation of this enzyme at different pH values. The time-resolved spectra for the reductive half-reaction (obtained via the rapid-scanning stopped-flow method) at different pH values reveal that the amplitude of the intermediary (X) spectral band is more pronounced at a lower pH (pH 6.4) than at a higher pH (pH 9.0). Single-wavelength transient kinetic data for the reductive half-reaction (in both the forward and the reverse direction) at all pH values are consistent with fast ($1/\tau_1$) and slow ($1/\tau_2$) relaxation rate constants. Of these, whereas the fast relaxation rate constant for the reaction in the forward direction ($1/\tau_{1f}$) decreases with an increase in pH, the corresponding slow relaxation rate constant ($1/\tau_{2f}$) increases with an increase in pH. The pH-dependent steady-state kinetic data reveal that, like $1/\tau_{2f}$, k_{cat} for the MCAD-catalyzed oxidase reaction increases with an increase in the pH of the buffer media. These results coupled with the substrate and product concentration-dependent relaxation studies (both in the forward and the reverse direction) as well as the direct measurements of the rate constants of E–$FADH_2$ oxidation at different pH values lead us to conclude the following: (1) The catalytic efficiency of the oxidase reaction is primarily determined by the forward rate constant for the conversion of X to the E–$FADH_2$–P complex. (2) The increase in pH destabilizes the intermediary species X by promoting its distribution toward both the E–FAD–S and the E–$FADH_2$–P complex. (3) There is no discernible effect of pH on the rate of oxidation of E–$FADH_2$ by the buffer-dissolved O_2. (4) The steady-state kinetic parameters for the oxidase reaction are predictable by the microscopic rate constants of the overall enzyme-catalyzed reaction at different pH values. The effector role of the substrate and/or the pH responsible for the origin of the oxidase activity during the MCAD catalysis is discussed.

The medium-chain fatty acyl-CoA dehydrogenase-catalyzed (MCAD[1] -catalyzed) reaction proceeds via a concerted abstraction of a proton and a hydride ion from the α- and β-carbons, respectively, of fatty acyl-CoA chains, concomitant with the reduction of the MCAD-bound FAD to $FADH_2$ [for reviews, see Beinert (1963) and Engel (1990)]. The repetitive turnover of the enzyme under physiological conditions is believed to be maintained by transfer of electrons from MCAD–$FADH_2$ to the electron-transferring flavoprotein (ETF)–FAD (Crane & Beinert, 1956; Ghisla & Massey, 1989). Due to a variety of spectroscopic signals associated with both flavin cofactor and the chromophoric acyl-CoA substrates, this enzyme has been a subject of intense mechanistic investigation in recent years (Frerman et al., 1980; McFarland et al., 1982; Ghisla et al., 1984; Lau et al., 1989). By utilizing indolepropionyl/indoleacryloyl-CoA as the chromophoric substrate/product pair (eq 1), we have elaborated on certain aspects of ligand-binding and reductive and oxidative half-reactions of this enzyme (Johnson et al., 1992, 1993; Johnson & Srivastava, 1993).

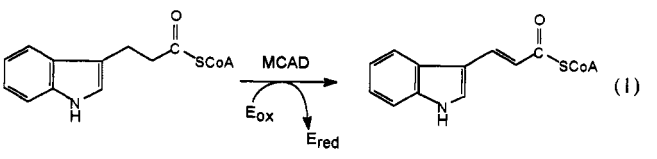

(1)

Due to a characteristic absorption band of the reaction product, indoleacryloyl-CoA (absorption maximum = 367 nm), we could monitor the (steady state) time course of the enzyme-catalyzed reaction without recourse to the signals of external electron acceptors (Johnson et al., 1992). In this way, we observed that the MCAD-catalyzed reaction proceeds via two pathways: (A) a "dehydrogenase" pathway which predominates in the presence of a variety of "organic" electron acceptors such as ETF/DCPIP, $FcPF_6$, and others and (B) an "oxidase" pathway in which the buffer-dissolved O_2

† Journal article no. 2148 of the North Dakota Agricultural Experiment Station. Supported by the American Heart Association, Dakota Affiliate.

* To whom correspondence should be addressed: Biochemistry Department, North Dakota State University, Fargo, ND 58105.

® Abstract published in *Advance ACS Abstracts*, April 1, 1994.

[1] Abbreviations: MCAD, medium-chain fatty acyl-CoA dehydrogenase; IPCoA, 3-indolepropionyl coenzyme A; IACoA, *trans*-3-indoleacryloyl coenzyme A; $FcPF_6$, ferrocenium hexafluorophosphate; FAD, flavin adenine dinucleotide; $FADH_2$, reduced flavin adenine dinucleotide; EDTA, ethylenediaminetetraacetic acid; RSSF, rapid-scanning stopped-flow; E_{ox}, oxidized form of the electron acceptor; E_{red}, reduced form of the electron acceptor.

0006-2960/94/0433-4738$04.50/0

exclusively acts as an electron acceptor. The steady-state kinetic investigation for these reactions revealed that the K_m (for IPCoA) and the k_{cat} for the dehydrogenase reaction were about 1 order of magnitude higher than those for the oxidase reaction (Johnson et al., 1992). This observation led us to suspect that the microscopic pathways for the dehydrogenase and the oxidase reactions might be different.

Transient kinetic investigations into the mechanism of the MCAD-catalyzed reductive half-reaction allowed us, as well as other investigators, to delineate the sequence of events during the single turnover of the enzyme (Johnson & Srivastava, 1993; Schopfer et al., 1988). Utilizing indolepropionyl-CoA as a substrate, we demonstrated that the reductive half-reaction proceeds via formation of an intermediary species, "X", that is characterized by a unique absorption band at 400 nm (Johnson & Srivastava, 1993). The time course for the formation and decay of X was found to be similar to the appearance and disappearance of the charge-transfer complex band at 600 nm (Johnson & Srivastava, 1993). By transient kinetic methods, we determined all of the microscopic constants for the reductive half-reaction of this enzyme at pH 7.6. A casual perusal of these parameters vis-à-vis the steady-state kinetic parameters for the dehydrogenase-catalyzed (K_m(IPCoA) = 10.3 μM, k_{cat} = 0.46 s^{-1}) and oxidase catalyzed reactions (K_m(IPCoA) = 0.49 μM, k_{cat} = 0.016 s^{-1}) (Johnson et al., 1992) allowed us to propose that the rate-limiting step for the dehydrogenation reaction might be the formation of X (0.57 s^{-1}), whereas that for the oxidase reaction might be the decay of X (0.01 s^{-1}) (Johnson & Srivastava, 1993).

The MCAD-catalyzed oxidase reaction is not novel to the use of IPCoA as the enzyme substrate. A number of previous investigators have noted oxidase activity of this enzyme by utilizing a variety of CoA substrates (McFarland et al., 1982; Schopfer et al., 1988; Wang & Thorpe, 1991). Recently, Vanhove et al. (1993) have demonstrated that an analogous enzyme, short-chain fatty acyl-CoA dehydrogenase, catalyzes the oxidase reaction involving a variety of fatty acyl-CoA substrates.

It should be pointed out that the oxidase activity of the enzyme usually remains elusive with aliphatic-CoA substrates (due to the colorless form of their corresponding enoyl-CoA products) unless special efforts are made (McFarland et al., 1982; Vanhove et al., 1993). Such efforts include assay conditions designed to detect the reduced oxygen species, viz., hydrogen peroxide (McFarland et al., 1982; Wang & Thorpe, 1991), superoxide anion (Nishino et al., 1989), and others. This is presumably the reason why the enzyme-catalyzed oxidase reaction has not been seriously investigated. To the best of our knowledge, we have been the first to propose that the MCAD-catalyzed oxidase reaction exhibits a Michaelian dependence on its substrate concentration (Johnson et al., 1992).

Our interest in the MCAD-catalyzed oxidase reaction emerged from the mechanistic as well as the structural–functional point of view (Johnson et al., 1992). Given that the pH influences the isomerization equilibrium between the E–FAD–IACoA and E–FAD*–IACoA** complexes (Johnson et al., 1992), it occurred to us that pH might affect the distribution between X and the E–$FADH_2$–IACoA complex during the reductive half-reaction (Johnson & Srivastava, 1993) and thus would effect the oxidase activity of the enzyme. The experimental results presented below clearly substantiate these expectations.

MATERIALS AND METHODS

Materials. Coenzyme A, glucose oxidase (type VII), and EDTA were purchased from Sigma. 3-Indolepropionic acid and *trans*-3-indoleacrylic acid, used in the synthesis of substrates, were purchased from Aldrich. All other reagents were of analytical reagent grade.

Methods. The CoA derivatives of 3-indolepropionic acid (IPCoA) and *trans*-3-indoleacrylic acid (IACoA) were synthesized and purified according to Johnson et al. (1992). Medium-chain fatty acyl-CoA dehydrogenase (MCAD) was purified in our laboratory as described previously (Johnson et al., 1992).

MCAD was routinely assayed in 50 mM potassium phosphate buffer (pH 7.6) containing 0.3 mM EDTA at 25 °C, utilizing 30 μM octanoyl-CoA and 200 μM ferrocenium hexafluorophosphate ($FcPF_6$) as described by Lehman et al. (1990). The active enzyme concentration was determined in terms of the flavin content by using an extinction coefficient of 15.4 mM^{-1} cm^{-1} at 446 nm (Thorpe et al., 1979). IPCoA and IACoA concentrations were determined using extinction coefficients of 18.2 mM^{-1} cm^{-1} at 259 nm and 26.5 mM^{-1} cm^{-1} at 367 nm, respectively (Johnson et al., 1992). Experiments involving pH effects were performed in the following buffers: for pH ranges between 6 and 8, 50 mM potassium phosphate containing 0.3 mM EDTA was used; for pH ranges between 8 and 10.5, 0.1 M Tris-HCl plus 50 mM potassium phosphate buffer containing 0.3 mM EDTA was used.

Steady-state kinetics for the enzyme-catalyzed oxidase reaction was performed on a Perkin Elmer Lambda 3B spectrophotometer, utilizing a 10-cm-path-length cuvette. Other experiments and data analyses were performed as described by Johnson and Srivastava (1993) and Johnson et al. (1993). Single-wavelength transient kinetic studies and data analysis were performed on an Applied Photophysics MV-14 sequential-mixing stopped-flow system (optical path length = 1 cm; dead time = 1.34 ms). The time-resolved spectra were acquired on a Durrum stopped-flow system (optical path length = 1.5 cm; dead time = 3–5 ms), configured in our laboratory as a rapid-scanning device (Johnson & Srivastava, 1993).

Oxidation of MCAD–$FADH_2$ by O_2. MCAD–$FADH_2$ was generated by incubation of MCAD–FAD with sodium dithionite in an appropriate anaerobic buffer (at different pH). The anaerobic buffers used for these experiments were prepared by a repeated cycle of degassing and purging with oxygen-free argon. Since these buffers did not contain glucose and glucose oxidase to scavenge the residual traces of oxygen, a higher concentration of sodium dithionite (about 50–70 μM) was required for a quantitative reduction of the enzyme. The amount of sodium dithionite required to reduce a fixed concentration of MCAD–FAD was predetermined by measuring the absorption at 450 nm. Oxygen concentration in different buffers was adjusted by mixing an appropriate ratio of anaerobic buffer (prepared as described above) and fully oxygenated buffer. The final concentration of oxygen in the buffer was determined by Yellow Spring Instrument (YSI) biological oxygen monitor (Model 5300).

The time-dependent increase in absorption at 450 nm was monitored upon mixing of sodium dithionite-reduced MCAD and (buffer-dissolved) oxygen via the stopped-flow syringes. The concentrations of enzyme and oxygen (after mixing) were 5 and 240 μM, respectively, at different pH values. The reaction profiles were analyzed according to a single-exponential rate law. At pH 7.6, we measured the rates of oxidation of the reduced enzyme at different concentrations

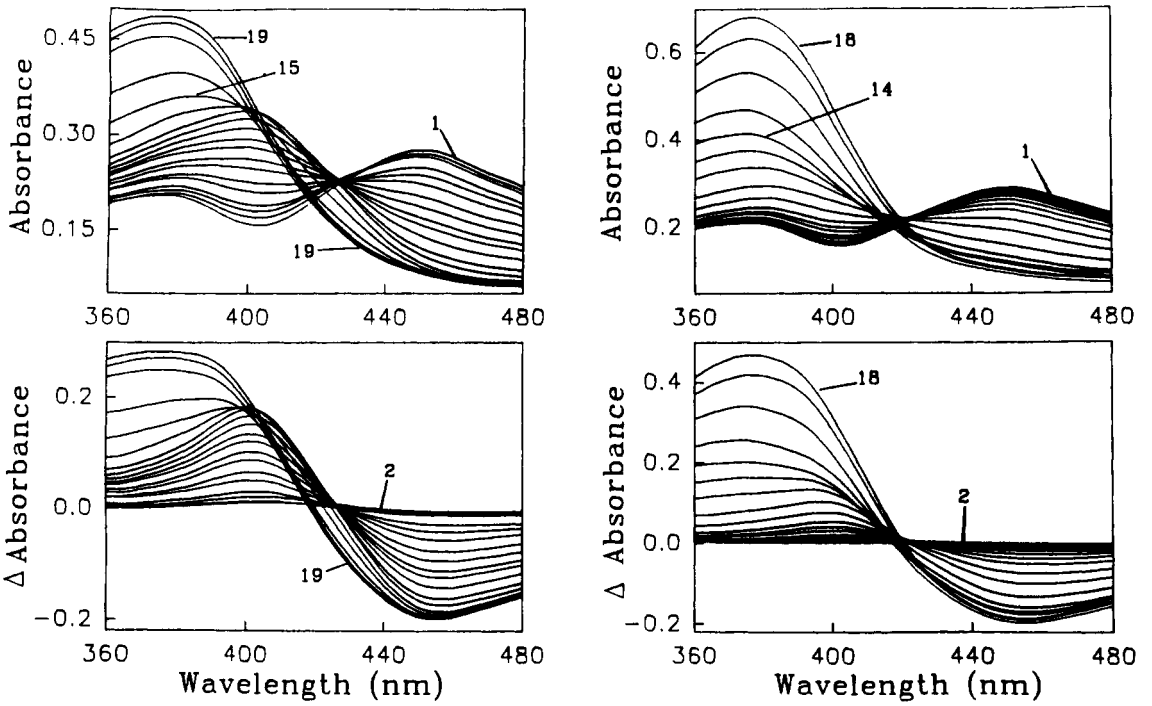

FIGURE 1: Rapid-scanning stopped-flow spectra for the reaction of MCAD–FAD with IPCoA ([IPCoA] ≫ [MCAD–FAD]) at pH 6.4 (left panels) and 9.0 (right panels) under anaerobic conditions. The concentrations of MCAD–FAD (syringe 1) and IPCoA (syringe 2) prior to mixing were 20 and 200 μM, respectively. The top and bottom panels show normal spectra and difference spectra (spectra at given times minus the first spectrum) at the corresponding pH values. The time delays (in seconds) for the spectral traces (1–20) in the left panels (pH 6.4) were as follows: 0, 0.034, 0.052, 0.069, 0.138, 0.224, 0.31, 0.48, 0.654, 0.895, 1.08, 1.51, 2.37, 4.1, 11.9, 24.8, 51.5, 138, 241, and 282. The time delays (in seconds) for the traces (1–18) in the right panels (pH 9.0) were as follows: 0, 0.026, 0.052, 0.138, 0.224, 0.31, 0.48, 0.654, 0.895, 1.51, 2.37, 4.1, 6.28, 9.26, 14.5, 103, 241, and 282.

of buffer-dissolved oxygen. The data were analyzed for a linear dependence of the observed rate constant as a function of the oxygen concentration. The slope of this plot was taken as a measure of the second-order rate constant.

RESULTS

Having surmised that pH might influence the equilibrium distribution of the intermediary species (see the introduction), we undertook a pH-dependent transient kinetic study of the reductive half-reaction of the medium-chain fatty acyl-CoA dehydrogenase (MCAD) utilizing indolepropionyl-CoA (IPCoA) as a chromophoric substrate. In this pursuit, we compared the time-resolved spectral changes (acquired via the rapid-scanning stopped-flow, or RSSF, method) at selected pH values (viz., pH 6.4, 7.6, and 9.0). Figure 1 shows the RSSF spectra for the reaction of MCAD–FAD with IPCoA (after-mixing concentrations of 10 and 100 μM, respectively) under anaerobic conditions at pH 6.4 and 9.0, respectively. Although the timing sequences for different spectral traces are more or less the same, the spectral patterns at these two pH values are remarkably different. The most noticeable difference is the amplitude of the intermediary spectral band at 400 nm (due to the formation of X; Johnson & Srivastava, 1993). This band is more pronounced at pH 6.4 than at pH 9.0. This feature is further explicit in the difference spectra (i.e., the spectra at given times minus the first spectrum) of Figure 1 (bottom panels). The spectral pattern obtained at pH 6.4 was found to be similar to that observed at pH 7.6 (data not shown).

Given that pH influences the electronic spectrum of neither E–FAD nor IACoA (Johnson et al., 1992), the pronounced spectral band (at 400 nm) at pH 6.4 vis-à-vis that at pH 9.0 can be envisaged to originate from some pH-dependent changes in the kinetic and/or the thermodynamic properties of the

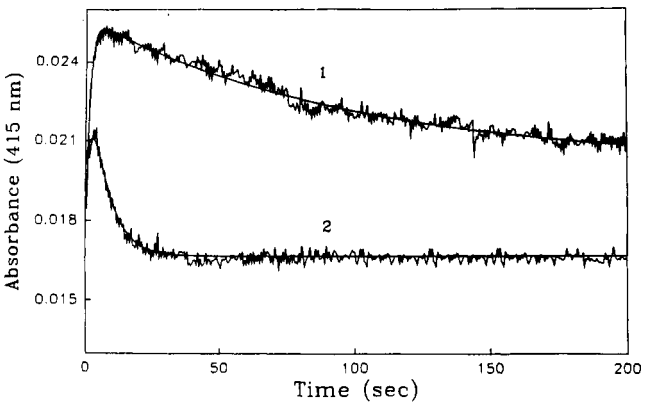

FIGURE 2: Single-wavelength (415 nm) stopped-flow traces (trace 1 at pH 6.4, trace 2 at pH 9.0) for the reaction of 2.4 μM MCAD–FAD (syringe 1) and 200 μM IPCoA (syringe 2). Solid lines are the best fits of the experimental data according to the two-exponential rate equations (for increasing and decreasing phase). The relaxation rate constants for the fast ($1/\tau_{1f}$) and slow ($1/\tau_{2f}$) phases are 1.03 and 0.0083 s^{-1} at pH 6.4 and 0.45 and 0.16 s^{-1} at pH 9.0, respectively.

enzyme. To ascertain whether the amplitude of the intermediary spectral band (X) is kinetically controlled, we performed a single-wavelength stopped-flow study (under anaerobic conditions) for the reaction of MCAD–FAD and IPCoA at pH 6.4 and 9.0, utilizing a lower concentration of the enzyme. Figure 2 shows the time course of the absorption changes at 415 nm upon mixing MCAD–FAD with IPCoA (after-mixing concentrations of 1.2 μM and 100 μM, respectively) via the stopped-flow syringes. Note that at pH 6.4 a rapid increase in absorption (at 415 nm) follows a slow decrease. This pattern is different from that observed at pH 9.0. At the latter pH, a somewhat slower rate of increase in absorption is followed by a rapid decrease. Upon analyzing these kinetic traces by a two-exponential rate equation, we

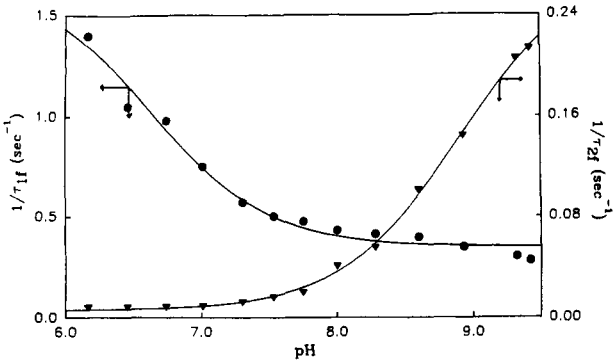

FIGURE 3: pH-dependent changes in the fast ($1/\tau_{1f}$) and slow ($1/\tau_{2f}$) relaxation rate constants for the reaction of 2.4 μM MCAD–FAD (syringe 1) and 200 μM IPCoA. The magnitudes of $1/\tau_{1f}$ and $1/\tau_{2f}$ were obtained from the best fits of the experimental data at 400 and 415 nm, respectively. Note that as pH increases, $1/\tau_{1f}$ and $1/\tau_{2f}$ decrease and increase, respectively. The solid lines are the best fits of the experimental data according to the Henderson–Hasselbalch equation with pK_a values equal to 6.63 ± 0.10 (from the data of the $1/\tau_{1f}$ versus pH plot) and 8.90 ± 0.03 (from the data of the $1/\tau_{2f}$ versus pH plot).

determined the fast ($1/\tau_{1f}$, increasing phase; the "f" in the subscript stands for the reaction in the forward direction) and slow ($1/\tau_{2f}$, decreasing phase) relaxation rate constants to be 1.03 and 0.008 s^{-1} at pH 6.4 and 0.45 and 0.16 s^{-1} at pH 9.0, respectively. These results coupled with the fact that the amplitude of the absorption changes is higher at pH 6.4 than at pH 9.0 suggest that the equilibration rate leading to the formation of X is faster than that leading to its decay at pH 6.4. Hence, the higher amplitude of the intermediary absorption band at 400 nm (at pH 6.4) is clearly due to a rapid production of X followed by its slow decay.

The time courses for the absorption changes at most of the wavelengths (except at isoabsorption points) are consistent with two-exponential processes (increase, decrease, or a combination of the two) corresponding to the relaxation rate constants $1/\tau_{1f}$ and $1/\tau_{2f}$, respectively (Johnson & Srivastava, 1993). To ascertain the influence of pH on these relaxation rate constants, we performed experiments similar to that presented in Figure 2 at different pH values. The concentrations of E–FAD and IPCoA (after mixing) were maintained at 1.2 and 100 μM, respectively, in the stopped-flow syringes for all pH-dependent experiments. For convenience, the magnitudes of $1/\tau_{1f}$ and $1/\tau_{2f}$ were calculated from the best fit of the experimental data at wavelengths of 400 and 415 nm, respectively. As noted by us previously, $1/\tau_{1f}$ calculated from the data at 415 nm was the same as that calculated at 400 nm (Johnson & Srivastava, 1993).

Figure 3 shows the pH-dependent variations in $1/\tau_{1f}$ and $1/\tau_{2f}$. It is noteworthy that $1/\tau_{1f}$ sharply decreases with increasing pH over the pH range 6.2–7.0, and after that it becomes constant. This is in marked contrast to the dependence of $1/\tau_{2f}$ on pH. The magnitude of $1/\tau_{2f}$ remains invariant with increasing pH over the pH range 6.2–7.0, and after that it starts increasing rather sharply. From the best fit of the experimental data according to the Henderson–Hasselbalch equation, we have determined the pK_a values of 6.63 ± 0.10 and 8.90 ± 0.03 from the data of $1/\tau_{1f}$ and $1/\tau_{2f}$, respectively. It should be pointed out that these pK_a's have no physical meaning with regard to the dissociability of specific active site groups. Rather, they are a complex function of the various pH-dependent processes. From the data of Figure 3, it is noteworthy that the ratio of $1/\tau_{1f}$ and $1/\tau_{2f}$ decreases from 177 at pH 6.2 to 1.3 at pH 9.4. Although the pH-dependent variation of this ratio is not a quantitative measure

Table 1: Summary of $1/\tau_{max}$, $1/\tau_{min}$ and $K_{0.5}$ Values Derived from the Dependence of Relaxation Rate Constants on IPCoA/IACoA Concentrations at Different pH Values

	pH		
	6.4	7.6	9.0
IPCoA			
$1/\tau_{1f(max)}$ (s^{-1})	1.32	0.63	0.69
$1/\tau_{1f(min)}$ (s^{-1})	0.03	0.08	0.12
$1/\tau_{2f(min)}$ (s^{-1})	0.005	0.01	0.11
$K_{0.5}$ (μM)	11.5	11.5	11.2
IACoA			
$1/\tau_{1r(max)}$ (s^{-1})	1.99	4.38	12.90
$1/\tau_{1r(min)}$ (s^{-1})	0.005	0.01	1.43
$1/\tau_{2r(min)}$ (s^{-1})	0.03	0.08	0.04
$K_{0.5}$ (μM)	23.7	14.9	6.4

of the equilibrium distribution among the various forms of the enzyme species, it provides some indication as to the distribution of the enzyme species among E–FAD–IPCoA, X, and E–FADH$_2$–IACoA complexes. A higher ratio of $1/\tau_{1f}$ and $1/\tau_{2f}$ at lower pH values attests to the fact that the microscopic steps intrinsic to $1/\tau_{1f}$ are not intimately coupled to those with $1/\tau_{2f}$ (Bernasconi, 1976). This is clearly not the case under conditions (i.e., at higher pH values) where the magnitudes of $1/\tau_{1f}$ and $1/\tau_{2f}$ are comparable (see Discussion).

We performed the IPCoA concentration dependent relaxation studies for the reaction of E–FAD + IPCoA (under condition where [IPCoA] $\gg$ [E–FAD]) at pH values 6.4, 7.6, and 9.0. As observed by us previously (Johnson & Srivastava, 1993), at all these pH values, $1/\tau_{1f}$ increases hyperbolically (with an offset) with an increase in IPCoA concentration. On the contrary, $1/\tau_{2f}$ decreases with an increase in IPCoA concentration. These data were analyzed essentially as described by Johnson and Srivastava (1993), except the magnitude of the "offset" was set equal to the slow relaxation rate constant in the reverse direction ($1/\tau_{2r}$) at a saturating concentration of IACoA. This strategem minimized the error introduced by extrapolation of $1/\tau_{1f}$ to zero concentration of IPCoA. The magnitudes of $1/\tau_{1f}$ at zero (offset) and saturating (asymptote) concentrations of IPCoA are taken to be the measures of the maximum ($1/\tau_{1f(max)}$) and minimum ($1/\tau_{1f(min)}$) relaxation rate constants. The concentrations of IPCoA required to attain one-half of the total changes are represented by $K_{0.5}$. These values are given in Table 1. We have not rigorously analyzed, at this time, the (decreasing) hyperbolic dependence of $1/\tau_{2f}$ on [IPCoA], except for determining its magnitude at saturating concentrations of the latter. Under these conditions, $1/\tau_{2f}$ attains a minimum value and is represented by $1/\tau_{2f(min)}$ (Table 1) at different pH's.

We performed analogous transient kinetic experiments for the reaction in the reverse direction, i.e., between E–FADH$_2$ (generated by sodium dithionite reduction) and IACoA. The time courses for the reaction of 2 μM E–FADH$_2$ and varying concentrations of IACoA ([IACoA] > [E–FADH$_2$]) were measured at 415 nm, at selected pH values. Like the reaction profiles in the forward direction, the reverse reaction profiles were consistent with two relaxation rate constants, $1/\tau_{1r}$ and $1/\tau_{2r}$ ("r" denotes the reaction in the reverse direction), and showed hyperbolic increasing and decreasing dependence on IACoA concentrations, respectively. These data were analyzed as described above, and the magnitudes of $1/\tau_{1r(max)}$, $1/\tau_{1r(min)}$, $1/\tau_{2r(min)}$, and $K_{0.5}$ were determined (Table 1). The experimental data of Table 1 have been used to calculate the microscopic parameters for the overall reductive half-reaction at different pH values (see Table 3, and Discussion).

Steady-State Kinetics for the Oxidase Reaction. We performed the steady-state kinetics for the MCAD-catalyzed

Table 2: Steady-State Kinetic Parameters for the MCAD-Catalyzed Oxidase Reaction

	experimentally determined		predicted[a]	
pH	K_m(IPCoA) (μM)	k_{cat} (s^{-1})	K_m(IPCoA) (μM)	k_{cat} (s^{-1})
6.4	0.21 ± 0.017	0.008 ± 0.0002	0.30	0.005
7.6	0.49 ± 0.040	0.016 ± 0.0004	1.60	0.008
9.0	0.79 ± 0.085	0.038 ± 0.0014	3.25	0.046

[a] According to eqs 5A and 5B, utilizing the microscopic parameters of Table 3.

Table 3: Microscopic Parameters for the MCAD-Catalyzed Reductive Half-Reaction at Different pH Values

	pH		
	6.4	7.6	9.0
K_s (μM)	11.5	11.5	11.2
k_2 (s^{-1})	1.29	0.55	0.50
k_{-2} (s^{-1})	0.03	0.08	0.15
k_3 (s^{-1})	0.005	0.010	0.070
k_{-3} (s^{-1})	1.99	4.38	12.79
K_p (μM)	23.70	14.90	6.40
k_5 (s^{-1})	0.97	1.03	1.00

oxidase reaction utilizing IPCoA as the enzyme substrate. Due to a low K_m value for IPCoA during the oxidase reaction, these experiments were performed in a 10-cm-path-length cuvette. The initial rates of the enzyme-catalyzed conversion of IPCoA to IACoA were measured at 367 nm, in the absence of any externally added organic electron acceptors. The initial rate of the enzyme-catalyzed reaction showed a Michaelian dependence on IPCoA concentration at all the pH values examined (i.e., pH 6.4, 7.6, and 9.0). From the best fit of the experimental data according to the Michaelis–Menten equation, the K_m(IPCoA) and k_{cat} for the oxidase reaction were calculated at these pH values (Table 2). Although we have not determined whether the buffer-dissolved oxygen (240 μM) is saturating for the IPCoA-dependent oxidase reaction, the K_m for oxygen during the enzyme-catalyzed oxidation of indolepropionyl pantetheine phosphate (3′,5′-ADP truncated IPCoA) to indoleacryloyl pantetheine phosphate is about 28 μM (our unpublished results). However, the steady-state parameters are still considered to be "apparent" since they have not been obtained by extrapolation of initial rates at infinite concentrations of O_2.

From this limited experimental data, it is evident that as the pH increases both k_{cat} and K_m(IPCoA) increase (Table 2). Given that the K_m for IPCoA at all these pH values (Table 2) is less than 1 μM, we measured the turnover number of the MCAD-catalyzed oxidase reaction at different pH values (ranging from pH 6.0 to 10.5) in the presence of a saturating (50 μM) concentration of IPCoA (Figure 4). It is noteworthy that the turnover rate (k_{cat}) for the MCAD-catalyzed oxidase reaction remains more or less constant over the pH range 5.8–7.8, but it starts increasing (rather sharply) beyond the latter pH value. This pattern is analogous to the dependence of $1/\tau_{2f}$ on pH (see Figure 3). The pH-dependent oxidase reaction is consistent with a pK_a of 9.91 ± 0.05. This pK_a is 1 unit higher than that observed for the dependence of $1/\tau_{2f}$ on pH. This discrepancy is presumably due to the fact that the oxidase reaction is primarily limited by the forward rate constant for the decay of X, whereas $1/\tau_{2f}$ is a combined function of the various microscopic rate constants (see Discussion).

Oxidation of MCAD-Bound FADH₂ by Buffer-Dissolved O_2. To provide a detailed molecular basis for the MCAD-catalyzed oxidase reaction, we decided to determine the rate

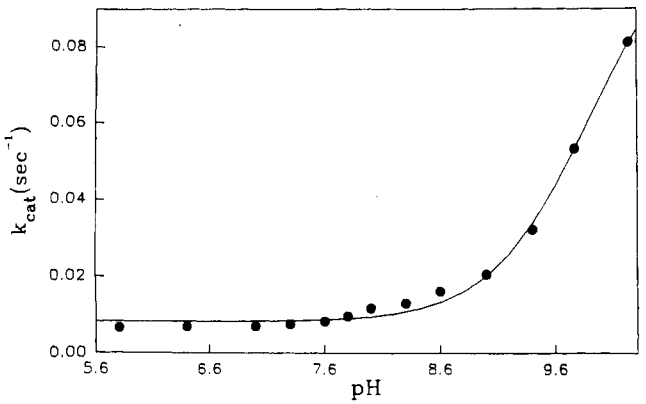

FIGURE 4: Effect of pH on the turnover rate (k_{cat}) for the MCAD-catalyzed oxidase reaction in the presence of buffer-dissolved O_2 (240 μM). The concentrations of the enzyme and IPCoA were 0.77 and 50 μM, respectively. The solid line is the best fit of the experimental data according to the Henderson–Hasselbalch equation with a pK_a of 9.91 ● 0.05.

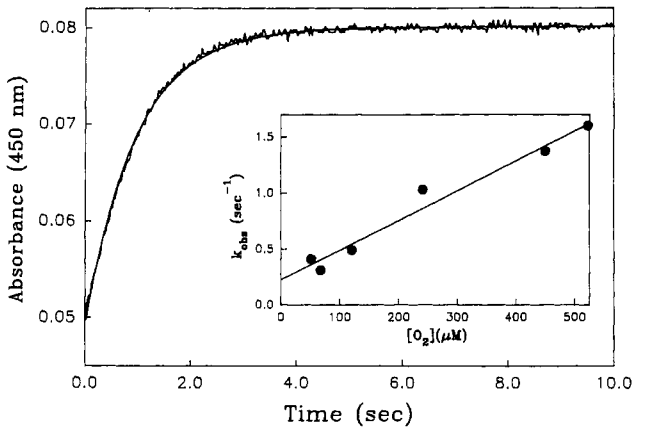

FIGURE 5: Reaction of MCAD–$FADH_2$ with buffer-dissolved oxygen at pH 7.6. The time-dependent change in the absorption at 450 nm for the reaction of 10 μM MCAD–$FADH_2$ (syringe 1) and 480 μM buffer-dissolved oxygen is shown (the after-mixing concentrations of enzyme and oxygen are 5.0 and 240 μM, respectively). The solid line is the best fit of the experimental data according to the single-exponential (increase) rate equation, for a rate constant of 1.03 s^{-1}. The inset shows the effect of oxygen concentration on the observed rate constant for the MCAD–$FADH_2$ oxidation. The solid line is the best fit of the experimental data, with a second-order rate constant of (2.65 ± 0.23) × 10^3 M^{-1} s^{-1}.

constant for the MCAD–$FADH_2$ oxidation by the buffer-dissolved oxygen at selected pH values. This experiment was performed by mixing sodium dithionite-reduced enzyme (10 μM) with an oxygen-saturated buffer (oxygen concentration = 480 μM) in the stopped-flow syringes (see Materials and Methods). In this way, the after-mixing concentration of oxygen was maintained at 240 μM (similar to the concentration of the buffer-dissolved oxygen under normal conditions). The time courses for the oxidation of MCAD–$FADH_2$, at different pH values, by (240 μM) buffer-dissolved oxygen were monitored at 450 nm. Figure 5 shows a representative trace for the oxidation of MCAD–$FADH_2$ at pH 7.6. From the best fit of the experimental data according to a single-exponential rate law (solid line), we have determined the first-order constant for the oxidation of E–$FADH_2$ by O_2 to be 1.03 s^{-1} (at pH 7.6). The corresponding rate constants at pH 6.4 and 9.0 (under identical experimental conditions) were found to be 0.97 and 1.0 s^{-1}, respectively.

We measured the rate of oxidation of MCAD–$FADH_2$ at different concentrations of the buffer-dissolved oxygen at pH 7.6. The oxygen concentration during these experiments was

maintained to satisfy pseudo-first-order conditions. The data were analyzed for a single-exponential increase in absorption at all oxygen concentrations. The inset of Figure 5 shows a linear dependence of the observed rate constant (k_{obs}) as a function of oxygen concentration, suggesting that the overall oxidation reaction is a second-order process. The slope of this plot [$(2.65 \pm 0.23) \times 10^3$ M^{-1} s^{-1}] is taken to be a measure of the second-order rate constant for the oxidation of MCAD–$FADH_2$ by oxygen at pH 7.6.

DISCUSSION

The pH-dependent investigation presented herein has been prompted by our realization that there is an intrinsic commonality between the microscopic pathways leading to E–FAD + IACoA interaction and E–FAD/$FADH_2$ + IPCoA/IACoA binding followed by chemical transformations (eq 2).

$$\text{E–FAD} + \text{IACoA} \rightleftharpoons \text{E–FAD–IACoA} \rightleftharpoons \text{E–FAD*–IACoA**} \quad (2A)$$

$$\text{E–FAD} + \text{IPCoA} \rightleftharpoons \text{E–FAD–IPCoA} \rightleftharpoons \text{X (E–FADH}_2\text{–IACoA*)} \quad (2B)$$

$$\text{E–FADH}_2 + \text{IACoA} \rightleftharpoons \text{E–FADH}_2\text{–IACoA} \rightleftharpoons \text{X (E–FADH}_2\text{–IACoA*)} \quad (2C)$$

Both of these processes occur in two steps. The first (fast) step involves the formation of a collision complex between the enzyme and the CoA derivative. This complex is slowly isomerized to a more stable complex during the second step. This two-step binding and/or catalysis has been observed not only with these chromophoric substrates but also with butyryl-crotonoy-CoA and octanoyl-octenoyl-CoA pairs, and even in the case of the E–FAD + acetoacetyl-CoA interaction (our unpublished results). The only difference between these two seemingly diverse phenomena is that the slow steps of eqs 2A and 2C are devoid of "chemistry", whereas that of eq 2B is coupled to the oxidation/reduction reaction.

The RSSF data, coupled with the single-wavelength stopped-flow studies, at different pH values substantiate that the intermediary species X is more pronounced at lower pH values than at higher pH values. This observation is further supported by the fact that as pH increases, $1/\tau_{1f}$ decreases, whereas $1/\tau_{2f}$ increases. Since these relaxation rate constants are the aggregates of the various microscopic parameters, they do not report on the specific effects of pH on the individual kinetic or thermodynamic parameters of the underlying kinetic model. Such information is extracted from the IPCoA/IACoA concentration dependent relaxation studies at different pH values. We have previously elaborated on the determination of the individual kinetic/thermodynamic parameters for the MCAD-catalyzed reductive half-reaction at pH 7.6, essentially according to a theoretical (two-step) model of Strickland et al. (1975). Since a qualitatively similar dependence of the relaxation rate constants on IPCoA/IACoA concentrations has been observed at other pH values (Table 1), we have adopted the same analytical protocol. To comprehend the effect of pH on the microscopic parameters of the MCAD-catalyzed reductive half-reaction, let us review our previously proposed kinetic model for this enzyme (eq 3):

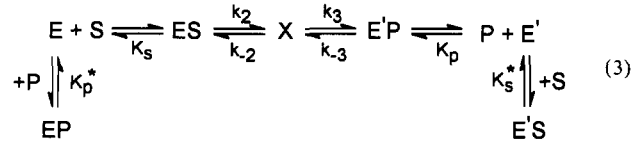

(3)

where E and E′ refer to MCAD–FAD and MCAD–$FADH_2$, respectively, and S and P refer to IPCoA and IACoA, respectively. This model is similar to that proposed by Schopfer et al. (1988) involving butyryl-CoA as the enzyme substrate. As discussed previously, the origin of the second relaxation step ($1/\tau_2$) in both forward and reverse directions lies in the formation of E′S and EP complexes, respectively. Given that $1/\tau_{1f} \gg 1/\tau_{2f}$ (at pH 6.4 and 7.6) and that $1/\tau_{1r} \gg 1/\tau_{2r}$ (at all pH's), the underlying steps can be considered to be uncoupled (Bernasconi, 1976). Hence, in accord with our earlier analysis, the relationships between the macroscopic rate constants (Table 1) and the microscopic parameters of eq 3 can be given as follows:

$$1/\tau_{1f(max)} = k_2 + k_{-2}; \quad 1/\tau_{1f(min)} = 1/\tau_{2r(min)} = k_{-2}$$

$$1/\tau_{2f(min)} = 1/\tau_{1r(min)} = k_3; \quad 1/\tau_{1r(max)} = k_3 + k_{-3}$$

$$K_{0.5(IPCoA)} = K_s; \quad K_{0.5(IACoA)} = K_p$$

On the basis of these relationships, we could translate the macroscopic rate constants of Table 1 into the microscopic parameters (Table 3) at pH 6.4 and 7.6. However, this approach could not be employed for the data at pH 9.0. This is because, due to comparable magnitudes of $1/\tau_{1f}$ and $1/\tau_{2f}$ at pH 9.0, the steps intrinsic to these relaxation rate constants could not be treated as uncoupled. Under this situation recourse was made to the numerical simulation for the model of eq 3 at pH 9.0, as described by Johnson and Srivastava (1993). The corresponding microscopic parameters at pH 9.0 are summarized in Table 3.

A close perusal of the data of Table 3 suggests that although the dissociation constant of the E–FAD–IPCoA complex is not affected within the pH range between 6.4 and 9.0, the dissociation constant of the E–$FADH_2$–IACoA complex varies by a factor of 4. At this time, we are uncertain whether this variation is real or is merely due to our inability to precisely determine $K_{0.5}$ values. However, from the data of Table 3, it is clear that as the pH increases, k_2 decreases, whereas k_{-2} increases. On the other hand, as pH increases, both k_3 and k_{-3} increase. This pattern can easily account for a higher amplitude of X at pH 6.4 than at pH 9.0 (see Figures 1 and 2).

The fact that k_3 of eq 3 (the rate constant for the decay of X) and the k_{cat} for the oxidase reaction both increase with an increase in the pH of the buffer media attests to our earlier proposition that the MCAD-catalyzed oxidase reaction might be limited by the rate of the decay of X. Since the increase in pH also increases k_{-3} (albeit not by an equal magnitude), it follows that the pH-dependent increase in $1/\tau_{2f}$ must be steeper than that of k_3. This is presumably the reason that the pH-dependent oxidase activity and $1/\tau_{2f}$ yield different pK_a values.

Can we predict the steady-state kinetic parameters for the oxidase reaction from the microscopic rate constants presented in Table 3? For making such a prediction, it is important to consider at what intermediary enzyme species the reduced flavin is oxidized by O_2. Clearly, the reduced flavin present in X is not oxidized by O_2, since the oxidation reaction is limited by the rate of collapse of X. Thus, either E–$FADH_2$ or its complex with IPCoA/IACoA is likely to be the target of the oxidation reaction. However, on the basis of X-ray crystallographic data (Kim et al., 1993) that the binding of fatty acyl-CoA's with MCAD "desolvates" the enzyme site environment, we consider the likely enzyme site for the oxidation of the reduced flavin to be E–$FADH_2$. This allows

us to propose the following steady-state kinetic scheme for the MCAD-catalyzed oxidase reaction (eq 4).

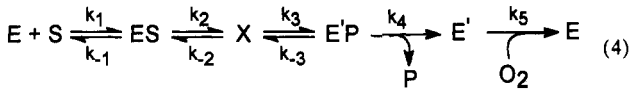

(4)

In this scheme, the last two steps are taken to be irreversible. The first irreversible step satisfies the condition of the initial rate measurements (i.e., when product is zero). The irreversibility of the second step is naturally justified since the electron transfer from E–$FADH_2$ to O_2 is a thermodynamically favorable reaction (Walsh, 1979). It is interesting to note that the rate of oxidation of MCAD–$FADH_2$ by O_2 (240 μM) remains unaffected over the pH range 6.4–9.0 (Table 3). The steady-state rate equation derived for the kinetic scheme of eq 4 provides relationships between the steady-state kinetic parameters (K_m for IPCoA and k_{cat}) for the oxidase reaction and the microscopic rate constants of eq 3:

$$K_m(\text{IPCoA}) = \frac{k_5\{k_3k_4(k_{-1} + k_2) + k_{-1}k_{-2}(k_{-3} + k_4)\}}{k_1\{k_4k_5(k_2 + k_{-2} + k_3) + k_{-3}k_5(k_2 + k_{-2}) + k_2k_3(k_4 + k_5)\}} \quad (5A)$$

$$k_{cat} = \frac{k_2k_3k_4k_5}{k_2k_3(k_4 + k_5) + k_{-3}k_5(k_2 + k_{-2}) + k_4k_5(k_2 + k_{-2} + k_3)} \quad (5B)$$

For predicting these steady-state kinetic parameters, the dissociation constant parameters K_s and K_p (of Table 1) were translated into the corresponding "on" and "off" rate constants on the assumption that the former is a diffusion-limited process (1×10^8 M^{-1} s^{-1}; Hammes, 1982). On this basis, the off rates (e.g., k_{-1} and k_4) are calculated from the dissociation constants of the E–FAD–IPCoA (K_s) and E–$FADH_2$–IACoA (K_p) complexes. Given these, as well as the microscopic parameters of Table 3, we could predict K_m for IPCoA and k_{cat} for the oxidase reaction at pH values 6.4, 7.6, and 9.0. These results are summarized, along with the experimentally determined parameters, in Table 2. The data of Table 2 show that both experimentally determined and predicted steady-state kinetic parameters increase with the increase in the pH of the buffer media. However, while the experimentally determined k_{cat}'s are more or less similar to those predicted at the corresponding pH values, K_m's for IPCoA under these conditions differ by a factor of 3–4. This variation is not significant in the light of the following two facts: (1) The experimentally determined K_m for IPCoA is in the sub-micromolar range at all pH values, and thus despite our effort to determine this parameter as carefully as possible, some variations can be expected. (2) The prediction of the steady-state kinetic parameters involves a complex function of the microscopic parameters, which have been determined by independent methods; thus, even small errors in these parameters can be expected to be amplified while predicting the steady-state kinetic parameters by eqs 5A and 5B. In the light of these considerations, the experimentally determined and predicted steady state kinetic parameters for the MCAD-catalyzed reaction can be taken to be remarkably similar.

On compilation of all of the experimental data presented herein, it is evident that both the substrate (IPCoA) and the pH of the buffer media serve as effectors of the MCAD-catalyzed oxidase reaction. Both of these effectors promote the oxidase activity by perturbing the equilibrium between X and the E–$FADH_2$–IACoA species such that the latter is favored. The substrate (IPCoA) accomplishes this task (rather indirectly) by combining with the E–$FADH_2$ form of the enzyme (Johnson & Srivastava, 1993), whereas the higher pH performs this function by destabilizing the electronic structure of IACoA within X such that the equilibrium distribution of this species (X) is favored toward both the E–FAD–IPCoA and E–$FADH_2$–IACoA complexes. Such an effect of pH is similar to that observed by us for the interaction of E–FAD with IACoA (Johnson et al., 1992). In this way, the effect of higher pH in promoting the oxidase activity of the enzyme is merely a happenstance, since pH promotes equilibration of X toward the E–$FADH_2$–IACoA species (responsible for the origin of the oxidase activity of the enzyme). The effect of higher pH on favorable equilibration of X toward the E–FAD–IPCoA complex is not realized in this regard. However, the latter effect becomes explicit as the K_m for IPCoA, during the dehydrogenation reaction, increases from 6.1 (pH 6.4) to 32.0 (pH 9.5; our unpublished results). We are currently testing our mechanistic principles, presented herein, for the origin of the oxidase activity involving different acyl-CoA substrates, including those (e.g., octanoyl-CoA) which are known to resist this activity, and we will report these findings subsequently.

REFERENCES

Beinert, H. (1963) *The Enzymes* (Boyer, P. D., Lardy, H., & Myrbach, K., Eds.) Vol. 7, pp 447–473, Academic Press, New York.

Bernasconi, C. F. (1976) *Relaxation Kinetics*, Academic Press, New York.

Crane, F. L., & Beinert, H. (1956) *J. Biol. Chem. 219*, 717–731.

Engel, P. C. (1990) *Chemistry and Biochemistry of Flavoenzymes* (Muller, F., Ed.) Vol. III, pp 597–655, CRC Press, Inc., London.

Frerman, F. E., Miziorko, H. M., & Beckman, J. D. (1980) *J. Biol. Chem. 255*, 11192–11198.

Ghisla, G., & Massey, V. (1989) *Eur. J. Biochem. 181*, 1–17.

Ghisla, S., Thorpe, C., & Massey, V. (1984) *Biochemistry 23*, 3154–3161.

Hammes, G. G. (1982) *Enzyme Catalysis and Regulation*, Academic Press, New York.

Johnson, J. K., & Srivastava, D. K. (1993) *Biochemistry 32*, 8004–8013.

Johnson, J. K., Wang, Z. X., & Srivastava, D. K. (1992) *Biochemistry 31*, 10564–10575.

Johnson, J. K., Kumar, N. R., & Srivastava, D. K. (1993) *Biochemistry 32*,11575–11585.

Kim, J. P., Wang, M., & Paschke, R. (1993) *Proc. Natl. Acad. Sci. U.S.A. 90*, 7523–7527.

Lau, S. M., Brantley, R. K., & Thorpe, C. (1989) *Biochemistry 28*, 8255–8262.

Lehman, T. C., Hale, D. E., Bhala, A., & Thorpe, C. (1990) *Anal. Biochem. 186*, 280–284.

McFarland, J. T., Lee, M., Reinsch, J., & Raven, W. (1982) *Biochemistry 21*, 1224–1229.

Nishino, T., Nishino, T., Schopfer, L. M., & Massey, V. (1989) *J. Biol. Chem. 264*, 2518–2527.

Schopfer, L. M., Massey, V., Ghisla, S., & Thorpe, C. (1988) *Biochemistry 27*, 6599–6611.

Strickland, S., Palmer, G., & Massey, V. (1975) *J. Biol. Chem. 250*, 4048–4052.

Thorpe, C., Matthews, R. G., & Williams, C. H., Jr. (1979) *Biochemistry 18*, 331–337.

Vanhove, G., Veldhoven, P. P. V., Eyssen, H. J., & Mannaerts, G. P. (1993) *Biochem. J. 292*, 23–30.

Walsh, C. (1979) *Enzymatic Reaction Mechanisms*, W. H. Freeman and Company, New York.

Wang, R., & Thorpe, C. (1991) *Biochemistry 30*, 7895–7901.

Understand the Chemical Basis of Human Diseases with

Pathophysiology for Chemists

New from the American Chemical Society

A Self-Paced, Audio-Cassette Learning Program from the American Chemical Society

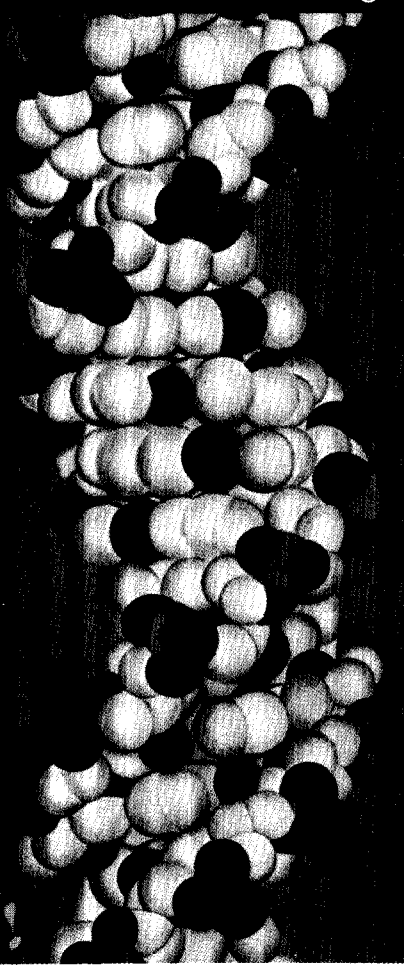

Perfect for Clinical Chemists, Medical Laboratory Technicians, Medical Technologists, Clinical Pathologists, and Chemists Interested in the Fascinating Area of Pathophysiology

Here's What You'll Learn About:

- The underlying basis for disorder in carbohydrate metabolism
- Diseases caused by defects in amino acid metabolism
- The relationship between disease and proteins
- The powerful analytical tools that have helped us to see how the immune system defends the body against disease
- How, under different circumstances, the immune system can malfunction and produce disease
- Enzymes and their roles in disease
- Nutritional diseases
- Coronary disease
- Diseases caused by abnormalities in coagulation and fibrinolysis

For a **FREE** brochure describing this information-packed course, mail or FAX the coupon below. Or, call the ACS Continuing Education Office at (202) 872-6124 or (800) 227-5558.

ORDER TODAY!

YES! Please send me a detailed brochure describing ***Pathophysiology for Chemists***, the new self-paced learning program from ACS.

NAME _____

TITLE _____

ORGANIZATION _____

ADDRESS _____

CITY/STATE/ZIP _____

Mail to: **American Chemical Society**, Dept. of Continuing Education,
1155 Sixteenth Street, N.W., Washington, DC 20036
FAX: (202) 872-6336